EXPERIMENTAL AND NUMERICAL STUDIES OF ALUMINUM-ALUMINA COMPOSITES

A Dissertation

by

PRADEEP GUDLUR

Submitted to the Office of Graduate Studies of
Texas A&M University
in partial fulfillment of the requirements for the degree of

DOCTOR OF PHILOSOPHY

Chair of Committee,	Anastasia Muliana
Co-Chair of Committee,	Miladin Radovic
Committee Members,	J.N.Reddy
	Tahir Cagin
Interim Head of Department,	Andreas Polycarpou

August 2013

Major Subject: Mechanical Engineering

ABSTRACT

The preliminary goal of this study is to determine the effects of processing conditions, compositions and microstructural morphologies of the constituents on the physical and thermo-mechanical properties of alumina (Al_2O_3) reinforced aluminum (Al) composites. Composites with 0, 5, 10, 20 and 25 vol% Al_2O_3 were manufactured using powder metallurgy method. The elastic properties (Young's and shear modulus) and the coefficient of thermal expansion (CTE) of the composites were determined using Resonant Ultrasound Spectroscopy (RUS) and Thermo Mechanical Analyzer (TMA) respectively at various temperatures. Increasing compacting pressure improved relative density (or lowered porosity) of the composites. Furthermore, increasing the Al_2O_3 vol% in the composite increased the elastic moduli and reduced the CTE of the composites. Increasing the testing temperature from 25 to 450 ^{o}C, significantly reduced the elastic moduli of the composites, while the CTE of the composites changed only slightly with temperatures.

Secondly, the goal of this study is to determine the effect of microstructures on the effective thermo-mechanical properties of the manufactured Al-Al_2O_3 composites using finite element (FE) method. Software OOF was used to convert the SEM micrographs of the manufactured composites to FE meshed models, which were then used to determine the effective elastic modulus and CTE. It was observed that, effective modulus dropped by 19.7% when porosity increased by 2.3%; while the effective CTE was mildly affected by the porosity. Additionally, the effect of residual stress on the effective thermo-mechanical properties was studied, and the stress free temperature of the composites was determined.

Another objective of this study is to examine the stress-strain response of Al-Al_2O_3 composites due to compressive loads at various temperatures. Elastic modulus, yield stress and strain hardening parameters were determined from the stress-strain curves and their dependency on temperature, porosity and volume fraction were studied. The experimental results were compared with the numerical results. It was observed that high-localized stresses were present near the pores and at the interfaces between Al and Al_2O_3 constituents.

Finally, functionally graded materials (FGMs) with varying Al_2O_3 concentration (0, 5and 10 vol%) in Al were manufactured; and their stress-strain response and CTE were determined at various temperatures.

DEDICATION

To my family

ACKNOWLEDGEMENTS

I would like to thank my adviser Dr. Muliana and co-adviser Dr. Radovic for their continuous guidance and support throughout the course of this research, without them this dissertation would not be possible. Apart from mechanical engineering concepts, humility and patience are the two most important qualities I learnt from them. I thank my committee members, Dr. Reddy and Dr. Cagin, for their valuable inputs and support throughout my association with them.

Many thanks to Rogelio Benitez for his help in setting up the compression testing machine, when I had a difficult time doing so. I would like to thank my friends Chien Hong Lin, Udaya Sunku, Varun Desireddi, Venakta Vasiraju and Kamran Khan for giving me a great time at the university. Thanks also go to my colleagues and department faculty, for making my time at Texas A&M University a pleasant one. I also want to extend my gratitude to the Air Force Office of Scientific Research (AFOSR) and National Science Foundation (NSF), for providing the necessary funds for this project.

NOMENCLATURE

BHN	Brinell Hardness Number
CPMMC	Ceramic Particulate Metal Matrix Composite
CTE	Coefficient of Thermal Expansion
FE	Finite Element
FG	Functionally Graded
FGM	Functionally Graded Material
OOF	Object Oriented Finite Element method
RUS	Resonant Ultrasound Spectroscopy
SEM	Scanning Electron Microscope
TMA	Thermo Mechanical Analyzer
VF	Volume Fraction
XRD	Xray Diffraction

TABLE OF CONTENTS

LIST OF FIGURES

LIST OF TABLES

CHAPTER I

INTRODUCTION AND LITERATURE REVIEW

1.1. Motivation

Ceramic particles are often used as reinforcement in metal matrix composites to increase their strength, hardness, stiffness, chemical stability, thermal stability and thermal resistivity. Ceramic particle-reinforced metal matrix composites (CPMMCs) provide a good combination of strength attained from the ceramic reinforcements and toughness due to the underlying metal matrix [1]. Hence, CPMMCs find various applications in machining, cutting, wear resistance, aerospace and military applications. Often they are the only choice in applications that involve high temperatures, such as thermal barrier coatings, turbine engines, and piston rod, due to their good resistance to elevated temperatures.

Aluminum is a widely used matrix material in CPMMCs primarily because of its low weight, low cost and ease of fabrication. The preferred reinforcement in CPMMCs should have high modulus, low density, good wettability, proper shape with a certain aspect ratio to minimize stress concentration, and thermal expansion coefficient comparable to that of the metal matrix to minimize the development of internal stresses due to temperature changes. Often the reinforcements in CPMMCs are either oxides or carbides and of them the most widely used are alumina (Al_2O_3), silicon carbide (SiC) and graphite in various configurations such as discontinuous particles or continuous agglomerates [2]. Aluminum based CPMMCs are designed for high temperature applications (up to 450-500^{o}C) and the properties of the constituents in CPMMCs can change significantly with temperatures, affecting the performance of these composites. Hence, it is essential to understand their thermal and mechanical properties at elevated temperatures.

1.2. Problem statement

In this study, we examine the thermo-mechanical properties of Al-Al_2O_3 composites at elevated temperatures. Al-Al_2O_3 composites are fabricated using powder metallurgy technique because this technique has proven to be favorable for distributing Al_2O_3 particles uniformly in Al matrix and for its ability to fabricate the material into practically any shape [3, 4]. As we are dealing with ceramics and metals which have drastic differences in the thermal and mechanical properties, residual stresses are developed during the manufacturing process of these composites, which is mainly due to cooling from sintering temperature to room temperature. The magnitude of these residual stresses could be significant and can induce cracking of ceramic particles or yielding of metal matrix in the composites. Thus, it is often necessary to take into account the effect of residual stresses when designing a composite for structural applications in order to avoid premature failure of the component.

Microscale parameters of the composite (particle size, particle distribution, porosity and volume fraction) can influence the overall behavior of the composite. For example, porosity can significantly reduce the stiffness of the composite and hence is not desired for most of the structural applications as it can lead to degradation in the performance. However, for applications where thermal insulation is the main criteria (e.g. thermal barrier coatings), porosity is desirable as it can decrease the effective thermal conductivity and increase thermal resistivity of the material. Hence, it is important to study and optimize the microstructural parameters of the composite in order to get the desired overall thermo-mechanical response of composites.

Various micromechanical models have been formulated for predicting the overall properties and response of metal matrix composites, while incorporating microstructural parameters of the composites. Most of available micromechanics models are derived based on idealized or simplified microstructures, which only give crude approximation of the overall response of composites. To increase accuracy in predicting the overall response of composites, it is necessary to include more detailed microstructural parameters, such as distribution of constituents, and size, shape, and location of inclusions. Only limited number of studies has been conducted to predict the overall response of the composites by incorporating the detailed microstructural morphologies of the metal matrix composites.

1.3. Literature review

Al-Al_2O_3 composites are widely used composite materials because of their appealing properties, i.e., in the physical (high modulus to density ratio), mechanical (high stiffness and Poisons' ratio), and tribological properties (low wear rate and high coefficient of friction). Hence they find applications in automotive (e.g. brake discs, drums, back-plate, engine block, piston and gearbox parts [5, 6]), aerospace (e.g. fan exit guide vane in gas turbine engine, rotating blade sleeves in helicopters and flight control hydraulic manifolds [5]), kitchen utilities (e.g. food and beverages packing) and sports applications (e.g. bike and golf components [5]). The overall response of these composites depends not only on their microstructural parameters but also on their processing methods. This section presents current knowledge related to the fabrication, properties characteristics, and microstructural modeling of Al-Al_2O_3 composites.

1.3.1. Composite fabrication

Common processing methods to manufacture Al-Al_2O_3 composites are squeeze casting (also called as metal infiltration), reactive processing, spray deposition and powder metallurgy. Powder metallurgy method involves mixing two or more powders, compacting them in a die and sintering at high temperatures. Hot pressing, Spark plasma sintering (SPS), Hot Isostatic

Pressing (HIP) and Cold Isostatic Pressing (CIP), use powder metallurgy techniques to manufacture composite materials.

In this work, Al-Al_2O_3 composite samples were fabricated with 0, 5, 10, 15, 20 and 25vol% of Al_2O_3 using powder metallurgy technique: blending and cold compacting of the powders followed by sintering process. Powder metallurgy method was used because, this technique offers complete control over the distribution of particles in the metal matrix e.g. uniform or random or gradient distribution, thus allowing tailorability of the physical and mechanical properties of the composite and to satisfy its design criteria and intended application. Powder metallurgy has the advantage of producing high quality parts cost effectively with good precision even for complex shapes, and has the ability to fabricate the material into practically any shape [3, 4]. The disadvantage of using powder metallurgy method is that one cannot produce fully dense composite samples [3, 7, 8]. Rahimian et al. [8, 9] used powder metallurgy technique to fabricate Al-Al_2O_3 composites and determined the effect of parameters such as Al_2O_3 particle size, concentration, sintering temperature and sintering time on the relative density, and room temperature mechanical and physical properties of these composites. Using finer Al_2O_3 particles and sintering temperature of 600^{o}C, composites with relative density ranging from 96.5-99% were manufactured. Banjuraizah et al. [10] and Schaffer and Hall [11] found that nitrogen is the best atmosphere for sintering Al to produce samples with high relative density, followed by argon. However, the use of nitrogen forms aluminum nitride (AlN) as an additional phase; and hence inert argon gas was used in our study to sinter the composite pallets. The wetting properties, interfacial energy and bonding strength of Al-Al_2O_3 composite system were studied by Ksiazek et al. [12], Kou et al. [13] and Zhang et al. [14]. The main problem limiting the wetting of Al by Al_2O_3 is the oxidation of Al. Hence, inert atmosphere was maintained throughout the sintering process to reduce the oxidation of Al.

1.3.2. Interface characteristics

CPMMCs have higher strength, mainly because ceramic particles (which are stiffer than the matrix material) bear more percentage of the load than the matrix material. Decohesion at the interface of ceramic and metal matrix needs to be avoided, to have any considerable improvement in strength for the CPMMC over the bare metal. Aluminum reinforced with alumina is a good choice for CPMMC, as there is no interfacial reaction (alumina is stable inside aluminum matrix), good wettability and the CTE mismatch is not that high to cause decohesion at the interface.

Though ceramics and metals have drastic differences in properties, it is well documented in literature that Al and Al_2O_3 adhere strongly to each other without the presence of any interface or thin intermediate transition layers. Saiz et al. [15] studied the wetting properties, strength and the interface characteristics of Al-Al_2O_3. They found that Al & Al_2O_3 form a very strong interface when they were joined in solid state (i.e. when Al is not a molten liquid). The strength of the bond at the interface increased with increase in bonding temperature, and the highest strength was obtained when bonding temperature was close to the melting temperature of aluminum (650^{o}C). Bonding strength decreased if the bonding temperature was increased beyond the melting point of aluminum. Saiz et al. [15] also noticed the presence of unbounded regions at the interface, which were identified by EDS (Energy Dispersive Xray Spectroscopy) as amorphous aluminum oxide, formed as islands close to the interface because of the oxidation of aluminum. These aluminum oxide islands can decrease the strength of the interface; however, the number of aluminum oxide islands can be minimized if the bonding temperature is brought closer to the melting temperature of aluminum. Timsit et al. [16], using HREM (High Resolution Electron Microscopy), also observed the absence of any intermediate chemical transition layers at the interface between Al and Al_2O_3. Furthermore, they too found the presence of amorphous aluminum oxide islands near the interface, indicating the oxidation of aluminum. These aluminum oxide islands create an extremely rough interface with short irregular ledges, whose heights usually are close to two interplanar spacings of aluminum.

1.3.3. Overall behavior of composite at macroscopic level

The overall properties of composites depend strongly on the microstructural morphologies, compositions of the constituents, and processing methods. The effect of alumina volume content on the porosity, experimental density and theoretical density of the composite was studied by Kok [17]. He found that the experimental density increased linearly with increasing alumina content; but the increase was smaller than predicted by rule of mixtures. The main reason for this was attributed to the porosity present in the composite, which increased with increase in alumina content, thereby limiting the increase in experimental density. McCormick et al. [18], manufactured Al-Al_2O_3 composite using a liquid metal infiltration method. They studied the effect of alumina particle size on the tensile strength, flexural strength and fracture toughness of these composites and found that these properties increase with a decrease in particle size. On the other hand, particle content did not seem to affect these properties significantly, however Young's modulus was observed to increase with increase in Al_2O_3 particle content of the composite, and for the composite with 46vol% of alumina, the effective modulus was observed to be 1.8 times that of pure aluminum. The yield stress of Al-Al_2O_3 composites is higher than that of pure aluminum because of hardening of the aluminum matrix, which is mainly due to increase in dislocation density. Arsenault and Haasen [19], showed that increase in dislocation density strongly depends on the CTE mismatch between the constituents. Hence the higher the CTE mismatch, the higher the yield stress of the composite. Another factor that greatly influences the yield stress of the composite is the distribution of alumina particles in the aluminum matrix. Mazen and Ahmed [7] used a modified powder metallurgy method to manufacture Al-Al_2O_3 composites, which involves mixing of aluminum and alumina powders thoroughly, followed by hot pressing and hot extrusion operations. Further, they compared the tensile properties of Al-Al_2O_3 composites manufactured using powder metallurgy method with the conventional casting method. They showed that composites manufactured using their powder metallurgy method had higher yield strength, tensile strength and % elongation than those manufactured using casting technique.

Haleem et al. [20] manufactured Al-Al_2O_3 composites using powder metallurgy method with varying Al_2O_3 (3, 6, 9 and 12 wt%) and determined the compression strength and Brinell hardness number at room temperature. They found that for the 12 wt% Al_2O_3 reinforced composite, there was an increase of 54% in compression strength and 89% increase in the Brinell hardness number from those of the unreinforced pure aluminum samples.

Kouzeli and Dunand [21] manufactured Al-Al_2O_3 composite samples with varying Al_2O_3 (34 to 37 vol %) using metal infiltration method. They conducted uniaxial compression tests at different temperatures (25^{o}C to 600^{o}C) and at very high strain rates (10^{-3} to 1 s^{-1}). They found that composite samples exhibited a significant increase in strength than that of pure aluminum sample, mainly because of increase in the flow stress which were attributed to two mechanisms, viz., direct strengthening (because of load sharing between ceramic particles and metal) and hardening (because of interactions between forest dislocations).

Ganguly [22] conducted tensile testing and uniaxial compression testing on Al-Al_2O_3 composites at three different temperatures 300^{o}C, 425^{o}C and 550^{o}C. They reported that, at lower temperatures (300^{o}C), the dominant void nucleation mechanism was particle cracking, whereas at higher temperatures (550^{o}C) the dominant mechanism was interfacial decohesion. In between 300^{o}C and 550^{o}C both particle cracking and interfacial decohesion were responsible for void evolution. The strain rate did not have much effect on ductility or failure strain of the composite, however higher strain rates lead to failure through particle cracking. The composites were less prone to particle cracking at higher temperatures (or lower strain rates) because increase in temperature (or decrease in strain rate) lead to lower flow stress in aluminum and in turn lower stress in alumina particles. Ductility was reduced when there were particle clusters in the composite sample, as damage occurred through coalescence of voids near the particle clusters.

RUS (Resonant Ultrasound spectroscopy) is a dynamic testing method used to determine the elastic properties of solid objects (metals, ceramics or composites). Radovic et al. [23] had shown that RUS is more accurate in determining the elastic properties than conventional static testing methods (e.g. Nano Indentation and 4 point bending test). The reason for this is that RUS requires low amplitude loading, which makes it possible for a reliable determination of the linear elastic moduli because of a significantly low stress and strain values involved. RUS is a non-destructive testing method. Unlike the conventional testing methods, RUS is a great tool to determine all the components of stiffness tensor in one run, even if the material is anisotropic. However, for asymmetric samples (i.e. samples with complex geometry with no axis of symmetry), RUS is tedious and complicated.

1. 3.4. Numerical analysis to determine the behavior of composite at microscale level

In order to improve our understanding of the overall mechanical response of composites, it is necessary to incorporate the detailed microstructural characteristics of the composites through the use of micromechanical models. The advantages of using the micromechanical models in modeling the overall mechanical response of the composites are: it allows incorporating different distribution of constituents in the composite and their behaviors, micromechanical models can capture the stress and strain concentrations (or discontinuities) at various locations within the microstructures of the composites and also take the residual stresses into account in predicting the overall response of the composites.

Several micromechanical models have been developed to predict the overall behavior of metal matrix composites. The first class of micromechanics models is derived based on a volume-averaging scheme of idealized composite microstructures, i.e., rule of mixtures, unit cell methods, Mori-Tanaka model, and other simplified micromechanical models. Examples are Aboudi [24], Eischen and Torquato [25], Dvorak et al. [26], Torquato [27], Dvorak and Srinivas [28], Yin and Sun [29], and Muliana [30]. These micromechanical models consider simpler microstructural geometries of the composites, such as assuming dilute or periodic distributions of particles, of spherical or ellipsoidal shape, in the homogeneous matrix. In some of the above micromechanics models the effect of particle interactions on the overall elastic properties of composites was also incorporated.

The second class of micromechanical models uses finite element (FE) method to obtain the effective thermo-mechanical properties of composites, in which the microstructures of composites having ordered or random distribution of idealized particles' geometries are meshed using finite elements. This approach allows examining the effect of the shape and size of the inclusions and spacing between the inclusions on the overall physical and mechanical properties of the composites. Examples of such micromechanical models can be found in Kari et al. [31], Pierard et al. [32], Barello and Levesque [33], and Khan et al. [34]. The actual microstructures of composites often contain constituents with complex shapes and various sizes distributed randomly and depend strongly on their manufacturing methods, which are significantly different than the idealized microstructures considered in the above two classes of micromechanical models. The third class of micromechanical models considers incorporating the actual microstructures of the composites in predicting their overall physical and mechanical properties. Scanning Electron Microscope (SEM) is commonly used in order to provide microstructural images of the studied composites. These images are then used to generate finite element meshes of the composite microstructures. The advantage of using this method is that it allows incorporating the details of the microstructure in predicting the overall response of the composites. In our study, we used an image based finite element software called OOF, where the actual microstructure of the composite obtained from the SEM images of the manufactured composites were used to generate FE meshed models. Intricate details of the microstructure were also taken into consideration, as the software replicates the actual microstructure accurately while generating meshes, which were then used in finite element analysis. Wojnar [35] discussed the basic steps involved in image acquisition and performing image analysis; whereas Langer et al. [36] and Chawla et al. [37] gave a detailed description of how software OOF can be used in creating different pixel groups for different phases based on difference in contrast in the SEM micrograph, assigning material properties to pixel groups and generating finite element meshes.

The third class of micromechanical models can incorporate detailed information of the effect of microstructural morphologies on the overall performance of composites; however, this approach has not been fully explored. Only limited number of studies has been conducted using this approach, for e.g. using software OOF, Chawla et al. [37, 38] determined the modulus and CTE of SiC reinforced Al matrix composites and Bakshi et al. [39] determined the thermal conductivity of carbon nanotube reinforced aluminum composites. Dong et al. [40] studied the tensile modulus of polypropylene-organoclay nanocomposites, while Wang et al. [41] obtained the modulus and thermal conductivity for plasma sprayed zirconia coatings. Zimmerman et al. [42] characterized the thermal residual stress in polycrystalline alumina and Cannillo et al. [43] determined thermal residual stress in alumina phase of borosilicate-alumina composite.

1.3.5. Effect of residual stress

Another factor that could influence the mechanical properties and performance of Al-Al_2O_3 composites is the residual stress, which in this study was considered as an existing stress in absence of external mechanical loads, generated during processing of the composites. The residual stresses, also known as thermal stresses, can arise as temperature changes during the composite processing. The source of the thermal stress is a significant mismatch in the free deformations (expansion or contraction) of the aluminum and alumina constituents due to temperature changes, which are measured through the use of thermal expansion coefficients. High thermal stresses can cause yielding in ductile constituents such as in the aluminum, while high tensile thermal stresses can induce cracking in the brittle constituents such as alumina. Both plastic deformation and cracking of microconstituents can affect the overall mechanical properties and performance of the composites. The residual stresses can also be formed during the compacting stage using powder metallurgy technique, in which the applied pressures could cause a plastic deformation in the aluminum constituent.

Several studies were conducted on understanding the effect of residual stresses on the overall mechanical properties of CPMMC composites. Aresnault and Taya [44] used a model based on Eshelby's theory and predicted the magnitude of thermal residual stress developed in Al-SiC composites, when they were cooled from fabrication temperature. They compared these theoretical results with experimental data obtained by doing tension and compression testing on Al-SiC and found them to be in close agreement with each other. Bruno et al. [45] and Fitzpatrick et al. [46] used neutron diffraction methods on Al-SiC composites to determine the residual stresses that develop during the fabrication process of the composite. They found that because of this thermal residual stresses, there was net tension in the matrix and compression in the reinforcement. They performed tensile test on the composite and found that plastic deformation actually relaxed the residual stresses effectively to zero in both matrix and particle phases. Further they found that any additional increase in strains of more than 0.2% could even reverse these residual stresses, i.e. compression in matrix and tension in reinforcement. Another set of tests conducted by them revealed that if the samples were first plastically deformed and then heat treated, the residual stress increased giving an opposite effect. From this observation they concluded that plastic deformation and heat treatment operations have opposite effects on residual stresses. Fernandez-Castrillo et al. [47], used Neutron and Synchroton radiation diffraction in order to characterize the residual stress evolution with plastic deformation in Al-Al_2O_3 composites. They observed that for plastic deformations (tensile or compressive) that were less than 2%, residual stress dropped by about 120 MPa. On the other hand, for high compressive strains (>2%) residual stresses increased instead of decreasing. Whereas, for high tensile strains (>2%), residual stresses did not change significantly.

1.3.6. Functionally graded material (FGM)

FGMs are useful when one end of the material needs to withstand harsh environments and the other end of the material needs to be connected to a substrate/base material (e.g. metal) that is needed to be protected from those harsh environments. FGMs are mostly ceramic particle reinforced metal matrix composites (CPMMCs) in which the ceramic composition is spatially varied in a controlled manner to obtain the desired spatial variation of macroscopic properties [48]. FGMs made of aluminum and alumina constituents typically find applications where a) one end of the material is exposed to high temperature and the other end is connected to a dissimilar material (e.g. metal) which needs to be protected from high temperatures and b) one end of the material needs to be hard (like a ceramic) and withstand high wear and tear; and the other end is connected to a dissimilar material (e.g. metal) which doesn’t have high wear resistance.

Various methods have been in use for manufacturing FGMs from a long time. Die Compacting (also called as Powder Stacking) is one of the earliest and simplest methods in which powders having different compositions are stacked one over the other as layers, compacted and later sintered [49]. The disadvantages of this method are the gradient distribution may not be smooth (as compaction and sintering stages can alter the distribution) and the size of the FGM and the number of layers are limited by the size of the die used [50]. However, this method involves less cost and can be used at laboratory level to study the overall thermo-mechanical properties of the FGM. For commercial purposes more advanced processing methods are used for fabricating FGMs. Centrifugal stir casting [51], Centrifugal Sedimentation [52, 53], Physical Vapor Deposition [54] and Chemical Vapor Deposition [55] are some of the more prominent methods used in the industry to manufacture FGMs.

Shabana et al. [56] used die compaction method followed by pressureless sintering method to manufacture Ni-Al_2O_3 FGM. They studied the shrinkage differences between different layers during the sintering process and the challenges these shrinkage differences bring in terms of altering the distribution, development of stresses, crack initiation and causing delamination. Rajan et al. [51] manufactured Al-SiC FGMs as thick hollow cylinders using centrifugal stir casting method and measured the hardness variation in the radial direction from 115 BHN to 145 BHN when the SiC composition varied gradually from 0 to 40vol%. Fukui et al. [57] manufactured Al-Al_3Ni FGM samples by centrifugal casting method. Using a combination of rule of mixtures and flexural forced resonant frequency method, they measured modulus of FGM to vary from 81 and 101 GPa in the gradient direction corresponding to 15.2 and 43.2vol% of Al_3Ni. Ben-Oumrane et al. [58] used theoretical methods to measure the displacement and axial stress distribution in bending of Al-Al_2O_3 FGM thick beams. As expected, they observed that deflections were more for metal rich beam than the ceramic rich beam. They also found that the axial stress distribution with the beam thickness was found to vary linearly in pure Al material and vary nonlinearly for the FGM.

1.4. Objectives and contributions of this work

The overall objectives of this project are:

- to manufacture Al-Al_2O_3 composites with different processing conditions and constituent morphologies,
- to characterize their elastic, plastic and thermal behavior (by defining their modulus, Poisson's, yield stress, strengthening coefficient(K), strain hardening coefficient(n) and CTE) and
- to study the micro and macro scale parameters affecting their behavior at various temperatures.

In this work, Al-Al_2O_3 composite samples were fabricated with 0, 5, 10, 15, 20 and 25vol% of Al_2O_3 through blending, cold compacting, and sintering processes. The structural (phase composition, microstructure, relative density and porosity), mechanical (elastic and shear moduli) and thermal (CTE) properties of the composites were then characterized at several isothermal temperatures: 25-450 ^{o}C. The effect of alumina particle size on the relative density of composites has been widely reported in the literature [8, 9, 18], however very limited work has been done to determine the effect of aluminum particle size on the thermo-mechanical properties of composites, and hence in this study two aluminum powders with different particle sizes are considered. Though the mechanical properties of Al-Al_2O_3 composite system using conventional methods (e.g. tensile test and three point bending test) are well documented in literature, most of the studies are done at room temperature [59-61]. The significance of this work is that a nondestructive testing method like RUS is used to measure the mechanical properties of Al-Al_2O_3 composites at various temperatures. The main advantages of using RUS over these conventional methods are: (i) it requires low amplitude loading, which makes a reliable determination of the linear elastic moduli because of a significantly low stress and strain values involved, and (ii) it gives all components of the elastic stiffness tensor in one run of the experiment [62]. The CTE of Al- Al_2O_3 composite system and their dependency on temperature and various microscale parameters are also studied using a Thermo-mechanical Analyzer.

Only limited number of studies has been conducted to predict the overall response of the composites by incorporating the detailed microstructural morphologies of the metal matrix composites. Of these, image based finite element software OOF is one of the latest techniques to incorporate detailed microstructural morphologies of the composite into finite element meshed models. This study uses software OOF to convert the actual microstructure of the composite obtained from the SEM images to FE meshed models. FE analyses are performed in order to predict the overall behavior of the composites, including incorporating the effect of residual stresses and plastic deformations on the overall response of composites.

CHAPTER II

EXPERIMENTAL METHODOLOGIES

2.1. Fabrication of Al-Al_2O_3 composite pallets

Powder metallurgy technique was used for manufacturing the composite specimens. The composite specimens were fabricated with different volume contents of alumina: 0, 5, 10, 15, 20, and 25vol%. To achieve a specific volume fraction of the composite (see Eq. 2.1), proper amounts of aluminum and alumina powders were first weighed in a balance ($m_{Al}$and $m_{Al_2O_3}$) and were then added to a glass vial.

$$\text{VF of } Al_2O_3 = \left(\frac{m_{Al_2O_3}}{\rho_{Al_2O_3}}\right) \Big/ \left(\frac{m_{Al_2O_3}}{\rho_{Al_2O_3}} + \frac{m_{Al}}{\rho_{Al}}\right) \qquad (2.1)$$

where $\rho_{Al_2O_3} = 3.96\ \text{g/cc}$ and $\rho_{Al} = 2.6989\ \text{g/cc}$.

The processing involved the following steps:

2.1.1. Blending

US Stoneware ball-milling machine was used to mix the aluminum and alumina powders. Alumina cylinders were used as grinding media to mix them consistently and the ball to powder ratio used was 2.5 (by mass). It was run at a speed of 100rpm for 3 hours. 35 wt% ethanol was added to the powders before ball milling, which acts as a process control agent by minimizing cold welding between powder particles (thus smaller particles can’t weld and become bigger particles), reduces the possibility of formation of agglomerates and also helps in formation of uniform particle size distribution throughout the powder [63]. After blending, the vials were left open to the outside atmosphere for 3 to 4 hours, to allow the evaporation of ethyl alcohol.

2.1.2. Compacting

Once ethyl alcohol evaporates from the powders, a hydraulic press was used to cold press the powders for 30 minutes at a constant uniaxial pressure in a cylindrical die. During this process the powder starts to become a solid due to compacting pressure. The effects of compacting pressure on the overall density and porosity of composite were also studied.

2.1.3. Sintering

The cold pressed specimens were further sintered in a quartz furnace (MTI, CA) at 600 ^{o}C. The samples were heated from room temperature to 600^{0}C at a rate of 5^{0}C/min , sintered at that temperature for 2 hours and then allowed to cool back naturally to room temperature. As aluminum is prone to oxidation at higher temperatures, during this entire process an inert atmosphere was maintained in the quartz tube by sending an ultra-high purity Argon gas, which helps in preventing the oxidation of aluminum. During the sintering process, bonds tend to form and pores are going to be filled with atoms of aluminum or alumina, as diffusion is higher at higher temperatures. Figure 2.1 shows the sintered composite samples using two different dies of diameters 25.4 mm and 12.7 mm respectively.

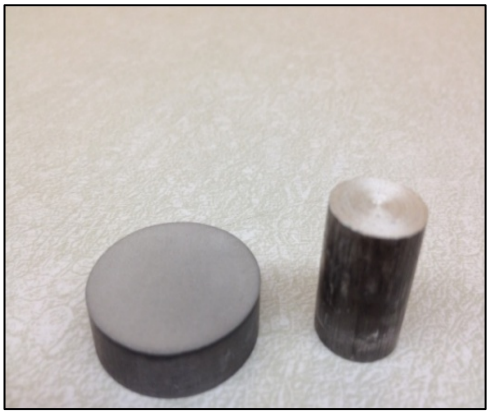

Figure.2.1. Sintered Al-Al_2O_3 composite samples of diameters 25.4 mm and 12.7 mm respectively

2.2. Phase composition and microstructural characterization

The microstructure and composition of the processed composites were characterized by Scanning Electron Microscopy, SEM, (JSM-7500F, JEOL, CA); X-ray Diffraction, XRD, (Bruker-AXS D8 Advanced Bragg-Brentano X-ray Powder Diffractometer, Bruker, WI) and particle imaging analysis software (ImageJ, NIH, USA).

2.2.1. X-ray Diffraction (XRD)

XRD was used to perform qualitative (to identify the phases present in the composite) and semi quantitative analyses (to identify the vol% of each phase in the composite). Bruker Powder short arm diffractometer was used to perform XRD on the samples. The samples were mounted on an arm (called goinometer) that was rotated in such a way that if the incident x-rays were at an angle θ then the diffracted x-rays were collected by a detector at an angle 2θ. The sample surface was scanned from $2\theta=20^0$ to $2\theta=70^0$ with a step size of 0.015^0 at a rate of 0.0375 degrees/sec; and LynxEye detector was used to record the XRD patterns. Different atomic planes in the sample diffract the x-rays at different angle, which can interfere with each other and can form peaks in the intensity (according to Bragg's law). The distribution of these peaks depends on the arrangement of atoms in the crystal structure. Hence, by recording the intensity of these diffracted rays and studying the distribution of these peaks, one can determine crystal structure and the phases present by using the XRD analysis software EVA (Bruker-AXS Diffrac EVA, Bruker, WI). XRD patterns in Figures 2.2 and 2.3 show that except aluminum and alumina, no other phases were present in fabricated composites. Aluminum as expected had face center cubic (FCC) crystal structure and alumina had orthorhombic crystal structure.

The black lines in Figure 2.2 and 2.3 show the XRD spectrum for the composite samples with10% and 20% alumina content and the colored lines were overlaid using EVA software to match the peaks of the black line exactly at the same 2θ angle. From this, one can identify the elements and phases present on the surface of composite specimens. It can be seen that peaks appear at fixed 2-theta angle for both the volume fractions of composites, and only the intensity of the peaks varies from one volume fraction to another. For aluminum, peaks appear at 37.5, 45 and 65 degrees; whereas for alumina peaks appear at 25.5, 35, 37.8, 43.5, 52.5, 57.5, 61.5, 66.5 and 68.5 degrees. As the volume content of alumina increases the height of aluminum peaks decreases whereas height of alumina peaks increases. The split peaks observed in Figures 2.2 and 2.3 are because of an overlapping of two peaks belonging to kalpha1 and kalpha2 wavelengths and the width/gap between the split peaks is observed to increase as the 2-theta angle increases. Upon identifying the phases present in the composite using XRD patterns, the amount of each phase present in the composite was determined using the XRD analysis software EVA. By adjusting the intensity of the overlaid color lines to match the intensity of the black spectrum line exactly, the quantity of each element or phase can be accurately determined.

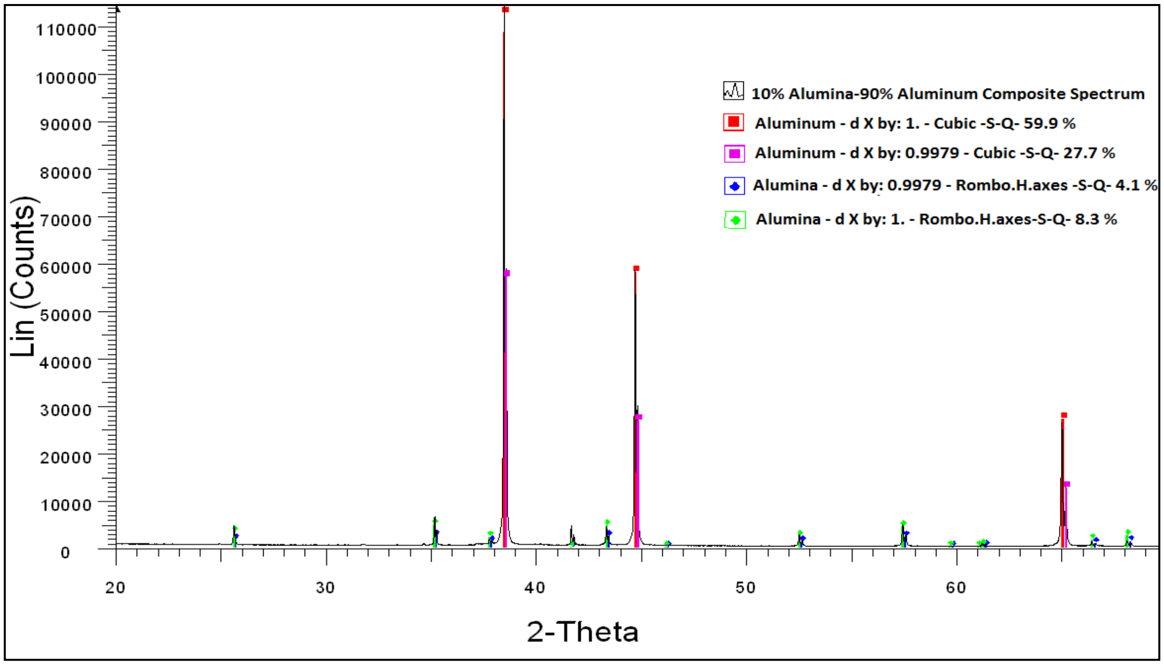

Figure 2.2. XRD spectrums for 10% volume fraction of alumina composite pallet

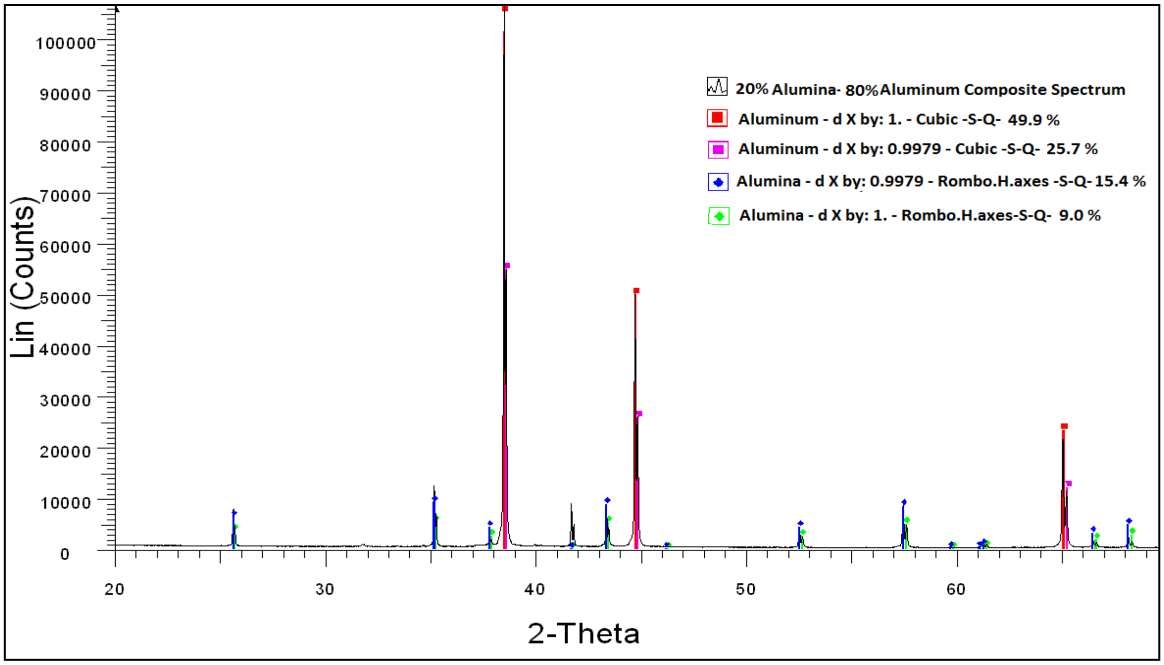

Figure 2.3. XRD spectrums for 20% volume fraction of alumina composite pallet

2.2.2. Scanning Electron Microscopy (SEM)

Jeol 7500 Field Emission Scanning electron microscope was used to study the microstructure of the composite. The conventional microscopes use light (photons) to reflect the surface of the object where as an electron microscope uses electron beam to scan the surface of the object. When electron beam impinges on the surface of the object, secondary electrons, backscattered electrons, cathadoluminescence, X-rays and Auger electrons are produced as shown in Figure 2.4, which are captured by corresponding detectors that in turn give information about the topology of the specimen. Sample preparation included cutting the composite pallet using a diamond saw, polishing the cut piece with 180, 320, 600, 1200, and 4000 sand papers along with diamond suspension particles of size 10, 3, 1, 0.1µm. SEM images were taken using Secondary electron (SE) and Backscattered (BS) detectors. Figures 2.5a-b show selected but typical SE and BS images of the composites reinforced with 10vol% Al_2O_3 respectively, while

Figures 2.6a-b show SE and BS images with 20vol% Al_2O_3 respectively. The dark gray phase in Figures 2.5b and 2.6b is Al_2O_3, while the light gray phase is aluminum. Here again, no other phases are identified, except alumina and aluminum. The dark black areas are pores.

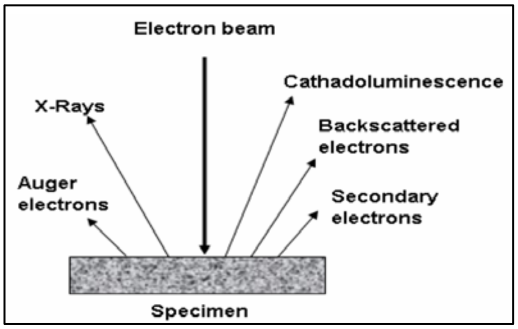

Figure 2.4. Different electrons produced when electron beam is impinged on SEM

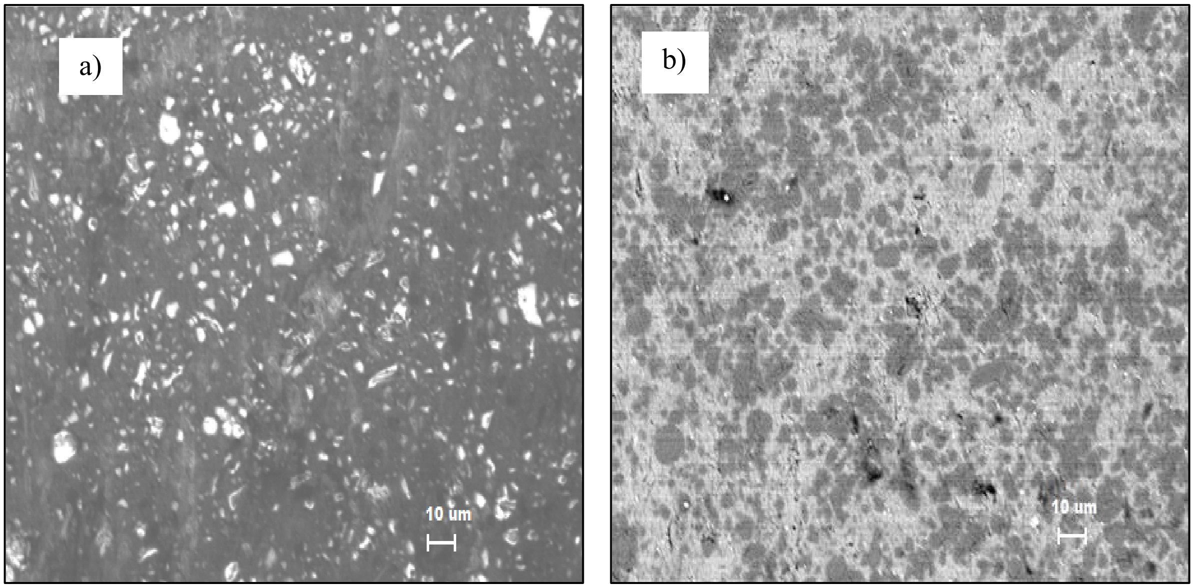

Figure 2.5 (a) Secondary electron and (b) Backscattered electron micrographs of 10 vol% alumina composite samples obtained from SEM

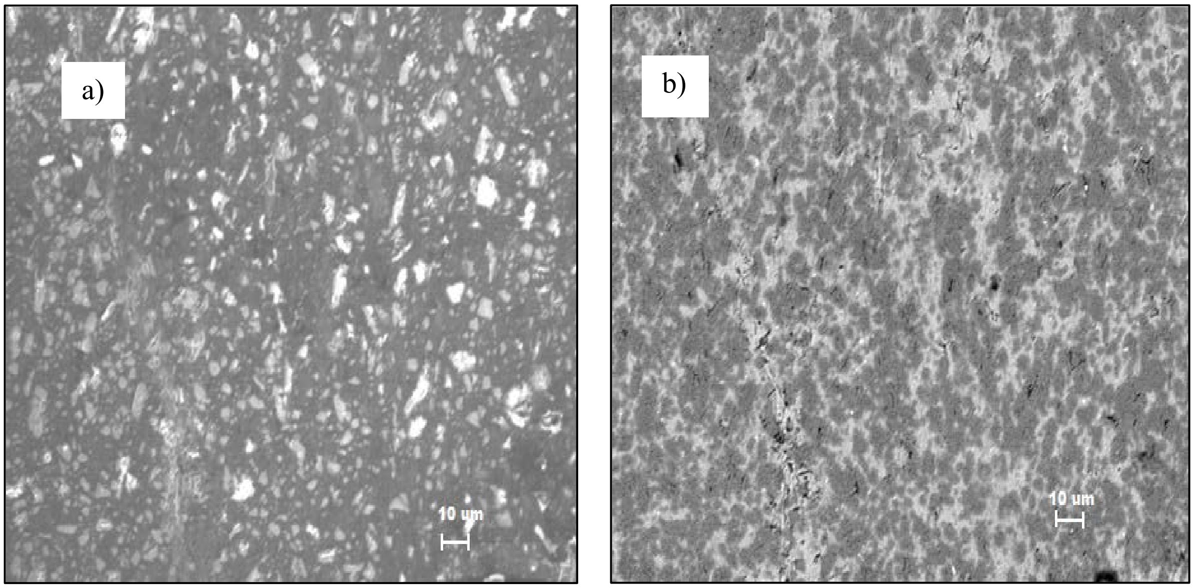

Figure 2.6 (a) Secondary electron and (b) Backscattered electron micrographs of 20 vol% alumina composite samples obtained from SEM

2.2.3. Image analysis

Image analysis was conducted using ImageJ software, to verify the volume fraction of the alumina in the composite pallet. The SE micrographs of 10% and 20% samples shown in Figures 2.5a and 2.6a, respectively, were converted to their equivalent binary images using ImageJ, as shown in Figure 2.7. Using ImageJ software, the area fraction (i.e. the ratio of area occupied by black regions in the rectangle to the total area of the rectangle) was calculated from these binary images. Further discussion on using ImageJ software is given in the Appendix. The comparison of alumina concentrations obtained using the ImageJ and XRD with the expected concentrations in the composite sample is shown in Table 2.1.

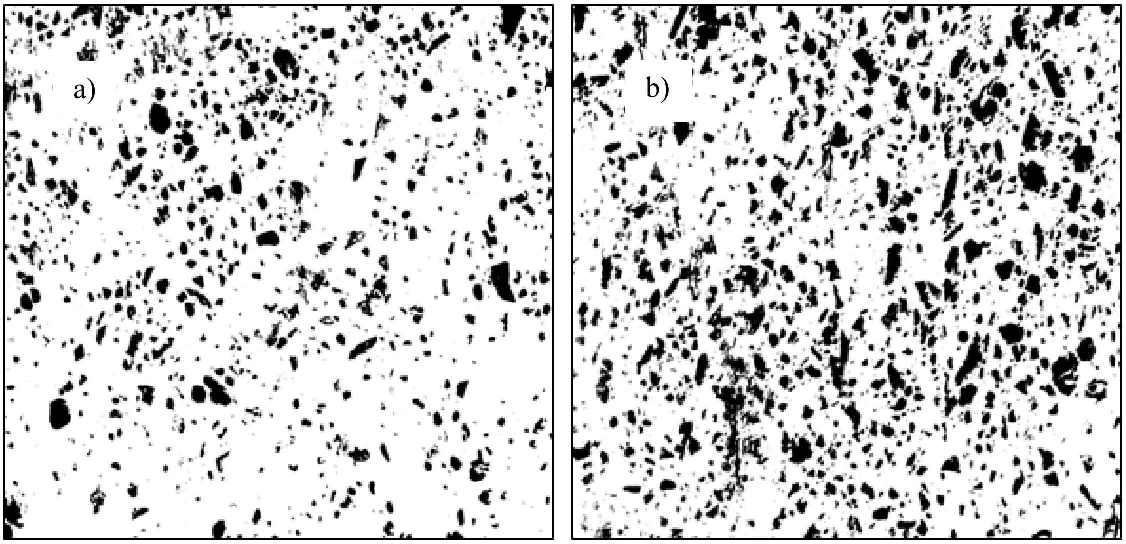

Figure 2.7. Binary images of (a) 10%, (b) 20%, composite sample used with ImageJ

Table 2.1. Comparison of alumina content measured using XRD and ImageJ with expected concentration in the composite pallet

alumina content in composite (as expected)	alumina content in composite (from XRD)	alumina content in composite (from imageJ)
10%	12.4%	12.71%
20%	24.4%	22.59%

2.3. Fabrication of functionally graded material (FGM)

Al- Al_2O_3 FGM samples were manufactured using die compacting method by stacking different powders one over the other as layers and compacting them all at once. For the CTE measurement, FGM samples were prepared by adding 2 grams of 0, 5, 10, 15, 20 & 25vol% of composite powders each to a 25.4 mm die one layer above another just by tapping them. Whereas for compression testing, FGM samples were prepared by adding 2.8 grams of 0, 5 and 10vol% composite powders each to a 12.7 mm die one layer above another just by tapping them. Once all the layers of powder were added to the die, a compacting pressure of 502 MPa was applied to all the layers. The compacted cylindrical FGM specimen was then sintered at 600^{o}C for 2 hours in an argon environment.

The distribution of particles in the manufactured FGM was then determined using SEM. The sample preparation for microscope included, cutting the FGM sample with a low speed diamond saw and polishing it carefully with diamond suspension particles of size 0.1 μm until an extremely flat and smooth surface was obtained. Inside the stage of the microscope, the sample was aligned in such a way that the thickness of the FGM sample (the direction in which different layers of alumina concentration are present) was along the y-direction of the microscope. Using the microscope, pictures were taken at different locations by moving the microscope stage only in the y-direction (i.e. the thickness direction for FGM sample). A gradient in the distribution of alumina particles was observed from one picture to another, which is as shown in the Fig. 2.8. From left to right alumina concentration is increasing from 0 to 25vol%. The fabricated FGM samples were tested for thermo-mechanical properties to determine the macroscopic behavior of the FGM (Chapter VI).

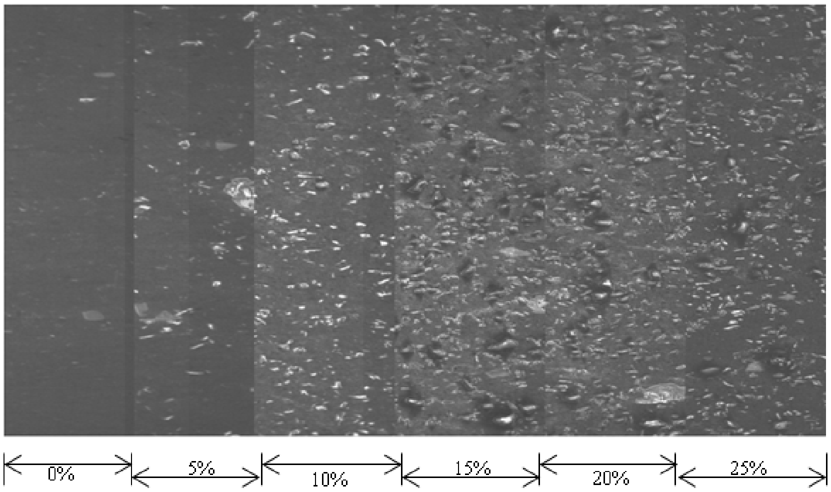

Figure. 2.8. SEM image of functionally gradient Al-Al$_2$0$_3$ composite material taken at various locations and overlaid the pictures on top of each other

2.4. Relative density and porosity

The relative density of the manufactured composite specimen was determined by taking the ratio of the experimental density of the composite pallet to the theoretical density as:

$$\% \text{ Relative density} = \left(\frac{\text{Experimental density}}{\text{Theoretical density}}\right) * 100 \qquad (2.2)$$

The experimental density was calculated using two methods. The first method, further referred as direct method, was based on measuring the mass of the dry sample (m_{dry}), diameter (d), and height (h) of the cylindrical composite specimen. The relative density was then determined as follows:

$$\text{Experimental density} = \frac{\mathrm{m_{dry}}}{\left(\pi \frac{\mathrm{d}^2}{4} \mathrm{h}\right)} \qquad (2.3)$$

The second method that was used to measure the experimental density of the specimen, further referred to as alcohol immersion method, was based on Archimedes' principle. As per ASTM C 20 [64], the specimen was immersed in a beaker filled with 200 proof ethanol and placed in a desiccator. A vacuum pump was connected to the desiccator during which the open pores of the composite specimen were filled with ethanol removing any oxygen present in them. The beaker was removed from the desiccator after 5 minutes and was placed in normal atmosphere for 30 minutes to stabilize the temperature of ethanol. At the end of this waiting period, temperature was noted in order to get the density of ethanol at that temperature. The beaker was placed on the weighing machine, the weight was tarred, and then a wire was suspended from top of the weighing machine as shown in the Figure 2.9. The weight of the wire was noted as the "wire weight". The sample was exchanged from bottom of the beaker onto the hanging wire and the "suspended weight" of the sample was noted. Throughout this entire process, care was taken to submerge the sample completely in ethanol. The sample was removed from ethanol, its surfaces were blotted with a towel and left in normal atmosphere exactly for 60 seconds and then measured the weight as the “wet weight”. The Archimedean density, percentage open and closed porosity were measured using equations 2.4-2.6.

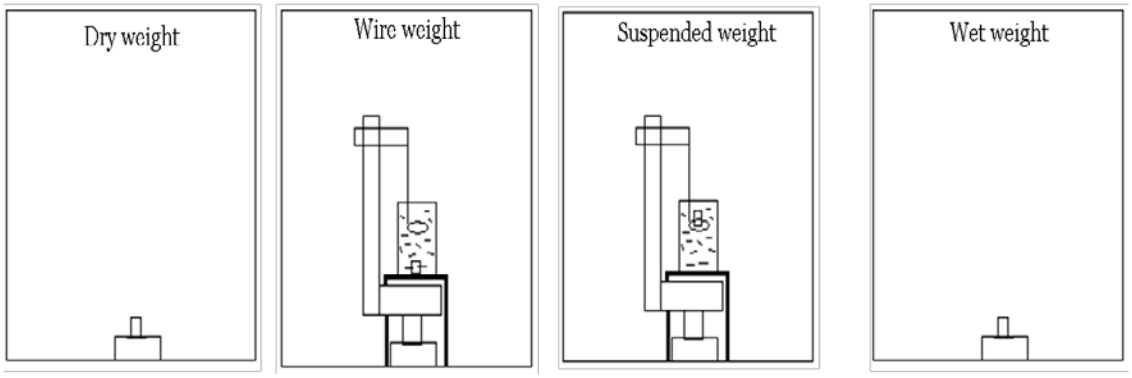

Figure 2.9. Schematic of alcohol immersion method

The experimental density of the sample was calculated as:

$$\text{Experimental density} = \frac{m_{dry} * \rho_{ethanol}}{m_{wet} - m_{suspended} + m_{wire}} \qquad (2.4)$$

where m_{dry} was dry mass of the sample, $m_{suspended}$ was mass of the sample suspended in 200 proof ethanol, m_{wet} was the mass of the sample after soaking in the ethanol, m_{wire} was mass of suspending system, and $\rho_{ethanol}$ was density of the ethanol. This method also allows determination of open and closed porosity according to the following:

$$\%\ \text{Open Porosity} = \frac{m_{wet} - m_{dry}}{m_{wet} - m_{suspended} + m_{wire}} * 100 \qquad (2.5)$$

$$\%\ \text{Closed porosity} = 100 - \%\ \text{Relative density} - \%\ \text{Open porosity} \qquad (2.6)$$

2.5. Experimental setup

2.5.1. Resonant Ultrasound Spectroscopy

Mechanical properties like elastic (Young's) modulus, Poisson's ratio, shear modulus and bulk modulus were measured at various temperatures using a nondestructive testing method called RUS (Resonant Ultrasonic Spectrometry).

RUS is a non-destructive testing method for determining the components of the elastic stiffness tensor of a solid by using mechanical resonance phenomena on a sample of known mass, geometry and dimensions [23, 65, 66]. For this study, a modified RUS apparatus was used to determine the natural frequencies of the samples at elevated temperatures. The composite specimens 5mm in diameter and 7mm in thickness were placed on 3 transducers as shown in Figure 2.10, of which one of them sends out an ultrasonic wave and the other two transducers record the natural frequencies at which the sample was vibrating. A graph was plotted with frequency on x-axis and amplitude on the y-axis, as shown in Figure 2.11. The actual frequency (experimental frequency) of the composite sample was recorded by the two receiving transducers to identify resonant peaks at the frequencies that correspond to the natural resonant frequencies of the examined composite pallet for different vibration modes. For determining the elastic moduli of the composite material from resonant spectra, it was assumed that the composite was isotropic and thus only two elastic constants, i.e., C_{11} and C_{44} were required. From the known sample dimensions, density, and a set of "guessed" elastic constants C_{11}, and C_{44}, an approximate spectrum was calculated, as shown in Figure 2.11. Multidimensional software Quasar RuSpec (Magnaflux Quasar Systems, Albuquerque, NM) that iteratively minimizes error between the measured and calculated resonant peaks by changing the initially "guessed" elastic constants, was used to determine elastic constants for the set of measured resonant frequencies of the sample. The elastic constants C_{11} and C_{44} were further used to calculate Young's and shear moduli of the composite samples. It is worth noting here that the root-mean-square (RMS) error between 20 measured and calculated resonant frequencies, never exceeded 0.4% for all tested samples. RUS produces very low amplitude strains (approximately of the order of 10^{-7}) and consequently low stresses in the sample [66].

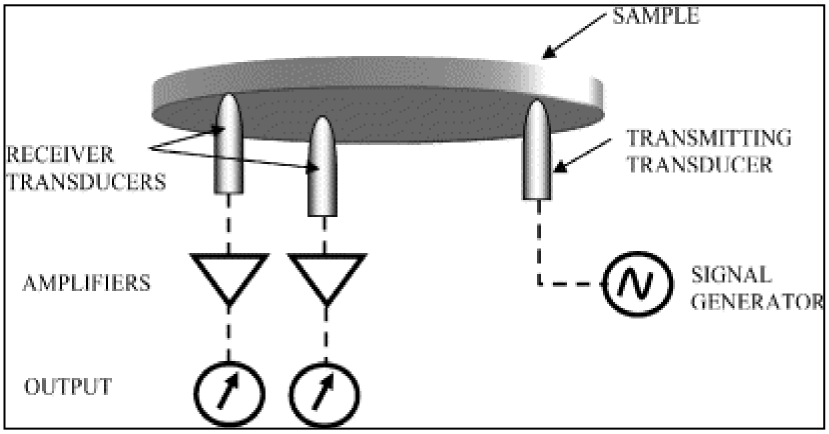

Figure 2.10. Schematic of RUS

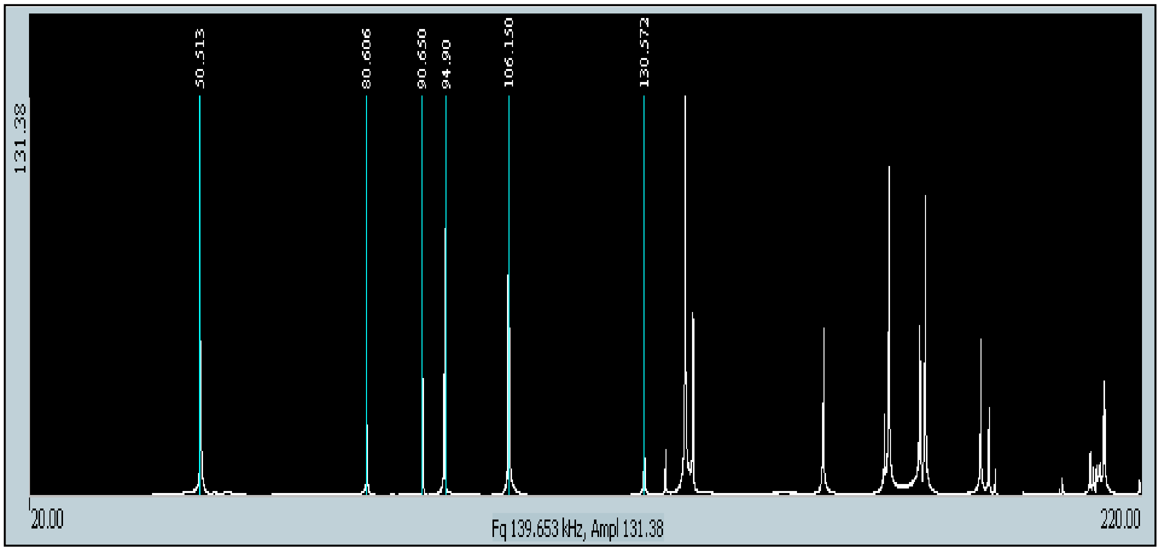

Figure 2.11. RUS of 0% alumina content composite sample

2.5.2. Thermo-mechanical Analyzer

Thermal expansion coefficient (CTE) of composite specimen was determined using a TA Q400 instrument, Figure 2.12a. A small rectangular piece of 8mmx5mmx3mm was cut from the composite pallet using a low speed diamond saw. The surfaces were polished using 600, 1200 and 4000 grid sand paper and care had been taken to achieve uniform thickness throughout the rectangular specimen. The sample was loaded into the furnace of TA Q400 instrument onto a quartz stage. The quartz stage consists of a thermocouple to measure the temperature and a probe to measure the thickness change (µm) with change in temperature, as shown in Figure 2.12b. A constant force of 0.1 N was applied through the probe to ensure a perfect contact between the probe and specimen at all times. The furnace was heated at a rate of 5°C/min from -20°C to 400°C and was cooled at a rate of 4.6°C/min from 400°C to -20°C, as given by the ASTM E 831 [67]. The software gives the variation of dimension change (µm) with temperature during both heating and cooling process. CTE (µm/m°C) of the specimen was calculated by taking the ratio of slope of dimension change (µm) vs temperature curve with the thickness (m) of the specimen at room temperature.

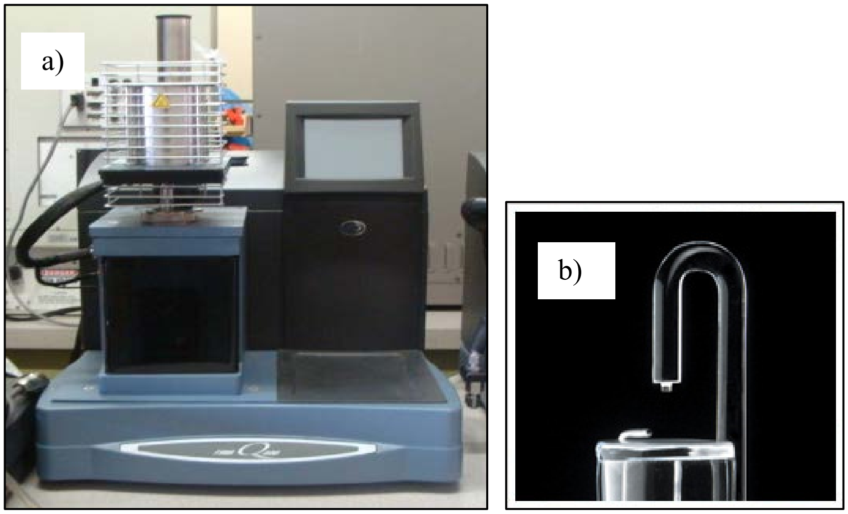

Figure 2.12 a) Thermo-mechanical Analyzer and b) probes to measure temperature and strain

2.5.3. Compression Testing

Aluminum-alumina samples were prepared as described in section 2.1. Cylindrical die of 12.5 mm diameter was used to make the 0, 5 and 10vol% alumina concentration composite samples. The surfaces of the sample need to be extremely flat and parallel to get accurate stress-strain curves. Hence the specimens were polished until their surfaces were flat.

The composite samples with 0, 5 and 10vol% alumina concentrations were subjected to compression testing at room temperature and elevated temperature cases. MTS compression testing machine, (MTS 810, MTS, MN) as shown in Figure 2.13a, was used. Displacement control mode was used to compress the prepared Aluminum-Alumina composites samples on the MTS machine. Load cell of the machine records the compressive force applied through crossheads, and axial stress was calculated by dividing the compressive force with the cross-sectional area. The corresponding axial strains until 5% were recorded using an extensometer (Figure 2.13b), which were used to determine the elastic modulus. Once this strain was reached, the samples were unloaded at the same strain rate (crossheads were moved away from each other). Axial stress and axial strain during the unloading step were again recorded using load cell and extensometer data respectively. Engineering stress-strain curves were thus plotted.

When the samples were getting compressed, the surfaces of the sample that were in contact with the compression plate act as if they were constrained in the lateral direction because of friction, whereas the rest of the cylindrical specimen tries to bulge freely in the lateral direction, which results in deforming the specimen into a barrel shape. In order to have a homogeneous deformation, friction between the sample surface and the compression plate was minimized [2-4] by using a lubricant (LPS2, LPS laboratories, GA).

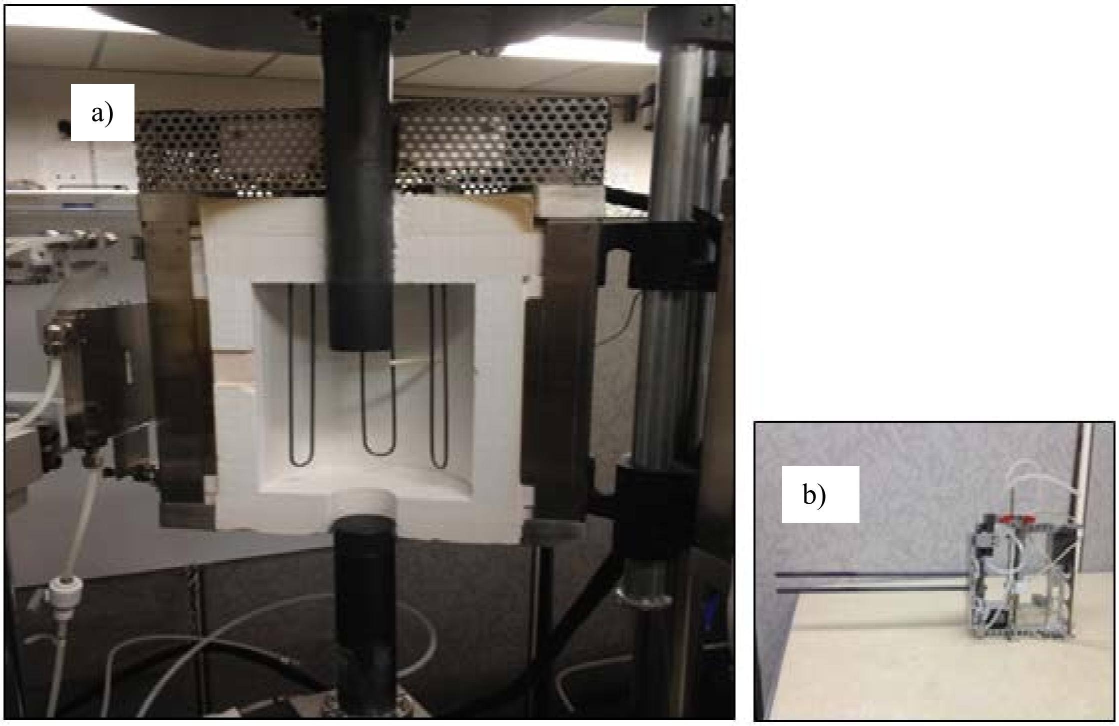

Figure 2.13 a) MTS high temperature compression testing machine and b) high temperature extensometer

CHAPTER III

PHYSICAL, MECHANICAL, AND THERMAL PROPERTIES OF COMPOSITES*

3.1. Characterization of physical properties and the effect of compacting pressure, particle size and alumina volume fraction on the physical properties of the composite

We have examined the effects of compacting pressure, particle size and volume fraction on the overall density and porosity of the composite, using two different sets of Al-Al_2O_3 composite systems. For the first system of composites which are labeled as composite system A, 99.5% pure aluminum powder of -100+325 mesh size (Alfa Aesar, MA) as shown in Figure 3.1a and 99.7% pure alumina (Sigma-Aldrich, MO) with average particle size of 10µm as shown in Figure 3.1b were used. The aluminum particles appeared to be mostly spherical and varied in size approximately between 1µm and 50µm in diameter whereas the alumina particles were about 10µm and were polygonal in shape. The above Al-Al_2O_3 composites are labeled in this Chapter as A-XX, where XX is the nominal volume percentage of Al_2O_3. Pure aluminum powder was examined using x-ray diffraction (XRD) which showed that the starting aluminum powder contained 2.3 vol% of alumina (Table 1). The Al-Al_2O_3 composite system B – further labeled in this Chapter as B-XX, where XX is the nominal volume content of Al_2O_3 – were processed using 97.5% pure aluminum powder with smaller particle size, i.e. 3-4.5µm (Alfa Aesar, MA) as shown in Figure 3.1c , while using the same alumina powder as that of the composite system A (Figure 3.1b). Powder metallurgy technique as explained in Chapter II was used for manufacturing the composite specimens.

---

* Reprinted with permission from Gudlur P, Forness A, Lentz J, Radovic M, Muliana A. Thermal and mechanical properties of Al/Al203 composites at elevated temperatures. Materials Science and Engineering A, 531(1), 18-27. Copyright 2011by Elsevier.

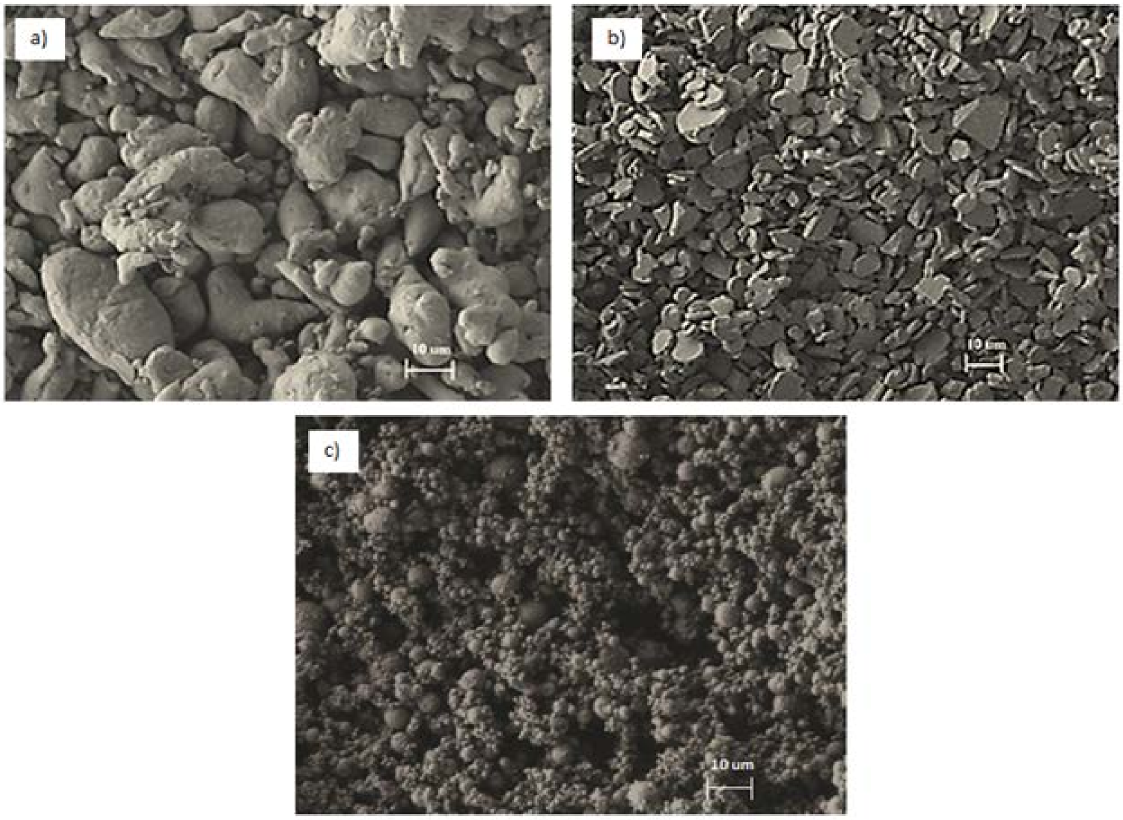

Figure 3.1. Secondary electron SEM images of (a) aluminum and (b) alumina powders of composite A; and (c) aluminum powder of composite B

The effect of compacting pressure and volume fraction on the relative density and porosity were studied on 0, 5, 10, 20 & 25% alumina concentrations for both the composite systems A and B. Three different compacting pressures viz. 212, 425 and 502 MPa were used for the composite system A, while for the composite system B compacting pressures of 502 and 580 MPa were considered. Prior to sintering, the relative green body density (RGBD) of each specimen was determined from the size and mass of green bodies and using them in Equations [2.1] and [2.2], as explained in Chapter II. Figure 3.2 shows the RGBD of the composite system A as a function of volume content of alumina for different cold pressing pressure. As expected, RGBD increases with increase in compacting pressure for all the volume fractions of the composite. In addition, the RGBD of the samples decreases with increasing amount of alumina in the composite samples, regardless of the cold compacting pressure used. Aluminum particles used have larger size than alumina, preventing the aluminum to fill empty gaps around alumina particles during compacting stage, thereby contributing to the porosity. Hence, when the alumina volume content increases, there is an increased chance of having an alumina particle surrounded by alumina particles thereby leaving interstitial gaps in between them. Furthermore, the drop in RGBD due to increase in alumina content has decreased, as compacting pressure was increased from 212 to 502 MPa.

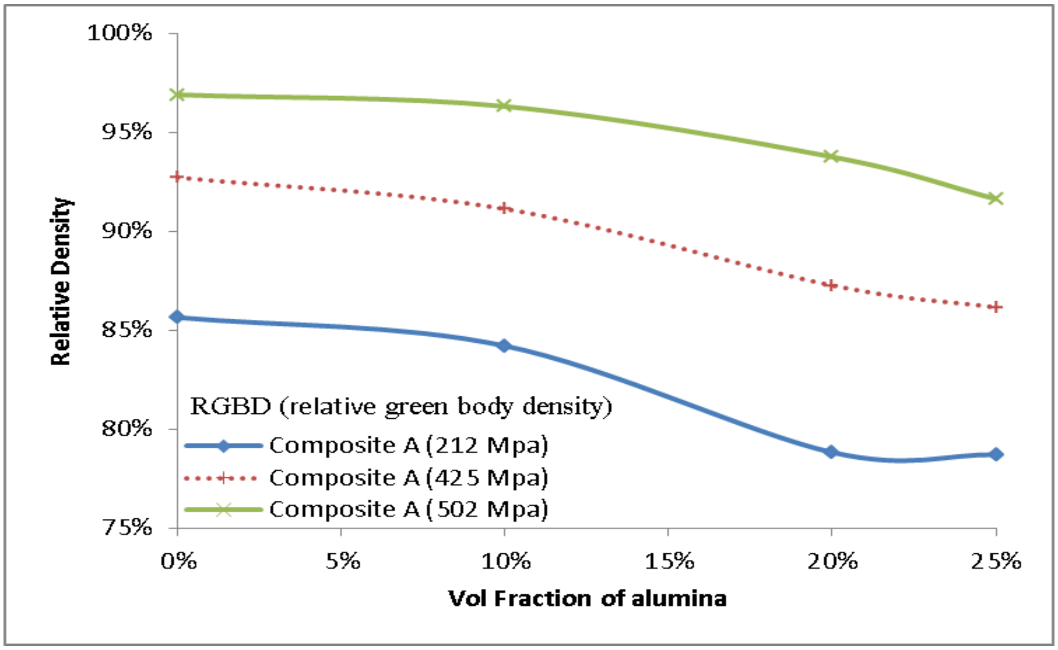

Figure 3.2. Effect of compacting pressure and volume fraction of alumina on relative green body density of composite A

The relative density after sintering (RDAS) of the composite system A is plotted as a function of alumina content for different cold compaction pressures in Figure 3.3. Two methods were used to determine RDAS – direct method (Equations [2.1] and [2.2]) and alcohol immersion method (Equations [2.1] and [2.3]) – which were described in more detail in Chapter II. Direct measurement of relative density was observed to be always less than that of alcohol measurement. This is because direct measurement of relative density assumes the sample surface to remain perfectly flat whereas in actual reality the sample surface tends to be uneven leading to larger sample volume thereby giving lower density. As expected, the relative density of the samples after sintering increased with increasing pressure. With increase in ceramic content, relative density has decreased for all the samples and the drop in relative density was observed to decrease, as compacting pressure was increased from 212 to 502 MPa. Figure 3.4 shows a comparison of relative green body density (RGBD) and relative density after sintering (RDAS) for the composite system A at different compacting pressures and volume contents of alumina in the composite. RDAS was higher than RGBD (density increased due to sintering) for any compacting pressure used. This is due to higher atomic diffusion at elevated temperatures during sintering, leading to better densities. It can be seen that both RGBD and RDAS increase with increasing cold compaction pressure. In addition, the difference between the RGBD and RDAS decreases as compacting pressure increases, or in other words, at high cold compacting pressures the contribution of sintering process to increase the relative density of the composite is less significant when compared to the contribution of high compacting pressures. Furthermore, it can be seen that as volume content of alumina increases in the composite, both RGBD and RDAS decrease for all compacting pressures used.

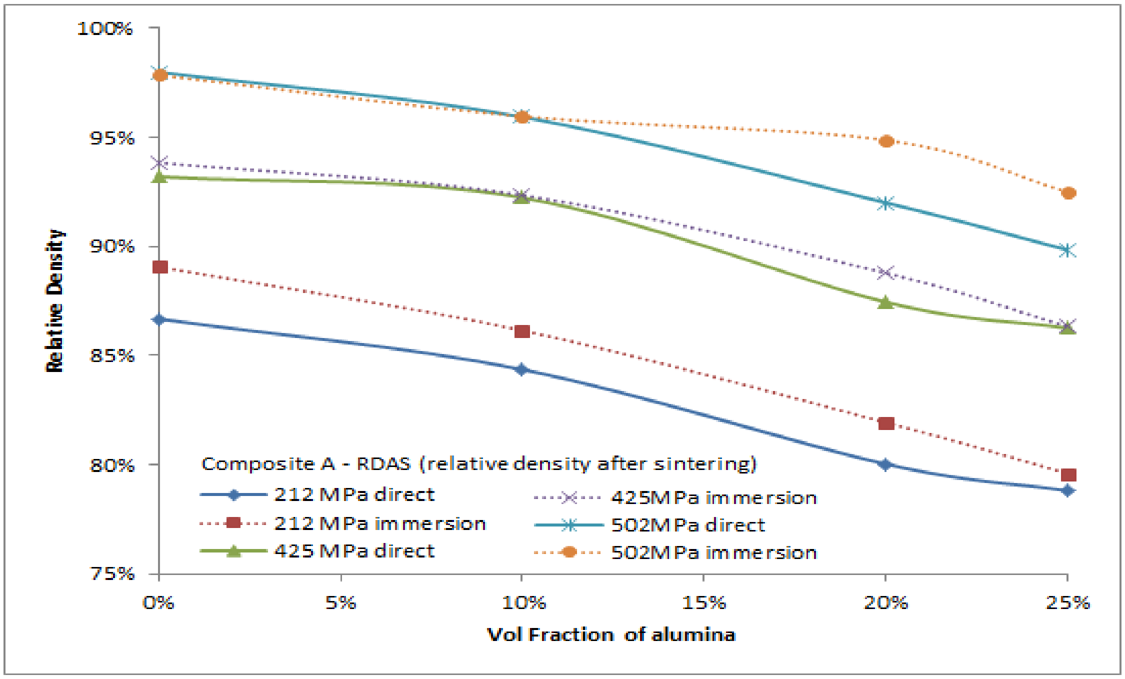

Figure 3.3. Comparison of direct and immersion methods for measuring relative density; and determination of effect of compacting pressure and volume fraction on relative density after sintering for composite system A

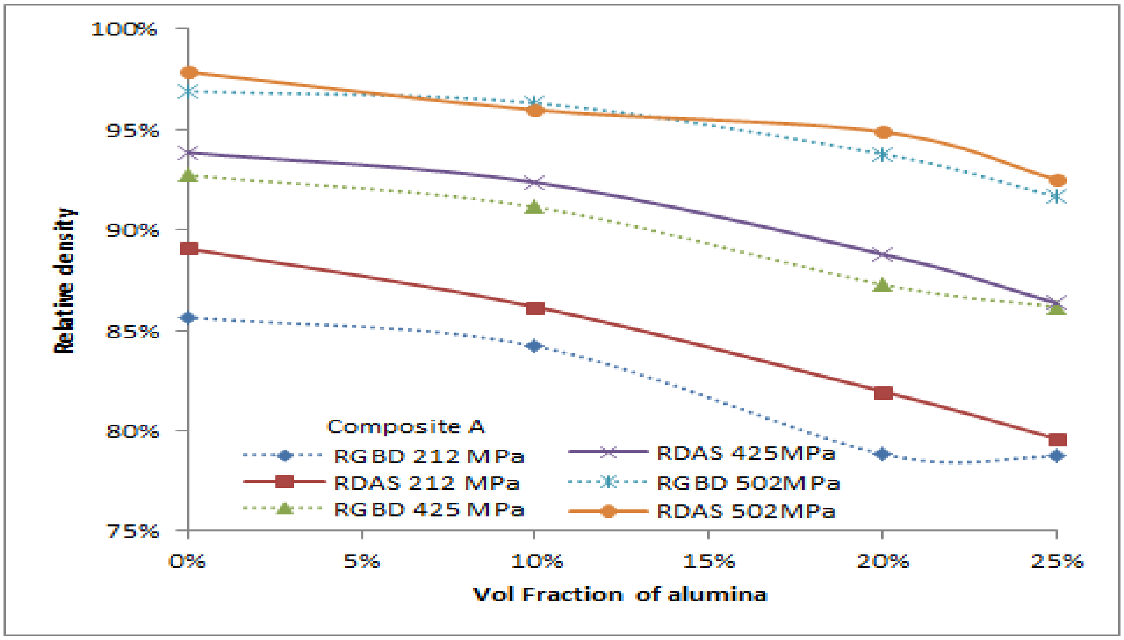

Figure 3.4. Effect of compacting pressure and volume fraction on relative density after sintering for composite system A

Figure 3.5 shows the effect of compacting pressure and volume fraction of alumina on porosity of composite system A. It can be seen that an increase in the alumina content results in an increase in the overall and open porosities of the samples and a slight decrease in the closed porosity. In addition, Figure 3.5 also illustrates that the open porosity, closed porosity and overall porosity decrease with an increase in compacting pressure for any particular volume content of the ceramic phase.

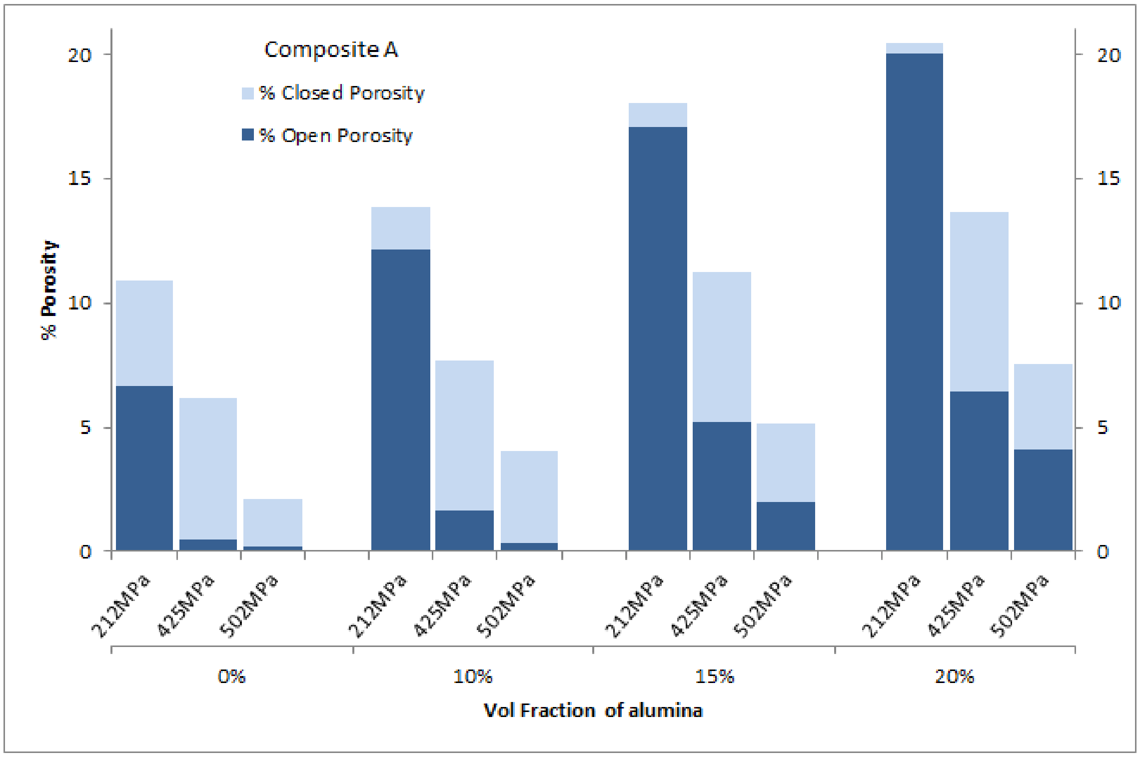

Figure 3.5. Effect of compacting pressure and volume fraction of alumina on open, closed and overall porosity of composite A

The relative density decreases with increase in volume content of alumina, due to an increase in porosity as discussed previously. Whereas an increase in compacting pressure, reduces the porosity and thereby increases relative density. Alternative way to reduce porosity or improve density for higher content of alumina is to have smaller size of aluminum particles or to have larger size of alumina particles. The size difference between aluminum and alumina particles should be in such a way that, if there are any gaps formed by a cluster of alumina particles, the aluminum particles should have size small enough to go into those gaps. Figure 3.6 shows the variation of relative density with compacting pressure and alumina content, when finer aluminum powder was used to process composite system B. It is observed that relative density after sintering does not decrease with increasing volume content of alumina as in the case of composite system A (Figure 3.4), for both cold compaction pressures used. This is as expected, since the smaller particles of aluminum can easily fill the empty gaps between the alumina particles during the cold pressing of green bodies. It is worth noting here that edges of composite specimens B-0 and B-10 were always chipped off, even after several attempts of cold pressing, thus resulting in apparently lower RGBDs measured using direct method, as seen in Figure 3.6. Although increase in cold pressing pressure from 212 MPa to 502 MPa significantly improves RGBD of the composite system A, as shown in Figure 3.4, further increase of cold pressing pressure from 502 MPa to 580 MPa changes the RGBD for less than 2% in the composite system B, as seen in Figure 3.6.

The overall porosity in the composite system B is less than 6% and increasing compacting pressures can reduce the porosity by up to 2%, Figure 3.7. The high porosity for specimens with 0% alumina content is due to low compaction after the cold pressing operation. It is worth noting here that only one specimen was used for each testing condition.

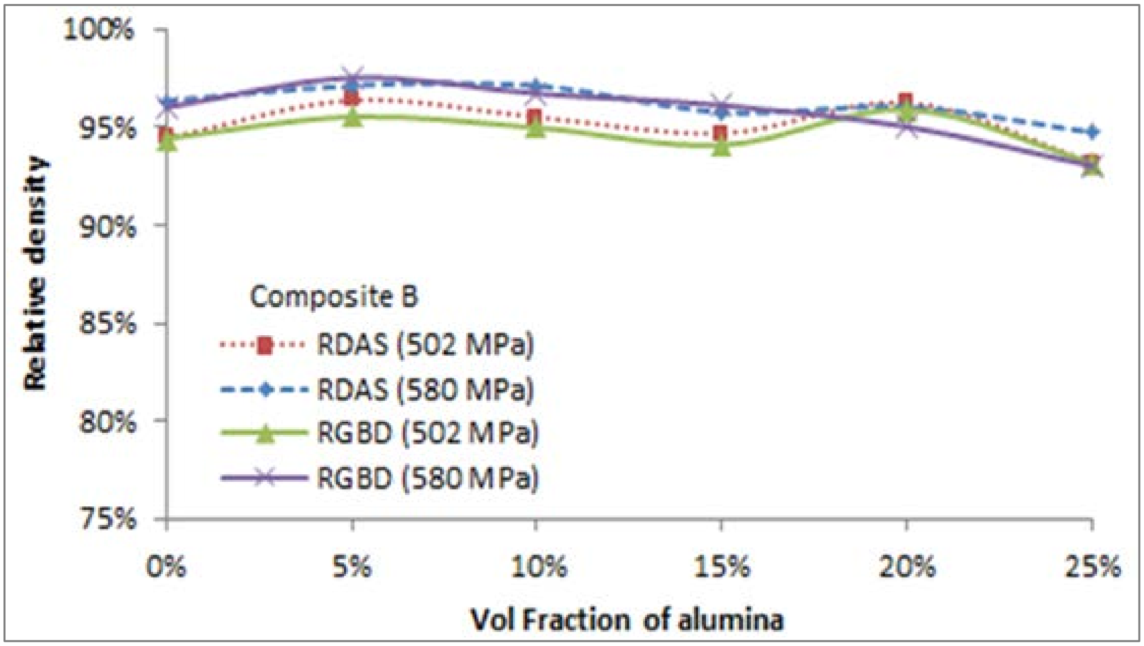

Figure 3.6. Relative density of composite system B before and after sintering as determined with alcohol immersion method

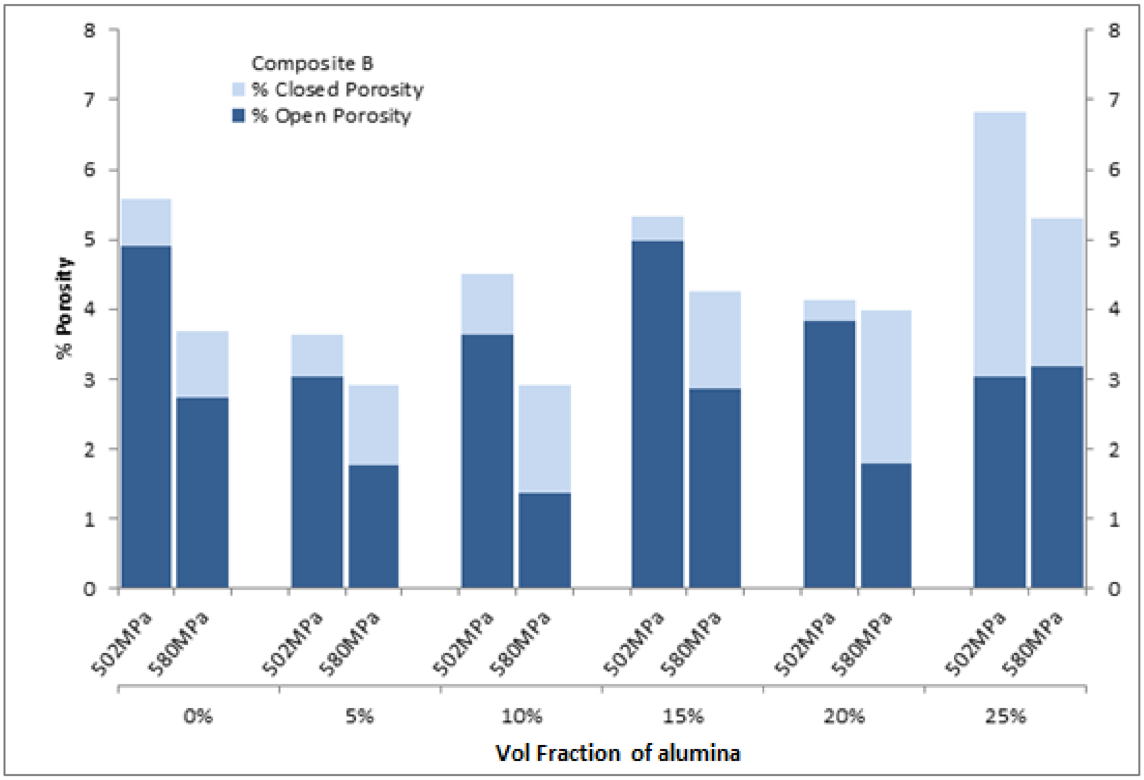

Figure 3.7. Effect of volume fraction and compacting pressures on the open, closed and overall porosity of the composite system B

As better densities and less porosity are observed at a higher pressure of 502 MPa than at 212 and 425 MPa, study has been conducted at constant compacting pressure of 502 MPa to see the effect of only the volume content of ceramic on the relative density. Furthermore, quality control is conducted by performing mechanical and thermal testing only on the composite specimens compacted at 502 MPa as they have porosity less than 10%, thereby ensuring the development of composites with good thermo-mechanical properties. To ensure consistency and repeatability of the manufacturing technique and density characterization, we repeat the procedure by manufacturing three samples each of 0, 5, 10, 15, 20 and 25% alumina content, with a compacting pressure of 502MPa.

Figure 3.8 shows the average relative density before and after sintering for the composite system A. As expected, both RGBD and RDAS decrease with increase in the ceramic volume content. It is worth mentioning that relatively high relative densities of 94-98% were achieved in sintered samples that were previously cold pressed at 502 MPa. However, Figure 3.8 has also another important implication – the relative density of the composite system A increases for less than 2% after sintering, indicating that sintering even at temperatures close to the melting point of aluminum does not result in significant additional densification of the samples. This finding is in good agreement with previously published results that showed that final density of the aluminum matrix composites is mainly controlled by cold compaction pressure and depends only slightly on the sintering temperature [68]. Figure 3.9 shows the effect of volume content of alumina on the average open porosity, average closed porosity and average overall porosity of the composite system A, which are cold pressed at 502 MPa, showing that the porosity increases with increasing volume content of alumina. Figure 3.10 compares the RDAS of composite systems A and B. Choosing aluminum with smaller particle size helps the aluminum particles to fill the empty gaps between the alumina particles, as shown by reduction in the porosity for the composite B with 20% and 25% alumina contents. However, there is no significant reduction in the overall porosity when using finer aluminum particles for the composites with a relatively low alumina contents (less than 20%) and in fact the overall open porosity increases when finer aluminum is considered at low alumina contents, Figure 3.7.

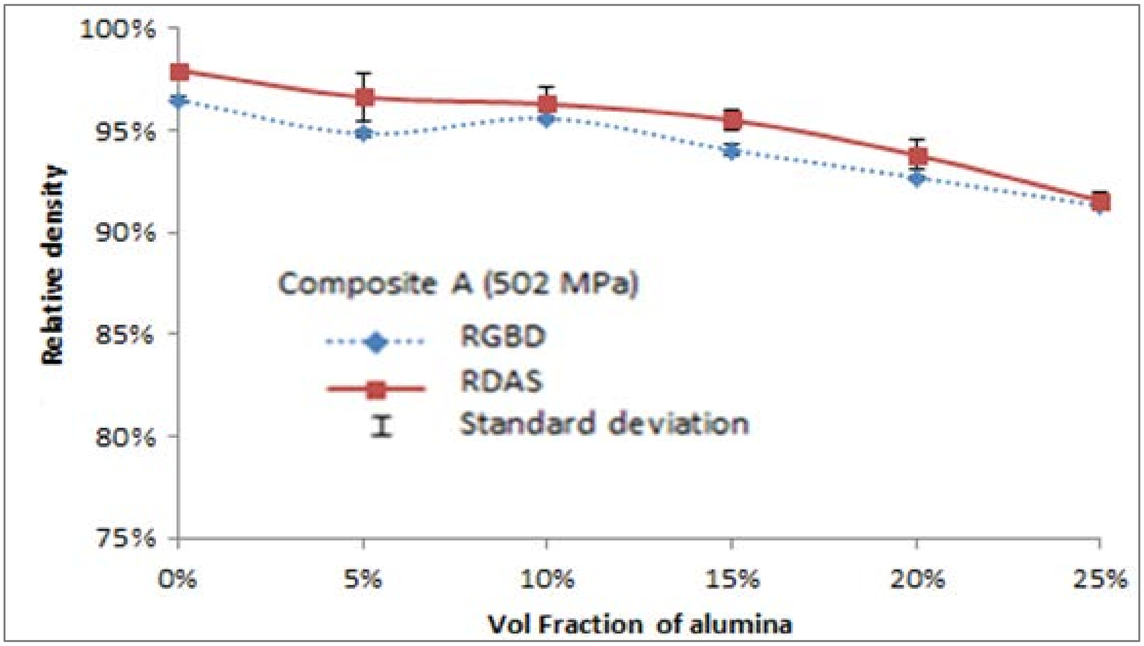

Figure 3.8. Relative density before and after sintering for composite system A when 502MPa compacting pressure used

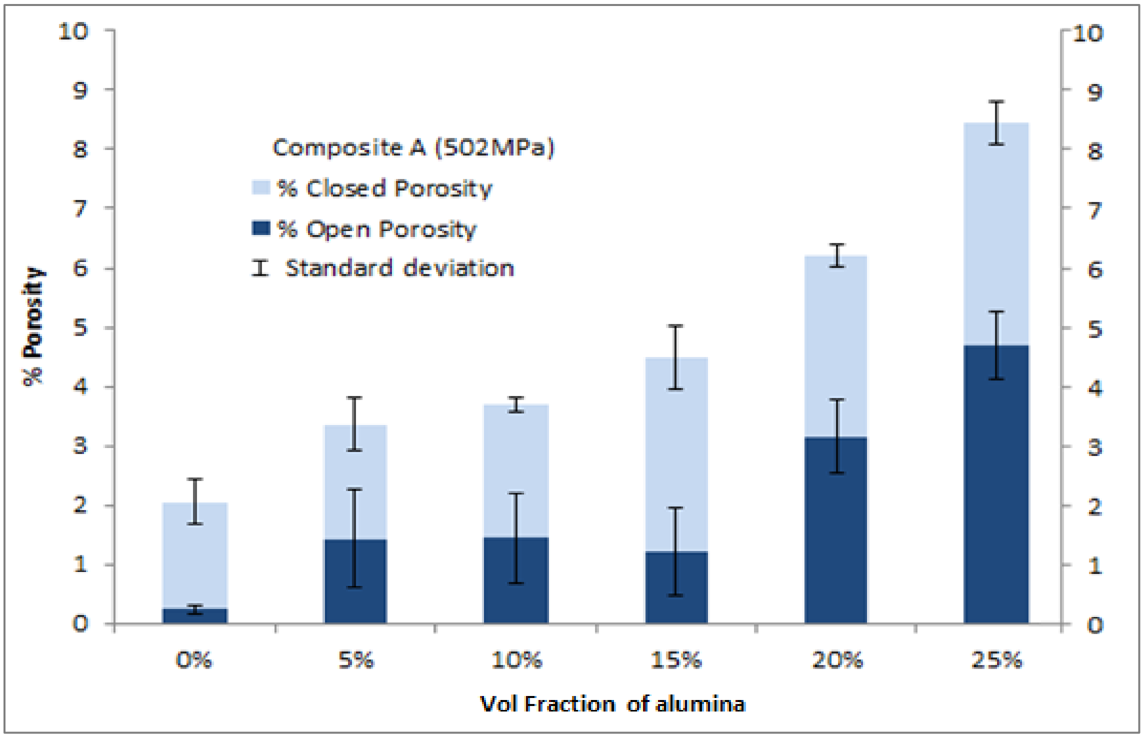

Figure 3.9. Effect of volume fraction on the open, closed and overall porosity of composite system A when 502 MPa compacting pressure used

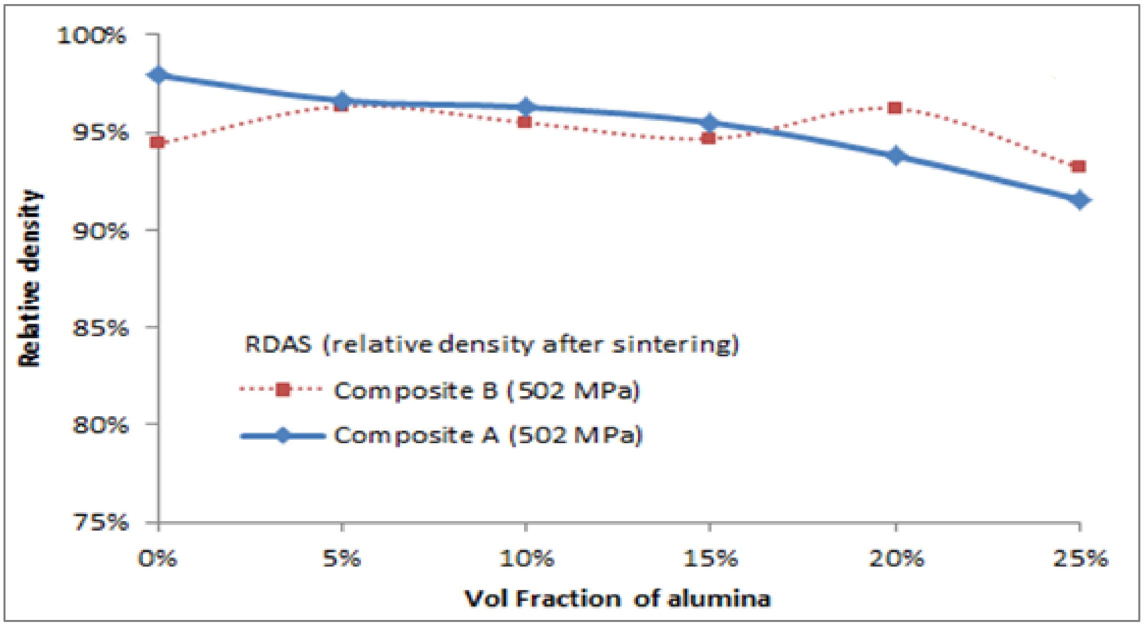

Figure 3.10. Comparison of relative densities after sintering for composite systems A and B when 502MPa compacting pressure used

3.2. Characterization of phases present and determination of VF of the composites

We use only the composite samples compacted at 502 MPa for further characterization, as they have lower porosity. XRD spectra of the two composite systems, for different volume fractions are shown in Figure 3.11. It can be seen that peaks appear at fixed 2-theta angle for all the volume fractions of composites; only the intensity of the peaks varies from one volume fraction to another. Table 3.1 shows a comparison of the measured volume content of alumina in the composites using XRD analysis software EVA, to the nominal volume content of alumina in the composites. The volume content of alumina was found to be a few percent higher than the nominal one in all the processed samples because starting aluminum powders already contained 2.3 or 3.4 vol% of alumina, as discussed earlier. However, it is possible that some of the aluminum additionally oxidized during the manufacturing process.

Table 3.1. Comparison of nominal vol% of alumina content in the composite with the vol% of alumina actually present in system A and system B as measured by XRD

Nominal VF of alumina	Actual VF of alumina in composite A (as given by XRD)	Actual VF of alumina in composite B (as given by XRD)
Aluminum powder	2.3%	3.4%
0% composite	2.8%	4.9%
5% composite	7.9%	9.4%
10% composite	12.4%	13.9%
15% composite	18.9%	19.8%
20% composite	24.4%	24.7%
25% composite	28.3%	28.7%

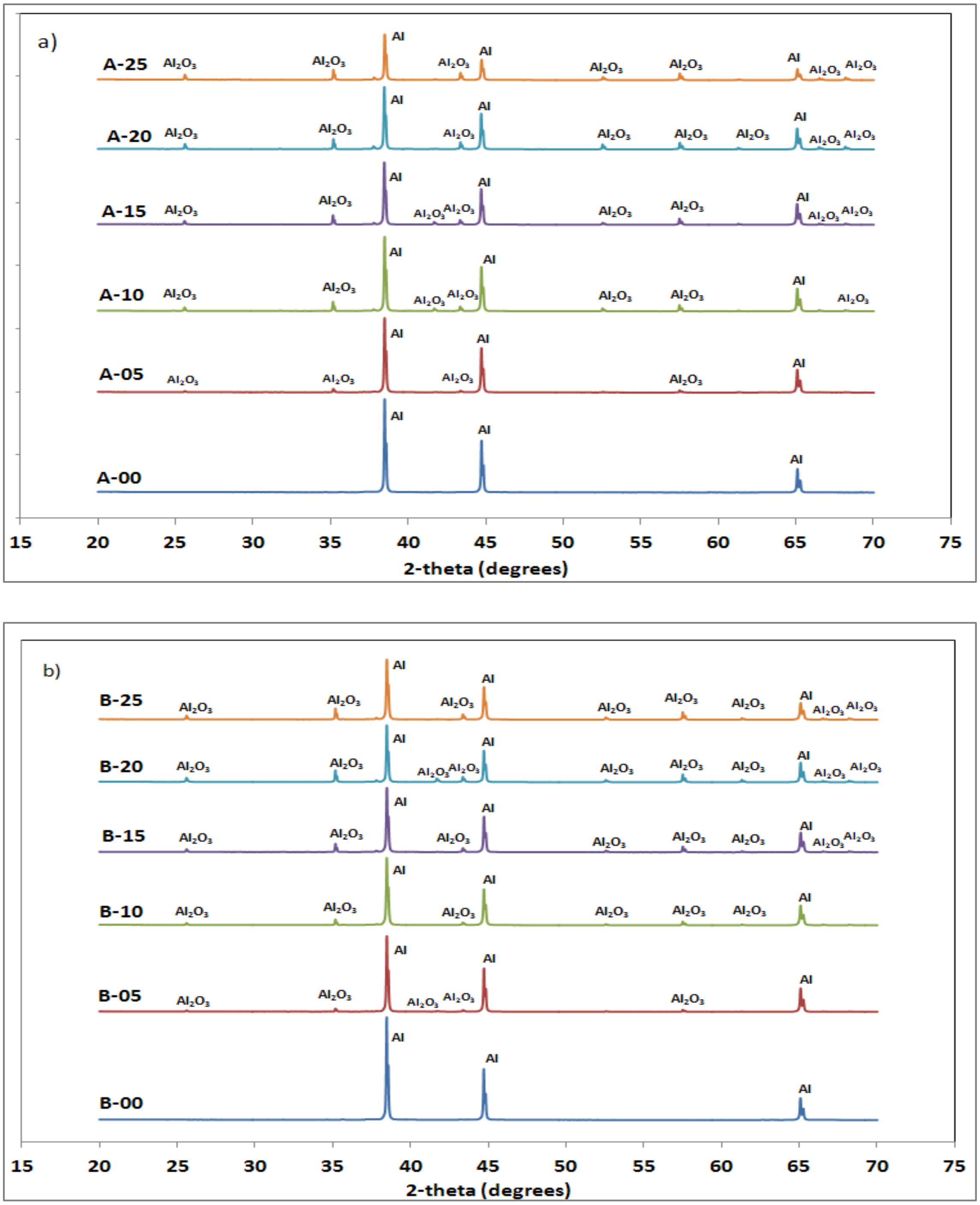

Figure 3.11. Identification of phases using XRD spectra for (a) composite A and (b) composite B

Fig. 3.12 shows the secondary electron images of 10 and 20 vol% composites for systems A and B, taken using a SEM. The bright white phase in Figures 3.12a-d is Al_2O_3, while the light gray phase is aluminum. Here again, no other phases are identified, except alumina and aluminum. The dark black areas in Figure 3.12 are pores. Another method used to verify the volume percent of the alumina phases in the composite pallet is by using ImageJ software and performing image analysis on the SEM micrographs shown in Figures 3.12a-d, as explained in Chapter II. Table 3.2 shows the concentration of alumina and pores obtained from binary images using imageJ. It can be seen in Table 3.2, that the alumina concentrations obtained using imageJ are higher than the nominal volume contents of alumina, which are expected to be present in the composites.

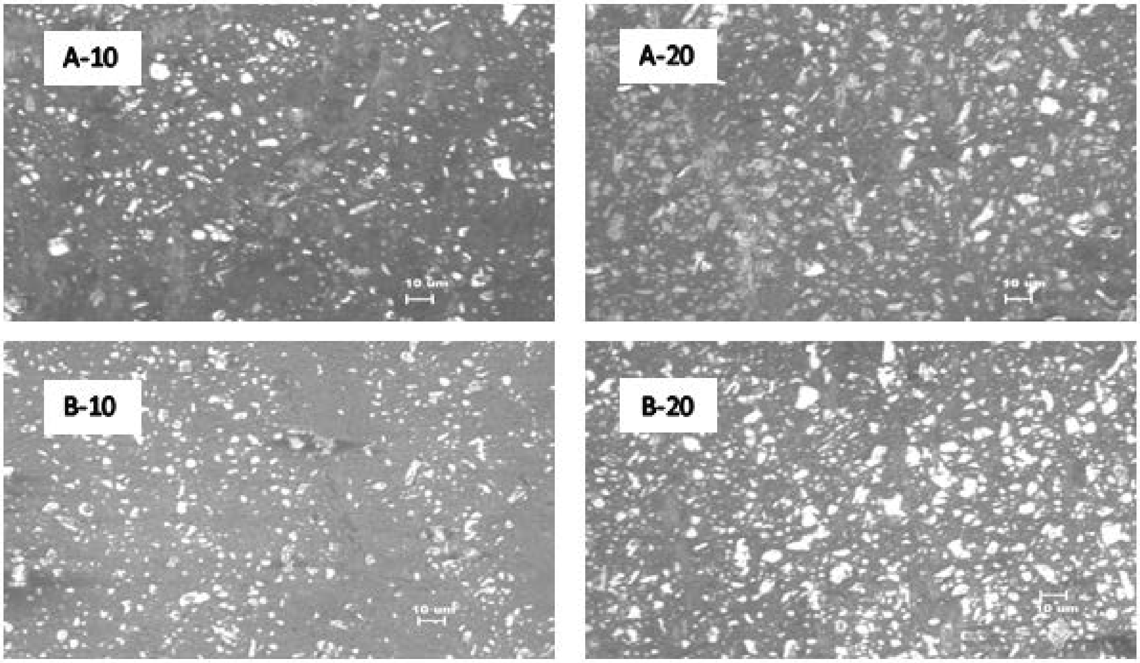

Figure. 3.12. Secondary electron images of composite samples prepared with compacting pressure of 502 MPa, taken by Scanning Electron Microscope (SEM)

Table 3.2. Volume fraction (%VF) of alumina and porosity in the composite samples determined using ImageJ

Sample	Alumina VF	Pores VF
A-10	12.7%	0.4%
A-20	22.6%	0.5%
B-10	13%	1.1%
B-20	26%	0.9%

3.3. Characterization of mechanical and thermal properties of Al-Al_20_3 composites

The composite specimens prepared from system A and system B, were characterized for their elastic moduli and thermal expansion coefficient in the 25 to 450°C temperature range and the results are discussed in the remainder of this section.

3.3.1. Mechanical properties

The elastic moduli were measured at various temperatures using RUS. It is worth noting here that fitting error, i.e. the root-mean-square (RMS) error between the measured and calculated resonant frequencies, never exceeded 0.4% for all tested samples. The composite was assumed to be an isotropic and linear elastic material.

Figure 3.13 illustrates the variation of Young's and shear moduli of the composite A that were fabricated at a cold compacting pressure of 502 MPa, with temperature and volume content of alumina. The elastic moduli of pure aluminum (sample A-00) from our results are compared with the RUS results of Pham et al. [69] on the pure aluminum sample, and were found to be in close agreement. Our sample A-00 had elastic moduli varying from 67 GPa at 25°C to 45 GPa at 450°C; whereas the elastic moduli of Pham et al. [69] varied from 70 GPa at 27°C to 48 GPa at 527°C. From Figure 3.13, the moduli consistently increased with increasing alumina volume contents at temperatures below 200^{o}C, as expected. The effective elastic moduli decreased with increase in temperatures and the reduction of the effective moduli with increase in temperature is more pronounced for the composites with higher volume content of alumina. This can be explained by the presence of large thermal stresses due to the CTE mismatch between the constituents, resulting most likely in interface debonding in the samples with larger amount of alumina phase, making the material inherently weak. As the temperature change increases, the developed thermal stresses, which could be either tensile or compressive, also increase. High stresses in the aluminum constituent could lead to plastic deformation, while high stresses in the alumina constituent could cause cracking. Increase in temperature changes could also result in large stress discontinuities in the interfaces between the aluminum and alumina, leading to debonding. The plastic deformation, cracking, and debonding could significantly reduce the elastic moduli of the composites.

The variation of the elastic and shear moduli of the composite B with temperature and volume content of alumina is shown in Figures 3.14a-b. The same trend is observed in the system A shown in Figure 3.13. However, the system B (which was made up of finer aluminum particles) had the elastic moduli of the composites higher than those of system A (which was made up of coarser aluminum particles), due to higher relative densities and reduced porosities. Figure 3.15 shows comparisons of Young's moduli of the two composite systems A and B at two different temperatures, 25^{o}C and 450^{o}C. It is seen that as temperature increases from 25^{o}C to 450^{o}C, there is a drop in the elastic modulus for both composite systems (up to 26 GPa). Temperature and composition of the aluminum and alumina constituents significantly affect the elastic modulus of the composites. The effect of particle size on the elastic modulus was quite insignificant, as the difference in the elastic moduli of the system A and B is within 5 GPa for all temperatures and volume contents of alumina in the composites.

The Young's modulus of composite A and composite B at room temperature obtained from RUS, is compared with experimental data obtained from Lim et al. [70], as shown in Figure 3.16. It can be seen that the moduli obtained from our composites are lower than those of Lim et al. [70]; and as volume fraction of alumina increases, the gap between the two curves also increases. The main reason for this could be attributed to the porosity present in our composite as discussed earlier, whereas the direct melt infiltration method used in Lim et al. [70], where molten aluminum was poured into alumina preform, produced less porosity even for higher volume fractions of alumina. Figure 3.16 also shows the effect of compacting pressure on the elastic moduli of the composite system B. It is seen that the high pressure consistently improved the elastic moduli only for composites with 20 and 25% Al_2O_3 contents, but for the ones with lower Al_2O_3 contents high compacting pressure gives lower effective moduli. After the RUS tests in the samples with lower Al_2O_3 contents and 580 MPa compacting pressure, we observed cracking in the specimens. The reason could be that the high compacting pressure leaves fracture and permanent deformation in the constituents and temperature changes can cause more severe cracking.

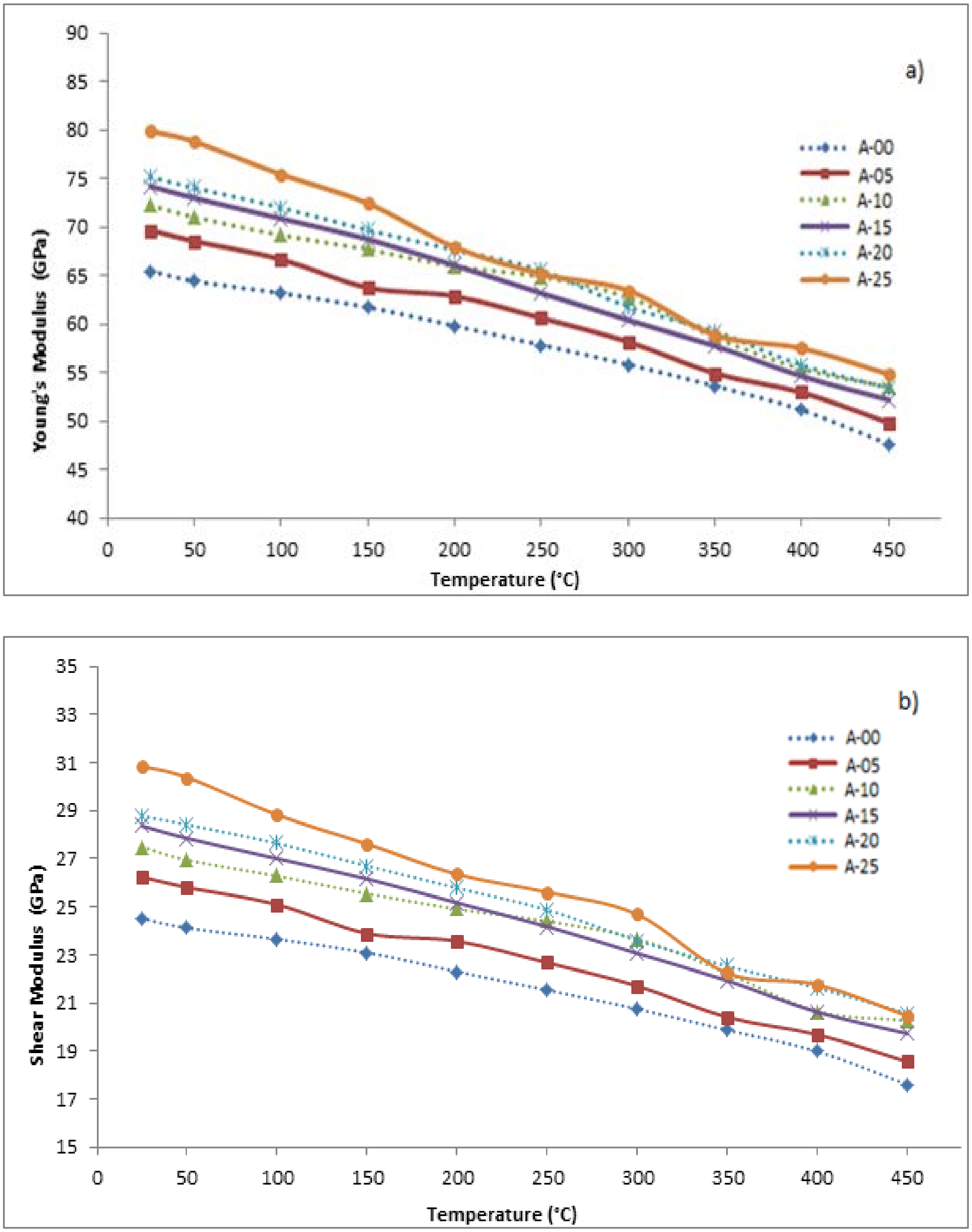

Figure 3.13. (a) Young's modulus and (b) Shear modulus of Composite A at different alumina volume contents and temperatures

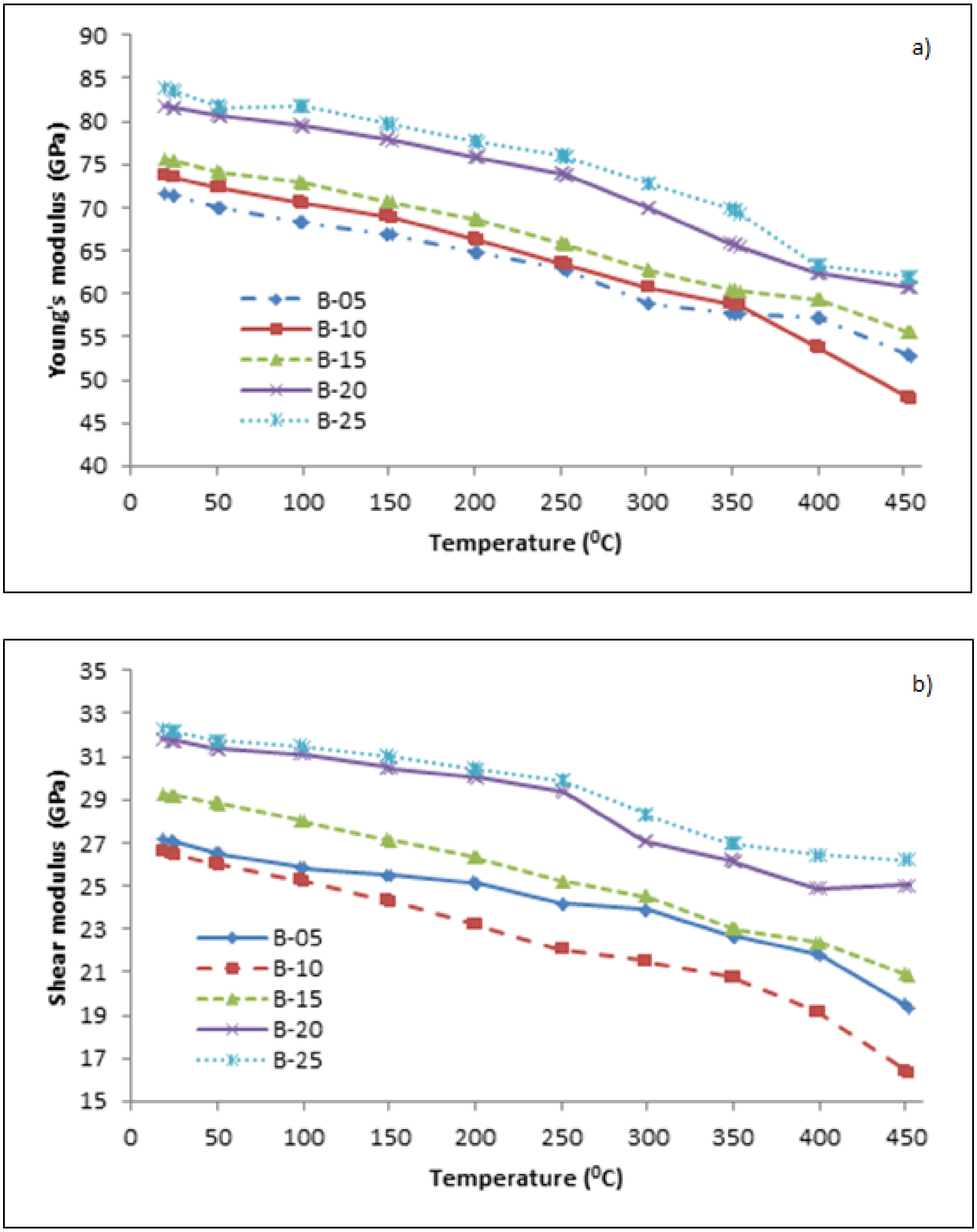

Figure 3.14. (a) Young's modulus and (b) shear modulus of composite B at different alumina volume contents and temperatures

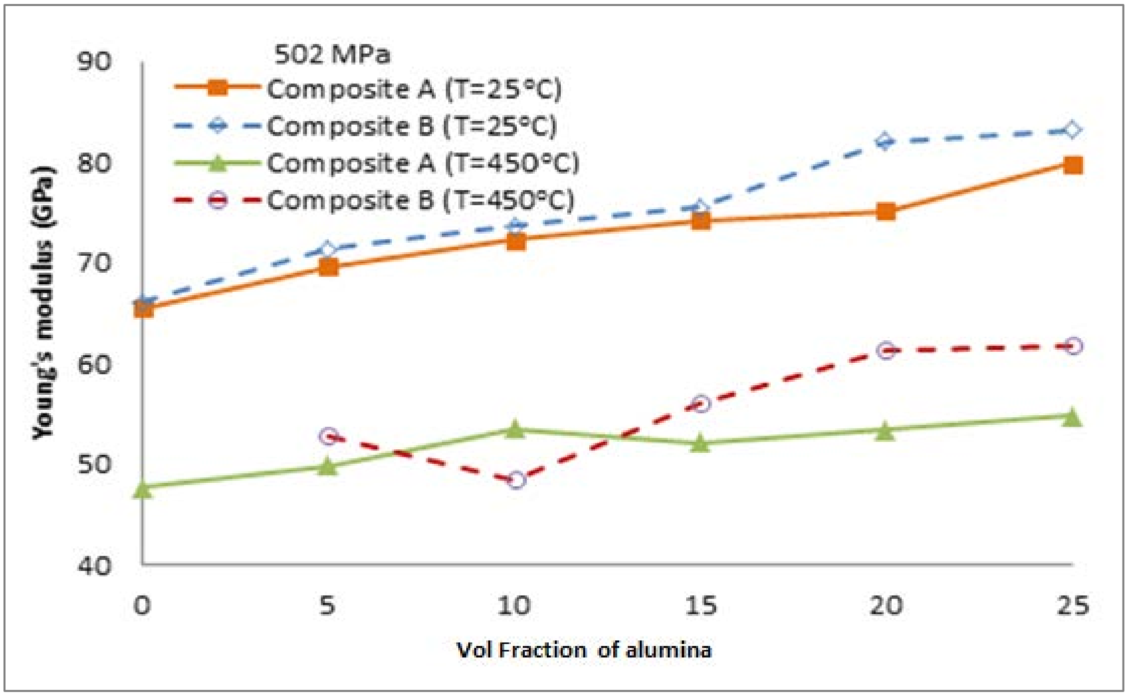

Figure 3.15. Comparison of Young's moduli of composites A and B at room temperature (25^{0}C) and at elevated temperatures (450^{0}C)

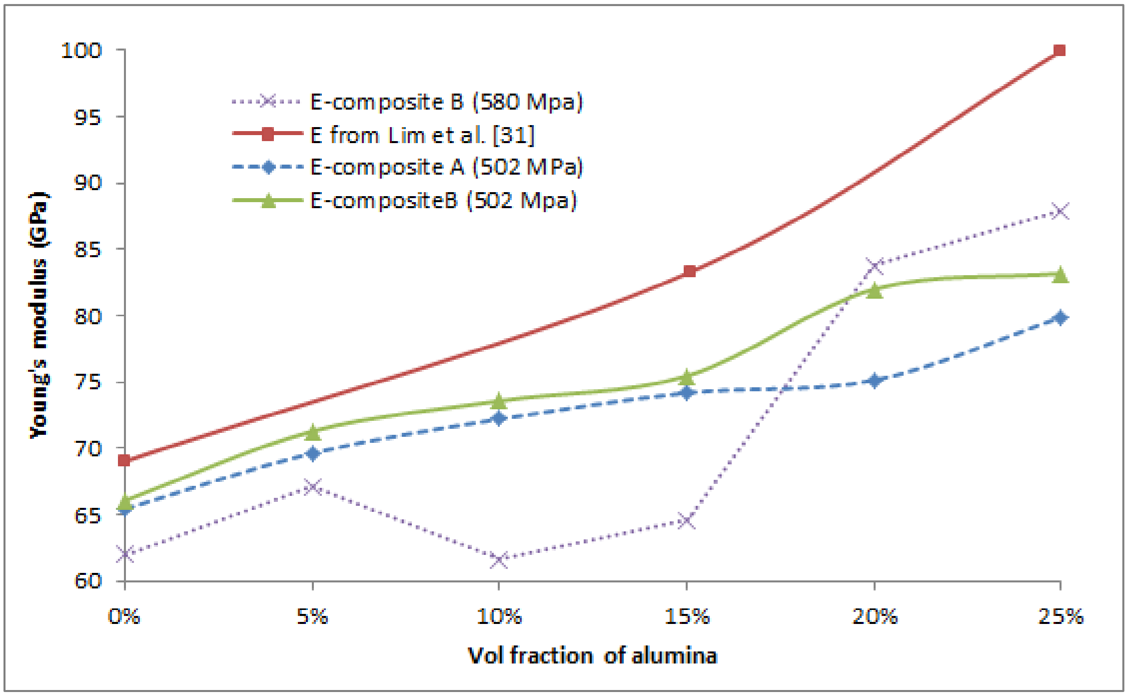

Figure 3.16. Comparison of Young's moduli of composite A and B with those from literature, at room temperature

3.3.2. Thermal expansion

The coefficient of thermal expansion (CTE) of the composite specimens was measured using a Thermo-mechanical Analyzer, (TA Q400, TA instruments, UT). The furnace was heated at a rate of $5^oC/min$ from -20^oC to 400^oC, and cooled at a rate of $4.6^oC/min$ from 400^oC to -20^oC. Changes in the height (μm) of the specimens with temperature during both heating and cooling process were constantly monitored. The thermal strains were then determined by taking the ratio of the changes in height to the initial height of the specimens. Figures 3.17a-b show the thermal strain vs. temperature curves for different volume contents of alumina during the heating and cooling processes. It was observed that strain gradually decreased as the ceramic content increased from 0 to 25%. Furthermore, the thermal strain increased linearly as temperature increased from 20^oC to 400^oC; and decreased linearly as temperature was decreased from 400^oC to 20^oC. A linear CTE ($\mu m/m^oC$) of the specimen is calculated in 25^oC to 400^oC temperature range, by taking the slope of thermal strain vs. temperature curves. As these curves are linear, the CTE of the composite specimen is taken as constant i.e. it does not vary with temperature. Figures 3.18a-b compare the linear CTE for each volume fraction of the composite systems A and B during heating and cooling phases. In addition, the average value of CTE from cooling and heating phases is also plotted in Figures 3.18a-b. The CTE values of 28.02 $\mu m/m^oC$ and 26.1 $\mu m/m^oC$ for pure aluminum of the systems A and B (samples A-0 and B-0) respectively, are in close agreement with previously published values for pure aluminum in 21.5-27.9 $\mu m/m^oC$ range [71]. As it can be seen in Figures 3.18a-b, the linear CTE decreases with increasing volume percent of alumina in the composite samples for both composite systems A and B. This is expected since the alumina has significantly lower linear CTE of 5.5 $\mu m/m^oC$ [72], when compared to that of pure aluminum. Particle size of aluminum should not affect CTE of the composite system; however, we observed that the composite B had slightly lower CTE than the composite A samples. This could be attributed to the presence of slightly more Al_2O_3 vol% present in composite B samples than those of composite A samples (see Table 3.1), resulting in lower CTEs for the composite B samples. The effects of porosity on the overall CTE of the studied composites are negligible as porosities even up to 6% in the composite sample do not seem to have significant effect on CTE. Also temperature and compacting pressure of the composite have an insignificant effect on the CTE of the composites. Figures 3.18a-b also show the comparison of CTE of composite systems A and B with those calculated from rule of mixtures and Muliana et al [73]. The average CTE for composite B are very close to those of Muliana [73] and rule of mixtures, for all volume fractions of alumina in the composite.

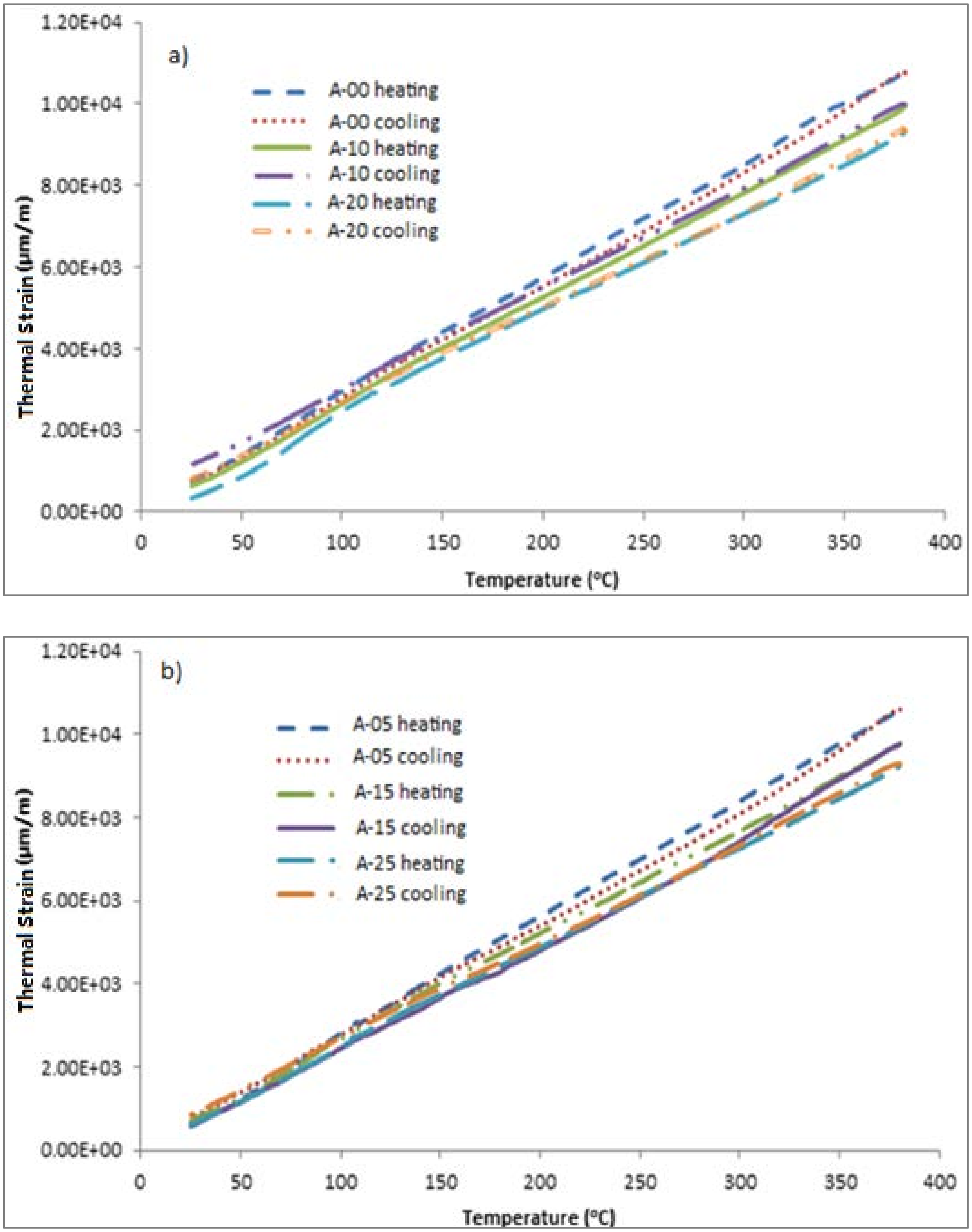

Figure 3.17. Thermal strain variation with temperature for composite system A with (a) 0, 10 and 20vol% alumina and (b) 5, 15 and 25vol% alumina, during heating and cooling phases

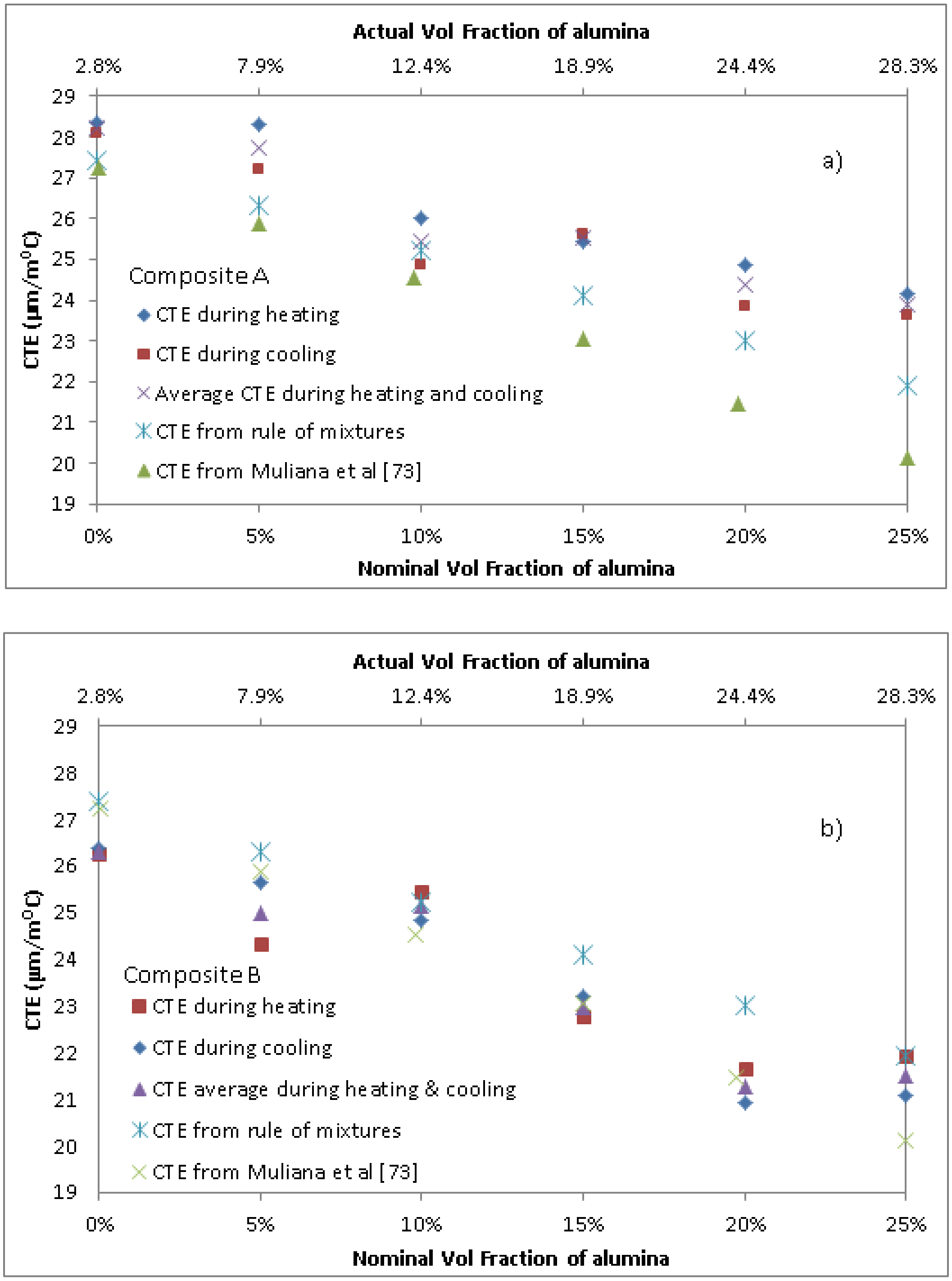

Figure 3.18. Variation of CTE with volume fraction of alumina for (a) composite system A (b) composite system B, during heating and cooling phases

CHAPTER IV

DETERMINATION OF THERMOMECHANICAL PROPERTIES USING MICROMECHANICS APPROACH (NUMERICAL STUDY)

This chapter examines the overall CTE, elastic modulus, and Poisson's ratio of the Al-Al_2O_3 composites based on their microstructural characteristics. The purpose is to study the effects of microstructural morphologies on the overall thermo-mechanical performance of composites. The microstructural models of the composite systems A and B at 10vol% and 20vol% alumina contents were generated from the SEM microstructural images shown in Figs.3.12a-d. Each microstructural image was approximately 208x166 μm. Table 3.2 summarizes the volume fraction[1] of alumina and %porosity present in these composite samples, determined by using image analysis software, ImageJ. These microstructural images were exported to 2D finite element (FE) and the overall performance of the composites was analyzed using FE method. Next, convergence studies in terms of the sizes of the representative microstructures and average sizes of the elements (coarse and fine meshes) on the thermo-mechanical behaviors of composites were conducted.

4.1. FE mesh generation of the composite microstructures

Figure 4.1a shows the overlap of grid onto the SEM micrograph of the A-20 sample. From this micrograph, four different 50 μm X 50 μm square regions having different microstructures were chosen as the representative microstructures of the A-20 composite (see Figure 4.1a). Figure 4.1b illustrates four FE microstructural models, corresponding to the chosen

---

[1] We actually determine the area fractions of the alumina constituent. However, in order to be consistent with the nominal alumina volume contents of the manufactured composite samples, we refer the measured alumina content as volume fraction.

micrograph images. Similarly, from each SEM image of A-10, B-10 and B-20 composite samples, four FE microstructural models were generated (see Appendix). Table 4.1 summarizes the vol% of alumina and the % porosity present in the four FE meshes of the A-10, B-10, A-20 and B-20 composites. It should be noted that the alumina (Al_2O_3) contents extracted from the 2D images and also from the 2D FE meshes are above the nominal volume contents of the Al_2O_3. The reasons are (1) oxidation on the surface of the aluminum particles prior to manufacturing the composite samples and (2) probably due to determination of the area fraction of the alumina constituent in the 2D models instead of determining the volume fraction. We also found that for the composites with smaller size of aluminum particles (composite B), the total surface area of the aluminum particles in the composite samples is higher than the one of the composites having larger size of aluminum particles (composite A). Thus, more oxidation of the aluminum particles are shown in the composite system B, resulting in much higher values of the measured alumina contents than the nominal alumina contents. Nevertheless the above 2D microstructural models are reasonably good in capturing the microstructural morphologies of the composites as the measured percent of alumina contents are relatively close to the nominal alumina volume fractions. For identifying the pores (black regions), brightness and contrast of the image was increased to differentiate between black and gray regions. The chosen FE meshes show slight variations in the volume content of the alumina and porosity among different locations. For example, among all FE models of the A-20 composite sample, FE models 2 and 4 have low porosity whereas FE models 1 and 3 have high porosity. Later we will discuss the effect of this porosity on the mechanical and thermal properties of the composites.

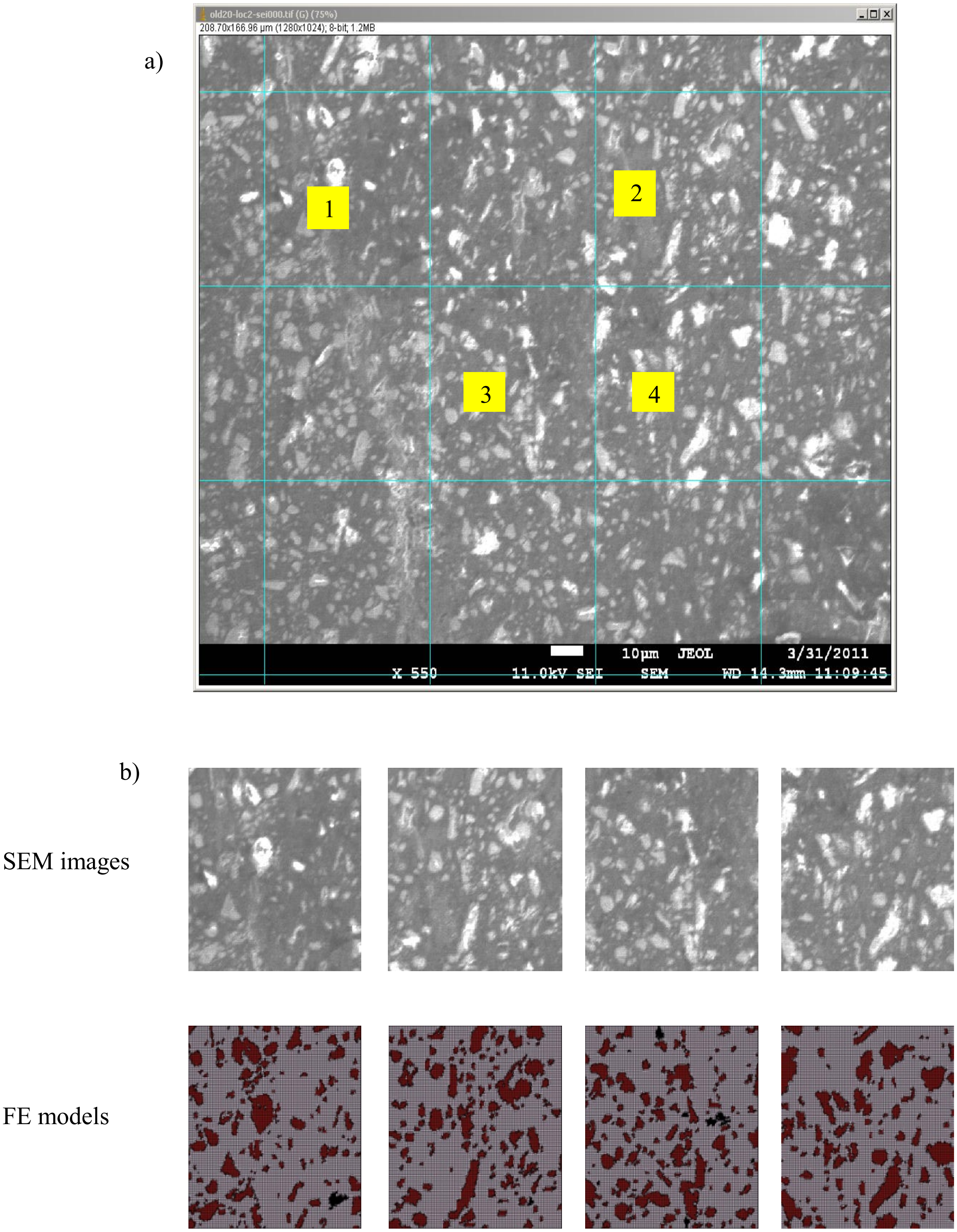

Figure 4.1 a) SEM Image of A-20 composite sample; b) four random square micrographs of A-20 composite sample and their corresponding FE microstructural models

Table 4.1. Volume Fraction (%VF) and Porosity (%Pores) of the four FE models generated

	A-10		B-10		A-20		B-20	
	%VF	%Pores	%VF	%Pores	%VF	%Pores	%VF	%Pores
FE model #1	11.7	0.0	12.6	1.0	20.2	0.4	26.3	0.4
FE model #2	13.2	0.5	13.7	0.4	21.7	0.1	25.3	0.3
FE model #3	11.6	0.0	15.8	0.7	20.9	0.7	25.8	0.2
FE model #4	11.5	0.0	15.0	0.3	21.1	0.0	22.9	0.5

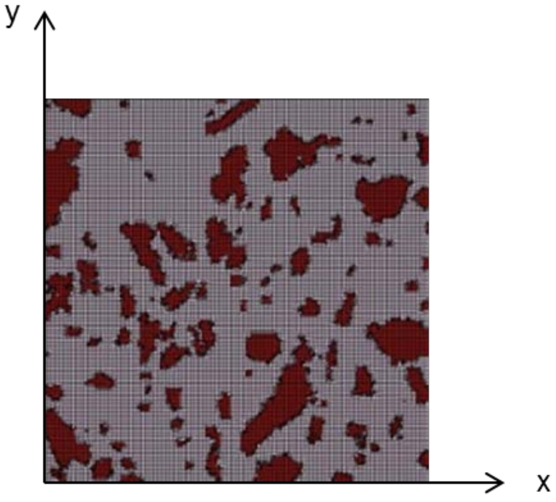

Figure 4.2. 2D square FE microstructural model with length of each side as 50 μm

The FE microstructural models were implemented in ABAQUS and used for determining the effective elastic modulus, Poisson's ratio and CTE of the composites numerically. These numerical results were compared with those obtained from experiments (Chapter III and [74]). Figure 4.2 illustrates an example of a representative square microstructure placed in the 2D Cartesian coordinate. The following mechanical boundary conditions were prescribed to the 2D FE microstructural model:

$$u_x(0,y) = 0;\ u_x(L,y) = u_{right} \qquad 0 \le y \le L$$
$$u_y(x,0) = 0;\ u_y(x,L) = u_{top} \qquad 0 \le x \le L \tag{4.1}$$

where $u_x(x,y)$and $u_y(x,y)$ were the displacements in the *x*- and *y*- directions, respectively. The initial temperature was taken as 600 °C, which was the sintering temperature, and at that temperature the composite was assumed at its stress-free condition. The composite was cooled down to room temperature prior to characterizing its thermo-mechanical properties. This was done in order to study the effect of thermal (residual) stresses on the thermo-mechanical properties. The numerically quantified thermal (residual) stresses were due to the mismatches in the CTEs of aluminum and alumina constituents. The linear elastic modulus and Poisson's ratio were determined by prescribing a small uniaxial stress $\sigma_{xx}(L,y) = \sigma_0 = 1$ MPa and monitoring the corresponding effective strains $\bar{\varepsilon}_{xx}$ and $\bar{\varepsilon}_{yy}$. The effective elastic modulus and Poisson's ratio, denoted by an overbar, were defined as:

$$\bar{\varepsilon}_{xx} = \frac{u_{right}}{L};\ \bar{\varepsilon}_{yy} = \frac{u_{top}}{L}$$
$$\bar{E} = \frac{\sigma_0}{\bar{\varepsilon}_{xx}};\ \bar{\nu} = -\frac{\bar{\varepsilon}_{yy}}{\bar{\varepsilon}_{xx}} \tag{4.2}$$

In order to examine the effect of loading directions on the overall properties of the composites, a uniaxial stress $\sigma_{yy}(x,L) = \sigma_0 = 1$ MPa was prescribed and the corresponding effective strains $\bar{\varepsilon}_{xx}$ and $\bar{\varepsilon}_{yy}$ were monitored. The effective elastic modulus and Poisson's ratio were defined as in Eq. (4.2) by interchanging the indices *x* and *y*. The effective CTE was determined by further heating the composite sample to 125 °C. The composite was initially at room temperature (25 °C) with existing residual stresses due to the sintering process. Once the composite reaches an isothermal temperature 125 °C or a uniform temperature change ΔT=100 °C, the effective CTEs were then obtained as:

$$\bar{\varepsilon}_{xx} = \frac{u_{right}}{L};\ \bar{\varepsilon}_{yy} = \frac{u_{top}}{L}$$

$$\bar{\alpha}_{xx} = \frac{\bar{\varepsilon}_{xx}}{\Delta T};\ \bar{\alpha}_{yy} = \frac{\bar{\varepsilon}_{yy}}{\Delta T}; \tag{4.3}$$

Parametric studies are also performed in order to examine the effects of loading directions, elastic and plastic deformations, temperature-dependent material parameters, particle distributions and porosity on the effective thermo-mechanical properties of the composite. The effect of residual stresses on the overall thermo-mechanical properties of the composites is also studied.

4.2. The effects of loading directions, microstructural geometries and material properties

The effect of loading directions on the effective elastic modulus, Poison's ratio, and CTE of the chosen representative microstructures is studied. The purpose is to validate the assumption of the isotropic response with regards to the thermal and mechanical properties of the studied composite. Both aluminum and alumina constituents are considered as linear elastic with properties given in Table 4.2. Figure 4.3 illustrates the effective elastic modulus and Poison's ratio of the composite A-20 generated from the numerical simulation of four FE microstructural models. The elastic modulus varies between 82-89 GPa and the Poison's ratio varies between 0.3-0.32 for all FE models loaded in all loading directions. This shows that the microstructures have nearly equal properties in both *x* and *y* directions and the composites have relatively homogeneous distribution of alumina particles in the aluminum matrix. By observing the elastic modulus, a slightly anisotropic behavior in the composites is observed which could be due to the uniaxial compaction during the processing of the samples. From Figure 4.3 and Table 4.1, it is seen that porosity reduces the overall elastic modulus of the composites. The Poisson's effect, however, seems to be insensitive to the amount of porosity and loading directions.

Table 4.2. Properties of aluminum [74] and alumina [72, 75] at a reference condition (T = 25 °C) used in the FE models

Constituent	Density (g/cm^3)	CTE (μm/m.°C)	Modulus (GPa)	Poisson's ratio	Thermal Conductivity (W/m.°C)	Specific Heat (J/Kg.°C)
Aluminum	2.67	28	65.4	0.336	210	900
Alumina	3.96	8.5	370	0.22	30	753

Heterogeneous materials often experience localized stresses (stress concentrations) within their microstructures. These localized stresses are often observed at the interfaces between different constituents in the composites and close to the voids. The magnitude of these localized stresses can even be greater than the externally prescribed mechanical stresses. When dealing with aluminum matrix composites, high localized stresses could induce a localized yielding within the microstructures of the composites. High tensile stresses in the alumina can induce cracking, reducing the load carrying capacity of the composites. The effect of the localized yielding on the overall elastic modulus, Poisson's ratio, and CTE of the composites is further examined by considering an elasto-plastic behavior for the aluminum constituent based on an overstress plasticity theory. The initial yield stress of the aluminum is taken as σ_{yo}=33 MPa, as shown in Figure 4.4[2]. Furthermore, the properties of materials can vary significantly with the environmental temperatures. In this study, the elastic properties of the aluminum are allowed to vary with temperatures (see Figure 4.5). The effective elastic modulus, Poison's ratio, and CTE of the composites are compared by considering the following mechanical response for the aluminum constituent: linear elastic behavior, linear elastic with temperature-dependent

---

[2] Although we consider an overall small deformation gradient problem in analyzing the linear elastic modulus, Poisson's ratio and CTE of the composites, stresses experience by the aluminum constituent can exceed the yield limit of the aluminum and the aluminum can undergo large deformations.

behavior (Figure 4.5), and elastic-plastic with temperature-dependent behavior (Figures 4.4 and 4.5). In all cases, the alumina is assumed linear elastic.

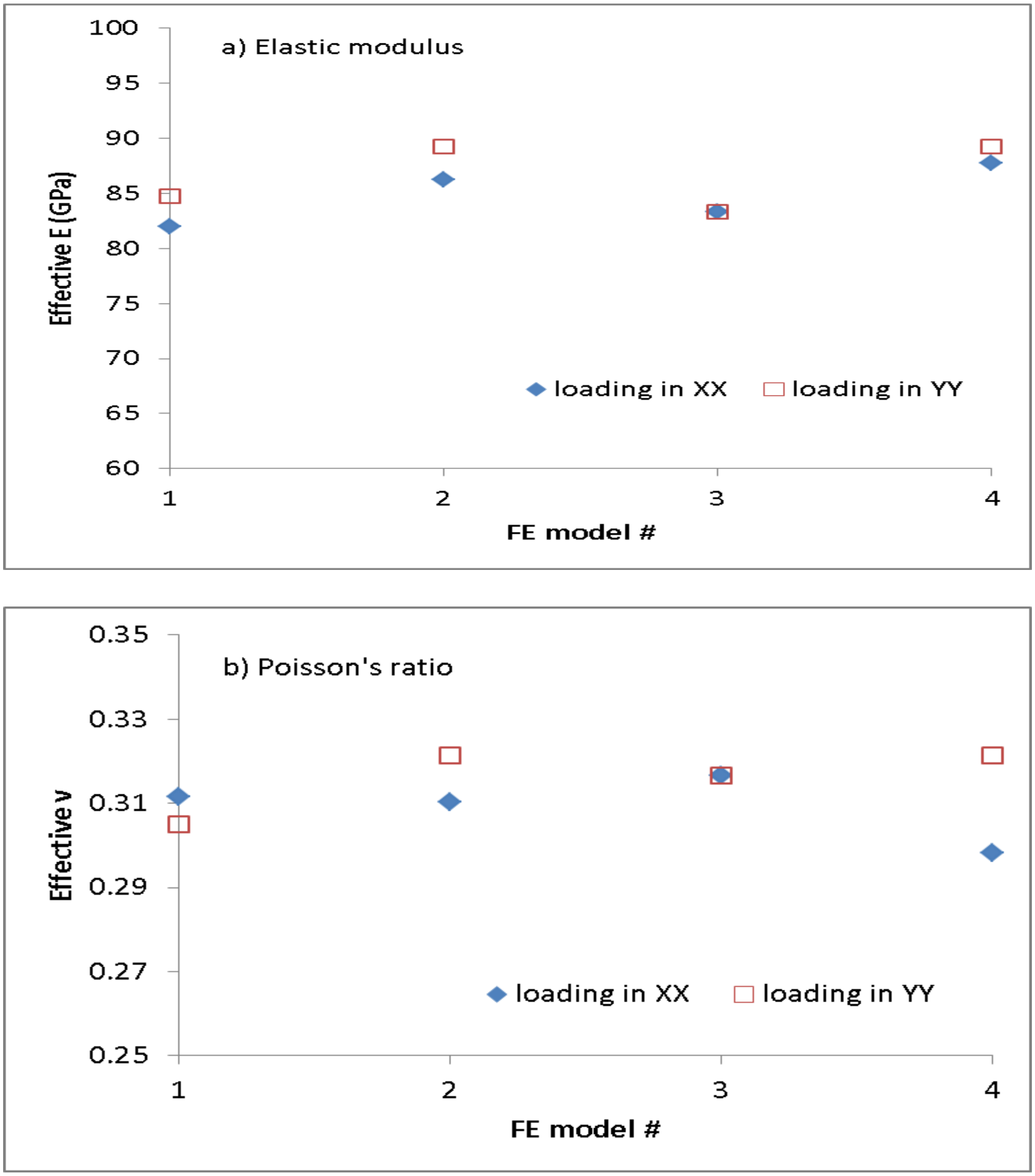

Figure 4.3 a) Effective elastic modulus and b) effective Poison’s ratio dependency on loading directions and microstructure for an A-20 composite sample with E_c/E_m=370/65

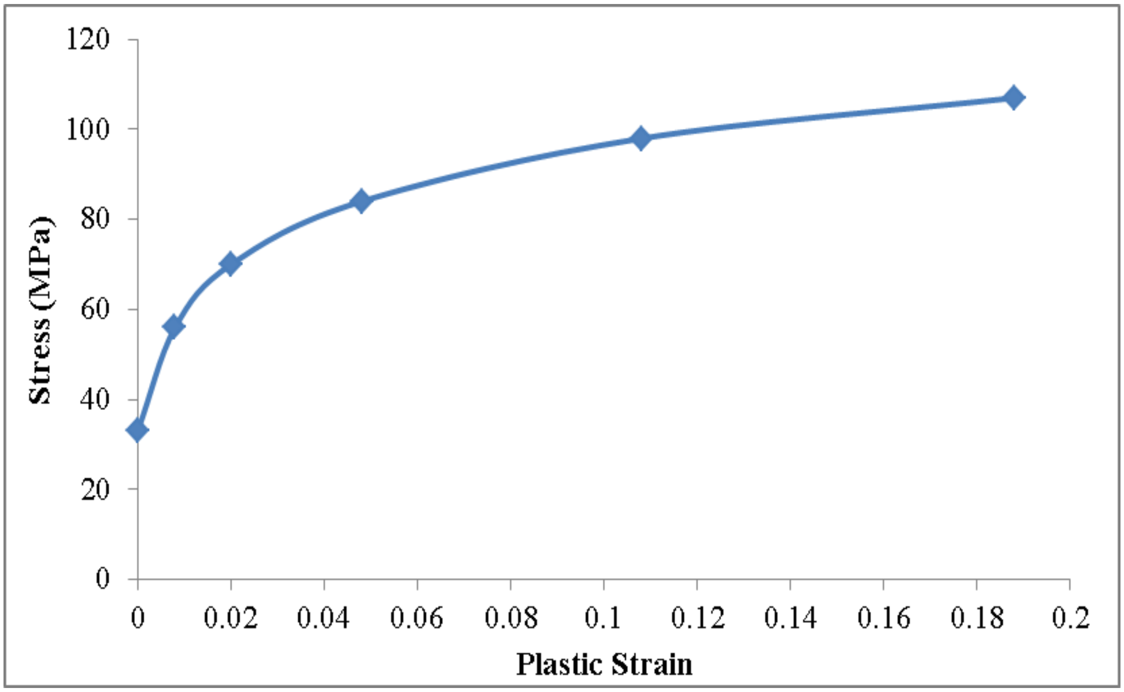

Figure 4.4. Plastic deformation of aluminum at room temperature [76]

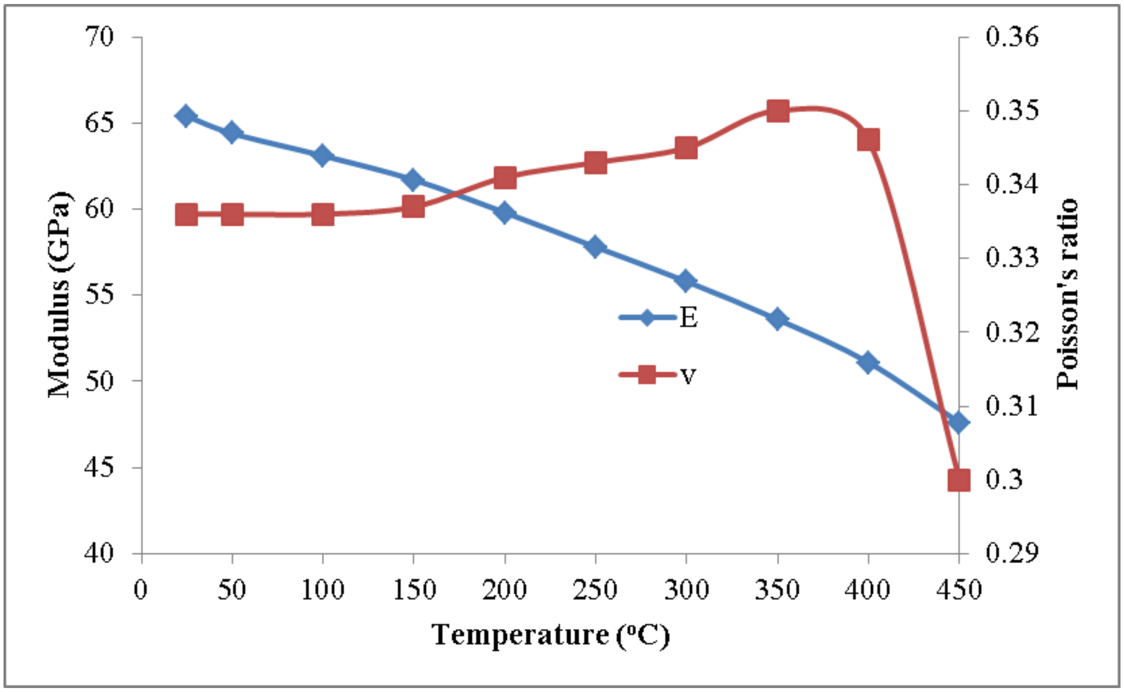

Figure 4.5. Temperature-dependent elastic modulus and Poisson's ratio of aluminum [74]

Figures 4.6a-b show the effective elastic modulus and Poisson's ratio of A-20 composite sample for different material behaviors of the aluminum. As discussed previously in Table 4.1, among the FE models of A-20 sample, FE models 2 and 4 have low porosity and hence they have high effective modulus as shown in Figure 4.6a, whereas FE models 1 and 3 have high porosity and therefore have low modulus as can be seen in Figure 4.6a. It is also seen that the plastic deformation in the aluminum constituent significantly reduces the overall elastic modulus and increase the overall Poisson's ratio of the composites. This indicates that the aluminum experiences a significant plastic deformation, which is due to different thermal shrinkage of both phases during cooling from the sintering temperature. This issue will be discussed in more detail later in this thesis. Qualitatively similar results are obtained for the A-10, B-10 and B-20 samples. The effective elastic moduli of the composite system B are higher than the ones of the composite system A. This is due to pronounced oxidation of the aluminum particle in the composite B, indicated by the higher values of the measured alumina contents (Table 4.1).

Figures 4.7a-b illustrate the effective CTEs from the numerical simulations. The effective CTE did not change significantly with the amount of porosity and it is slightly affected by the mechanical behavior of the aluminum, as seen in Figures 4.7a and 4.7b. As the aluminum constituent is getting softer with the temperature increases and plastic deformations, higher values of the overall CTE and lower effective elastic moduli of the composites are expected. It is also seen that the overall CTEs in two directions x and y axes are comparable, although some variations are observed.

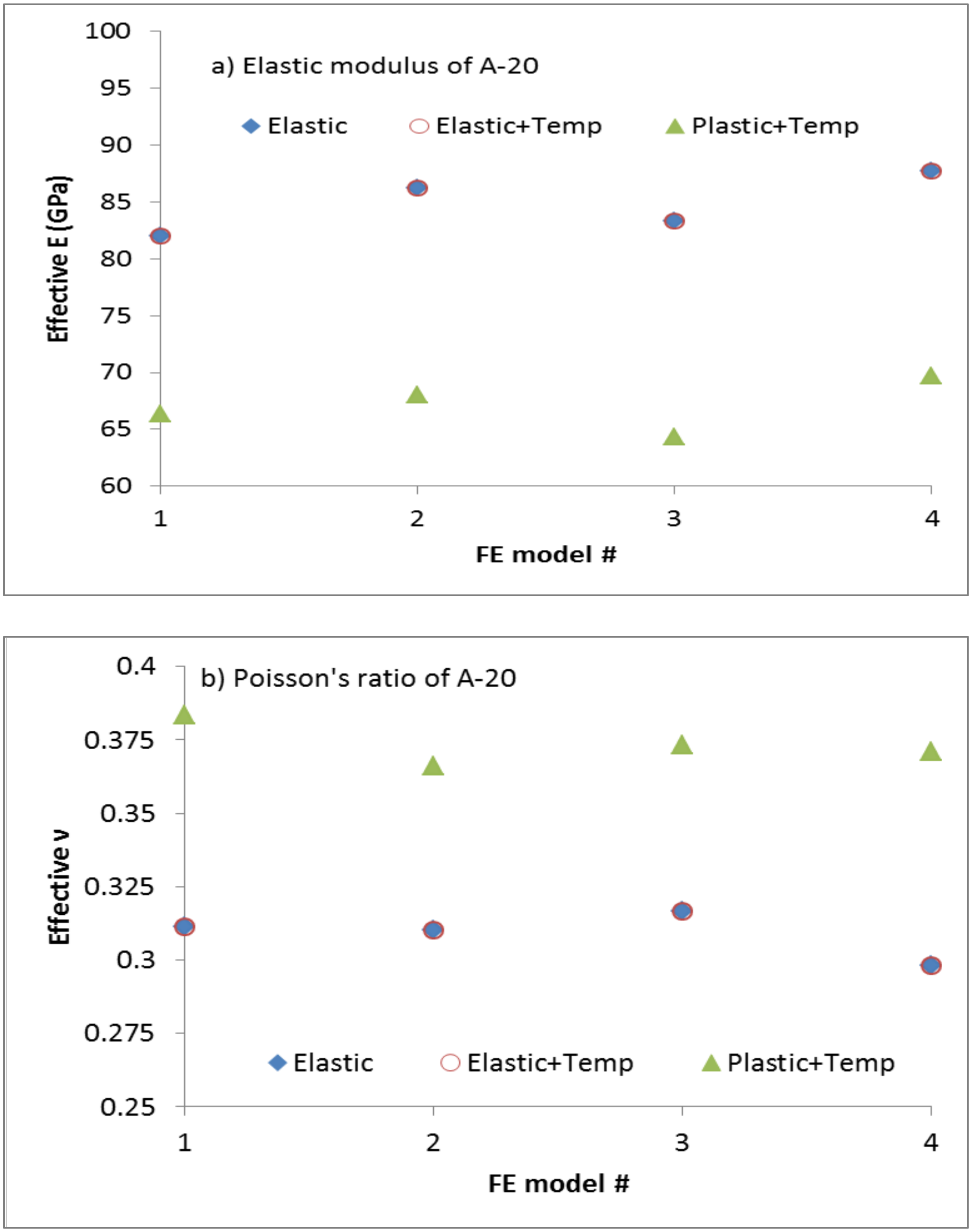

Figure 4.6. Effects of material properties and microstructures on the a) effective moduli and b) Poison's ratio of A-20; c) effective moduli and d) Poison's ratio of B-20 composite systems

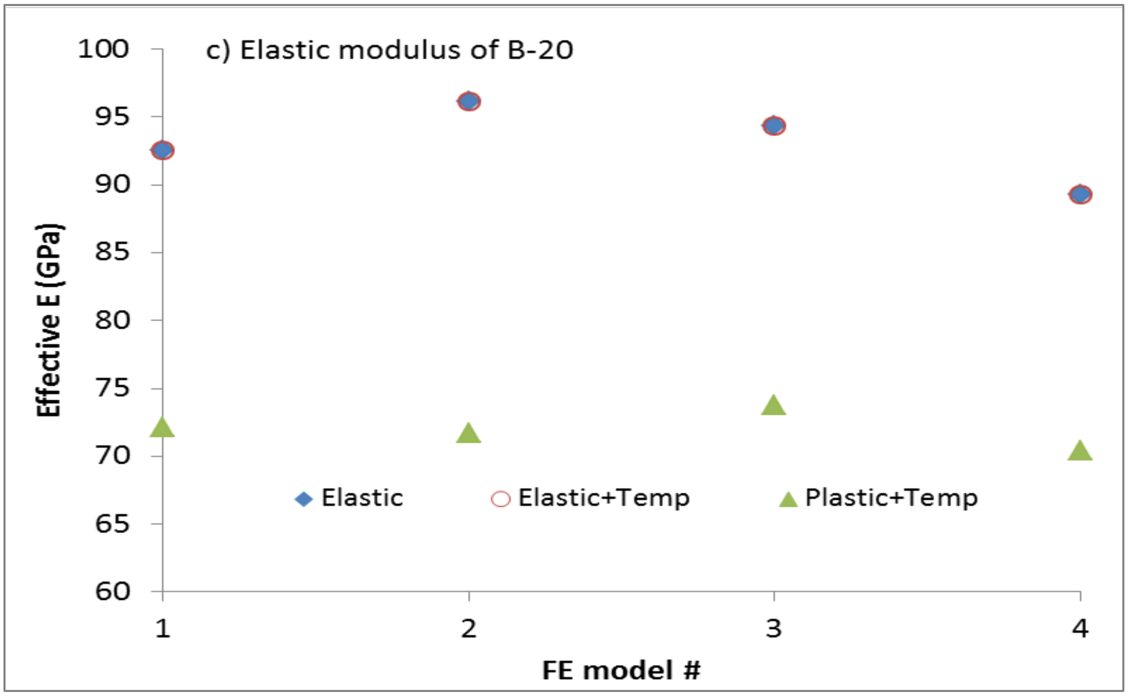

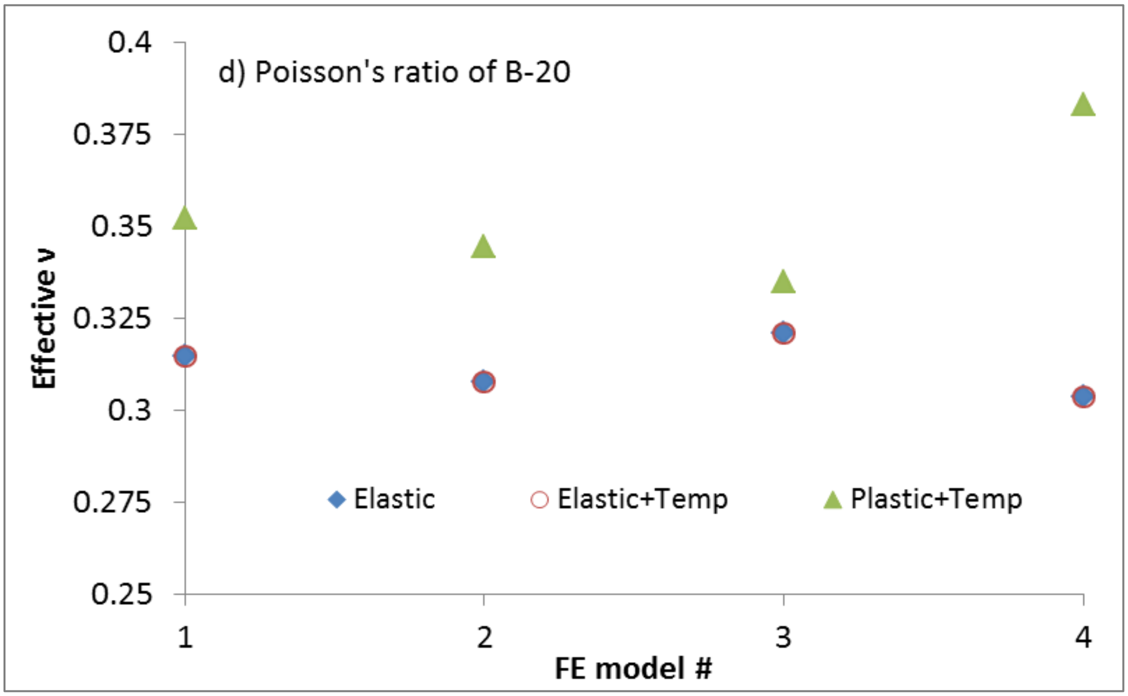

Figure 4.6. Continued

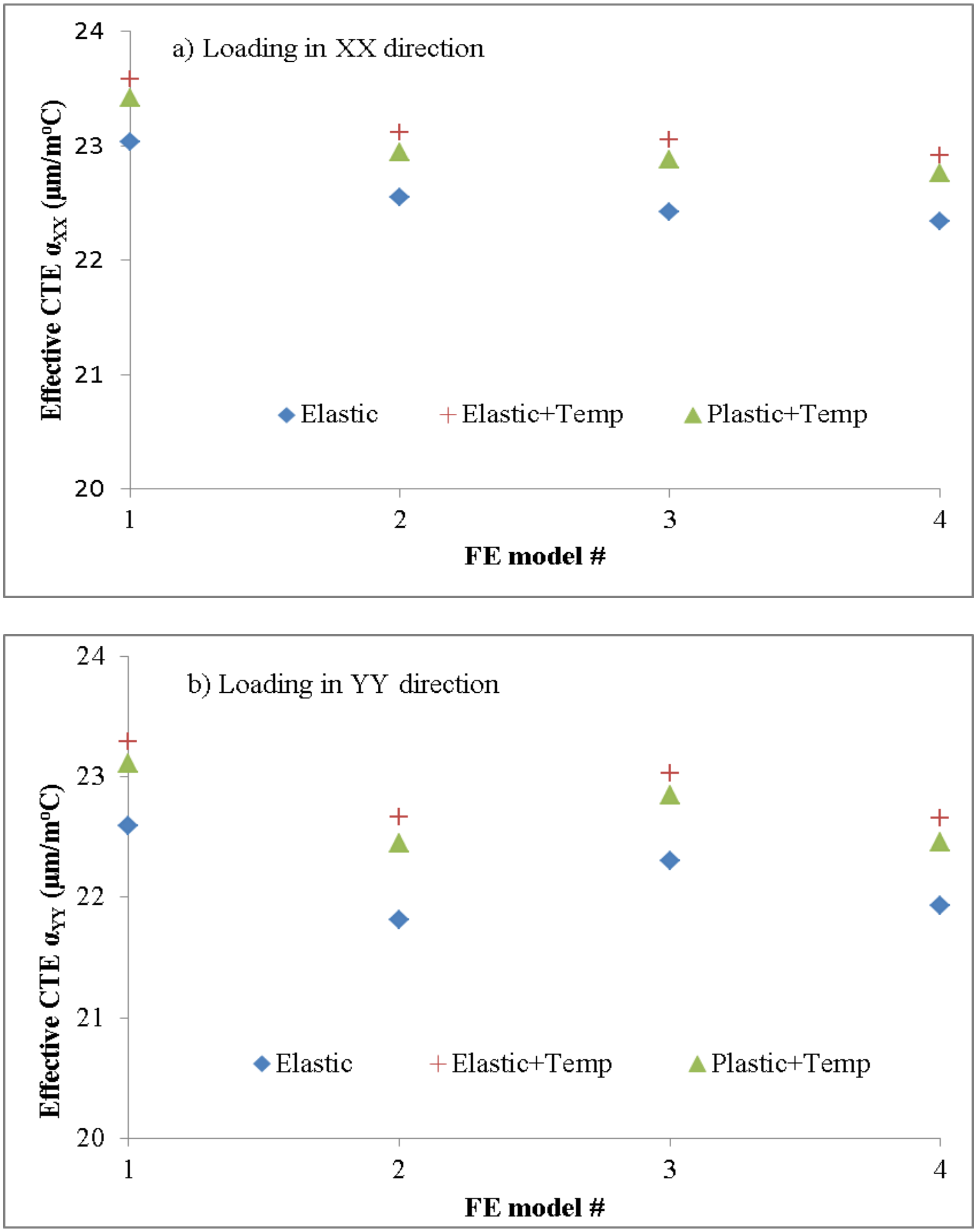

Figure 4.7 a) Effective CTE-XX and b) effective CTE-YY dependency on material properties & microstructure for an A-20 composite sample

It is also observed that non-negligible thermal stresses are generated from cooling the samples from the sintering temperature (600 ^{o}C) to room temperature. In the numerical analyses the composite samples are assumed to have zero stress at 600 ^{o}C and when they are cooled down to room temperature, residual stresses are developed in the aluminum and alumina as depicted in Figures 4.8b-d. These reported stresses are along the *x*-axis. When only the elastic behavior is considered, high thermal stresses are observed within the microstructure of the composites (Figure 4.8b). Compressive stresses are experienced mostly by the alumina particles and tensile stresses are shown in the aluminum matrix. In practice aluminum would have already yielded when subjected to stresses beyond its yield limit, reducing the internal stresses and affecting the overall response of the composites. Furthermore, at the interfaces of the aluminum and alumina constituents high stress discontinuities are observed which could lead to debonding between the constituents. It is seen that the magnitude of the residual stresses drops significantly in the case of an elastic-plastic deformation when a temperature dependent behavior for the aluminum is considered (Figure 4.8d). This is due to the softening of the aluminum during the plastic deformation. It is also interesting to note that the softening of the aluminum matrix also results in the reduction of the thermal stresses in the alumina particles, which is caused by maintaining balance of linear and angular momenta. Figure 4.8d shows that the magnitude of the residual stress is around 50 MPa (tension) in aluminum whereas it is around 500 MPa (compression) in alumina. At the interfaces of aluminum and alumina the magnitude of the residual stress is approximately around 400 MPa (tension). In this particular case, it is also found that the variation in the material parameters due to temperature changes on the overall thermo-mechanical properties of the composites is rather insignificant compared to the softening due to aluminum yielding.

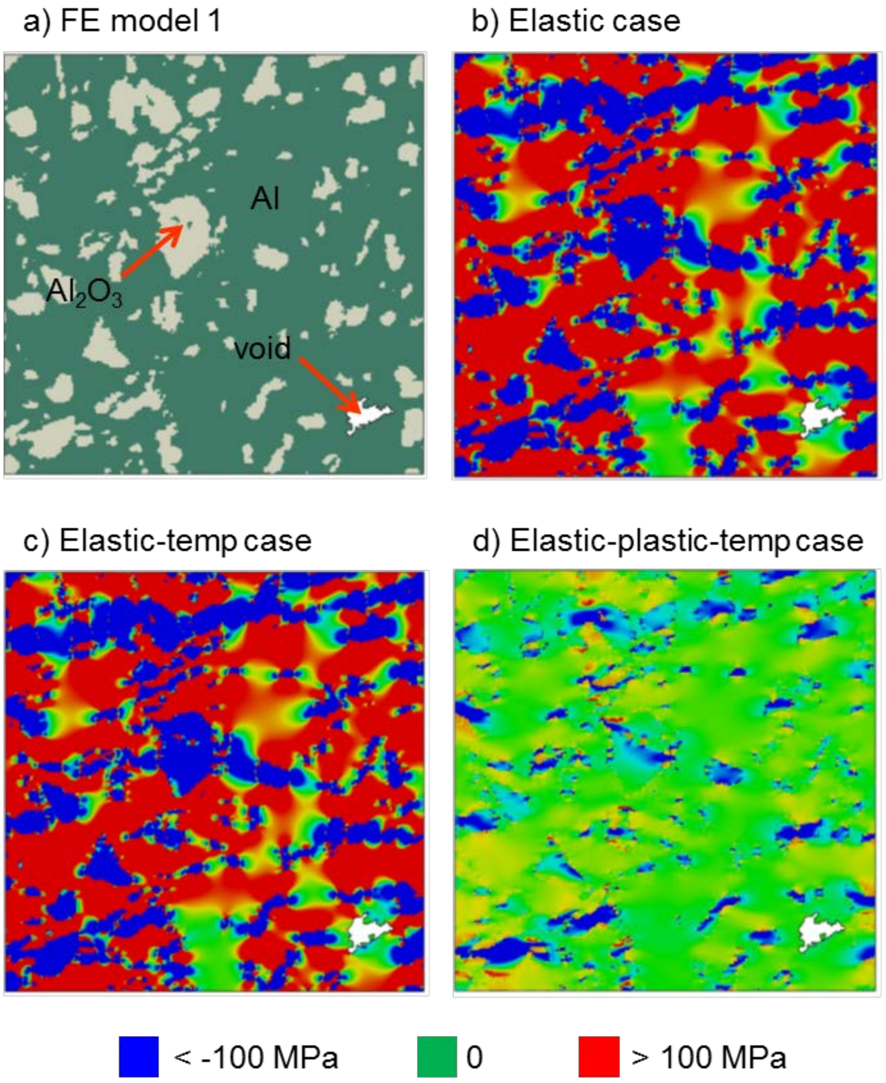

Figure 4.8. Thermal (residual) stress σ_{xx} contours for composite A-20 using FE model 1: a) FE microstructural model 1; b) elastic case; c) elastic case with temperature dependent behavior of the aluminum; d) elastic-plastic case with temperature dependent behavior of the aluminum

4.3. The effect of residual stresses

The cooling down process after sintering the composite samples takes about seven hours, which is a relatively slow process. At elevated temperatures, metal exhibits creep deformation and stress relaxation, and the creep deformation/stress relaxation occurs faster at higher temperature. Thus, the slow cooling process would give enough time for the material to significantly relax its internal (residual) stresses, which are accumulated in the compaction, heating, and sintering steps. Coming to the effect of residual stresses, for all the above cases we assumed that the material is stress free at the sintering temperature. It is not necessary that the composite sample is stress free at the sintering temperature and it is more likely that the stress-free condition is spatial and time dependent. Thus it might be possible that we can never achieve a stress-free condition in the sample. In order to numerically examine the effect of residual stresses, which is assumed due to the built up thermal and plastic deformation effect during the processing, on the overall thermo-elastic properties of the composites a parametric study is presented by taking several temperatures between the sintering and room temperatures at which the composite is considered stress-free or the residual stress is negligible. This temperature is referred as "zero stress temperature", T_{ZS}. As the sample is cooled from this zero stress temperature further down to room temperature, the residual stresses start increasing which are developed due to mismatch in the CTEs of the constituents.

As mentioned above we first perform thermal stress analysis by prescribing initial temperature $T(x, y, 0) = T_{ZS}$ followed by cooling down to room temperature. For determining the effective elastic modulus and Poison's ratio (using Eq. 4.2), a stress of $\sigma_{xx}(L, y) = \sigma_0 = 1$ MPa is prescribed; whereas for characterizing the effective CTE (using Eq. 4.3), temperature change of $\Delta T = 100\,^{o}C$ is prescribed. A parametric study is done on T_{ZS} for different temperatures from 25 ^{o}C to 600 ^{o}C. In Figures 4.9-4.11, the abscissa is the zero stress temperature (T_{ZS}) and the corresponding effective modulus, CTE and Poisson's ratio obtained from the FE analyses are plotted on the ordinate. Figures 4.9a-d are the effective moduli for the composite samples A-10, B-10, A-20 and B-20. The alumina properties are summarized in Table 4.2 and obtained from [17, 72]. The aluminum constituent is assumed elastic-plastic with temperature dependent material properties (Figures 4.4-4.5). The results from the experiment are also included. For all results, if 25 ^{o}C is considered as the zero stress temperature the numerical analysis results in higher elastic modulus than the experimental value (less softening in the material); and if the sintering temperature is taken as zero stress temperature, much lower elastic modulus than the experimental values (more softening in the material) is obtained from the numerical analysis. Between the zero stress temperatures 100 ^{o}C and 200 ^{o}C the effective moduli determined from all the FE analyses are close to the experimental modulus. Hence, when the sample is cooled from the sintering temperature, the stress relaxation process releases the pre-existing residual stress until it becomes nearly zero somewhere in between 100 ^{o}C or 200 ^{o}C and then again the residual stress starts increasing in the reverse direction until the room temperature.

T_{ZS} was observed to be inversely proportional to the amount of porosity, i.e. for the micromechanical model with high porosity T_{ZS} was observed to be lower; whereas for the micromechanical model with less porosity, T_{ZS} was observed to be higher. For example for the A-20 sample in Figure 4.9c, it can be seen that FE model 3 which has high porosity (0.7%) shows less T_{ZS} (100 ^{o}C) whereas for FE model 4 which has low porosity (0%) show high T_{ZS} (200 ^{o}C). The same trend was observed throughout Figs. 4.9a-d, for all the composite samples. The overall CTE seems to be only slightly affected by the zero stress temperature (Figure 4.10). Figure 4.11 shows the effective Poisson's ratio of the composite samples and their comparison with the experimental Poisson’s ratio. The effective Poisson’s ratio increased with zero stress temperature until 200 ^{o}C and remained almost a constant from 200 ^{o}C to 600 ^{o}C. We show that the numerical analyses are capable in predicting the overall elastic modulus, Poisson’s ratio, and CTE of Al/Al_2O_3 composites.

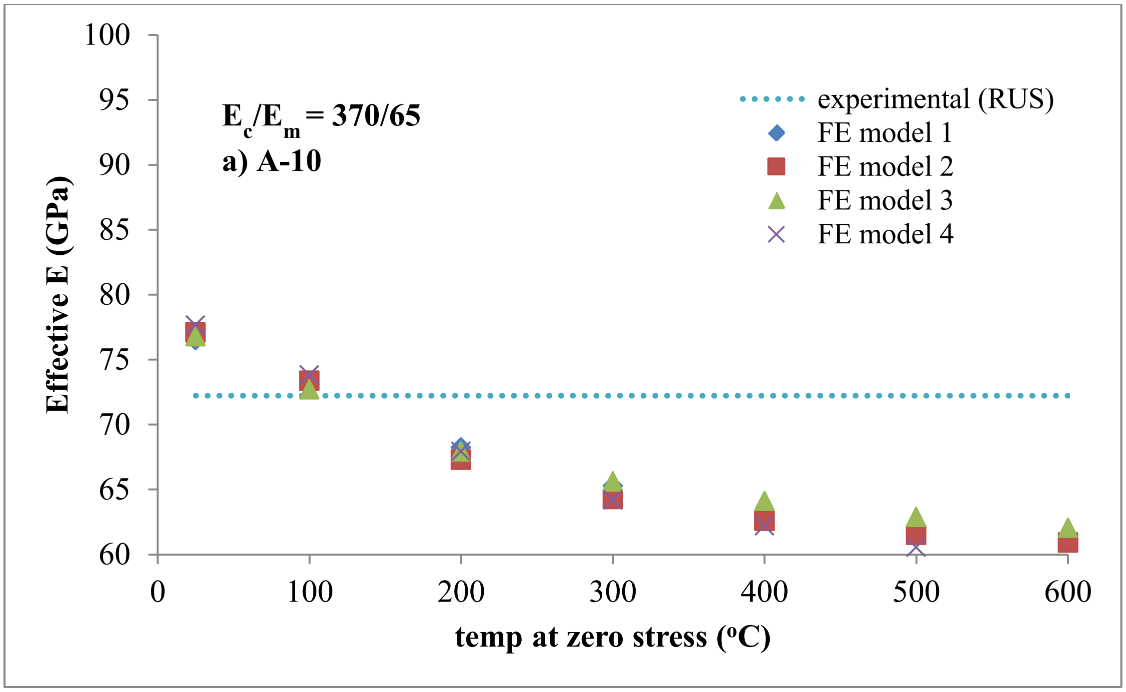

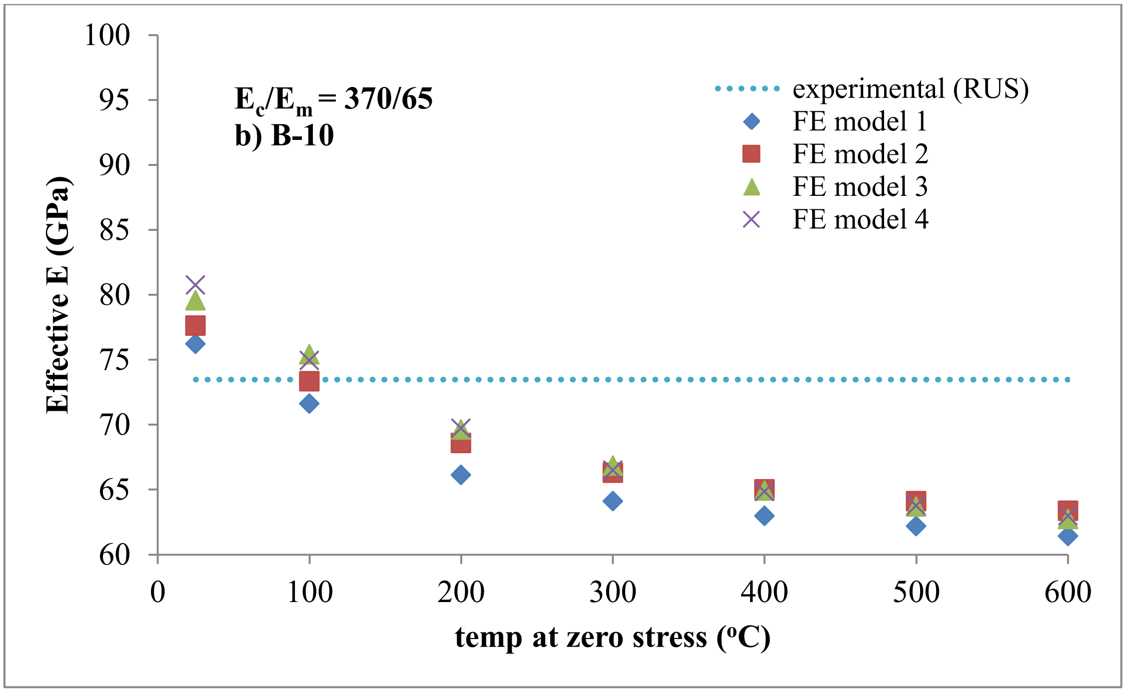

Figure 4.9. Effective modulus of a)A-10 b)B-10 c)A-20 d)B-20 composite samples when E_c/E_m=370/65 and comparison with experimental modulus obtained from RUS (see Chapter III)

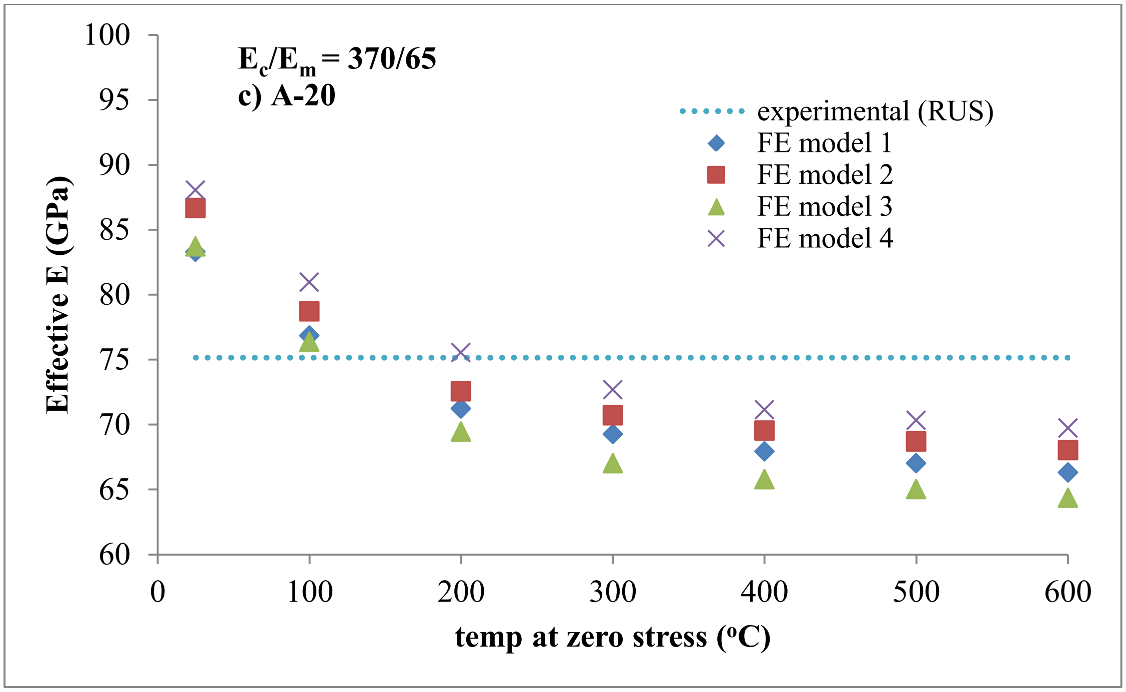

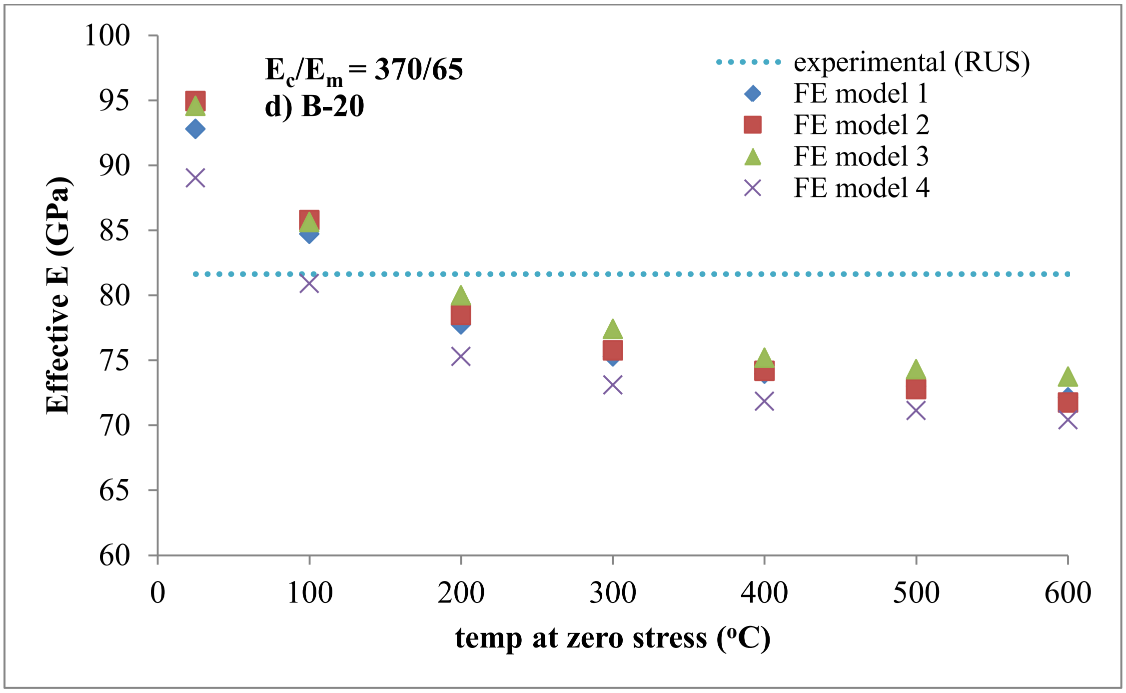

Figure 4.9. Continued

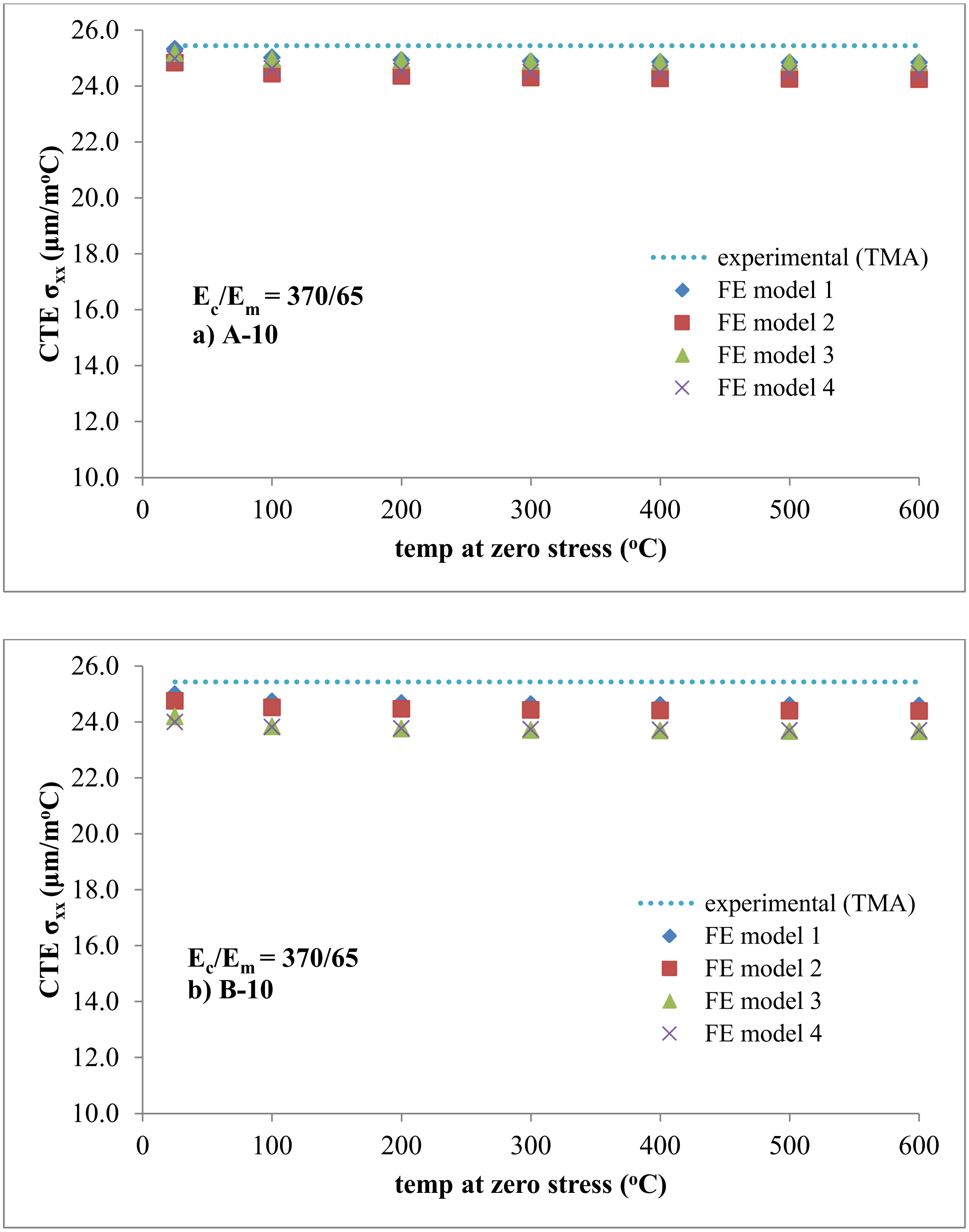

Figure 4.10. Effective CTE of a)A-10 b)B-10 c)A-20 d)B-20 composite samples when E_c/E_m=370/65 and comparison with experimental CTE obtained from RUS (see Chapter III)

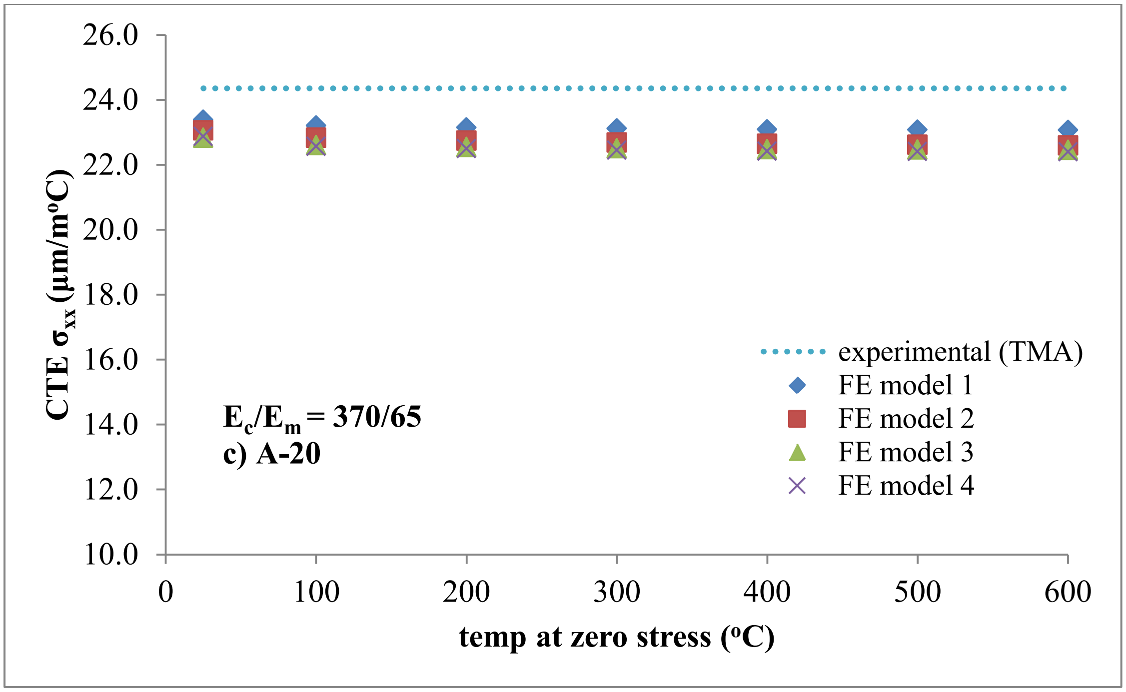

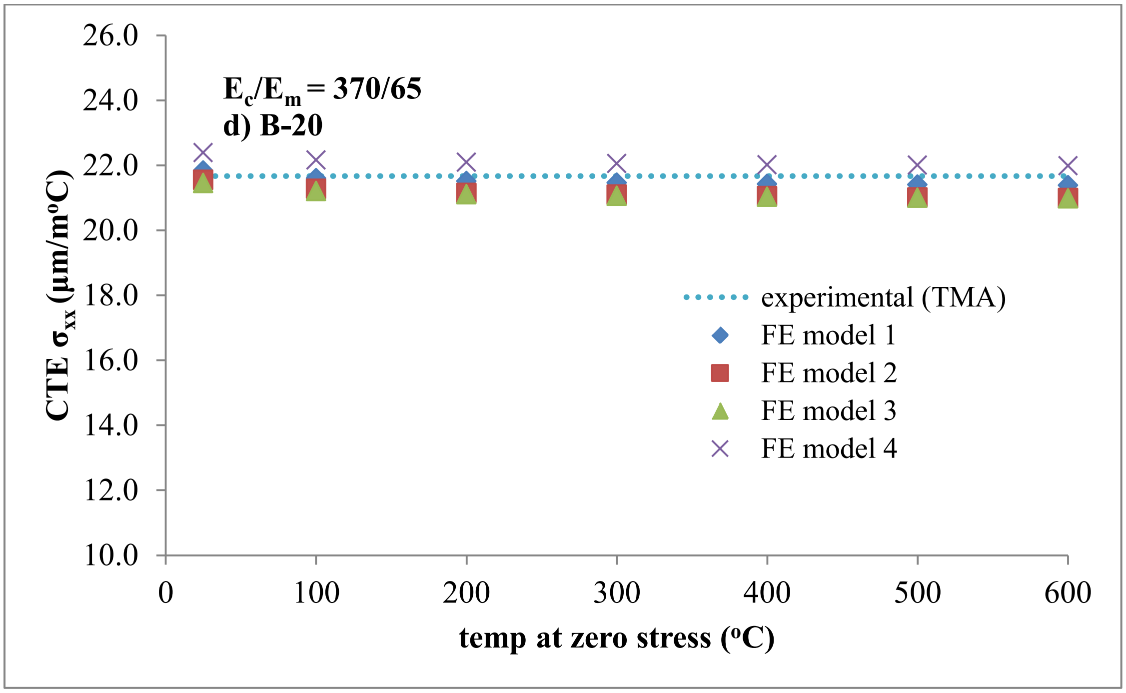

Figure 4.10. Continued

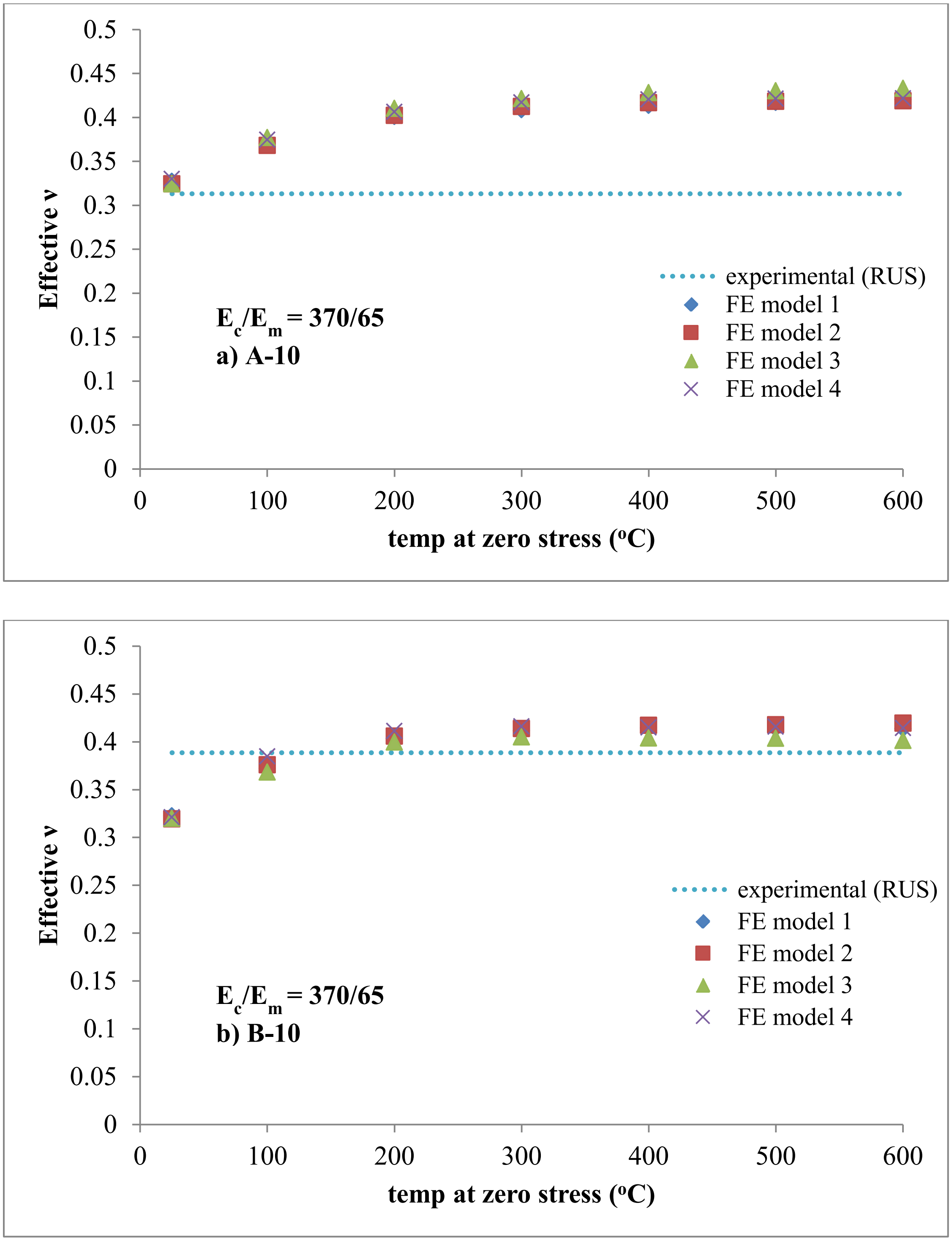

Figure 4.11. Effective ν of a)A-10 b)B-10 c)A-20 d)B-20 composite samples when E_c/E_m=370/65 and comparison with experimental ν obtained from from RUS (see Chapter III)

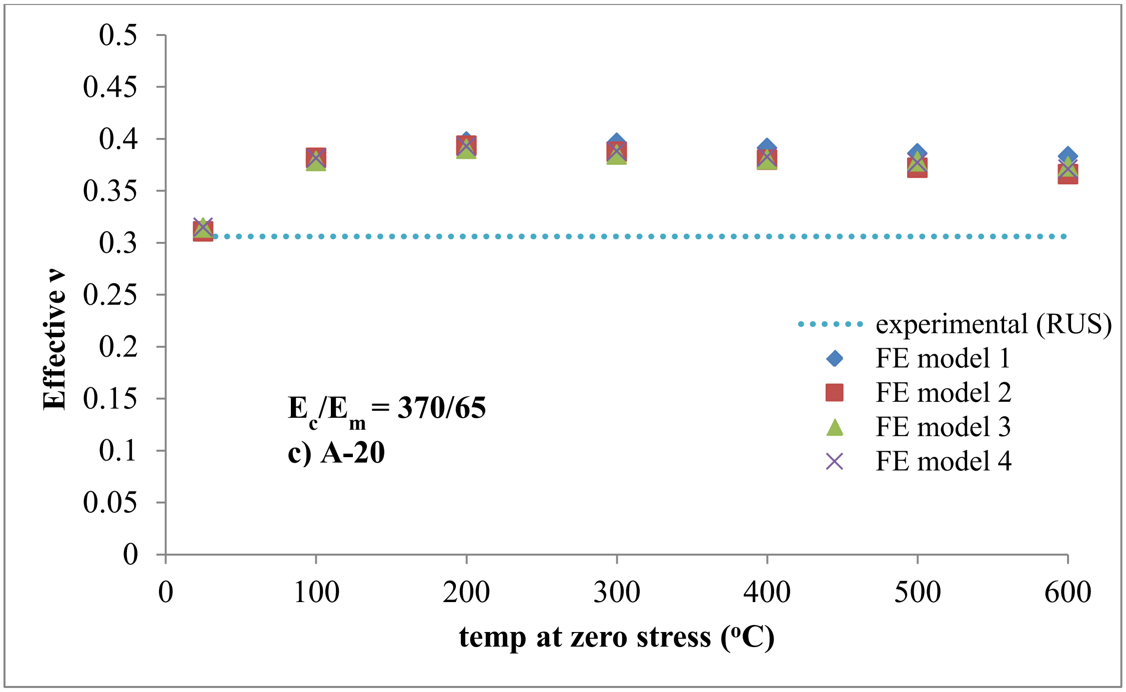

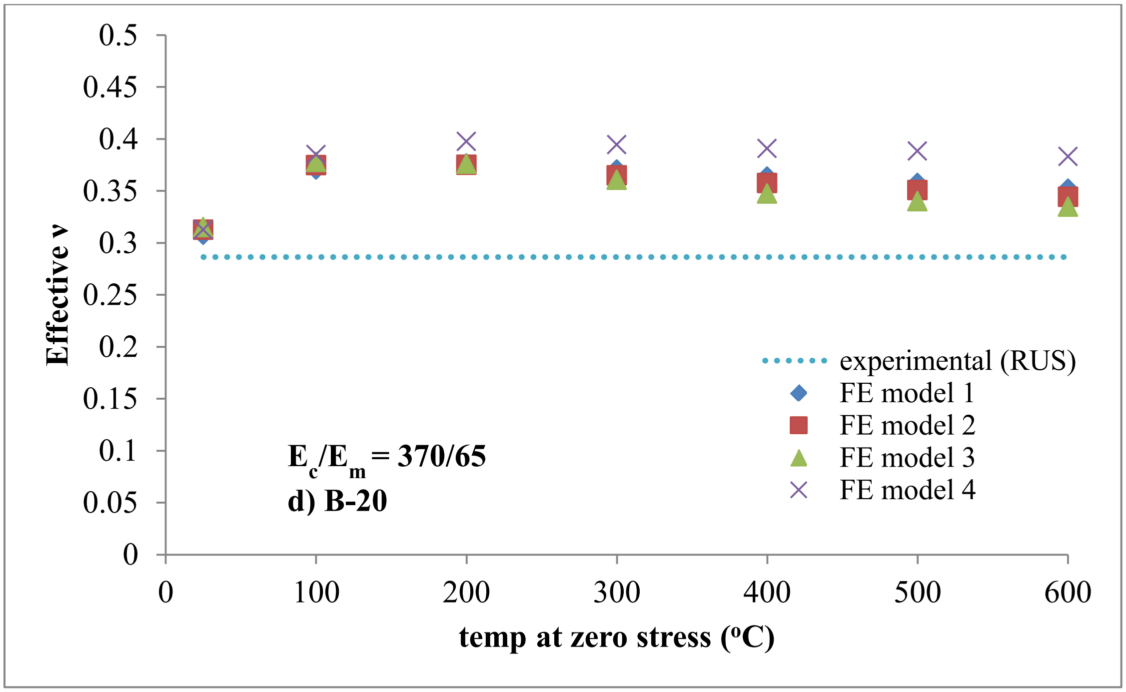

Figure 4.11. Continued

4.4. Convergence studies on the microstructure and element sizes

In order to see whether the sizes of the representative microstructures and elements chosen to conduct the above studies is sufficient to obtain reasonably accurate results, convergence studies are conducted to examine the effect of mesh size on modulus and Poison's ratio for the composite A with 20% alumina volume content (A-20) shown in Figure 4.1b. Figure 4.12 shows the same four FE meshes as in Fig. 4.1b with finer mesh. Software OOF2 was used to generate the meshes. For obtaining the coarser mesh, the maximum and minimum edge lengths of the elements were specified to the software as 3.27e-4 mm. For obtaining the finer mesh, the maximum and minimum edge lengths of the elements were specified as $1.96\text{x}10^{-4}$ mm. Tables 4.3-4.6 show the detailed comparison between the coarser and finer mesh for the four FE models, respectively. For determining the effective elastic modulus and Poison's ratio (using Eq. 4.2), we first perform thermal stress analysis by prescribing initial temperature as $T(x, y, 0) = T_{ZS}$=200 ^{o}C (from section 4.3, we found that T_{ZS} was close to 200 ^{o}C for the A-20 sample) and allowing it to cool down to room temperature, then followed by prescribing a stress of $\sigma_{xx}(L, y) = \sigma_0 = 1$ MPa. Figure 4.13 shows the comparison between the modulus obtained from coarser and finer mesh for the four FE meshed models of the A-20 composite sample. It can be seen that the difference in the effective moduli for the coarser and finer meshes is less than 1 GPa for all the microstructural models considered. This shows that the coarser mesh used for carrying out the numerical studies in sections 4.1- 4.3, is good enough to get accurate results.

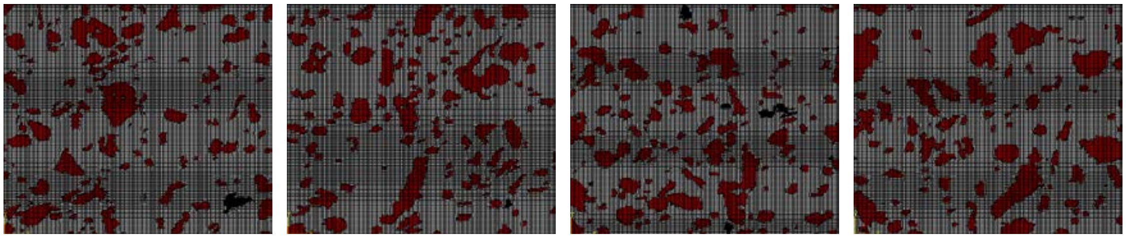

Figure 4.12. FE microstructural models of A-20 composite sample with finer mesh

Table 4.3. Comparison of coarser and finer mesh for FE meshed model 1

FE meshed model 1	**Coarser mesh (Figure 4.1)**	**Finer mesh (Figure 4.12)**
RVE size	0.05mm X 0.05mm	0.05mm X 0.05mm
Element size (max edge length X min edge length)	3.27x10^{-4}mm X 3.27x10^{-4}mm Average max edge length: 3.36x10^{-4} , Average min edge length: 2.86x10^{-4} , Longest edge: 5.23x10^{-4}, Shortest edge: 3.79x10^{-5}	1.96x10^{-4}mm X 1.96x10^{-4}mm Average max edge length: 1.99x10^{-4}, Average min edge length: 1.81x10^{-4}, Longest edge: 3.41 x10^{-4}, Shortest edge: 2.31x10^{-5}
# of elements	28994 (Linear Quad: 21815, Linear Tri: 7179)	73564 (Linear Quad: 63173, Linear Tri: 10391)
# of nodes	25783	68980
Average aspect ratio	For Quad elements: 1.14 For Tri elements: 1.53	For Quad elements:1.09 For Tri elements: 1.52
E, ν	$E = 71.23$ GPa, $\nu = 0.397435897$	$E = 70.82$ GPa, $\nu = 0.402266289$

Table 4.4. Comparison of coarser and finer mesh for FE meshed model 2

FE meshed model 2	**Coarser mesh (Figure 4.1)**	**Finer mesh (Figure 4.12)**
RVE size	0.05mm X 0.05mm	0.05mm X 0.05mm
Element size (max edge length X min edge length)	3.27x10^{-4}mm X 3.27x10^{-4}mm Average max edge length: 3.34x10^{-4} , Average min edge length: 2.81x10^{-4} , Longest edge: 5.23x10^{-4}, Shortest edge: 5.42x10^{-5}	1.96x10^{-4}mm X 1.96x10^{-4}mm Average max edge length: 1.99x10^{-4} , Average min edge length: 1.8x10^{-4}, Longest edge: 3.52x10^{-4}, Shortest edge: 2.48x10^{-5}
# of elements	29781 (Linear Quad: 21869 , Linear Tri: 7912)	73370 (Linear Quad: 63414 , Linear Tri: 9956)
# of nodes	26155	68933
Average aspect ratio	For Quad elements: 1.16 For Tri elements: 1.54	For Quad elements: 1.09 For Tri elements: 1.51
E, ν	$E = 72.57$ GPa, $\nu = 0.393323657$	$E = 72.15$ GPa, $\nu = 0.3997114$

Table 4.5. Comparison of coarser and finer mesh for FE meshed model 3

FE meshed model 3	**Coarser mesh (Figure 4.1)**	**Finer mesh (Figure 4.12)**
RVE size	0.05mm X 0.05mm	0.05mm X 0.05mm
Element size (max edge length X min edge length)	3.27x10^{-4}mm X 3.27x10^{-4}mm Average max edge length: 3.35x10^{-4} , Average min edge length: 2.81x10^{-4}, Longest edge: 5.31x10^{-4}, Shortest edge: 4.09x10^{-5}	1.96x10^{-4}mm X 1.96x10^{-4}mm Average max edge length: 1.99x10^{-4} , Average min edge length: 1.8 x10^{-4} , Longest edge: 3.10x10^{-4}, Shortest edge: 2.40x10^{-5}
# of elements	29762 (Linear Quad: 21795 , Linear Tri: 7967)	73710 (Linear Quad: 62960 , Linear Tri: 10750)
# of nodes	26241	69075
Average aspect ratio	For Quad elements: 1.16 For Tri elements: 1.51	For Quad elements: 1.09 For Tri elements: 1.51
E, ν	E = 69.44 GPa, ν = 0.390277778	E = 69.06 GPa, ν = 0.395027624

Table 4.6. Comparison of coarser and finer mesh for FE meshed model 4

FE meshed model 4	**Coarser mesh (Figure 4.1)**	**Finer mesh (Figure 4.12)**
RVE size	0.05mm X 0.05mm	0.05mm X 0.05mm
Element size (max edge length X min edge length)	3.27x10^{-4}mm X 3.27x10^{-4}mm Average max edge length: 3.35x10^{-4} , Average min edge length: 2.89x10^{-4}, Longest edge: 5.36x10^{-4}, Shortest edge: 5.23x10^{-5}	1.96x10^{-4}mm X 1.96x10^{-4}mm Average max edge length: 1.99x10^{-4}, Average min edge length: 1.82x10^{-4} , Longest edge: 3.09x10^{-4}, Shortest edge: 2.65x10^{-5}
# of elements	28418 (Linear Quad: 22235 , Linear Tri: 6183)	72699 (Linear Quad: 63794, Linear Tri: 8905)
# of nodes	25649	68774
Average aspect ratio	For Quad elements: 1.13 For Tri elements: 1.52	For Quad elements: 1.08 For Tri elements: 1.5
E, ν	E = 75.53 GPa, ν = 0.392749245	E = 75.08 GPa, ν = 0.394894895

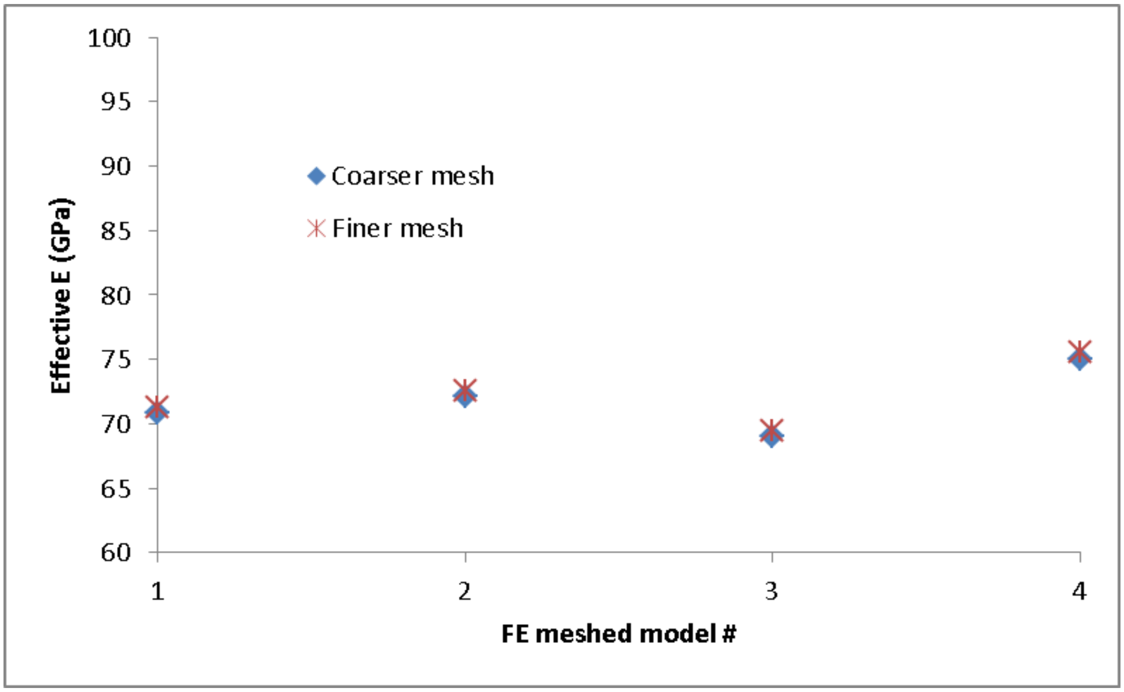

Figure 4.13. Comparison of modulus for the four FE models of A-20 composite sample when coarser and finer mesh are used

Next, the effect of sizes of the representative microstructures on the overall effective elastic properties is numerically examined. The numerical results obtained so far are obtained with a representative volume element (RVE) size of 0.05 mm X 0.05 mm (Figure 4.1b). In order to see whether the RVE size chosen is sufficient to represent the entire microstructure of the composite, we increase the RVE size to 0.1mm X 0.1 mm and see how significantly the effective modulus and Poison's ratio vary. Figure 4.14b shows the RVEs of size 0.1 mm X 0.1 mm obtained from the A-20 composite sample and Figure 4.14a shows the procedure used to obtain them by overlapping a grid. The volume content of alumina and %porosity for FE model#5 are 21.7 and 0.34 respectively, whereas for FE model#6 they are 19.09 and 0.17 respectively. Table 4.7 shows the details of two FE microstructural models with RVE size 0.1mm X 0.1 mm. Figure 4.15 shows the comparison between the effective moduli obtained using different RVE sizes for the A-20 composite sample. It is seen that the effective modulus did not significantly vary with an increase in RVE size. Therefore, the RVE size of 0.05 mm X 0.05 mm used for previous numerical studies is sufficient to get accurate results.

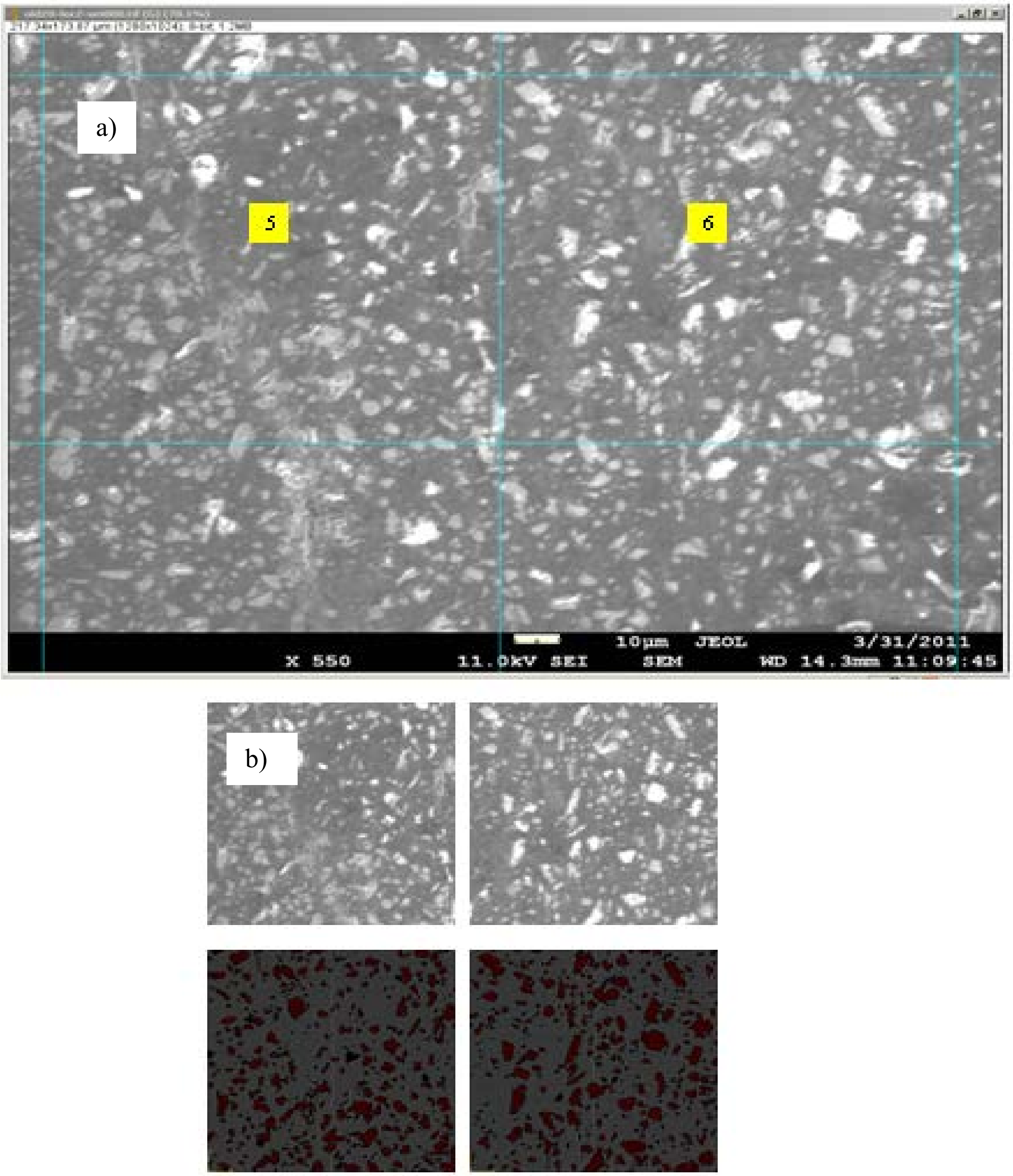

Figure 4.14 a) SEM image of A-20 composite sample overlapped with 0.1mm X 0.1 mm grid; b) Two square micrographs of 0.1mm X 0.1 mm and their corresponding FE microstructural models 5 and 6

Table 4.7. Details of the mesh for the two FE meshed models with RVE size 0.1mm X 0.1 mm

	FE meshed model 5	**FE meshed model 6**
RVE size	0.1mm X 0.1mm	0.1mm X 0.1mm
Element size (max edge length X min edge length)	$3.27\text{x}10^{-4}$mm X $3.27\text{x}10^{-4}$mm Average max edge length: $3.28\text{x}10^{-4}$, Average min edge length: $2.75\text{x}10^{-4}$, Longest edge: $5.52\text{x}10^{-4}$, Shortest edge: $8.46\text{x}10^{-5}$	$3.27\text{x}10^{-4}$mm X $3.27\text{x}10^{-4}$mm Average max edge length: $3.29\text{x}10^{-4}$, Average min edge length: $2.77\text{x}10^{-4}$, Longest edge: $5.52\text{x}10^{-4}$, Shortest edge: $8.56\text{x}10^{-5}$
# of elements	123143 (Linear quad: 87273, Linear tri: 35870)	121551 (Linear quad: 87953, Linear tri: 33598)
# of nodes	106126	105584
Average aspect ratio	For Quad elements:1.14 For Tri elements: 1.65	For Quad elements:1.14 For Tri elements: 1.66
E, ν	E=71.43 GPa, ν = 0.405	E=70.03 GPa, ν =0.396358543

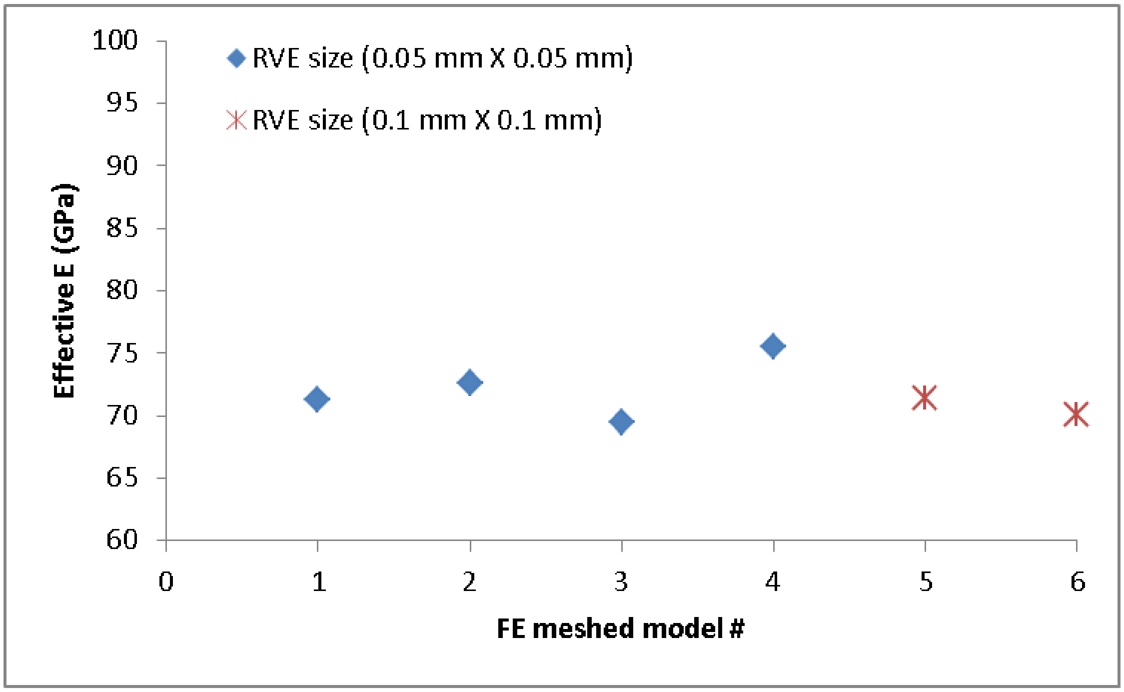

Figure 4.15. Effective moduli obtained using different RVE sizes for the A-20 composite sample

4.6. Effect of the shape of reinforcements and pores

The reinforcement and pores in Al-Al_20_3 composites, manufactured using powder metallurgy method, have no definite shape as shown in Figure 4.1. Analytical and numerical studies on micromechanics of composites are often done on idealized microstructures, i.e., assuming circular or spherical particles dispersed in homogeneous matrix, in order to reduce complexity in obtaining the overall/effective responses of the composites. In this section, the effect of idealizing the shapes of the inclusions (particles and pores) on the effective elastic properties of the composites is investigated. Numerical studies have been conducted on the four FE meshed models shown in Figure 4.1b, in order to see the effect of reinforcement shape on the effective modulus of the composite. Using the image analysis software ImageJ, the area of the actual shaped reinforcements and pores are calculated along with their centroids (see Appendix for the details), for each of the FE meshed models of the A-20 sample shown in 4.1b. Using ABAQUS Python script, circular shaped reinforcements and pores, with the areas same as those of their corresponding actual shaped reinforcement and pores, are substituted in their places at their respective centroids. Figures 4.16a-4.19a show the FE meshed models with actual shaped reinforcement and pores replaced with circular shape, whereas Figures 4.16b-4.19b show the contours of the corresponding axial stress along the loading direction (σ_{11}) respectively. As expected, the stress contours for the micromechanical models with actual shapes of the inclusions show higher magnitude of localized stresses: red (> 50 MPa) and blue (< -50 MPa) as indicated by wider regions with red and blue colors when compared to the microstructures with idealized inclusions (circular reinforcement and pores). That is because the sharp edges in the inclusions lead to the development of stress concentrations.

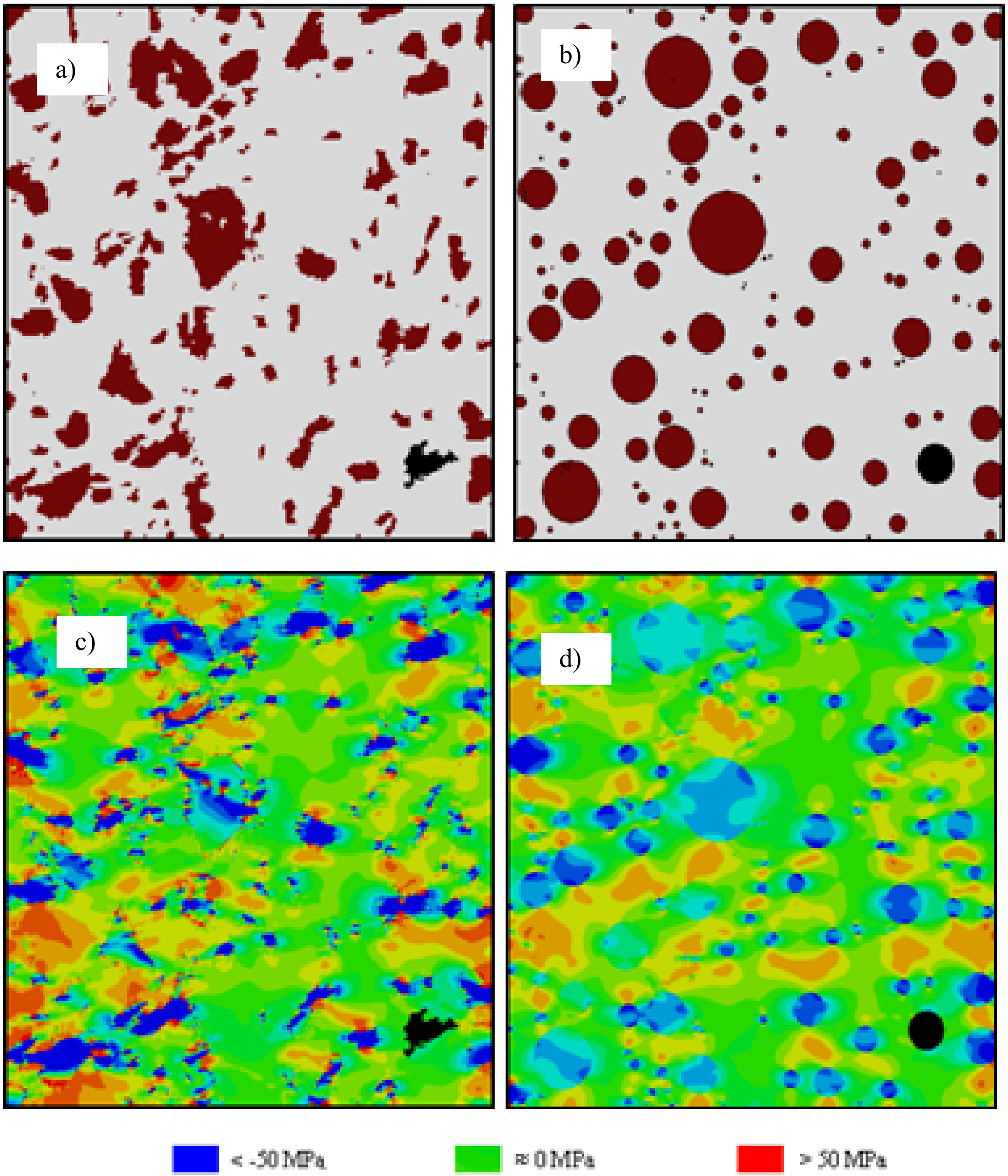

Figure 4.16. FE meshed model#1 of A-20 composite sample with a) actual shape and b) circular shape of reinforcement and pores; stress (σ_{11}) contour for c) actual shape and d) circular shape of reinforcement and pores

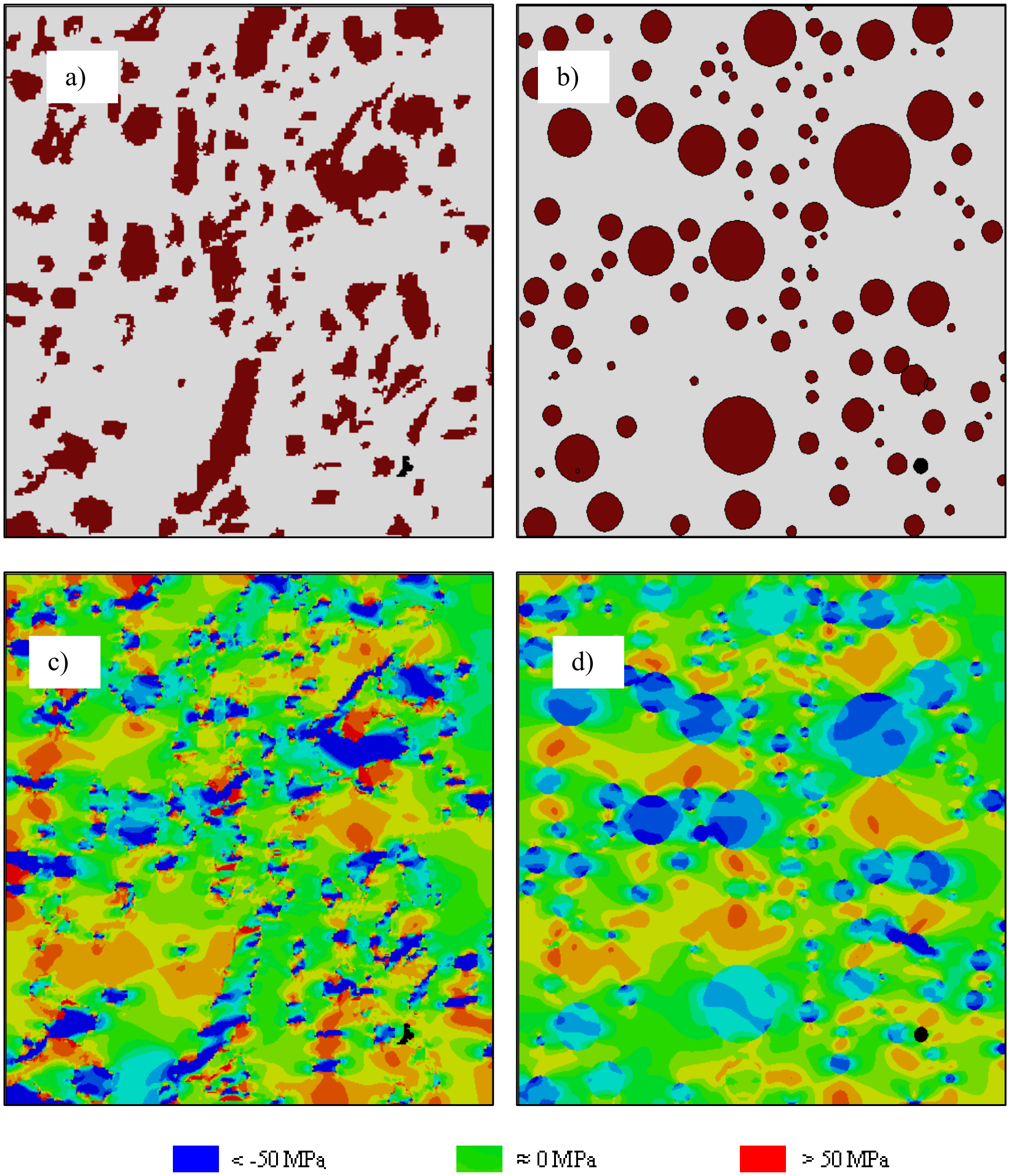

Figure 4.17. FE meshed model#2 of A-20 composite sample with a) actual shape and b) circular shape of reinforcement and pores; stress (σ_{11}) contour for c) actual shape and d) circular shape of reinforcement and pores

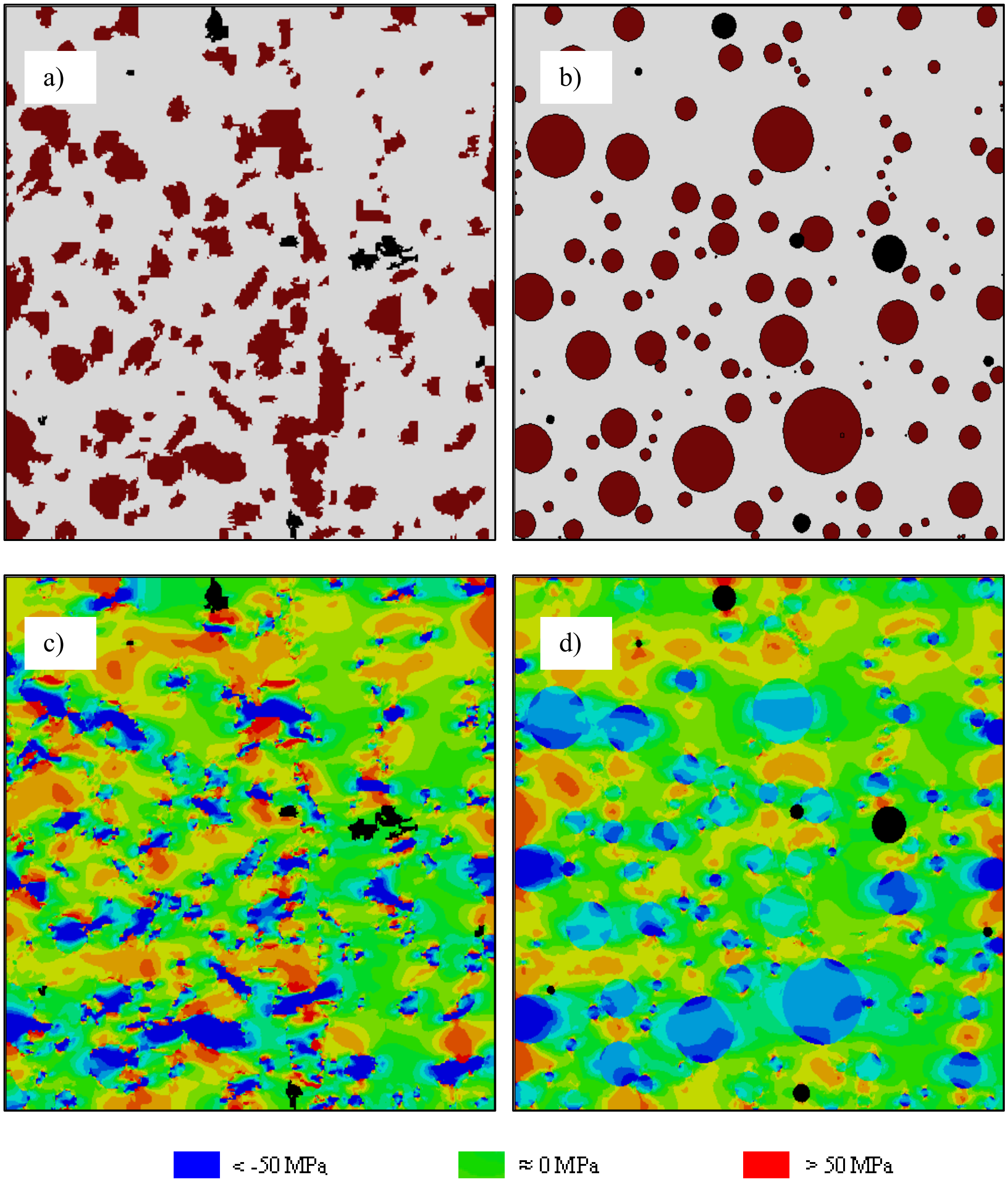

Figure 4.18. FE meshed model#3 of A-20 composite sample with a) actual shape and b) circular shape of reinforcement and pores; stress (σ_{11}) contour for c) actual shape and d) circular shape of reinforcement and pores

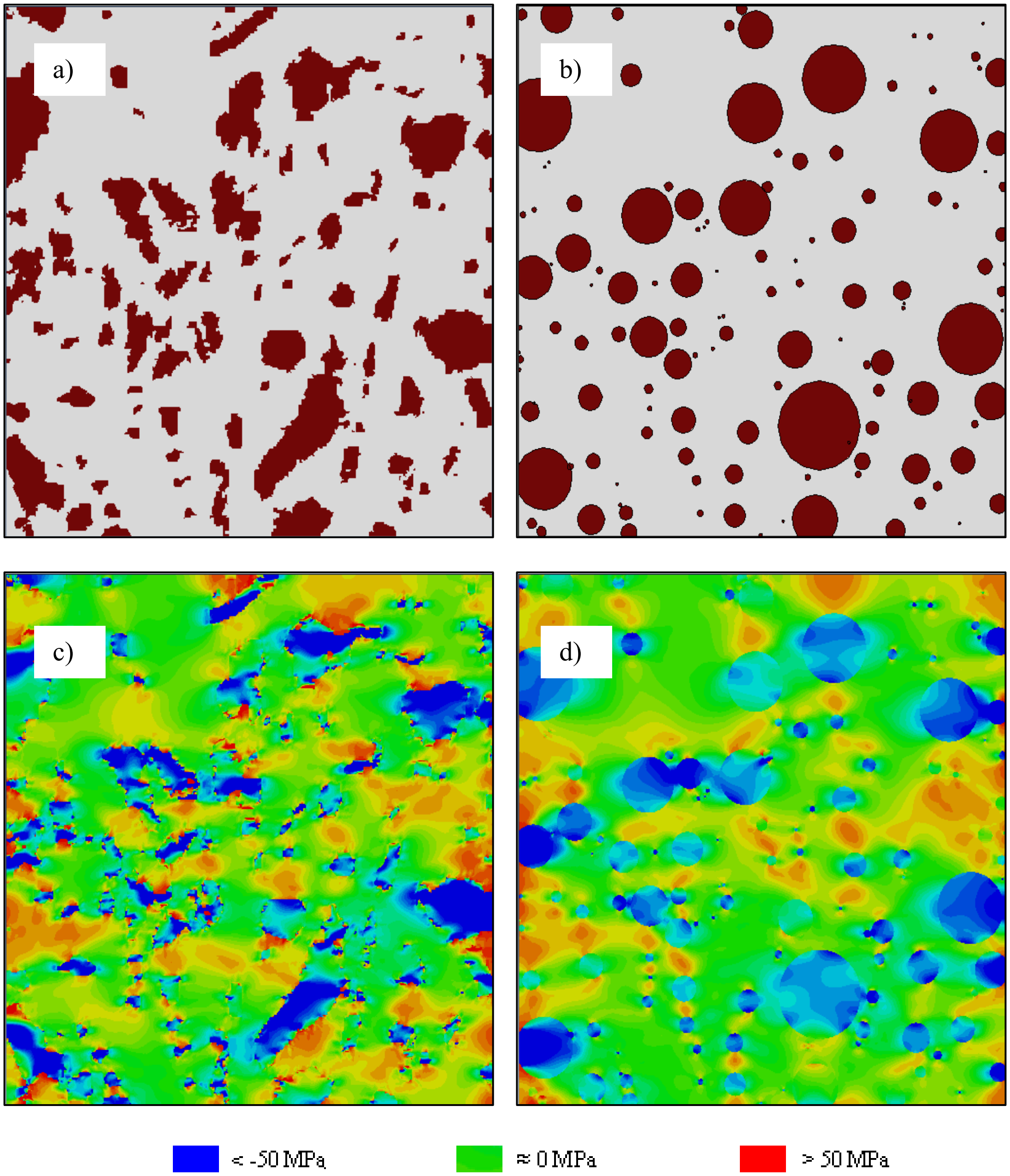

Figure 4.19. FE meshed model#4 of A-20 composite sample with a) actual shape and b) circular shape of reinforcement and pores; stress (σ_{11}) contour for c) actual shape and d) circular shape of reinforcement and pores

Figure 4.20 compares the effective moduli for microstructures with the actual shaped and circular shaped reinforcement and pores. The difference in the effective moduli was negligible for all the FE meshed models when the idealized shapes of the inclusions are considered. The FE meshed model 4 shows the maximum change of 2 GPa. The variation in the effective modulus from one FE meshed model to another shows that, the microstructure (distribution of reinforcement in the matrix along with its VF and porosity) has a significant affect than the reinforcement shape. It is concluded that the effect of microstructural geometries on the overall elastic response of composites is negligible, however when one is interested in understanding the degradation in composites due to localized effects, it might be necessary to incorporate detailed microstructural geometries of the composites.

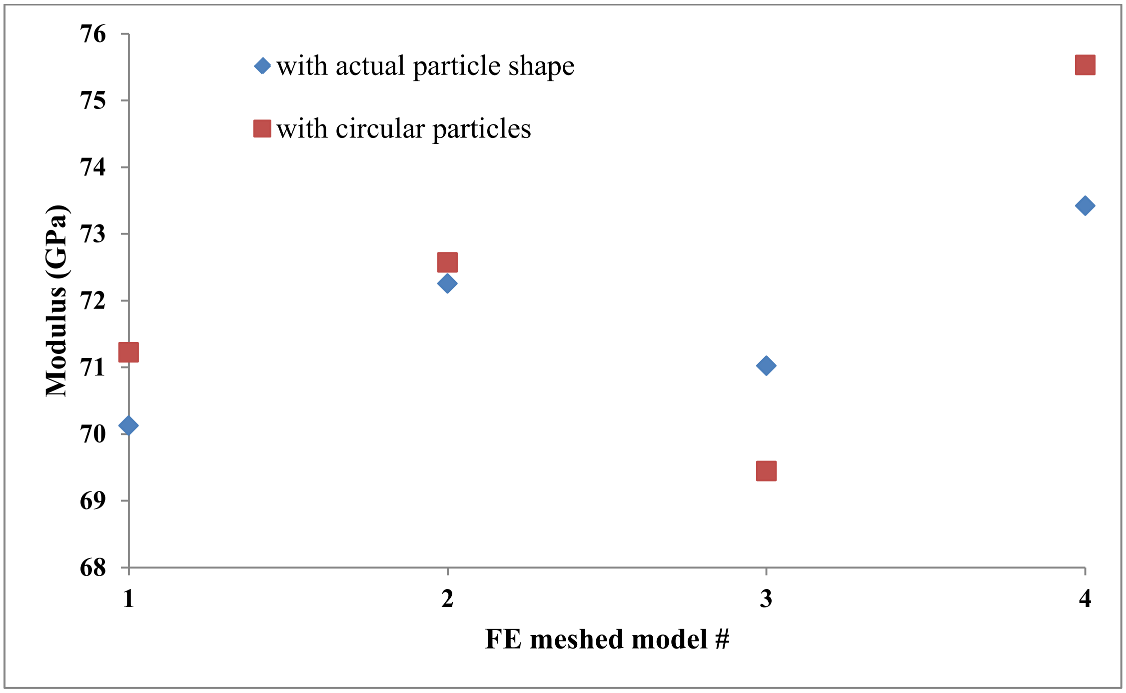

Figure 4.20. Elastic moduli comparison for FE models with actual shaped and circular shaped reinforcement and pores

CHAPTER V

MECHANICAL BEHAVIOR OF THE COMPOSITE AT VARIOUS TEMPERATURES

This chapter presents the mechanical behavior of the Al-Al_2O_3 composites under uniaxial compressive loadings (up to 5% axial strain) followed by unloading the stresses. Composites with 0, 5, and 10% alumina contents are manufactured and tested at various isothermal temperatures: 25°C, 200°C, and 400°C. Numerical studies are also conducted to examine the effect of microstructural morphologies on the overall compressive behavior of the composites.

5.1. Compression Testing

Experimental setup for the uniaxial compression testing is described in Section 2.4c of Chapter II. At room temperature (25°C), three different strain rates were used to test the pure aluminum or 0% composite sample viz. 0.0833 min^{-1}, 0.1 min^{-1} and 1min^{-1}; and two samples weare used at each strain rate to test the repeatability of the results. The purpose is to investigate the possible effect of loading rates, within quasi-static loadings, on the responses of the composites. As seen in Figure 5.1, for the above strain rates considered, the effect of strain rate on the overall responses of the samples at room temperature are negligible and hence for testing all the other samples, the strain rate of 0.0833 $min^{-1}$was used. It should be noted that at elevated temperatures, it might be possible that the aluminum matrix experiences rate-dependent behavior even under quasi-static loadings. However, the focus of this study is to examine the effect of temperatures on the overall response of the studied composites under uniaxial compressive loads; thus, it is necessary to keep the same strain rates at all considered temperatures. It is widely reported in literature [77-80] that if the matrix material is strain rate sensitive then its composite is also going to be strain rate sensitive; and if the matrix material is insensitive to the strain rate then most likely that the composite material is going to be insensitive to the strain rate effect. This is because of the fact that the compressive flow stress dependency on strain rate for the reinforced composite follows that of the bare metal.

Al-Al_2O_3 composite samples with 0, 5 and 10 vol% alumina concentrations were prepared using powder metallurgy method as described in Chapter II. The composite samples were subjected to compression testing at room temperature (25^0C) and elevated temperature (200^0C and 400^0C) cases. Composite specimens which were cylindrical in shape with dimensions of (12.7 mm in diameter) × (23.87±1.778 mm in length), with length to diameter ratio varying from 1.72 to 2.0, were used for compression testing. Table 5.1 shows the physical attributes viz. height, diameter, relative density and volume fraction obtained from XRD, of the composite samples used for compression testing. Figures 5.2 a-c show XRD spectra of composite samples 0, 5 and 10% after they were compression tested at 25^0C, 200^0C and 400^0C respectively. Aluminum and alumina peaks occur at the same 2-theta angle for different volume fractions of the composite and the relative difference in height between aluminum and alumina peaks decrease as volume fraction increases from 0 to 10%. Figures 2.3-2.4 show the analysis of XRD spectrum with software EVA to determine phase volume fraction of the composite. Table 5.1 presents the volume fraction of alumina in the composite samples used for the compression testing.

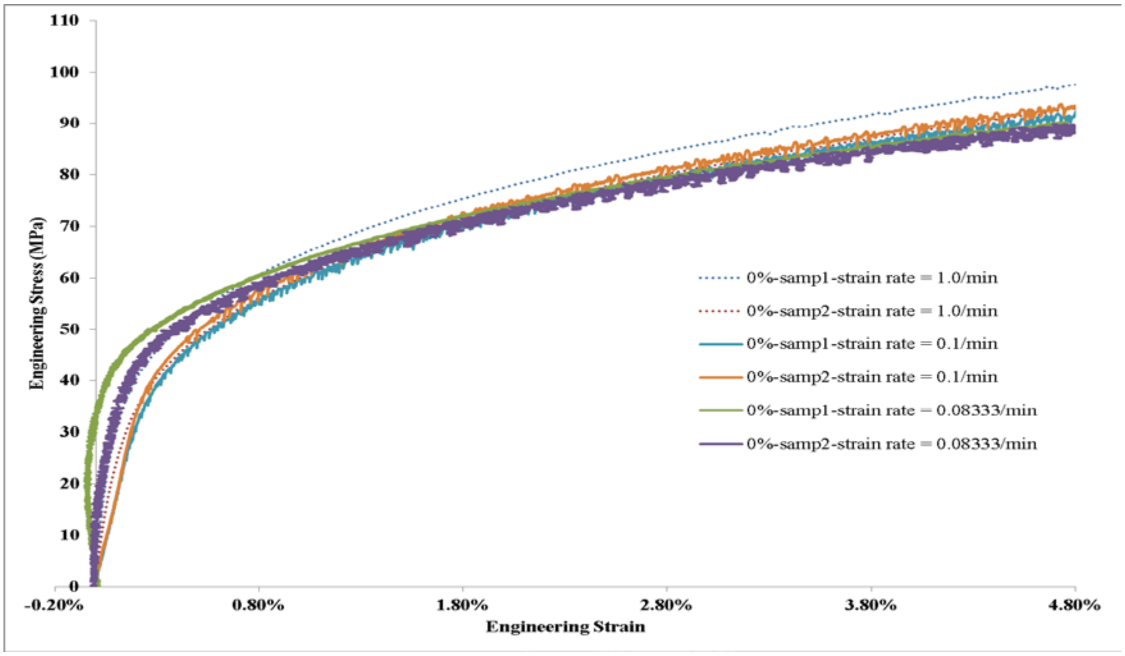

Figure 5.1. Effect of strain rate on 0% composite samples which are compression tested at 25^{0}C. As the effect is negligible, strain rate of 0.08333/min is used for the rest of the samples

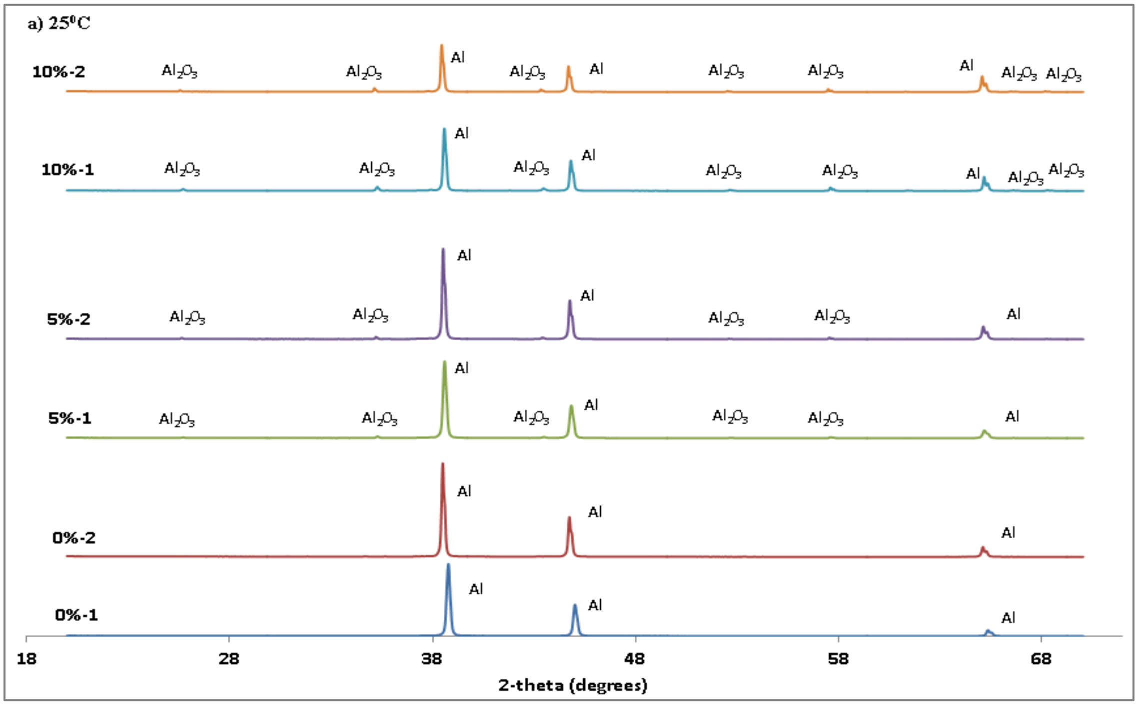

Figure 5.2. a-c XRD spectra of composite samples which are used for compression testing at 25^{O}C

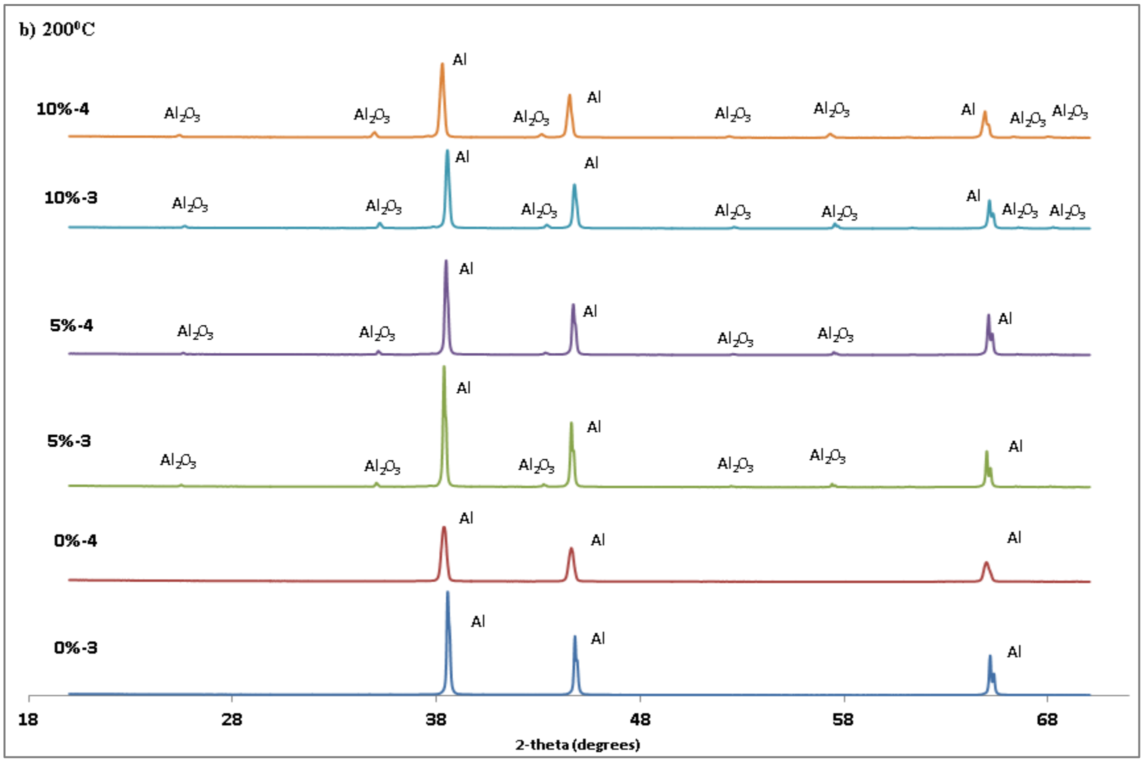

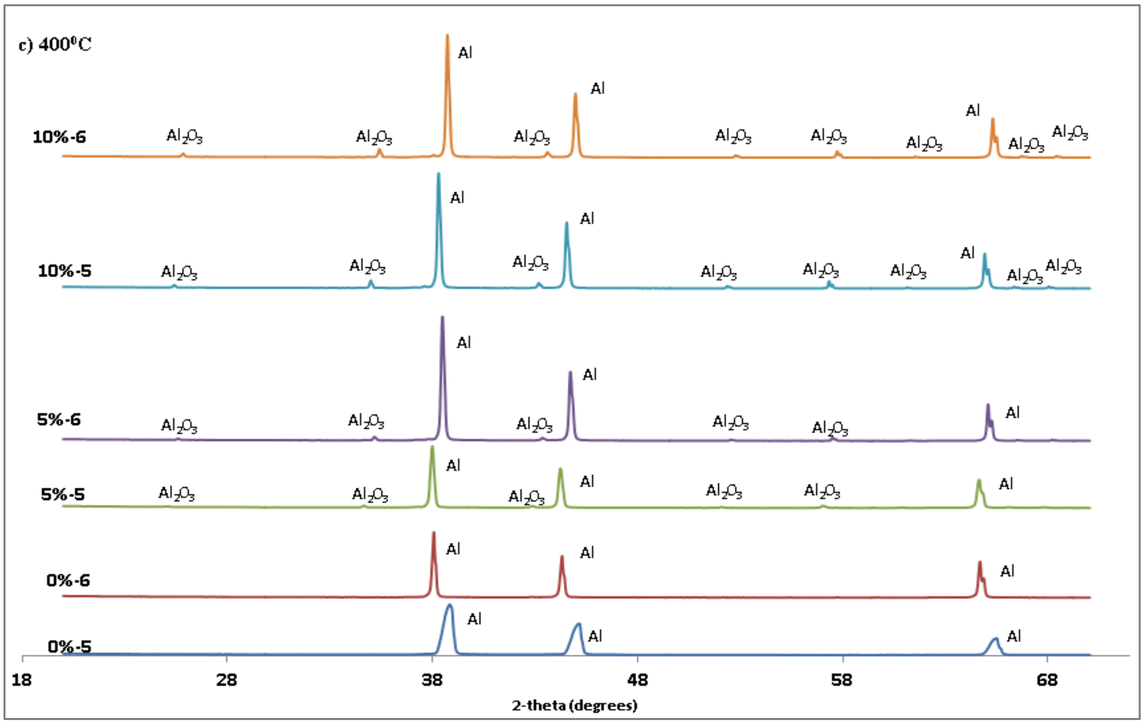

Figure 5.2. Continued

Table 5.1. Physical attributes of the composite samples used for compression testing at various testing temperatures

Testing temp	Sample	Height (mm)	Diameter (mm)	Relative Density (%)	Porosity (%)	V.F (XRD)
25^{0}C	0%-1	25.7937	12.7	95.78	4.22	0.9
	0%-2	25.0952	12.7	95.71	4.29	1.1
	5%-1	24.2443	12.7	94.098	5.90	6.7
	5%-2	22.0522	12.7	94.674	5.32	6.4
	10%-1	21.59	12.7	90.37	9.63	11.9
	10%-2	25.4635	12.7	93.85	6.15	11.6
200^{0}C	0%-3	23.495	12.7	95.346	4.654	1.6
	0%-4	24.0792	12.7	96.4	3.6	1.4
	5%-3	24.2189	12.7	95.27	4.73	5.9
	5%-4	25.2349	12.7	93.9	6.10	6.3
	10%-3	24.8793	12.7	93.38	6.62	11.2
	10%-4	24.0665	12.7	94.29	5.71	11.4
400^{0}C	0%-5	23.3426	12.7	96.25	3.75	1.5
	0%-6	24.9555	12.7	95.341	4.65	1.7
	5%-5	22.6314	12.7	95.18	4.82	6.9
	5%-6	24.4983	12.7	95.096	4.90	7
	10%-5	23.7998	12.7	92.97	7.03	11.7
	10%-6	22.4282	12.7	92.37	7.63	12.2

Figure 5.3a-c shows the stress strain curves of Al-Al_2O_3 composites at three different temperatures 25, 200 and 400^{0}C. At each testing temperature, two composite samples of 0, 5 and 10% volume fraction of alumina were tested, at a strain rate of 0.0833 min^{-1}. The physical attributes of the composite samples tested (viz. height, diameter, relative density, volume fraction of alumina determined from XRD) are listed in Table 5.1. It can be seen from Figure 5.3a-c that as the testing temperature increases the stress strain curves drops significantly for all the volume fractions of the composites. This is expected because with an increase in temperature

the material becomes softer and the dislocation motion gets activated and hence the flow resistance of the material decreases at higher temperatures [81]. On the other hand, there is no significant variation in the stress strain curves with increase in volume fraction of the tested composites; however, the stresses developed in the composite sample increase slightly for the same strain with an increase in volume fraction. The main reasons could be due to an increase in the pore contents as the volume content of the composites increase (see Table 5.1), which soften the overall response of the composites. The behavior of stress strain curves with temperature, volume fraction and microstructure is discussed further by characterizing the elastic modulus, yield stress, strain hardening coefficient (n) and strengthening coefficient (K) of the composite samples.

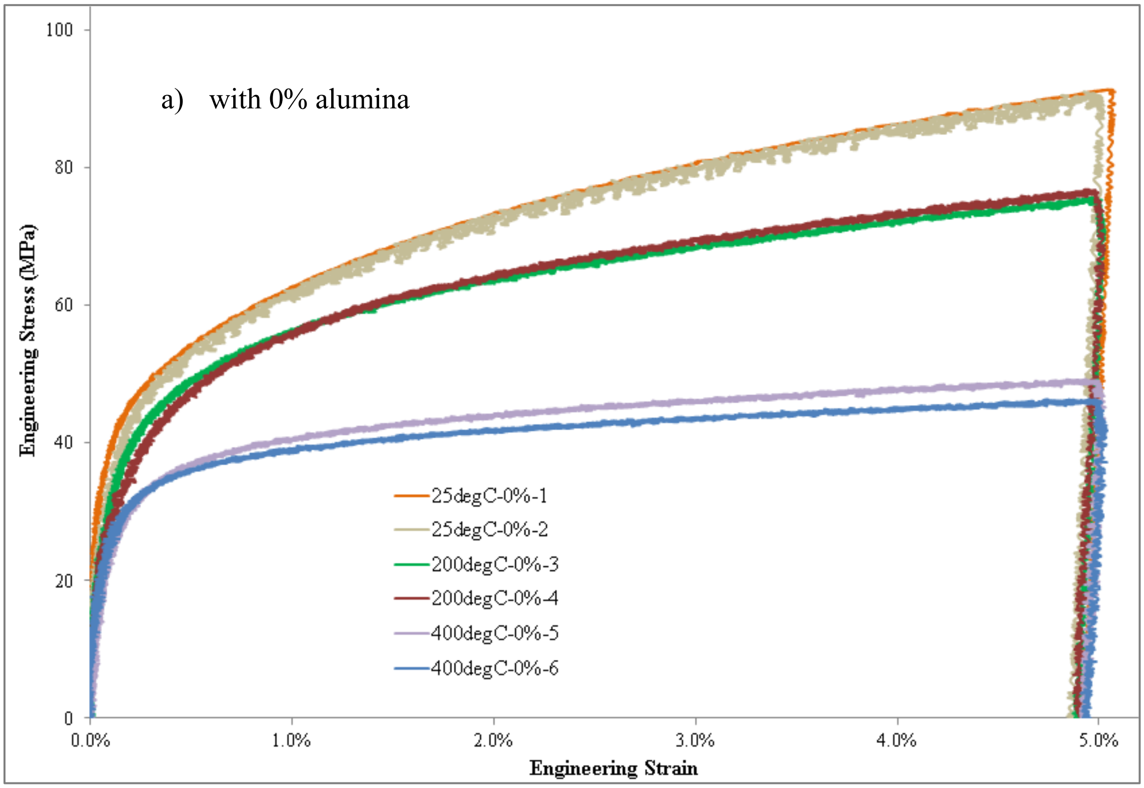

Figure 5.3. Stress-strain response of composite samples with a) 0% b) 5% and c) 10% alumina volume contents at various temperatures

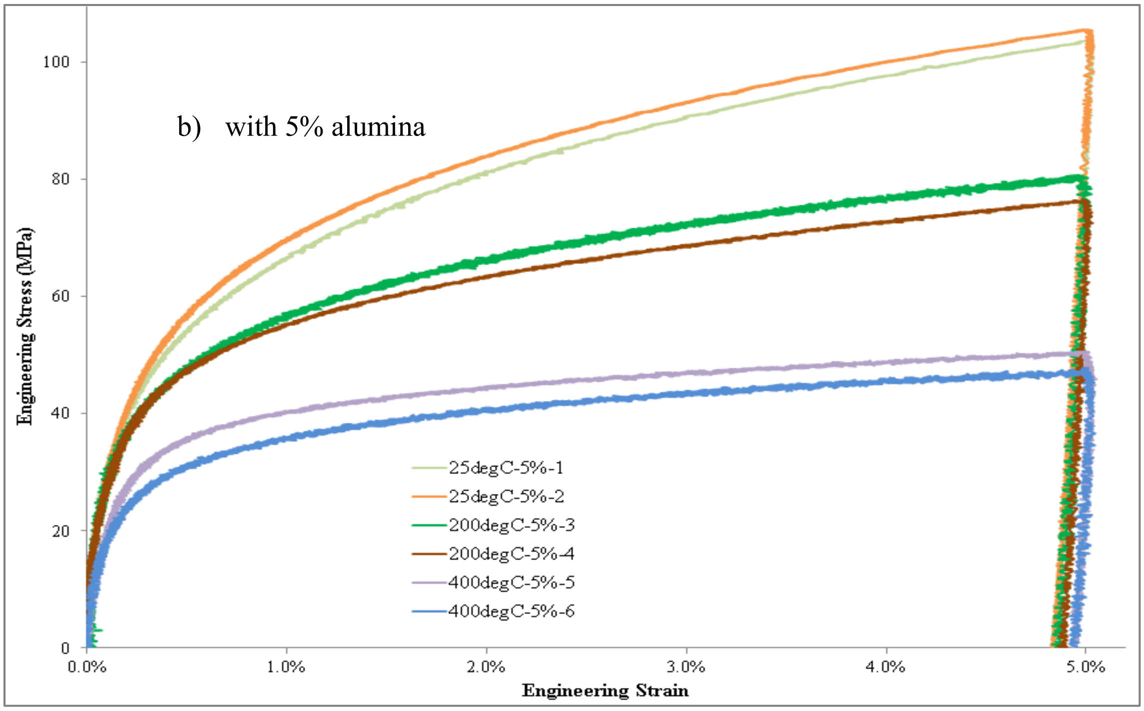

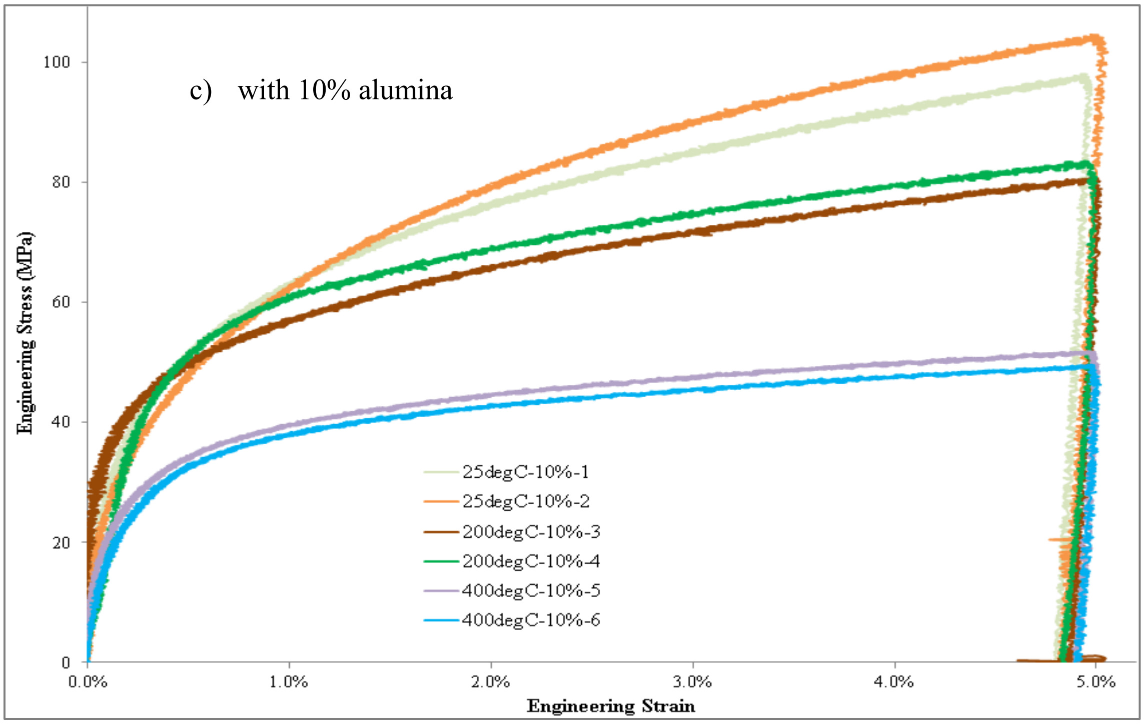

Figure 5.3. Continued

The elastic modulus and yield stress of the composite samples tested at various temperatures are determined from the stress strain curves. Figures 5.4a-b show the stress-strain responses of the composite with 0% alumina content during the start of loading and the unloading portions of the curves. During the loading step, it was observed that all the curves show nonlinear elastic behavior with only a small portion of the curves appearing to be linear. Elastic modulus was measured during the unloading step by taking the slope of stress and strain curve [82]. Unloading was done until the stress in the composite material was zero (until the cross heads lose contact with the sample) but there was still some residual strain present in the composite due to plastic deformations in the samples during the loading stage and hence the stress-strain curves do not go back to the original state. The unloading portion of the stress-strain curve shows the residual strain and elastic strain recovery of the composite samples.

Figure 5.5 illustrates the procedure used to measure the yield stress of the 0%-2 composite sample that was tested at 25^0C. For determining the yield stress, first a line was drawn at 0.2% stain with an elastic modulus of the composite sample as its slope (as shown in Figure 5.5), and then the stress corresponding to the intersection of this line with the stress-strain curve was noted down as the yield stress of the composite sample. Table 5.2 summarizes the corresponding elastic modulus and yield stress of the composite samples obtained from their stress-strain curves.

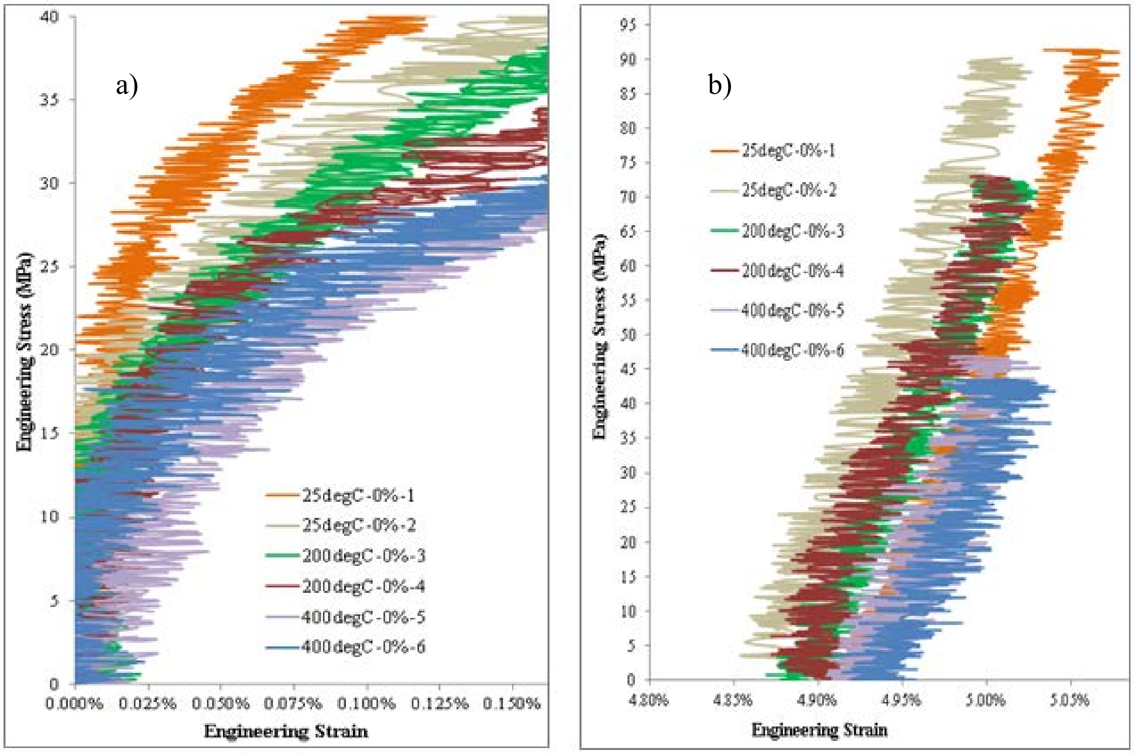

Figure 5.4. Stress strain curves of 0% composite samples during a) the start of loading and b) unloading

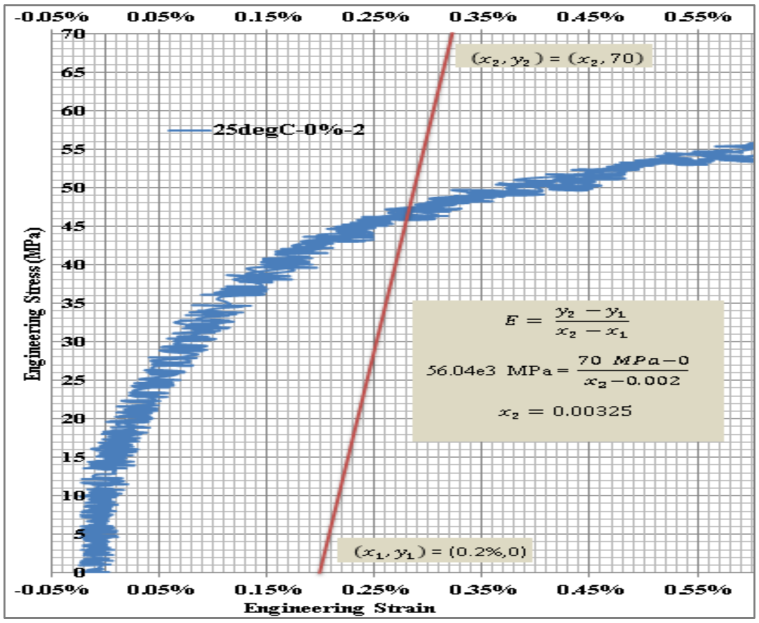

Figure 5.5. Determination of yield stress of 0%-2 composite sample tested at 25^{O}C

Table 5.2. Details obtained from the stress strain curves of the composite samples tested at various temperatures

Testing temp	Sample	Modulus, E (GPa)	Yield Stress (MPa)	Porosity (%)	Flow curve: $\sigma_T = K \varepsilon_T^n$	
					K (MPa)	n
25^0C	0%-1	61.25	50	4.22	193.55	0.2383
	0%-2	56.04	46	4.29	199.11	0.2514
	5%-1	55.52	44	5.90	272.45	0.3043
	5%-2	56.97	46	5.32	268.34	0.2920
	10%-1	57.90	42	9.63	254.03	0.3017
	10%-2	55.50	38	6.15	328.24	0.3599
200^0C	0%-3	55.97	43	4.654	146.05	0.2059
	0%-4	51.16	39	3.6	160.03	0.2284
	5%-3	51.03	41	4.73	177.66	0.2469
	5%-4	55.43	39	6.10	158.41	0.2280
	10%-3	53.31	43	6.62	164.24	0.2262
	10%-4	51.23	40	5.71	177.58	0.2358
400^0C	0%-5	42.83	32	3.75	79.17	0.1445
	0%-6	43.77	33	4.65	69.95	0.1253
	5%-5	45.69	30	4.82	88.73	0.1719
	5%-6	42.868	26	4.90	91.81	0.2041
	10%-5	44.66	28	7.03	99.90	0.2017
	10%-6	44.89	25	7.63	97.36	0.2068

From Table 5.2, the average modulus and yield stress for each volume fraction of composite sample were calculated along with their standard deviation. Figure 5.6a-b shows the variation of the average elastic modulus and average yield stress with temperature, porosity and volume fraction of the composite. As expected, the modulus and yield stress of the composite samples decreased drastically with increase in temperature because of increase in atomic vibrations and dislocation movement at higher temperatures respectively. Further, it was also seen from Table 5.2 that both modulus and yield stress decreased with increase in volume fraction of alumina (which is against our perception). The reason for this trend can be attributed to the increase in porosity with increase in the volume fraction of alumina, as summarized in Table 5.2. For the same height and diameter of the composite specimens, as the volume fraction of alumina increased in the composite samples, it became more difficult to manufacture them without introducing porosity substantially than those of the unreinforced 0% composite sample. The goal was to increase the modulus with the addition of ceramic particles in metal matrix without substantially decreasing the density (or increasing porosity). However, in the composite samples manufactured here for compression tests, it certainly beats the purpose of reinforcing the aluminum material with alumina, as the pure aluminum had more density and better modulus than the composite. Different processing methods might be necessary to manufacture composites with high volume contents of alumina and low porosity contents.

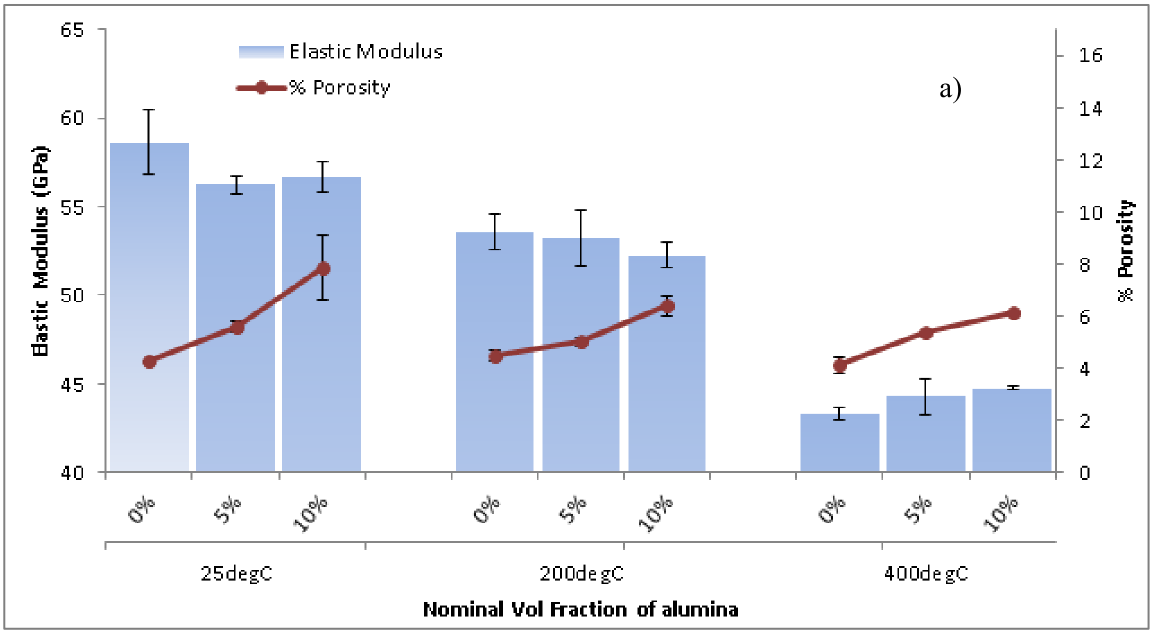

Figure 5.6. Effect of temperature, porosity and volume fraction on a) elastic modulus and b) yield stress of composite samples

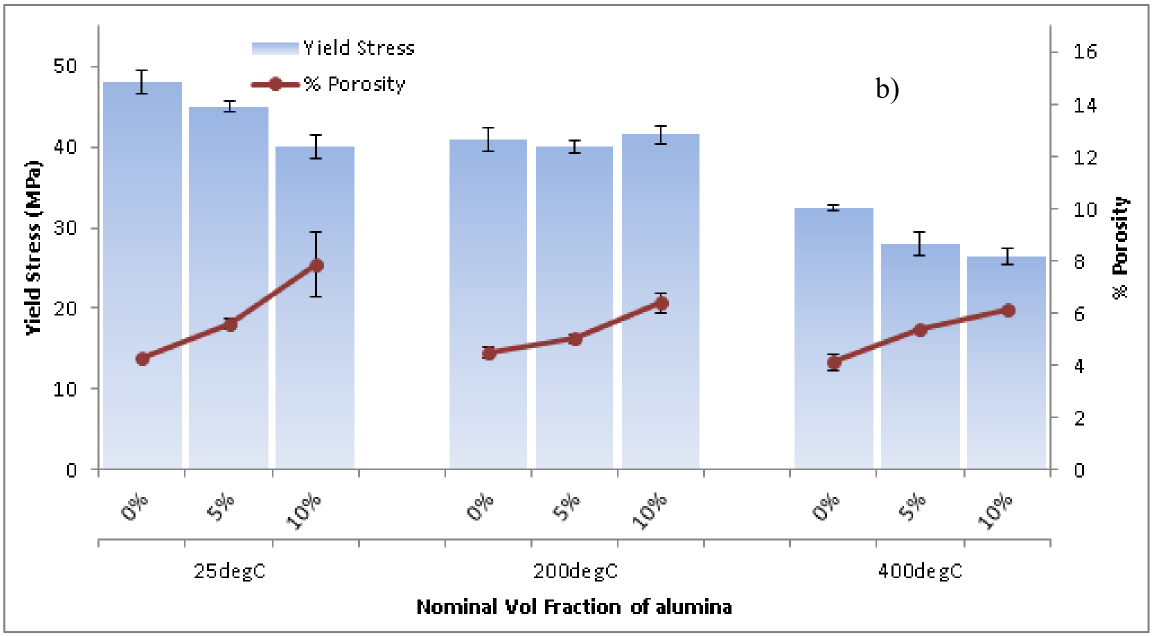

Figure 5.6. Continued

Yield stress indicates only the onset of plastic deformation. However, the material does not continuously flow after yield point, because the material undergoes strain hardening (stress required to maintain the flow increases with increasing strain) after the yield point. The stress at which continuous plastic deformation occurs is called as flow stress, and it increases with increasing strain. Equation 5.1 shows the empirical model of the flow stress as a function of strain. To define the material's behavior in the strain-hardening region, it is necessary to find the strain hardening coefficient (n) and strengthening coefficient (K) in the empirical equation, as these parameters define the basic plastic flow of the material. The true stress and strain values were used for this purpose and were calculated from the yield point to the 5% strain as follows:

$$\sigma_T = \sigma_e(1+\varepsilon_e) \text{ and } \varepsilon_T = \ln(1+\varepsilon_e)$$

$$\text{True stress strain curve or Flow curve } \sigma_T = K\,{\varepsilon_T}^n \qquad (5.1)$$

$$\log\sigma_T = \log K + n\log\varepsilon_T$$

Figure 5.7 shows the true stress strain curve of the 0%-2 composite sample overlapped with the engineering stress-strain curve. Figures 5.8a-c show the procedure used to determine the strain hardening coefficient (n) and strengthening coefficient (K) from the true stress strain curves for 0%, 5% and 10% composite samples at various temperatures, respectively. The strain hardening coefficient (n) is the slope of the log true stress vs log true strain curve; whereas the strengthening coefficient (K) is the true stress for true strain=1, or in other words log(K) is the y-intercept of the log(true stress) vs log(true strain curve). Table 5.2 summaries n and K values for different composite samples.

Figure 5.9 shows the variation of strengthening coefficient (K) and strain hardening coefficient (n) with compression testing temperature and volume fraction of the composite. Both n and K decreased with increase in temperature, which is expected. This is due to increase in the dislocation mobility at higher temperatures making it easier for the materials to undergo plastic deformations without much of strain hardening. With an increase in volume fraction, they increased slightly, as expected, due to the hindrance provided by the alumina reinforcement for the dislocation motion. The strain hardening coefficient lies between 0 (for perfectly plastic material) and 1 (for perfectly elastic material)[83]. Lower n and K values means the material has less tendency to strain harden and requires lower stresses to deform plastically; and higher n and K values means higher the strain hardening effect on the material[84]. Totten and MacKenzie[85] published that for commercial aluminum alloys, n and K were usually found to lie between 0.18-0.24 and 146-479MPa respectively at room temperature.

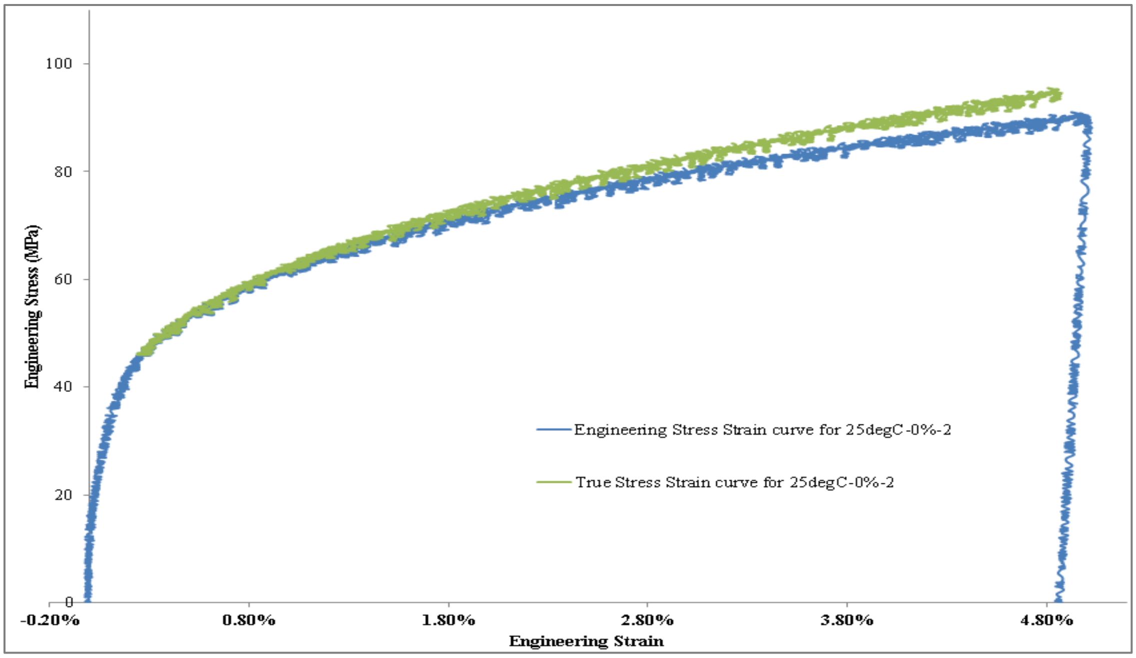

Figure 5.7. True stress strain curve overlapped with engineering stress strain curve for the 0%-2 composite sample

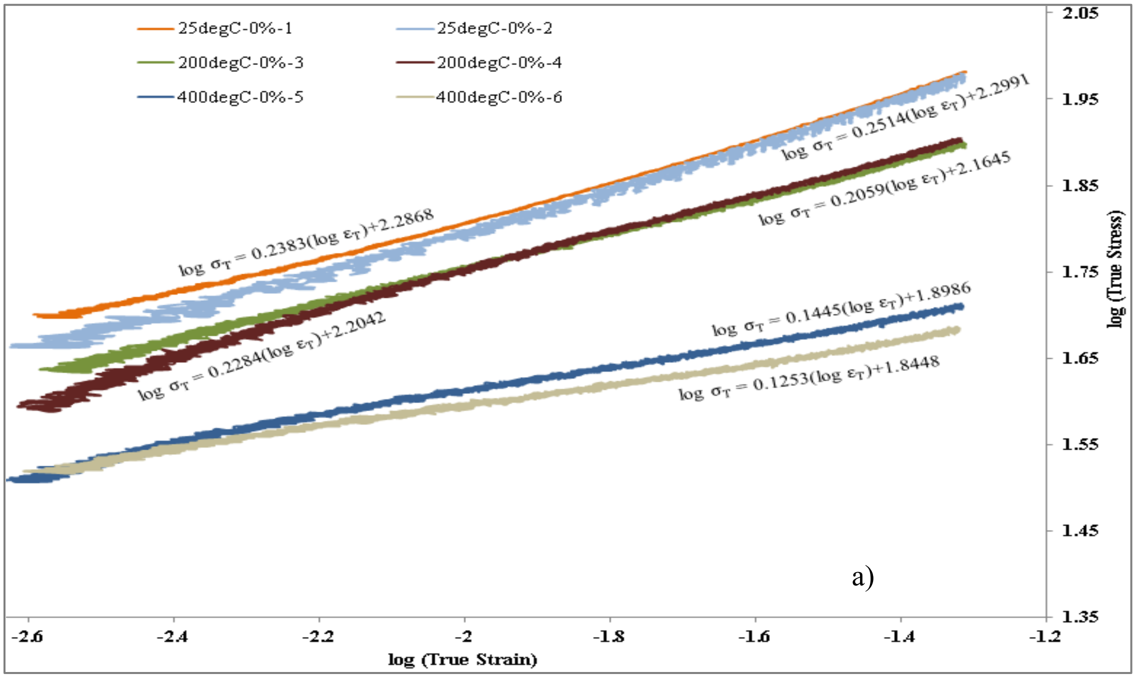

Figure 5.8. Determination of n and K from the true stress strain curves for a) 0% b) 5% and c) 10% composite samples at various temperatures

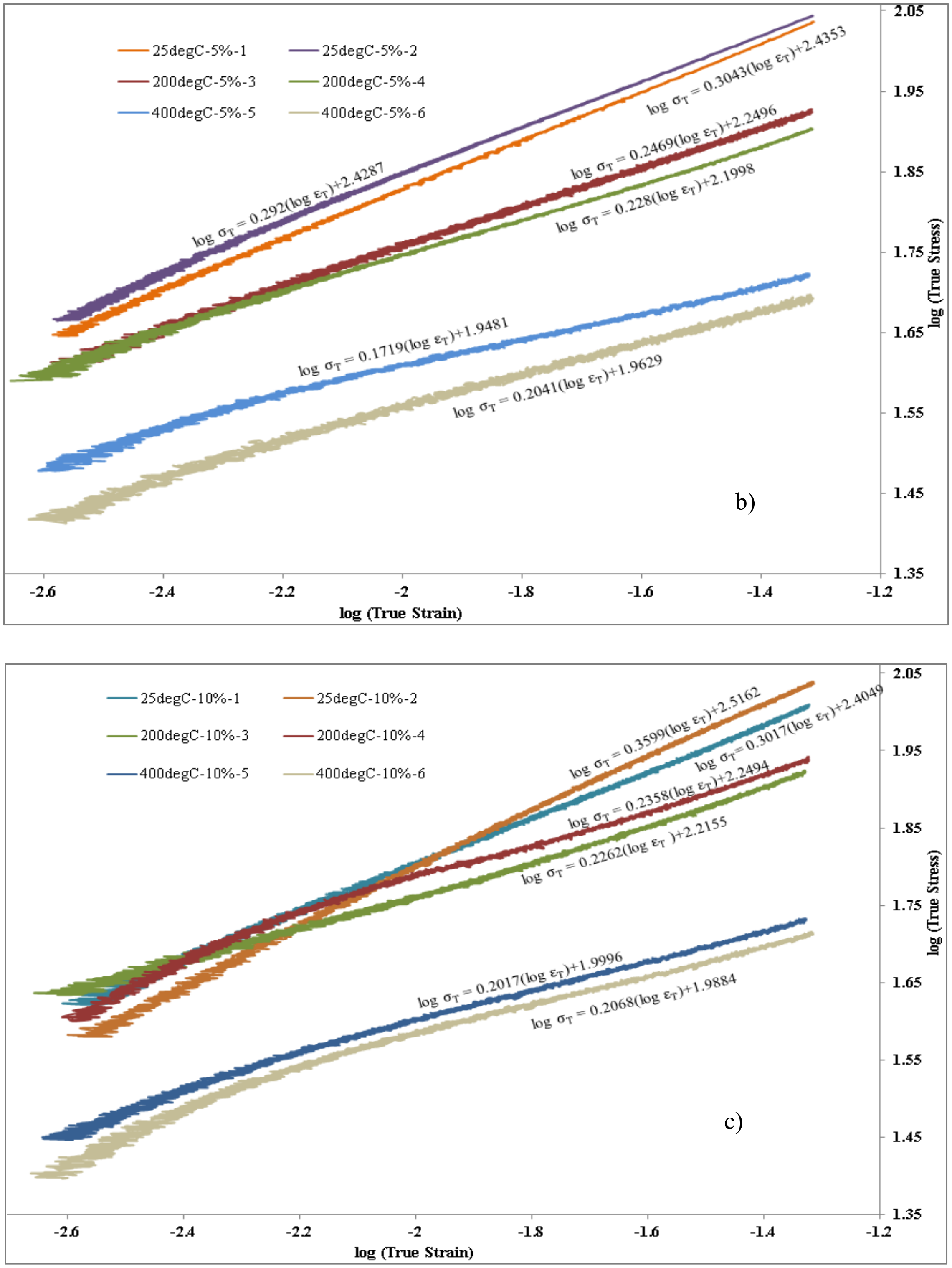

Figure 5.8. Continued

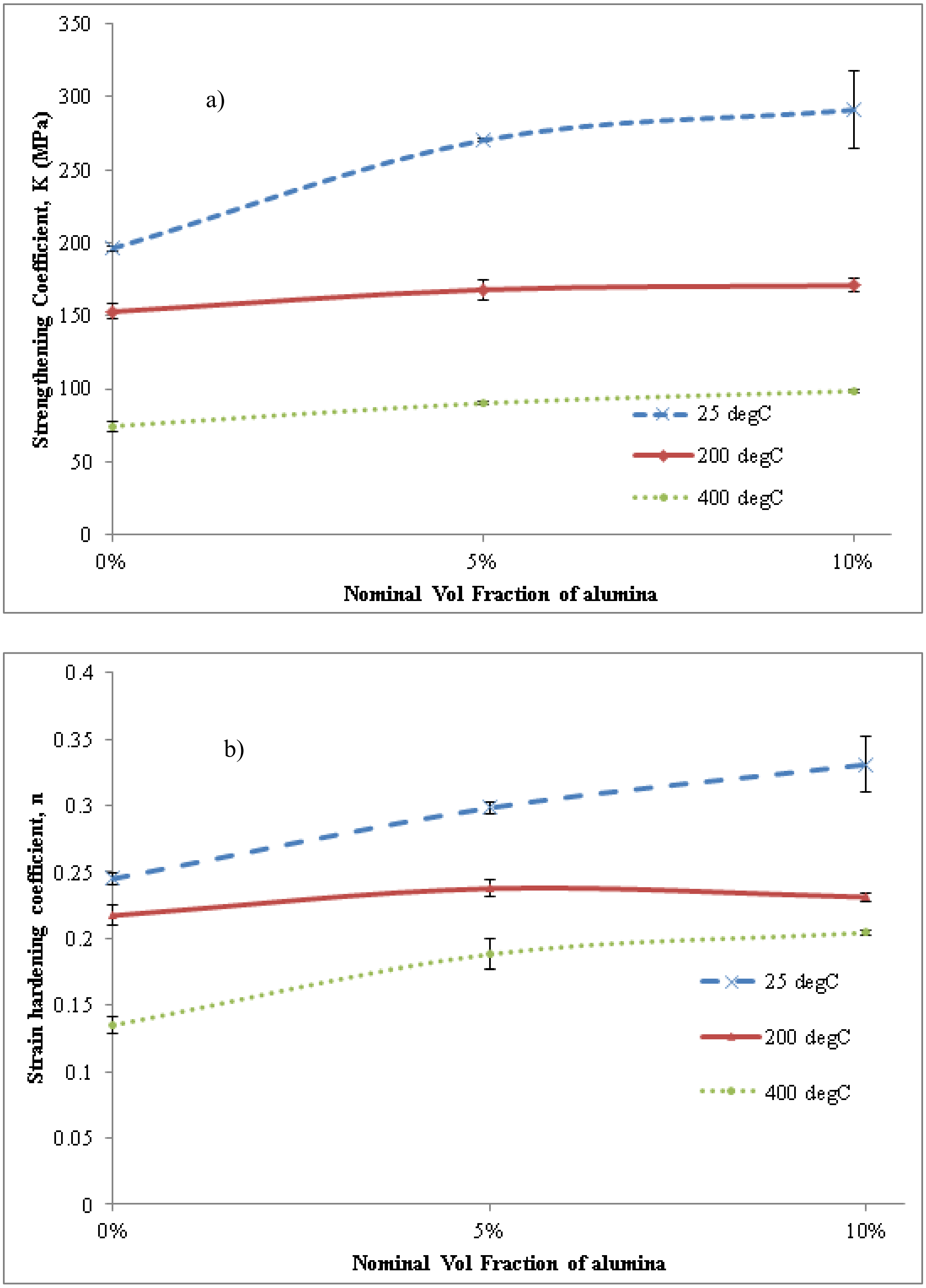

Figure 5.9. Variation of a) strengthening coefficient (K) and b) strain hardening coefficient (n) with compression testing temperature and volume fraction of the composite

5.2. Comparison of RUS and Compression Testing (CT) results

5.2.1. RUS vs CT - experimental results

Table 5.3 shows the physical properties of the composite samples used for RUS (viz. height, diameter, relative density and volume fraction obtained from XRD) along with their moduli obtained from RUS. Figure 5.10 compares the elastic modulus variation with temperature for the compression testing samples and RUS samples. Modulus decreased with increase in temperature both for compression testing and RUS samples. The modulus of composite samples obtained from the compression testing is less than those of RUS, because of more porosity present in the samples used for compression testing. As volume fraction increases, relative density decreases (porosity increases) both for the compression testing and RUS samples. However, the decrease was less for the RUS samples compared to those of the compression testing samples. This is because the compression testing samples were bigger in size with more porosity than RUS samples. Hence, as volume fraction increases, the elastic modulus decreases for the compression testing samples whereas it increases for the RUS samples. Further, it was found that as volume fraction increases, the drop in modulus because of temperature raise is less for both compression testing and RUS samples.

Table 5.3. Composite samples used for RUS, their phase volume fractions and mechanical properties

RUS Samples	Height (mm)	Dia (mm)	R.D (%)	E (GPa)	V.F (XRD)	Testing temp
0%	7.1882	25.4	98.55	Varied from 65.47 (at 25^0C) to 47.61 (at 450^0C)	2.8	25^0C to 450^0C
5%	7.2491	25.4	97.79	Varied from 69.66 (at 25^0C) to 49.82 (at 450^0C)	7.9	
10%	6.8478	25.4	95.96	Varied from 72.22 (at 25^0C) to 53.50 (at 450^0C)	12.4	

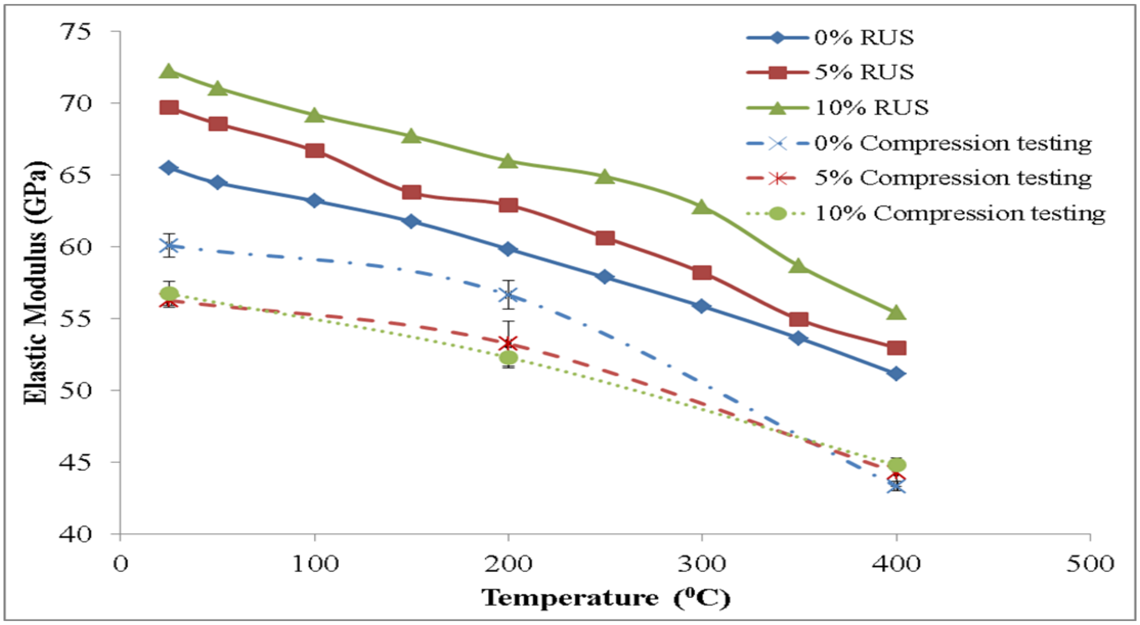

Figure 5.10. Comparison of modulus of composite samples tested with compression testing with those tested using RUS

To further illustrate the results the relative density, porosity, and elastic moduli for the 10vol% composite from RUS and uniaxial compression tests (CT) are summarized in Table 5.4. The uniaxial compression test also gives the overall stress-strain responses of the composite. Four specimens were used for the CT, while only one specimen was used for RUS. All tests were done at room temperature. It is seen that the specimen used for RUS (i.e. sample RUS-10) has higher relative density and less porosity when compared to the specimens used for CT (i.e. Samples CT-10-1 to CT-10-4). This could be attributed to the difference in sizes of the composite samples used for RUS and CT. The RUS samples are approximately (25.4 mm in diameter and 7.62 mm long) cylinders whereas the CT samples are approximately (12.7 mm in diameter and 17.78 mm long) cylinders. As the CT samples are longer, they have more porosity compared to RUS samples due to the issue with manufacturing larger composite samples. Also a slight difference in the procedure is followed for manufacturing RUS and CT samples during the compaction stage of composite fabrication. For making RUS samples, Al-Al_2O_3 powder mixture was introduced into the die in the powder form. Whereas for making CT samples, Al-Al_2O_3 powder mixture was not introduced into the die in powder form because the relatively thin diameter of the sample with longer length was making the edges of the sample torn during the compaction stage of manufacturing the composite. Hence to avoid this, Al-Al_2O_3 powder mixture was mixed with ethyl alcohol and introduced into the die in the form of a paste.

Table 5.4. Measured density, porosity, and alumina content of composite samples with 10% nominal Al_2O_3 volume content

Sample	Relative density (%)	Porosity (%)	Alumina content (%)	Modulus (GPa)
CT-10-1	93.68	6.31	11.5	60.90
CT-10-2	93.51	6.49	11.2	51.40
CT-10-3	92.65	7.34	11.7	55.40
CT-10-4	93.92	6.07	11.4	62.24
RUS-10	95.96	4.04	12.7	71.05

5.2.2. RUS vs CT - numerical results (using micromechanical models)

The microstructural models of the Al-Al_2O_3 composite system used for CT with 10% alumina volume content were generated from the SEM microstructural images, as shown in Fig.5.11. The size of the microstructural image was 217µm x 173µm. This micrograph image was divided into uniform sub-images (regions) using a photo editing program. In this case the image was divided into 12 uniform regions with 50µm x 50µm. Three different 50 µm x 50 µm square regions having different microstructures were randomly chosen as representative microstructures of the composite[3]. Using software OOF2, the aluminum matrix, the pores and

---

[3] There have been several approaches in determining the representative microstructures of composites in developing micromechanical models. One approach considers the representative microstructures to

the alumina particles in each of the selected microstructure were determined based on their color contrast. After defining the geometry and boundaries of the different pixel groups, meshes were generated and converted to two-dimensional (2D) finite elements. The FE microstructural models were implemented in ABAQUS for analyzing the mechanical response and numerically characterizing the effective elastic modulus of the composite. The continuum plane stress element (CPS4) was used in the FE analyses. Figure 5.12 illustrates the images of three different microstructures of the composite sample used for CT obtained from the FE, labeled as FE-1, FE-2, and FE-3. As discussed above the specimen used for RUS has higher density and lower porosity; thus we also generate micromechanics models from the RUS specimen, labeled as FE-4, FE-5, and FE-6 (Fig. 5.12).

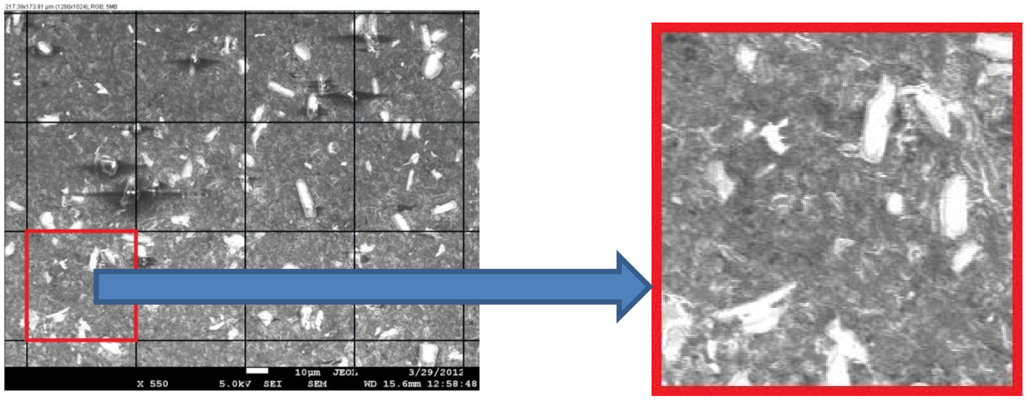

Figure 5.11. SEM image of Al-Al_2O_3 composite system with 10vol% alumina content (light color: alumina; grey color: aluminum; dark color: void/pore)

---

include all possible microstructural characteristics which generally lead to large microstructures, while another approach considers the smallest microstructural regions that can give reasonable approximations of the overall response of composites. The main objective of this study is to understand the effects of microstructural characteristics such as existence of porosity, distributions of particles, and properties of the constituents on the overall mechanical response of composites. Thus, instead of choosing micromechanical models based on certain approaches in order to achieve converged representative microstructures of Al-Al_2O_3 composites, we randomly choose square regions of 50x50µm as our representative microstructures. We validate the chosen representative microstructures by calculating the percent alumina content.

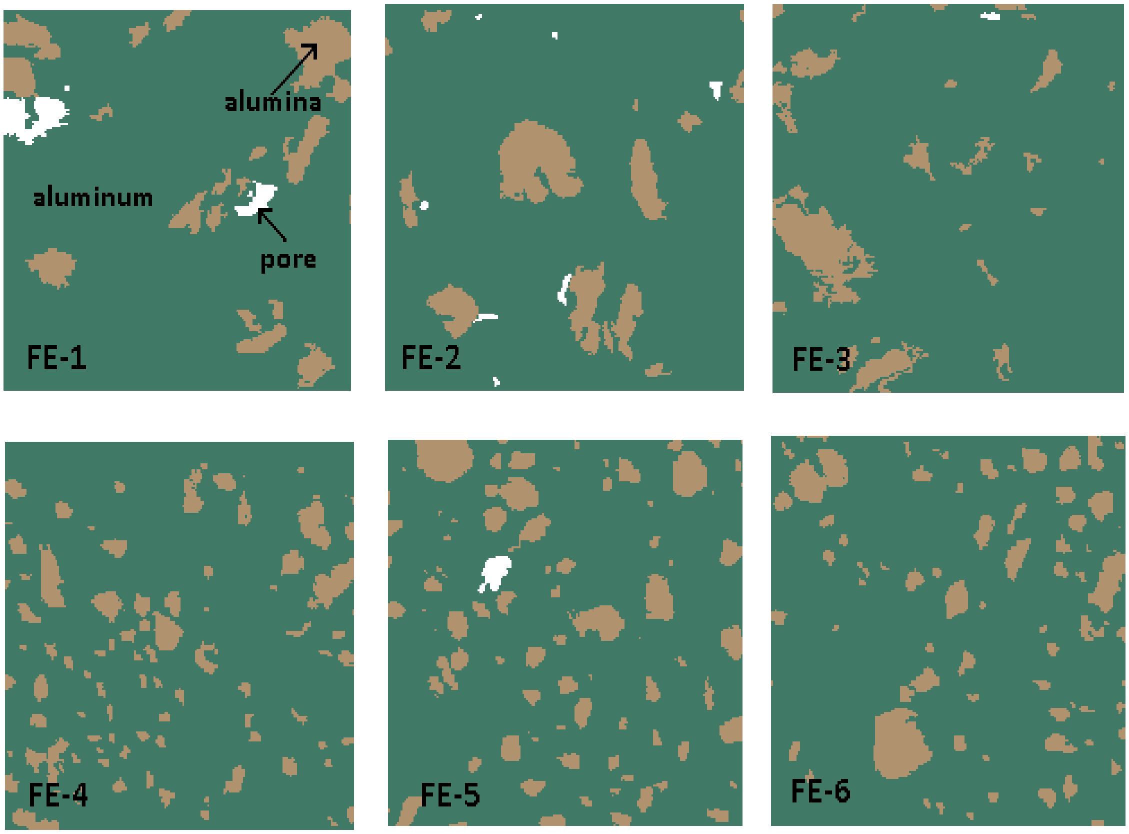

Figure 5.12. FE microstructural images of 10% composite samples used for compression testing (FE-1, FE-2 and FE-3) and 10% composite samples used for RUS (FE-4, FE-5 and FE-6)

Table 5.5. Area Fraction of alumina (%AF), porosity (%Pores), elastic modulus, and Poisson's ratio of the FE models generated from composite with 10% Volume Fraction (%VF)

Model	%AF of Alumina	%Pores	*E* (GPa)	ν
FE-1	9.774	1.947	57.5	0.314
FE-2	9.657	1.603	64.2	0.358
FE-3	8.788	0.328	53.2	0.396
FE-4	11.7	0.0	73.0	0.370
FE-5	13.2	0.5	73.4	0.368
FE-6	11.6	0.0	72.7	0.377

Table 5.5 presents the alumina area fraction (%AF) and porosity (%Pores) of the six FE meshes generated. The alumina is modeled as linear elastic while the aluminum is assumed to exhibit an elastic-plastic deformation. Both aluminum and alumina are modeled as isotropic materials undergoing small deformation gradients. The linear elastic constitutive model for the alumina is:

$$\varepsilon_{ij} = \varepsilon_{ij}^{e} + \varepsilon_{ij}^{th} = \frac{S_{ij}}{2G} + \frac{\sigma_{kk}}{9K}\delta_{ij} + \alpha\delta_{ij}\left(T - T_{ref}\right) \tag{5.2}$$

where the linearized strain is defined as $\varepsilon_{ij} = \frac{1}{2}\left(u_{i,j} + u_{j,i}\right)$, u_i is the scalar component of the displacement vector, S_{ij} is the scalar component of the deviatoric stress, σ_{kk} is the volumetric stress, G and K are the shear and bulk moduli, respectively, that depend on the elastic modulus E and Poisson's effect ν, δ_{ij} is the Kronecker delta, T and T_ref are the current and reference temperatures, respectively, and α is the thermal expansion coefficient. The aluminum follows the deformation theory of plasticity (Hencky-Ilyushin):

$$\begin{aligned} &\varepsilon_{ij} = \varepsilon_{ij}^{e} + \varepsilon_{ij}^{p} + \varepsilon_{ij}^{th}; \quad \varepsilon_{ij}^{e} = \frac{S_{ij}}{2G} + \frac{\sigma_{kk}}{9K}\delta_{ij}; \\ &\varepsilon_{ij}^{th} = \alpha\delta_{ij}\left(T - T_{ref}\right); \quad \varepsilon_{ij}^{p} = \begin{cases} \frac{3}{2}\frac{\bar{\kappa}}{\bar{\sigma}}S_{ij}, & F=0 \\ 0, & F<0 \end{cases} \end{aligned} \tag{5.3}$$

The equivalent plastic strain is $\bar{\kappa} = \sqrt{\frac{2}{3}\varepsilon_{ij}^{p}\varepsilon_{ij}^{p}}$, where ε_{ij}^{p} is the component of the plastic strain, and the effective stress is $\bar{\sigma} = \sqrt{\frac{3}{2}S_{ij}S_{ij}}$. It is assumed that the material is rate-independent and the yield criterion is given as $F = \bar{\sigma} - \sigma_{y}\left(\varepsilon_{ij}^{p}\right)$. The small strain definition is used in Eq. (5.3), while upon yielding aluminum can experience moderate to large deformations in that the higher order terms of the deformation gradients are not negligible. In such cases it is more suitable to consider finite strain plasticity theories. In this study, our aim is to examine the effect of microstructures, i.e., porosity, local yielding, and distribution of the alumina particles in the homogeneous aluminum matrix, on the overall linear elastic moduli[4] and response of the Al-Al_2O_3 composites. It is noted that due to the plane stress assumption the out of plane strain component is not derived from the kinematic relation but instead from imposing zero out of plane stress condition.

The FE simulation was carried out in two steps. The first step was on prescribing a uniform temperature change from 100^oC to room temperature, which was assumed as the stress-free condition (see Chapter IV), to 25^oC and examining the residual stresses. The thermal expansion coefficients for the aluminum and alumina at room temperature are $28x10^{-6}/^oC$ and $4.6x10^{-6}/^oC$, respectively. The second step was simulating a uniaxial mechanical boundary condition to determine the uniaxial elastic moduli and stress-strain response of the composite. Here we examine the effect of thermal (residual) stresses on the overall elastic properties of the composites. The elastic moduli of the aluminum and alumina at room temperature are 65 GPa and 370 GPa, respectively. The Poisson's ratios of the aluminum and alumina are 0.35 and 0.22, respectively. The above thermal expansion and elastic properties of the aluminum and alumina are obtained from Wefers [86], Bauccio [87] and Gauthier [88]. The yield stress of the aluminum is 33 MPa and the uniaxial stress-strain response of the aluminum at room temperature is shown in Fig. 5.13. The stress-strain response of the aluminum was used to obtain the plastic deformation for the aluminum constitutive model.

---

[4] By determining the overall linear elastic moduli of the composite one suggests that the macroscopic (average) behavior of the composite is linearly elastic, in which no dissipation of energy is allowed and no permanent (residual) deformation is exhibited by the composite upon removal of the external loading. While the macroscopic response of the composite might show a linear effective stress-strain relation and an elastic response under a sufficiently small overall strain, the stress field inside the composite microstructure could vary significantly and the stress concentrations and/or discontinuities could occur at various locations within the microstructure of the composite. The localized stresses within the microstructure could lead to local yielding and/or fracture.

Consider a FE microstructure of a square region with a side length L=50μm placed in the 2D Cartesian coordinate system with the bottom left corner of the microstructure is at the origin. The microstructure is subjected to the following displacement boundary conditions:

$$u_1(0,x_2) = u_2(x_1,L) = 0.0 \quad \text{and} \quad u_2(x_1,0) = \delta_o \tag{5.4}$$

where u_1 and u_2 are the displacements in the x_1- and x_2- directions, respectively. The linear elastic modulus from the RUS is predicted by prescribing a uniaxial compressive stress $\bar{\sigma}_{22}(x_1,0) = \sigma_o = 1MPa$ and monitoring the corresponding overall (average) strain $\bar{\varepsilon}_{22}$. It is noted that the strain induced by the vibration of the sample during the RUS test is significantly small; and thus we prescribed a relatively small stress so that we can minimize the effects of the possible plastic deformation. The effective elastic modulus $\bar{E}$ is then defined as:

$$\bar{\varepsilon}_{22} = \frac{\delta_o}{L}; \qquad \bar{E} = \frac{\bar{\sigma}_{22}}{\bar{\varepsilon}_{22}} \tag{5.5}$$

The uniaxial compressive stress was simulated by prescribing a uniaxial displacement $\delta_o = 2.5x10^{-3} mm$, which corresponds to the axial strain 5%[5] followed by removal of the strain. As we mentioned earlier the constitutive models for the aluminum and alumina (Eqs. (5.2) and (5.3)) are applicable for materials undergoing small deformation gradients, in which we neglect the higher order terms of the deformation gradients in calculating the strains. During the compressive stress, we deal with a moderate strain and neglecting the higher order terms of the deformation gradient could result in an appreciable amount of error. We will discuss this issue in the following section.

---

[5] This is an engineering strain defined as the overall axial displacement divided by the original length of the specimen.

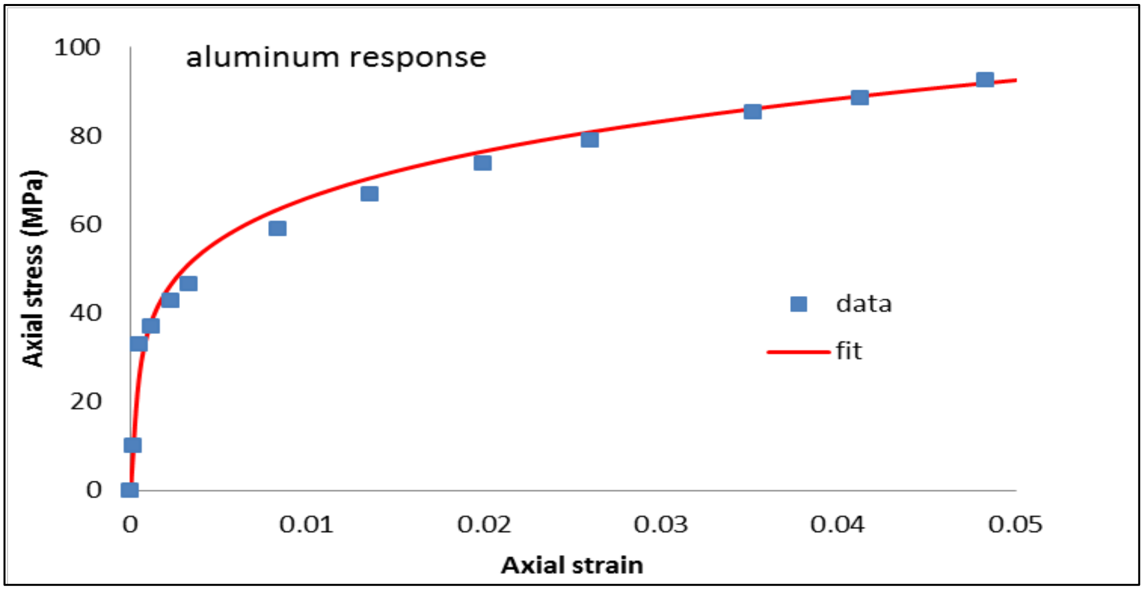

Figure 5.13. Uniaxial response of pure aluminum at room temperature

5.2.3. RUS vs CT - comparison of experimental and numerical results

The responses from the FE analyses are compared to the ones obtained from the experiment. The first numerical study considers a relatively small applied effective stress (1 MPa) in order to determine the elastic modulus of the composite and compare to those obtained from RUS. Figure 5.14 shows the stress-strain responses of the composite with 10 vol.% alumina content from the FE analyses, which can be described by a linear stress-strain relation. In each FE analysis, the slope between the axial stress and strain denotes the effective elastic modulus (Eq. (5.5)). The average moduli and Poisson's effect from the FE analyses are given in Table 5.4. It is noted that the elastic modulus determined from RUS is 72.2 GPa (see Chapter III). Most importantly, Figure 5.14 shows that effective (average) elastic moduli determined from the FE analyses of FE-4, FE-5, and FE-6 are close to the experimental data obtained from RUS, which is expected as these FE models have the alumina content close to the alumina content of the RUS specimen (Table 5.5) and have low porosity. The lower values of the effective elastic modulus from FE-1, FE-2, and FE-3 are due to the high porosity and low alumina content as depicted in Fig. 5.12 and Table 5.5. As explained in Chapter IV, the stress free temperature occurs at approximately 100^{o}C for the 10% composite samples. Hence in the FE analyses, the composites were first cooled from 100^{o}C to room temperature. The mismatches in the thermal expansion coefficients of the aluminum and alumina give rise to thermal stresses as illustrated in Figure 5.15. High compressive thermal stresses are seen in the alumina particles, while most of the aluminum regions are under relatively low stresses (green zone). The aluminum experiences an appreciable amount of tensile thermal stress (close to 50 MPa, greater than its yield stress) in the regions close to the alumina particles or when the spacing between the alumina particles is relatively small, thereby inducing plastic deformation. To determine the effective modulus of the composite, a small external stress $\bar{\sigma}_{22}(x_1, 0)$ was then prescribed for the three FE models, FE-1, FE-2 and FE-3. Insignificant changes in the internal stress fields are observed in the three FE analyses because of the applied small external stress.

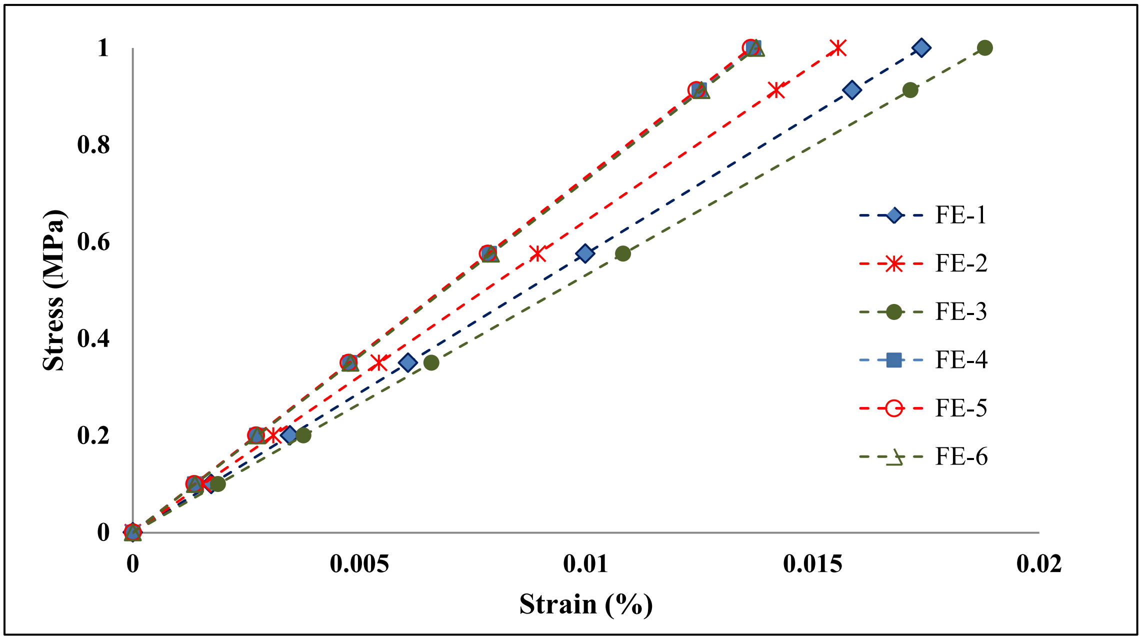

Figure 5.14. Uniaxial response from FE analyses under small stress (1 MPa)

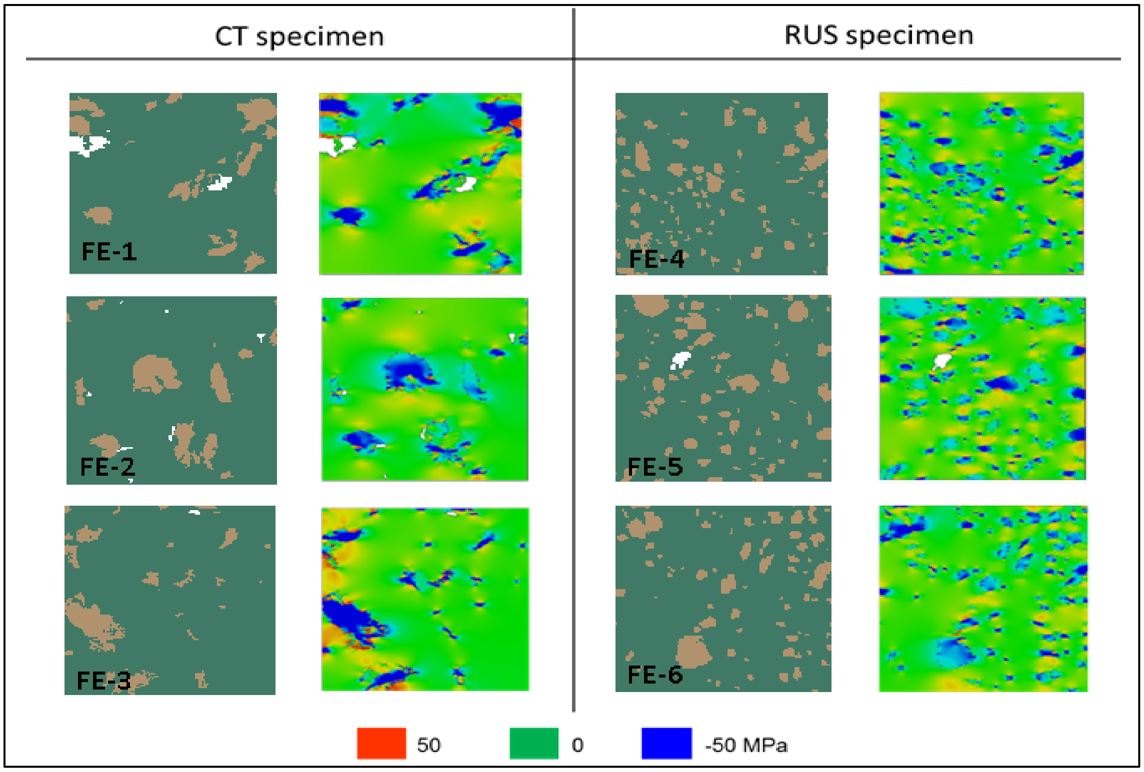

Figure 5.15. Thermal stress field (σ_{xx}) due to temperature change from 100°C to room temperature

Next, we simulate the uniaxial compressive tests on the composite with 10 vol% alumina. The stress-strain responses from the three FE analyses are compared to the experimental data, as shown in Fig. 5.16. Responses from the FE analyses are capable in capturing the experimental data when the composites are undergoing relatively small strains (less than 10^{-3} axial strain). As the strain increases, the mismatches between the results from the FE analyses and experimental data are more pronounced. The FE results under-predict the experimental data. In Figure 5.16a, the experimental stress strain curves(exp-1 to exp-4) showed slightly more strain hardening behavior than the numerical stress strain curves (FE-1, FE-2 and FE-3).This can be explained by the difference in alumina content present in the experimental and numerical models. From Table 5.4, the vol% of alumina for the compression testing samples CT-10-1 to CT-10-4 range from 11.2 to 11.7, whereas from Table 5.5, the %AF of alumina for FE-1, FE-2 and FE-3 are 9.774, 9.657 and 8.788 respectively. Slightly higher alumina content in the experimental models results in higher hindrance to dislocation motion and further the regions which can have dislocation motion (i.e. aluminum) is decreasing. Therefore, plastic deformation occurs at relatively higher stresses in the experimental stress strain curves than the numerical stress strain curves. It is important to note here that we did not incorporate the dislocation motion into the numerical model. Furthermore, aluminum can oxidize during the fabrication process and at the interface of Al and Al2O3, the possibility of an intermediate third phase being present other than Al and Al2O3 phases, is imminent. This intermediate third phase is not considered for the numerical modeling. Another reason for the mismatches is perhaps from considering the 2D plane stress analyses instead of performing three-dimensional (3D) FE analyses and due to the use of the small strain measure while the composite exhibit moderate strains (max 5%). Nevertheless, the FE analyses give reasonable qualitative predictions of the uniaxial compressive tests.

Once again, the significant effect of porosity, from the FE-1, in reducing the mechanical properties of the composite can be observed in Figure 5.16. The elastic moduli are also obtained from the uniaxial compressive stresses by assuming that the responses are linear up to the strain level of $2x10^{-3}$. The elastic moduli from the three FE analyses are about 48, 56, and 58 GPa. The relatively low value from the FE-1 is due to the existence of high porosity. The elastic moduli determined from the experiments are found to vary between 51.4 - 62.24 GPa and thus very close to the elastic moduli form the FE-2 and FE-3 models that contain less porosity. Figure 5.17 illustrates the corresponding axial stress contours in the three FE analyses at different stages of uniaxial loadings: A is close to the yield limit, B is at the peak loading, and C is during the unloading stage. It is seen that at stages A and B high compressive stresses are shown in the stress contours, causing significant plastic deformations in the aluminum matrix in the regions closer to the alumina particles. The soft aluminum matrix contributes to a reduction in the overall elastic moduli of the composites even at relatively small strain levels. This study might explain the lower elastic moduli obtained from the uniaxial compressive stress as compared to the one from RUS. It is also noted that during the uniaxial compressive stresses, the unleveled surface of the specimens can cause localized plastic deformation in the composite samples which can significantly reduce the elastic modulus of the composites as in the case labeled as 'exp 2' in Fig. 5.16. It is also noted that high tensile stresses in the alumina constituent or significantly high stresses in the aluminum could cause cracking/damage in the constituents, which can significantly reduce the mechanical response of the composites, as numerically shown by Muliana [30].

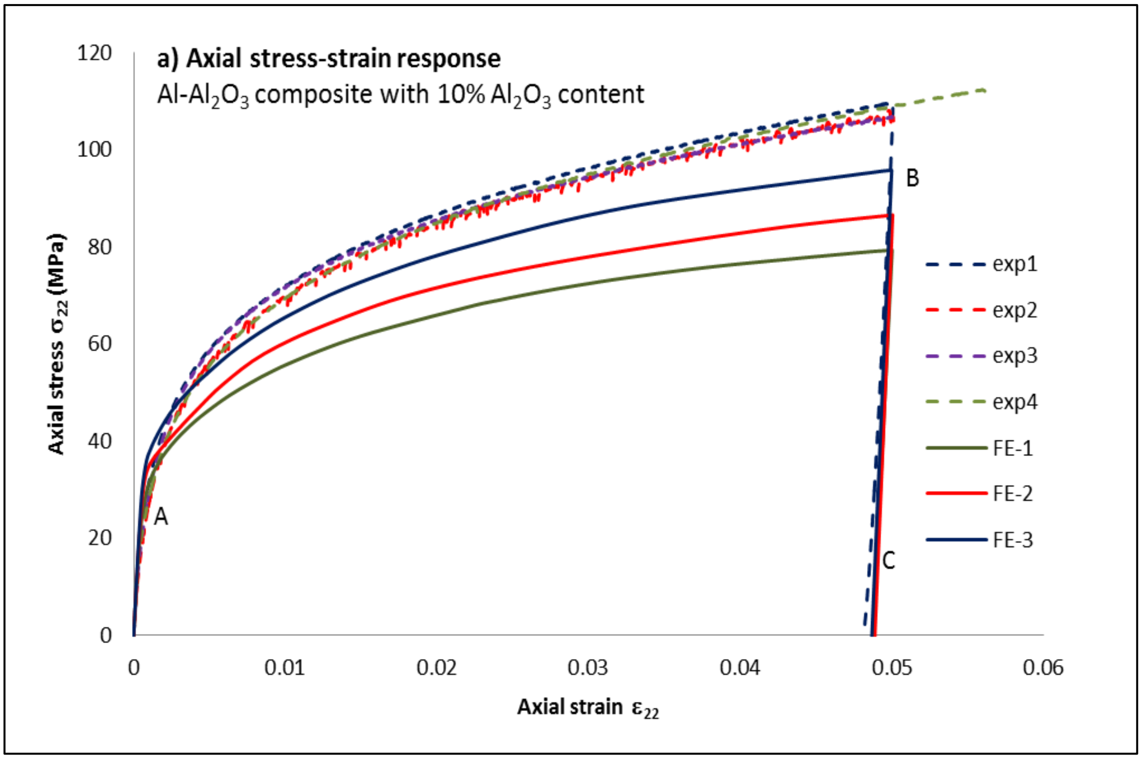

Figure 5.16. a-b Stress-strain response from the uniaxial compressive tests

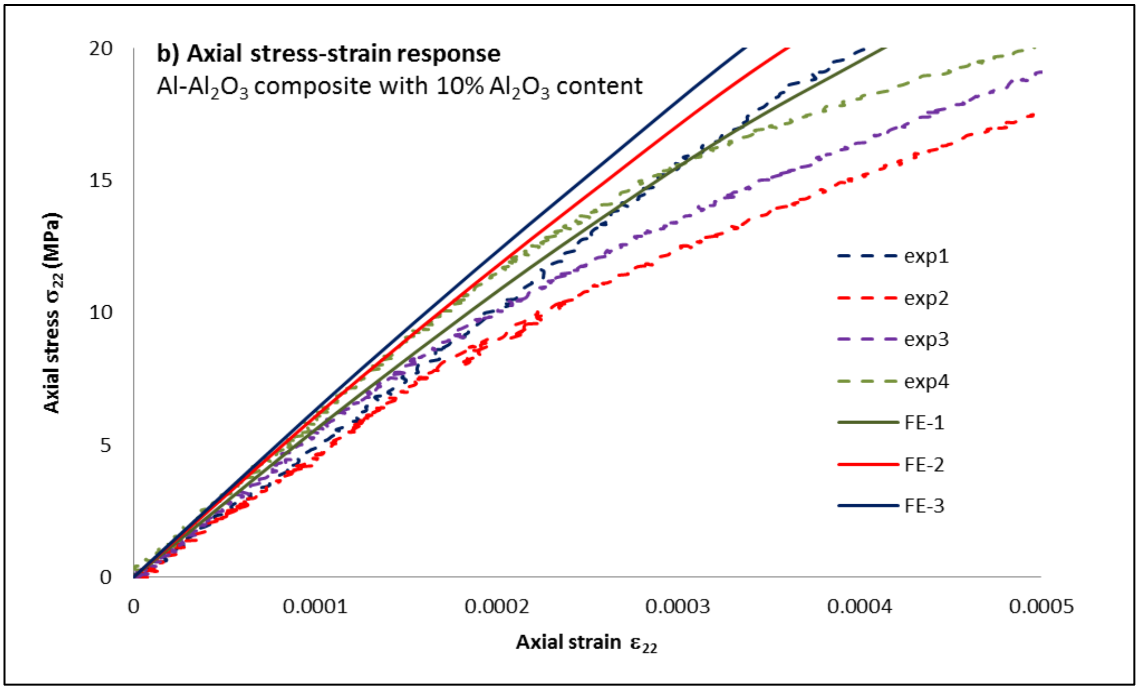

Figure 5.16. Continued

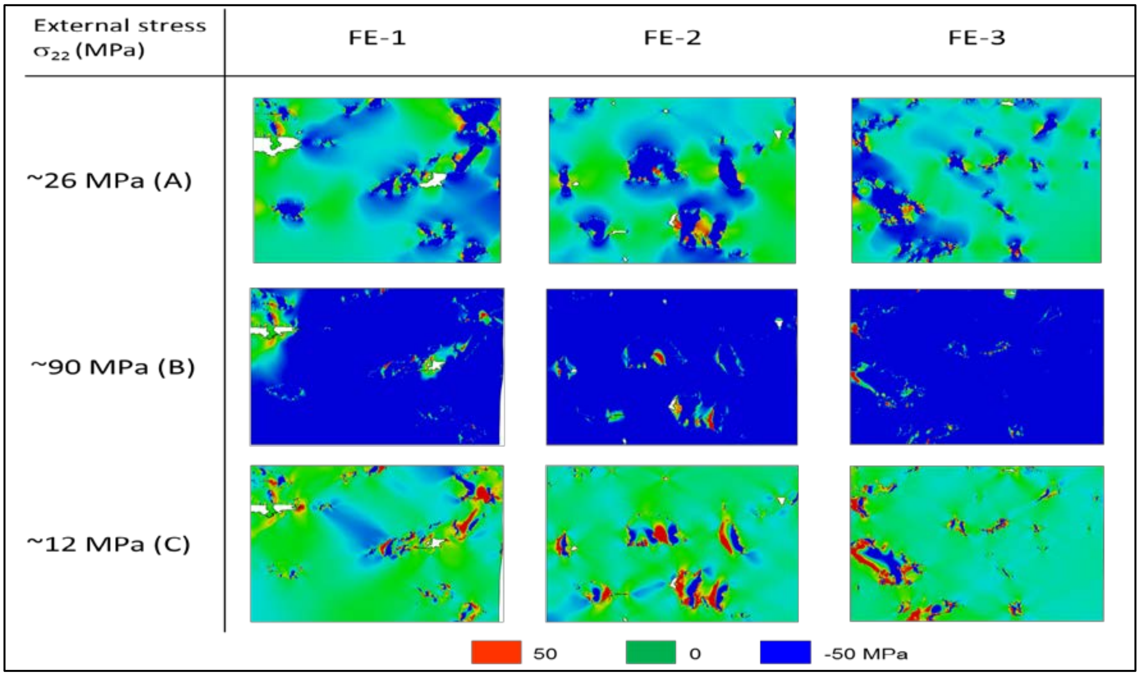

Figure 5.17. Axial stress contours at different stages during the uniaxial compressive loadings

5.3. Study on the RVE size

The numerical results obtained so far are obtained using Figure 5.12 with an RVE size of 0.05 mm X 0.05 mm. In order to see whether the RVE size chosen is sufficient to represent the entire microstructure of the composite, the RVE size is increased from 0.05 mm X 0.05 mm to 0.1mm X 0.1 mm and the corresponding stress-strain curves are studied. Figure 5.18c shows the RVEs of size 0.1 mm X 0.1 mm obtained from the A-20 composite sample and Figure 5.18a shows the procedure used to obtain them by overlapping a grid. Figure 5.19 shows the stress strain response of 10 vol% composite. Figure 5.20 illustrates the comparison between effective moduli obtained using different RVE sizes for the A-20 composite sample. The maximum difference in the effective modulus was about 10Gpa or 14.9%, between FE-1 and FE-4 microstructures. This could be attributed to variation in RVE size, distribution of reinforcement in the matrix along with its VF and porosity.

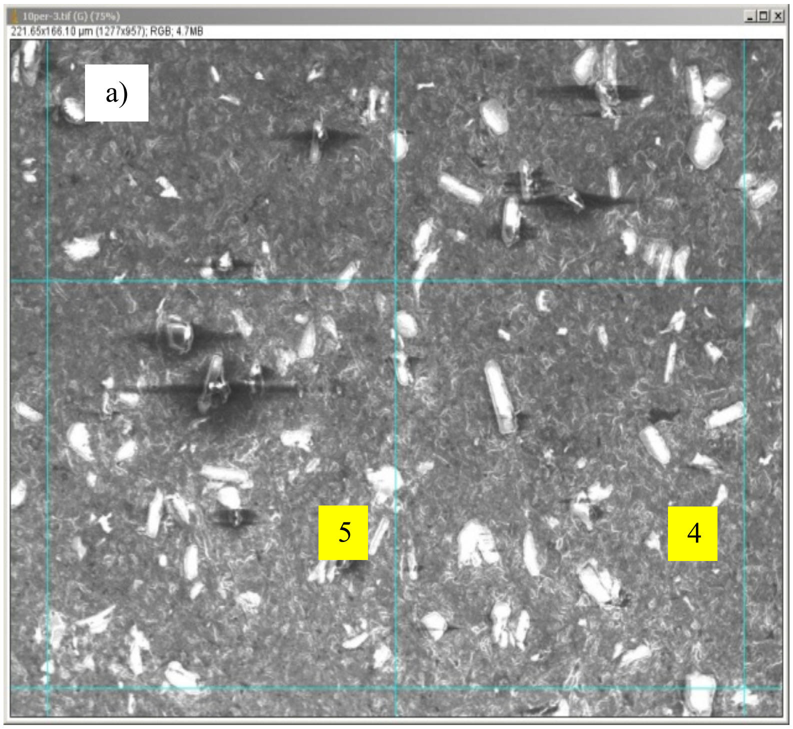

Figure 5.18 a) SEM image of Al-Al_2O_3 composite with 10vol% alumina, b) RVEs of size 0.1 mm X 0.1 mm cut from the SEM images and c) FE microstructural models with RVE size 0.1 mm X 0.1 mm

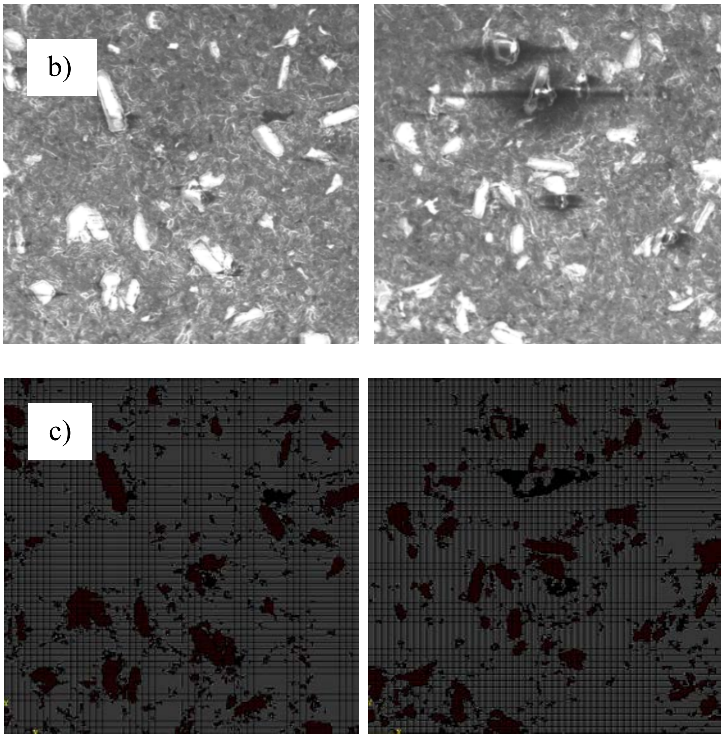

Figure 5.18. Continued.

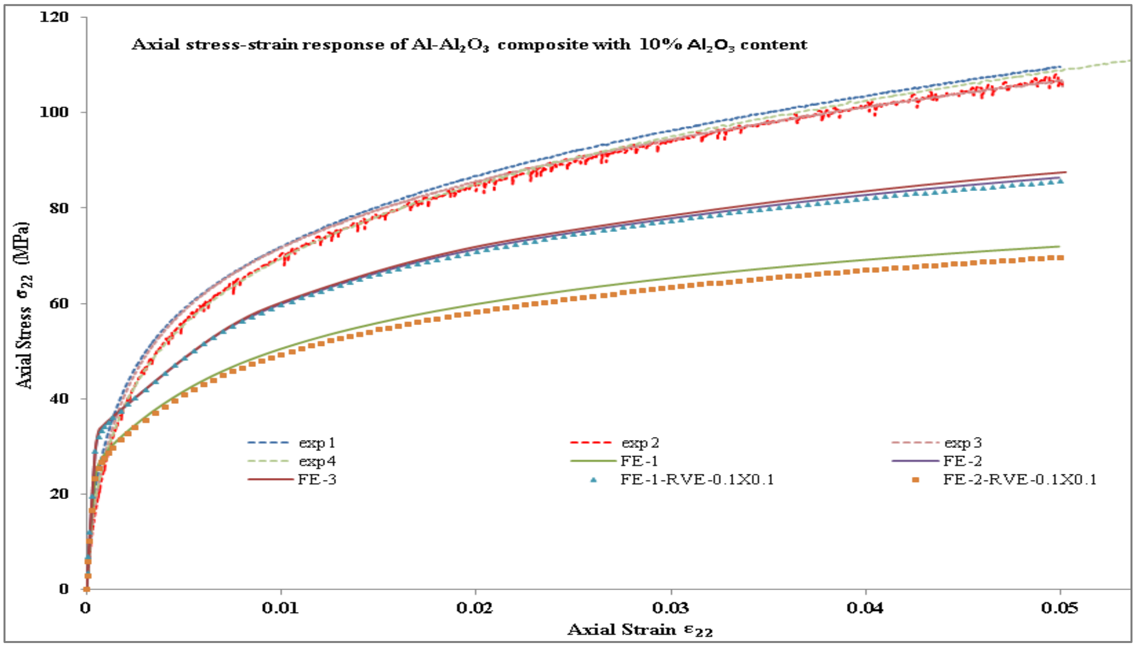

Figure 5.19. Comparison of stress-strain response using different RVE sizes with experimental results

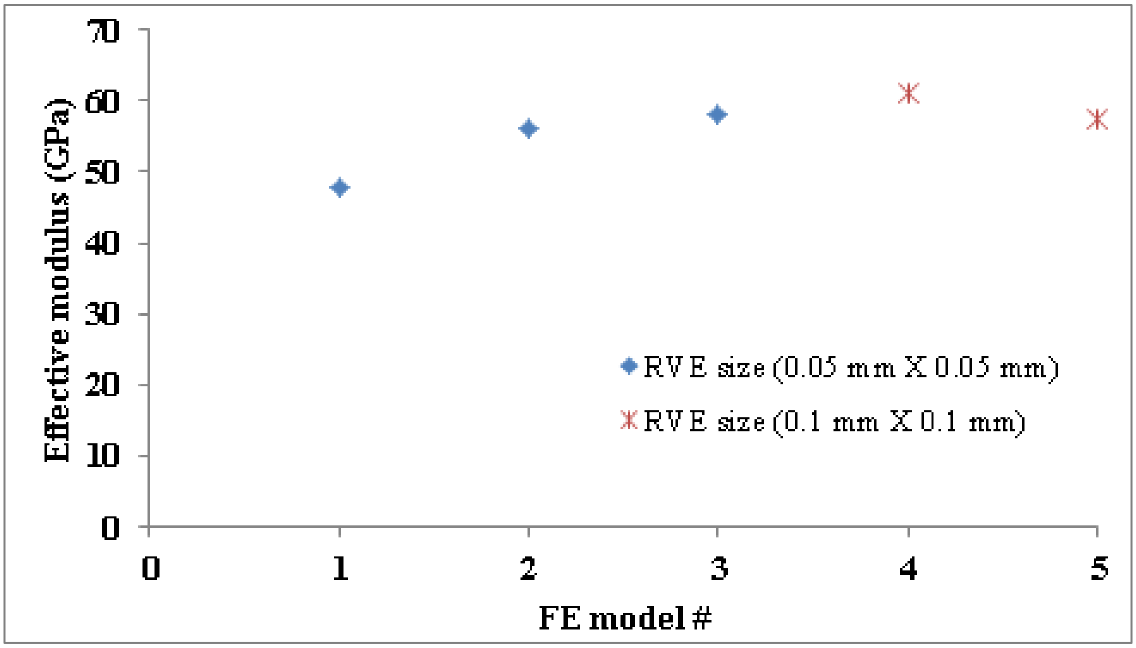

Figure 5.20. Elastic moduli comparison for FE models with actual shaped and circular shaped reinforcement and pores

CHAPTER VI

THERMOMECHANICAL BEHAVIOR OF ALUMINUM-ALUMINA FUNCTIONALLY GRADIENT MATERIALS (FGMs)

Aluminum-alumina FGMs are used for high temperature applications and for applications, which require high wear and tear resistance. They are used in engine components where one of their surfaces is exposed to high temperature (or wear and tear) and other surfaces are attached (or welded) to the substrate material or the base metal that is to be protected. To avoid delamination, thermo-mechanical properties should vary gradually between the dissimilar materials. Thermal stresses and stress discontinuity can be minimized at the interface if the FGM's surface that is attached to the substrate is mostly aluminum and gradually the alumina concentration is increased through the FGM so that the face that is exposed to high temperature (or high wear and tear) is made of high content of alumina.

In this chapter the overall thermo-mechanical behavior of $Al\text{-}Al_2O_3$ FGM samples under uniaxial compression are presented. The goal is to understand the overall elastic and inelastic response of the FGM samples at various temperatures. The FGM samples are made of layers of composites having alumina content 0, 5 and 10vol%. Also the net uniaxial thermal expansion of the $Al\text{-}Al_2O_3$ FGM samples with different layers of composites having alumina content varying from 0 to 25vol% are measured using Thermo mechanical analyzer and are presented later in this chapter.

6.1. Uniaxial compressive behavior of the functionally gradient material

The FGM samples were subjected to compressive loadings under quasi-static condition. For compression tests, FGM samples having layers of composites with alumina volume fraction

0, 5 and 10 vol% were manufactured by adding 2.8 g of each composite powder in the 12.7 mm die one layer above another, as explained in Chapter II .

Figure 6.1 shows the normalized force and displacement curves of Al-Al_2O_3 FGM samples at three different isothermal temperatures 25, 200 and 400^0C. It is noted that for the FGMs, instead of using the stress and strain measures, it is more desirable to use the normalized force, which is the applied uniaxial force divided by the original area, and the normalized displacement, which is the net displacement along the loading direction divided by the original length. The force was applied along the grading direction. In the FGM samples, as the material compositions vary continuously or discretely with the locations, the displacement field in the FGM samples is most likely not homogeneous (the deformation gradient is not constant), which results in non-uniform (non-constant) strain fields in the FGM samples. In the FGM sample, material properties change with the locations, leading to different deformations under the same stresses. In this study, the normalized displacement is called the net-strain and the normalized force is referred to the net-stress in order to keep the same terminology used in the composite samples with relatively uniform compositions of the constituents. At each testing temperature, two FGM samples were tested at a net-strain rate of 0.0833 min^{-1}until it reaches 5% strain followed by removal of the forces. The steps followed during the compression testing are as described in section 2.4c. The physical attributes of the FGM samples tested (viz. dimensions, % open porosity and density) are listed in Table 6.1. The stress-strain curves of aluminum matrix under compressive stresses at various temperatures are also added in Fig. 6.1 for comparison. The light gray lines with markers in Figure 6.1 are the stress strain responses of 0% composite (aluminum) samples. It can be seen from Figure 6.1 that as the testing temperature increased the net stress strain curves dropped significantly both for FGM and composite samples. This behavior is expected because with increase in temperature the material becomes softer and the dislocation motion gets activated and hence the flow resistance of the material decreases at higher temperatures. The FGM samples have almost identical response in the elastic region when compared to those of 0% composite samples. However, the FGM samples experience slightly higher net-strain hardening effect than the 0% samples, because of the hindrance provided by the alumina reinforcement to plastic deformation in the FGM samples. For conducting compression tests, we needed samples longer than 0.9 inches. During cold pressing of powders, it was difficult to make thin and long samples (with length greater than 0.9 inches using a die of 0.5 inches diameter) as volume fraction in the composite increases. Cold pressing of higher volume fraction(15, 20, 25vol%) composites resulted in samples having their edges torn off and any polishing the samples to get flat surfaces resulted in shorter samples making them not suitable for compression testing. Similar problem was faced when manufacturing FGM samples with higher volume fraction alumina layers. Hence for compression testing, because of the specimen's length/diameter requirements, only 0, 5 and 10vol% composites were manufactured and used for compression testing. If the manufactured FGM samples have higher ceramic contents, perhaps significantly different responses from that of normal composite samples can be achieved.

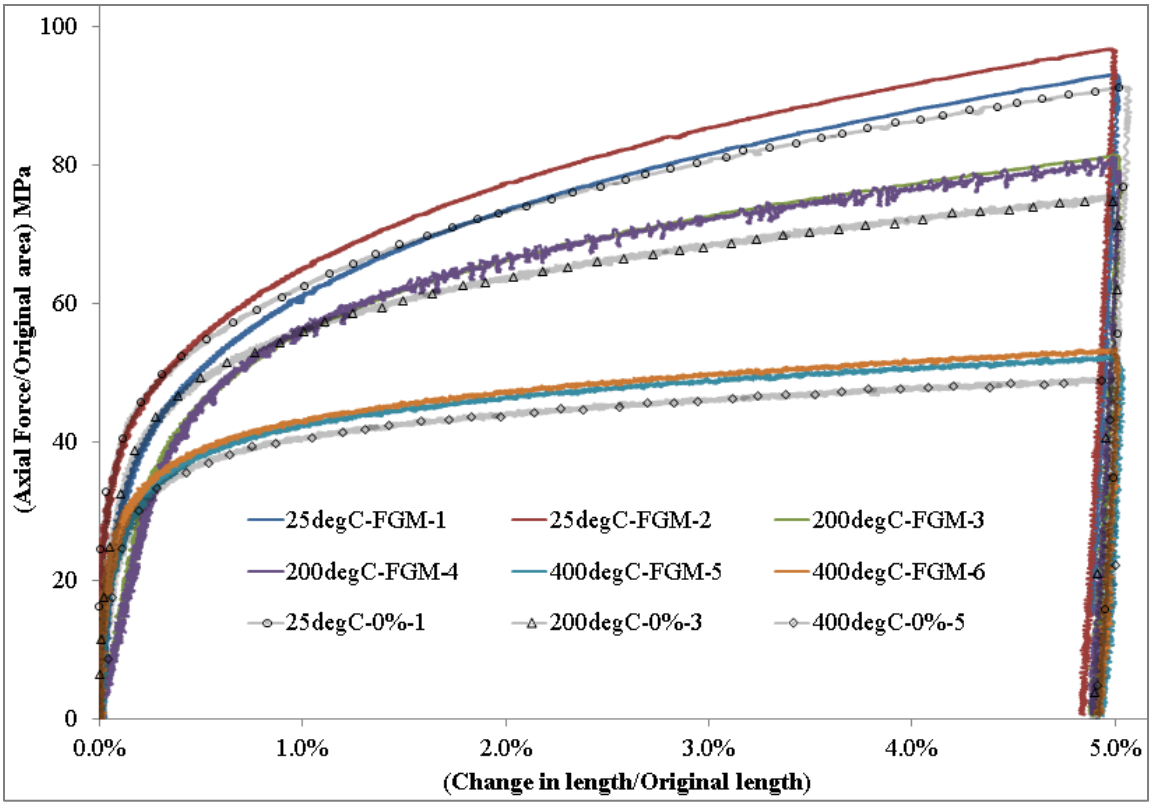

Figure 6.1. Stress Strain behavior of FGM samples along with 0% composite samples

Table 6.1. Physical attributes of the FGM samples used for compression testing at various testing temperatures

Testing temp	Sample	layers of FGM with alumina VF	Mass (g)	Ht. (mm)	Dia (mm)	Density (g/cc)	% Open Porosity
25^0C	FGM-1	0, 5 & 10%	8.7354	25	12.7	2.758	0.3992
	FGM-2	0, 5 & 10%	8.197	24.2	12.7	2.673	0.1710
200^0C	FGM-3	0, 5 & 10%	8.2278	24.5	12.7	2.651	0.3975
	FGM-4	0, 5 & 10%	8.2063	24.2	12.7	2.676	0.2458
400^0C	FGM-5	0, 5 & 10%	8.3365	24.9	12.7	2.642	0.5882
	FGM-6	0, 5 & 10%	8.277	24.5	12.7	2.666	0.3461

Table 6.2. Details obtained from the stress strain curves of the composite samples tested at various temperatures

Testing temp	Sample	Modulus, E (GPa)	Yield Stress (MPa)	Flow curve: $\sigma_T = K \varepsilon_T{}^n$	
				Strengthening Coefficient, K (MPa)	Strain Hardening exponent, n
25^0C	FGM-1	57.36	42	231.15	0.2867
	FGM-2	60.09	47	223.97	0.2648
200^0C	FGM-3	57.64	34	200.07	0.2789
	FGM-4	56.57	33	196.47	0.2759
400^0C	FGM-5	45.92	34	87.29	0.1560
	FGM-6	49.92	35	88.83	0.1557

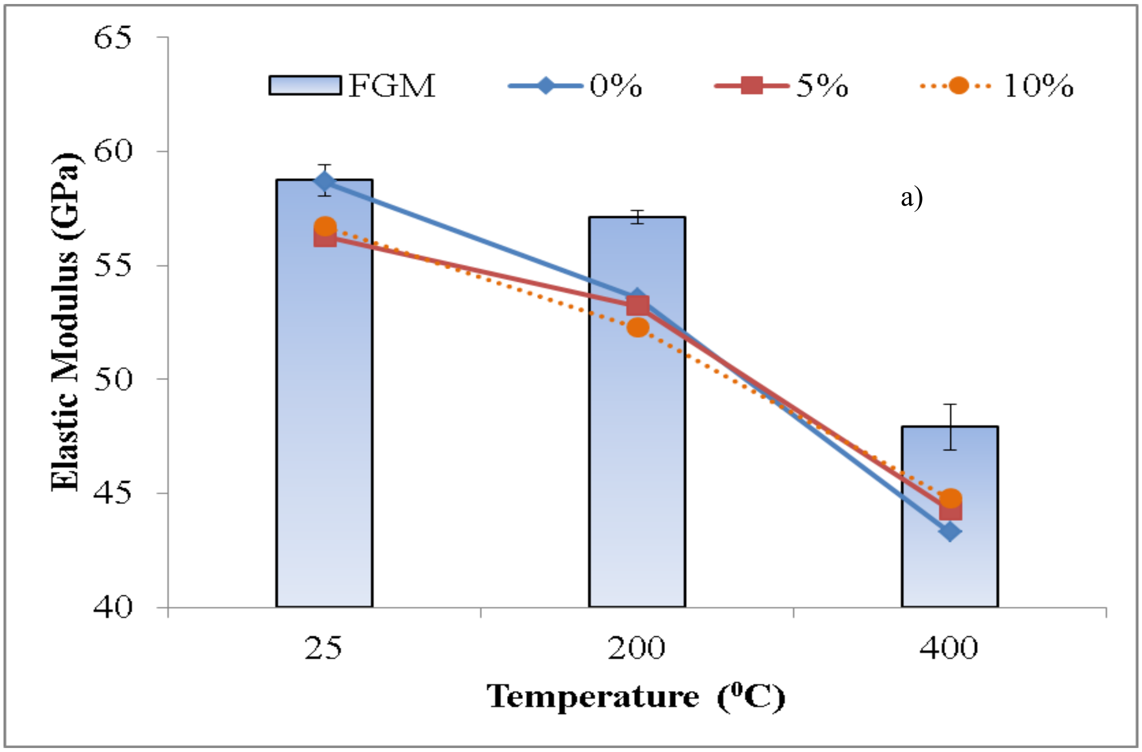

Figure 6.2. Effect of temperature on a) elastic modulus and b) yield stress of FGM and composite samples

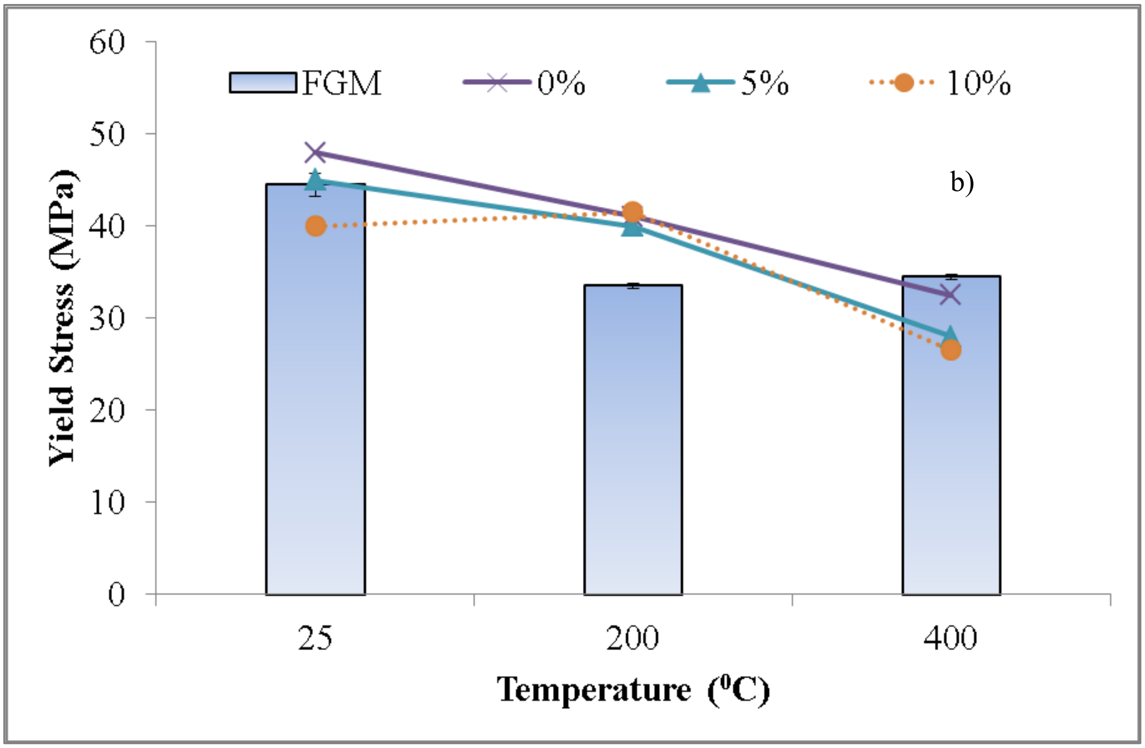

Figure 6.2. Continued

The overall (net) elastic modulus and yield stress of the FGM samples tested at various temperatures are determined from the stress strain curves. It should be noted that in the FGM samples, the overall (net) modulus is defined as the ratio of the normalized force (force/original area) to the normalized displacement , which is not the same as the modulus that relates the local stress to the local strain in linear elastic response. The same discussion also applies to the net-yield stress and net-hardening parameters of the FGM samples. From Table 6.2, the average modulus and yield stress for each FGM sample are calculated along with their standard deviation. Figure 6.2a-b shows the variation of the average elastic modulus and average yield stress with temperature for the FGM samples along with those of 0, 5 and 10 vol% composite samples. As expected, the net modulus and net yield stress of the FGM samples and the composite samples decreased significantly with increase in temperature because of increase in atomic vibrations and dislocation movement at higher temperatures. Further, the decrease in net modulus with increase in temperature was higher for the normal composite samples than that of the FGM samples. The FGM samples had higher net-modulus than the normal composite samples for all the volume fractions of the composite and for all the temperatures tested. However, the trend is not that clear for the yield strength. The FGM samples had higher yield strength than the normal composite samples, except at 200^{o}C.

To define the material's behavior in the strain-hardening region, it is necessary to determine the strain hardening coefficient (n) and strengthening coefficient (K) in the empirical flow curve equation (Eq.5.1) described in Chapter V. Figure 6.3 shows the procedure used to determine the net strain hardening coefficient (n) and strengthening coefficient (K) from the net stress strain curves for the FGM samples at various temperatures. Table 6.2 summarizes the net n and K values for all the FGM samples. Figure 6.4 shows the variation of the net strengthening coefficient (K) and strain hardening coefficient (n) with compression testing temperature for the FGM samples along with 0, 5 and 10 vol% composite samples. Both n and K decreased with increase in temperature, which is expected. This is due to increase in the dislocation mobility at higher temperatures making it easier for the materials to undergo plastic deformations without much of strain hardening. The FGM samples had n and K higher than the 0% samples, and further, with an increase in volume fraction, both n and K increased due to the hindrance provided by the alumina reinforcement for the dislocation motion.

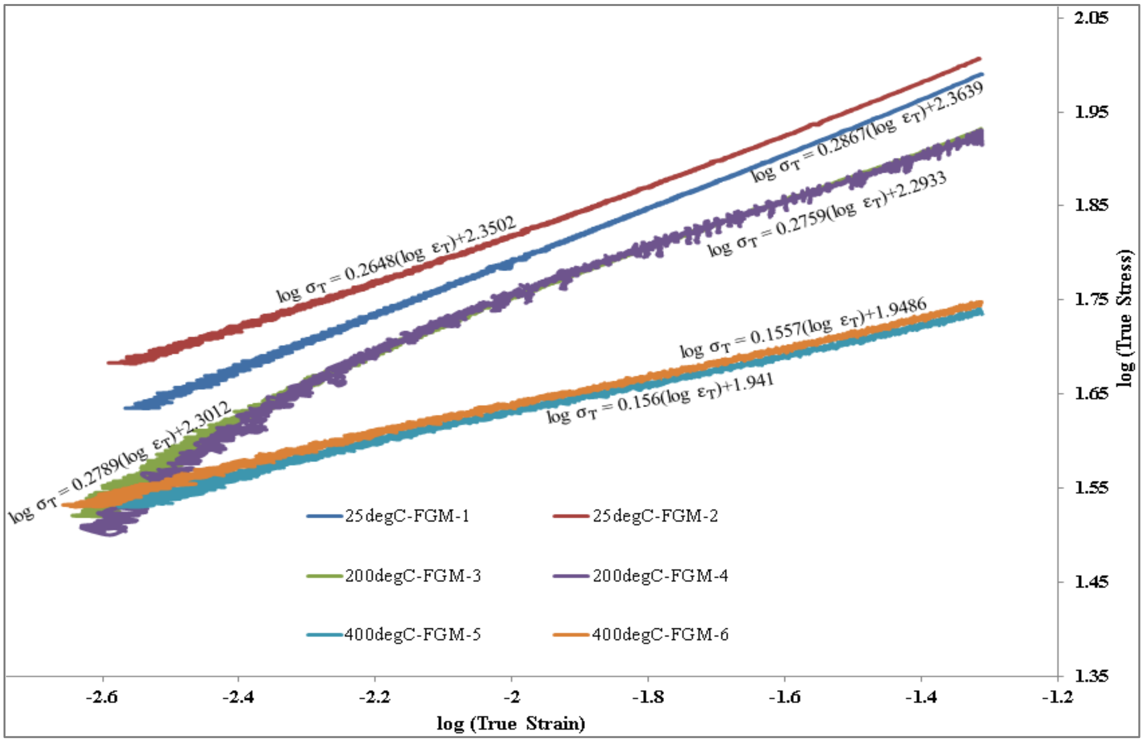

Figure 6.3. log true stress vs log true strain curve for FGM samples

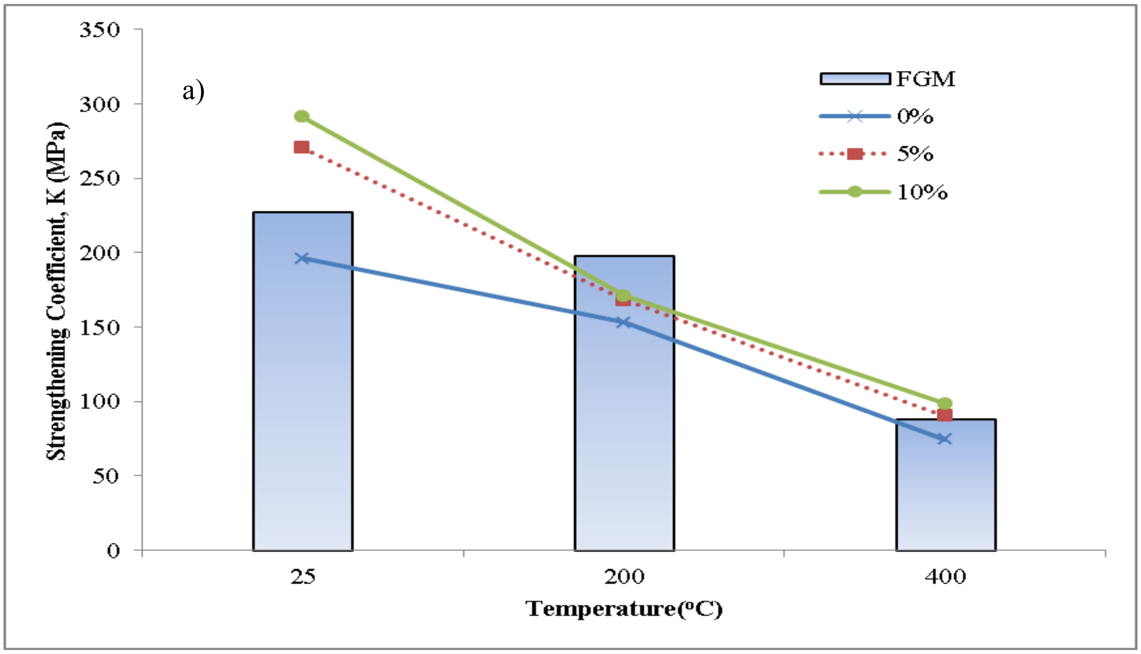

Figure 6.4. Effect of temperature on a) K and b) n of FGM and composite samples

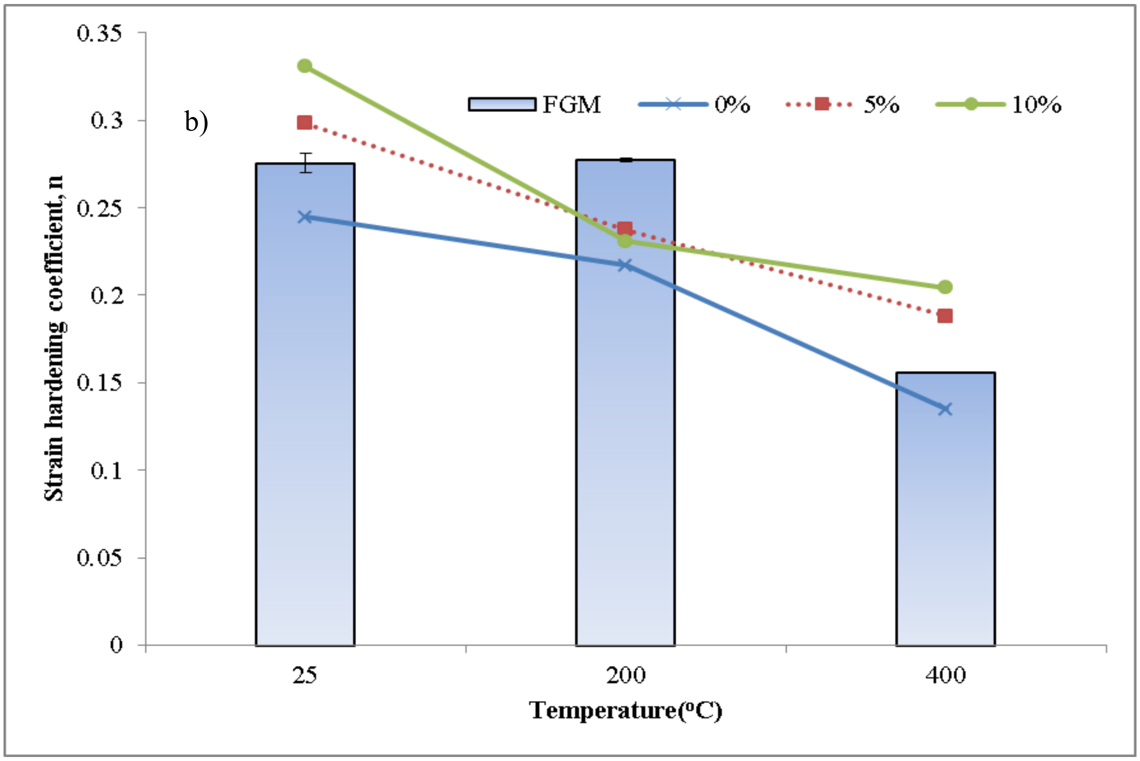

Figure 6.4. Continued

6.2. Thermal expansion coefficient of FGM samples

As explained in Chapter II, FGM samples having layers of alumina volume fraction 0, 5, 10, 15, 20 and 25 % were manufactured by adding 2 g of each composite powder in the 25.4 mm die on top of each other respectively. Using a diamond saw, samples with rectangular cross sections were cut out from these cylindrical samples with dimensions as shown in Table 6.3. The physical attributes of the Al-Al_2O_3 FGM samples used for CTE measurement are shown in Table 6.3.

Table 6.3. Physical attributes of the FGM samples used for CTE

Sample	layers of FGM with alumina VF	Mass (g)	Height (mm)	Length (mm)	Width (mm)	Density (g/cc)	% Open Porosity
FGM-1	0, 5, 10, 15, 20 & 25%	1.306	13.326	5.675	6.867	2.515	0.431
FGM-2	0, 5, 10, 15, 20 & 25%	1.670	13.328	7.566	7.075	2.341	0.637

Figure 6.5 shows the net thermal strain vs. temperature curves for the tested FGM samples along with composite samples with different volume contents of alumina during the heating and cooling processes. The net thermal strain increased linearly as temperature increased from 20°C to 400°C; and decreased linearly as temperature was decreased from 400°C to 20°C. A linear net CTE (µm/m°C) of the specimen is calculated in 25°C to 400°C temperature range, by taking the slope of net thermal strain vs temperature curves. As these curves are linear, the effective net CTE of the composite specimen is taken as constant i.e. it does not vary with temperature. Figure 6.6 compares the linear net CTE for FGM samples along with composite samples with different volume fraction of alumina, during heating and cooling phases. The effective net CTE gradually decreases as the ceramic content increased from 0 to 25%. The FGM samples had effective CTE lying in between those of 0% and 25% composite samples (closer to the CTE of 25% composite samples) during both the heating and cooling cycles. This is expected since the alumina reinforcement present in the 5% and 10% layers of the FGMs have significantly lower linear net CTE (5.5 µm/m°C), when compared to that of pure aluminum and thereby they would have constrained the thermal expansion of the entire FGM.

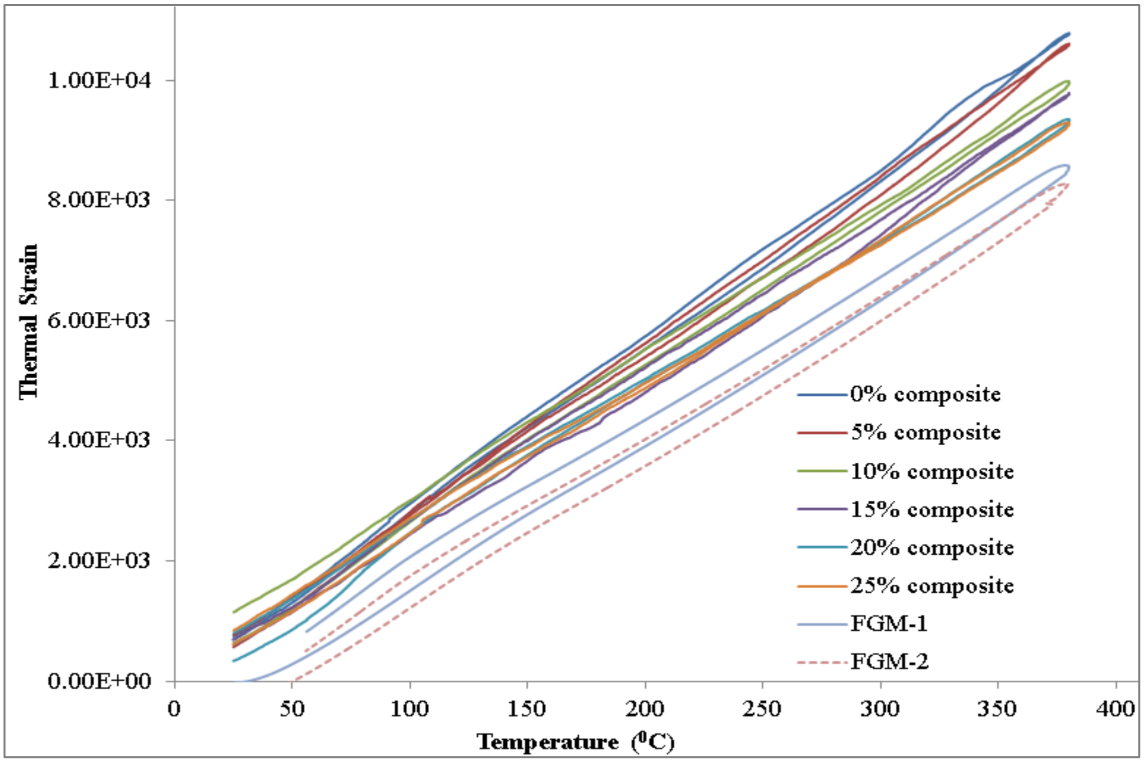

Figure 6.5. Thermal strain variation with temperature for 0, 5 and 10% composite and FGM samples

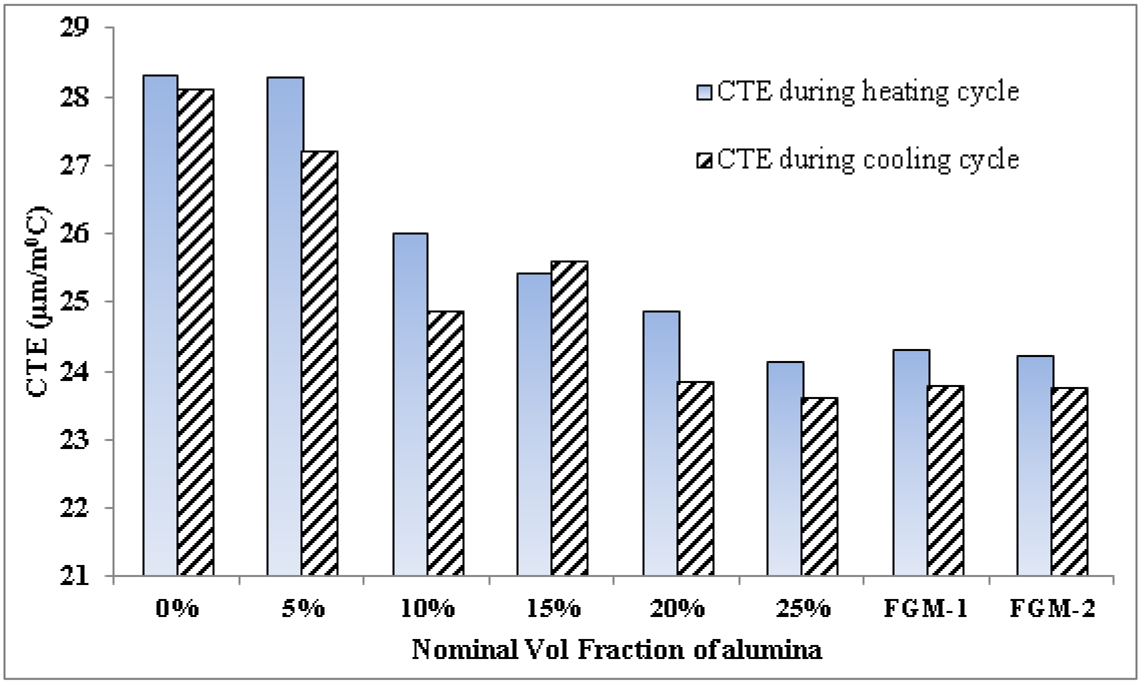

Figure 6.6. CTE variation with VF of alumina for 0, 5 and 10% composite and FGM samples

From the current study, it can be concluded that the FGMs behave mostly like a normal composite with higher volume content of alumina. The main advantage of FGM is its ability to have gradient in temperature and thereby minimizing the thermal stresses both inside the FGM and at the interface of FGM and the base metal to which it is attached. To see how effective our aluminum-alumina FGM is in protecting the base metal, further studies need to be done either experimentally or numerically to determine the drop in temperature from one end to the other end of FGM and to see the magnitude of thermal stresses developed. If we have manufactured FGM with higher ceramic contents, perhaps we could have seen significantly different responses from that of normal composite samples.

CHAPTER VII

CONCLUSIONS AND FUTURE STUDIES

This study focuses on understanding the effects of microstructural characteristics on the thermo-mechanical properties of Al-Al_2O_3 composites at elevated temperatures through combined experimental and numerical works. The microstructural characteristics and mechanical properties of Al-Al_2O_3 composites depend strongly upon the manufacturing process and compositions of the composites. The concluding remarks from all chapters, corresponding to the physical and thermo-mechanical properties, microstructural morphologies (uniform and functionally graded distributions of the constituent) and compressive mechanical response, are summarized in the following sections.

7.1. Effect of compacting pressure, particle size and volume fraction on the physical and thermo-mechanical properties of the composite

Al-Al_2O_3 composites with two different sizes of aluminum particles and various volume fractions of the alumina have been manufactured and their physical, elastic, and thermal properties have been characterized. The composite system A prepared with coarser aluminum powder had higher porosity than the composite system B prepared with finer aluminum powder. Also, it was found that the porosity for both composite systems increases significantly with increase in the alumina volume contents. For composites with higher contents of alumina particles, the alumina particles are close to each other and some of them are possibly in contact, preventing the aluminum particles to fill the gaps in between them during cold pressing. Choosing the aluminum with smaller particle size helps the aluminum particles to fill the empty gaps between the alumina, as shown by reduction in the porosity for the composite B with 20%

and 25% alumina contents. However, there is no significant reduction in the overall porosity when using finer aluminum particles for the composites with a relatively low alumina contents (less than 20%). In fact the overall open porosity increases when finer aluminum is considered. Increasing the compacting pressures up to 502 MPa increases the relative density of the composite. Further increase in the compacting pressure insignificantly increases the density of the composites. Increasing compacting pressures help in reducing the porosity, but high compacting pressures could distort the particles and cause permanent deformation or cracking in the particles. It was also found that the cold compaction pressure, together with particle size of initial powders are predominant parameters that affect the final density of the sintered composites, shown by the fact that the density of the composites increases for less than 2% after sintering even at temperatures that are close to the melting point of aluminum.

Young's modulus (E) and Shear modulus (G) of the composites depend not only on the alumina volume content of the composite samples, but also on the porosity of the samples, and thus on the processing parameters used. Increasing alumina content and reducing porosity improves the overall elastic moduli (E and G) of the composites. The elastic moduli decrease significantly with increasing temperatures as the constituents become softer with increase in temperature. The reduction of the effective moduli (E and G) with increase in temperature is more pronounced for the composites with higher volume contents of alumina, which could be due to the existence of high thermal stresses in the composite. High stresses in the aluminum constituent could lead to plastic deformation, while high tensile stresses in the alumina constituent could cause cracking. In addition, increase in temperature changes could also result in large thermal stress discontinuities between the interfaces of aluminum and alumina, leading to debonding. Plastic deformation, cracking, and debonding could significantly reduce the effective elastic moduli of the composites.

It has been observed that the effective CTE of the composite depends mainly on the volume content of alumina. As volume percent of alumina in the composite samples increases, the CTE decreases for both composite systems A and B. The effects of porosity on the overall CTE of the composites are insignificant, as porosities even up to 6% in the studied composite sample did not have significant effect on the CTE. Also temperature and compacting pressure on the composite had an insignificant effect on the CTE of the composite. The effective CTEs measured during heating and cooling are nearly on top of each other.

7.2. Numerical study on the effect of microstructural characteristics and residual stresses on thermo-mechanical properties and determination of stress free temperature

The effects of microstructural characteristics, i.e., the size, shape, distribution, and properties of the constituents, interactions between the constituents, existences of porosity, loading direction, and thermal (residual) stress on the effective elastic modulus, Poisson's ratio and coefficient of thermal expansion (CTE) of Al/Al_2O_3 composites have been studied. Microstructural models of the composites with 10 and 20vol% alumina contents were constructed from the micrograph images of the composite samples. These microstructural models were implemented in Finite Element for analyzing the effective elastic modulus, Poison's ratio and CTE of the composite samples. The numerical results were compared with the experimental data obtained from RUS and TMA. The parameters that affect these effective properties were studied.

It has been observed that the composite samples having smaller aluminum particles experienced noticeable oxidation on the surfaces of the aluminum particles, increasing the overall content of the alumina constituent. Some voids/pores were developed in the composite samples, which could be due to incomplete sintering and/or stresses being released during cooling down of the samples from the sintering temperature. The numerical study showed that the effective elastic modulus depended strongly on the amount of porosity and alumina content, whereas the effective Poison's ratio and CTE did not vary significantly with the amount of porosity. This is perhaps due to the fact that both Poisson's effect and CTE are the results of free expansion and the amount of porosity is relatively small compared to the overall size of the composite samples. The direction of loading only slightly affected the effective modulus, but did not seem to significantly affect the effective Poisson's ratio and CTE. It is then concluded that the composite samples have relatively good distributions of alumina particles in the aluminum matrix and could be treated as an isotropic material with regards to their thermo-mechanical properties. The softening in the aluminum matrix significantly influenced the thermo-mechanical properties of the composites and it was also necessary to incorporate the existence of the thermal (residual) stresses in characterizing the overall thermo-mechanical properties of the composites. Finally, the possible effects of the stress relaxation at elevated temperatures on the overall properties of the composites have been studied. This is because the cooling down process after sintering the composite samples takes about seven hours, which is a relatively slow process and thus would give enough time for the constituents to relax partially the internal (residual) stresses. The numerical results suggested relatively significant stress relaxation experienced by the constituents during the cooling down from the sintering temperature to room temperature.

7.3. Uniaxial compressive stress-strain behavior of the composites

Stress-strain curves are obtained for the Al-Al_2O_3 composite samples with different alumina volume contents at three different isothermal temperatures (25, 200 and 400^0C). From the compression testing results, the effective modulus and yield stress were found to decrease with increase in temperature, as expected. However, with increase in volume fraction of alumina in the composite, modulus and yield stress were found to decrease because of increase in porosity of samples with increase in alumina content. The compression test results were compared to the RUS results. As volume fraction increases, relative density decreased (i.e. porosity increased) both for the compression testing samples and RUS samples. However, the decrease was less for RUS samples than those of compression testing samples, because compression testing samples were bigger in size with more porosity than RUS samples. Hence, as volume fraction increases, the elastic moduli decreased for the compression testing samples whereas it increased for RUS samples. Further, it was found that as volume fraction increases, the drop in modulus because of temperature raise is less for both compression testing and RUS samples.

7.4. Microstructural models for composites used for RUS and compressive testing

The effects of microstructural characteristics, i.e., amounts of porosity, distributions of alumina particles, and constituent properties, on the overall mechanical properties and response of Al-Al_2O_3 composites have been studied. The microstructures of the composites are obtained from the SEM images and converted to FE meshes. FE method is used to solve boundary value problems of the composite microstructural models in order to determine the overall response and field variables of the composites. The localized stresses are shown within the microstructures of the composites even when the overall (macroscopic) response of the composites is under relatively small strains. The high localized stresses could lead to yielding of the aluminum constituent and/or cracking of the alumina particles. The localized stresses in the aluminum matrix are more pronounced in the regions closely bounded by the alumina particles or when the spacing between the alumina particles is relatively small. The localized stresses have a significant influence on the overall elastic modulus of the composites. These numerical exercises might explain the relatively low elastic modulus determined from the uniaxial compressive test as compared to the one determined from RUS, in which a relatively small strain is induced on the specimens. The amount of porosity in the composites significantly reduces the mechanical properties and response of the composites.

7.5. Thermo-mechanical responses of Al-Al_2O_3 functionally gradient materials

Functionally graded materials (FGMs) have been manufactured and tested for their compressive uniaxial responses and overall thermal expansion coefficient. For the compressive testing, the FGM samples with alumina volume contents varying from 0 to 10% are considered, while for the net thermal expansion measurement the FGM samples comprised of layered composites with alumina volume contents varying from 0 to 25%. The FGM samples have almost identical response with those of 0% composite samples in the elastic region. However, the FGM samples showed slightly more net strain hardening than the 0% samples, because of the hindrance provided by the alumina reinforcement to plastic deformation in the FGM samples. As expected, the net modulus and yield strength of the FGM samples and the composite samples decreased significantly with increase in temperature because of increase in atomic vibrations and easier dislocation movement at higher temperatures. Further, the decrease in modulus with increase in temperature was higher for the normal composite samples than that of the FGM samples.

To define the material's behavior in the strain-hardening region, we determine the net-strain hardening coefficient (n) and strengthening coefficient (K) in the empirical flow curve equation. Higher n and K means higher the rate at which the material strain hardens and hence superior the mechanical properties. The net hardening parameters n and K decreased with increase in temperature for the FGM and composite samples, which is expected. This is due to increase in the dislocation mobility at higher temperatures making it easier for the materials to undergo plastic deformations without much of strain hardening. The FGM samples had higher hardening parameters than the 0% samples, and further, with an increase in volume fraction, both hardening parameters increased due to the hindrance provided by the alumina reinforcement for the dislocation motion.

As the net thermal strain vs. temperature curves are linear for the FGM and composite samples, the net CTE are taken as constant i.e. it does not vary with temperature. The net CTE gradually decreased as the ceramic content increased from 0 to 25%, and the FGM samples had the CTE close to the 25% composite samples during both the heating and cooling cycles.

7.6. Future studies

- Al-Al_2O_3 composite samples were manufactured using cold pressing of powders followed by pressureless sintering which produces composite samples with considerable porosity, large grain growth and hence lower mechanical properties. More advanced, but more costly fabrication methods such as Hot Isostatic Pressing (HIP) and Spark Plasma Sintering (SPS) can be used to overcome these problems.
- The current study uses experimental and numerical methods to determine the overall thermo-mechanical responses of Al-Al_2O_3 composites, but it has been limited to only elastic and plastic behavior of the composites at different temperatures. The current work can be extended to time dependent behavior (e.g. including creep, including viscoelastic behavior in micromechanical analysis etc.) for determining the thermo-mechanical responses.
- FE analysis has been done using 2D microstructural models assuming plane stress conditions. To represent the microstructure more accurately and thereby determine their

thermo-mechanical response accurately, we need to construct microstructural models from 3D microstructural images (e.g. by using X-ray Tomography).

- Compression testing has been done at various temperatures in an open heating chamber in the presence of air. However, to reduce the possibility of oxidation, all the testing needs to be done in controlled atmosphere (e.g. Argon).
- Al-Al_2O_3 FGM samples were manufactured using a simple 'Die compacting method' which has limitations in terms of obtaining accurate gradient distribution of alumina with exact thickness of layers(as compaction and sintering stages can alter them). More advanced manufacturing method can be used which can produce accurate gradient distribution and which allows great control over the thickness of each layers.

REFERENCES

[1] Mortensen A, Llorca J. Metal matrix composites. Annual Review of Materials Research. 2010;40:243-270.

[2] Mishnaevsky L. Computational mesomechanics of composites: numerical analysis of the effect of microstructures of composites on their strength and damage resistance. New Jersey: Wiley-Interscience; 2007.

[3] Dobrzanski LA, Wlodarczyk A, Adamiak M. The structure and properties of PM composite materials based on EN AW-2124 aluminum alloy reinforced with the BN or Al2O3 ceramic particles. J Mater Process Tech. 2006;175(1-3):186-191.

[4] Torralba JM, da Costa CE, Velasco F. P/M aluminum matrix composites: an overview. J Mater Process Tech. 2003;133(1-2):203-206.

[5] Surappa MK. Aluminium matrix composites: Challenges and opportunities. Sadhana-Acad P Eng S. 2003;28:319-334.

[6] Kopeliovich D. Tribological properties of alumina reinforced composites. SubsTech; 2012.

[7] Mazen A, Ahmed A. Mechanical behavior of Al-Al2O3 MMC manufactured by PM techniques part I—scheme I processing parameters. Journal of Materials Engineering and Performance. 1998;7(3):393-401.

[8] Rahimian M, Ehsani N, Parvin N, Baharvandi HR. The effect of particle size, sintering temperature and sintering time on the properties of Al-Al2O3 composites, made by powder metallurgy. J Mater Process Tech. 2009;209(14):5387-5393.

[9] Rahimian M, Parvin N, Ehsani N. Investigation of particle size and amount of alumina on microstructure and mechanical properties of Al matrix composite made by powder metallurgy. Mat Sci Eng a-Struct. 2010;527(4-5):1031-1038.

[10] Banjuraizah J, Rejab N, Su N, Talib M. Effect of sintering environment to the physical properties of Al/calcined dolomite composite. 2007.

[11] Schaffer G, Hall B. The influence of the atmosphere on the sintering of aluminum. Metallurgical and MaterialsTransactions A. 2002;33(10):3279-3284.

[12] Ksiazek M, Sobczak N, Mikulowski B, Radziwill W, Surowiak I. Wetting and bonding strength in Al/Al2O3 system. Mat Sci Eng A-Struct. 2002;324(1-2):162-167.

[13] Kou H, Pan Y, Guo J. Microstructures and mechanical properties of Al/Al2O3 Cermet composites reinforced by Al/Al2O3 core-shell particles. Advanced Materials Research. 2007;15-17:240-245.

[14] Zhang Q, Cagin T, van Duin A, Goddard WA, Qi Y, Hector LG. Adhesion and nonwetting-wetting transition in the Al/alpha-Al2O3 interface. Phys Rev B. 2004;69(4).

[15] Saiz E, Tomsia AP, Suganuma K. Wetting and strength issues at Al/alpha-alumina interfaces. J Eur Ceram Soc. 2003;23(15):2787-2796.

[16] Timsit RS, Waddington WG, Humphreys CJ, Hutchison JL. Structure of the Al/Al2O3 Interface. Appl Phys Lett. 1985;46(9):830-832.

[17] Kok M. Production and mechanical properties of Al2O3 particle-reinforced 2024 aluminium alloy composites. J Mater Process Tech. 2005;161(3):381-387.

[18] McCormick AL, Aghajanian MK, Marshall AL. The effect of particle size, particle loading and thermal processing conditions on the properties of alumina reinforced aluminum metal matrix composites. Ceramic Engineering and Science Proceedings. 2010;30(5):105-111.

[19] Arsenault RJ, Haasen P. Deformation and fracture behavior of metal-ceramic matrix composite materials: Pergamon Pr.; 1994.

[20] Ali Hubi H, Newfal Z, Newal Muhammad D. Preparing and studying some mechanical properties of aluminum matrix composite materials reinforced by Al2O3 particles. Journal of Babylon University. 2012;20(1):30-38.

[21] Kouzeli M, Dunand DC. Effect of temperature and strain rate on the compressive flow of aluminum composites containing submicron alumina particles. Metall Mater Trans A. 2004;35A(1):287-292.

[22] Ganguly P. High temperature deformation and failure in aluminum-alumina particulate metal matrix composites. The University of British Columbia, Department of Metals and Materials Engineering, 1998.

[23] Radovic M, Lara-Curzio E, Riester L. Comparison of different experimental techniques for determination of elastic properties of solids. Materials Science and Engineering A. 2004;368(1-2):56-70.

[24] Aboudi J. Inelastic behavior of metal-matrix composites at elevated temperature. International journal of plasticity. 1985;1(4):359-372.

[25] Eischen J, Torquato S. Determining elastic behavior of composites by the boundary element method. Journal of applied physics. 1993;74(1):159-170.

[26] Dvorak G, Wafa A, Bahei-El-Din Y. Implementation of the transformation field analysis for inelastic composite materials. Computational mechanics. 1994;14(3):201-228.

[27] Torquato S. Effective stiffness tensor of composite media: II. Applications to isotropic dispersions. Journal of the Mechanics and Physics of Solids. 1998;46(8):1411-1440.

[28] Dvorak GJ, Srinivas MV. New estimates of overall properties of heterogeneous solids. Journal of the Mechanics and Physics of Solids. 1999;47(4):899-920.

[29] Yin HM, Sun LZ. Elastic modeling of periodic composites with particle interactions. Philosophical Magazine Letters. 2005;85:163-173.

[30] Muliana A. The effects of residual stresses and degradation on the response of viscoplastic functionally graded materials. Composite Structures. 2012.

[31] Kari S, Berger H, Rodriguez-Ramos R, Gabbert U. Computational evaluation of effective material properties of composites reinforced by randomly distributed spherical particles. Composite Structures. 2007;77(2):223-231.

[32] Pierard O, LLorca J, Segurado J, Doghri I. Micromechanics of particle-reinforced elasto-viscoplastic composites: Finite element simulations versus affine homogenization. International Journal of Plasticity. 2007;23(6):1041-1060.

[33] Barello RB, Lévesque M. Comparison between the relaxation spectra obtained from homogenization models and finite elements simulation for the same composite. International Journal of Solids and Structures. 2008;45(3-4):850-867.

[34] Khan KA, Barello R, Muliana AH, Lévesque M. Coupled heat conduction and thermal stress analyses in particulate composites. Mechanics of Materials. 2011;43(10):608-625.

[35] Wojnar L. Image analysis: applications in materials engineering: CRC Press; 1999.

[36] Langer SA, Fuller Jr ER, Carter WC. OOF: an image-based finite-element analysis of material microstructures. Computing in Science and Engineering. 2001;3(3):15-23.

[37] Chawla N, Patel BV, Koopman M, Chawla KK, Saha R, Patterson BR, et al. Microstructure-based simulation of thermomechanical behavior of composite materials by object-oriented finite element analysis. Materials Characterization. 2002;49(5):395-407.

[38] Chawla N, Ganesh V, Wunsch B. Three-dimensional (3D) microstructure visualization and finite element modeling of the mechanical behavior of SiC particle reinforced aluminum composites. Scripta Materialia. 2004;51(2):161-165.

[39] Bakshi SR, Patel RR, Agarwal A. Thermal conductivity of carbon nanotube reinforced aluminum composites: A multi-scale study using object oriented finite element method. Computational Materials Science. 2010;50(2):419-428.

[40] Dong Y, Bhattacharyya D, Hunter PJ. Experimental characterisation and object-oriented finite element modelling of polypropylene/organoclay nanocomposites. Composites Science and Technology. 2008;68(14):2864-2875.

[41] Wang Z, Kulkarni A, Deshpande S, Nakamura T, Herman H. Effects of pores and interfaces on effective properties of plasma sprayed zirconia coatings. Acta Materialia. 2003;51(18):5319-5334.

[42] Zimmermann A, Fuller Jr ER, Rödel J. Residual stress distributions in ceramics. Journal of the American Ceramic Society. 1999;82(11):3155-3160.

[43] Cannillo V, Leonelli C, Boccaccini AR. Numerical models for thermal residual stresses in Al2O3 platelets/borosilicate glass matrix composites. Materials Science and Engineering: A. 2002;323(1-2):246-250.

[44] Arsenault RJ, Taya M. Thermal residual-stress in metal matrix composite. Acta Metall Mater. 1987;35(3):651-659.

[45] Bruno G, Ceretti M, Girardin E, Giuliani A, Manescu A. Relaxation of residual stress in MMC after combined plastic deformation and heat treatment. Scripta Materialia. 2004;51(10):999-1004.

[46] Fitzpatrick ME, Dutta M, Edwards L. Determination by neutron diffraction of effect of plasticity on crack tip strains in a metal matrix composite. Mater Sci Tech Ser. 1998;14(9-10):980-986.

[47] Fernández-Castrillo P, Bruno G, González-Doncel G. Neutron and synchrotron radiation diffraction study of the matrix residual stress evolution with plastic deformation in aluminum alloys and composites. Materials Science and Engineering: A. 2008;487(1-2):26-32.

[48] Gudlur P. Thermoelastic properties of particle reinforced composites at the micro and macro Scales, Texas A&M University, 2010.

[49] Yang Z, Zhang L, Shen Q, Gong D. Theoretical design of sedimentation applied to the fabrication of functionally graded materials. Metallurgical and Materials Transactions B. 2003;34(5):605-609.

[50] Kieback B, Neubrand A, Riedel H. Processing techniques for functionally graded materials. Materials Science and Engineering: A. 2003;362(1):81-106.

[51] Rajan T, Pillai R, Pai B. Characterization of centrifugal cast functionally graded aluminum-silicon carbide metal matrix composites. Materials Characterization. 2010;61(10):923-928.

[52] Biesheuvel PM, Breedveld V, Higler AP, Verweij H. Graded membrane supports produced by centrifugal casting of a slightly polydisperse suspension. Chemical engineering science. 2001;56(11):3517-3525.

[53] Watanabe Y, Sato H. Review fabrication of functionally graded materials under a centrifugal force. 2011.

[54] Robson M, Blue C, Warrier S, Lin R. Sputter deposition of SiC coating on silicon wafers. Scripta Metallurgica et Materialia. 1992;27(5):565-570.

[55] Fujii K, Imai H, Nomura S, Shindo M. Functionally gradient material of silicon carbide and carbon as advanced oxidation-resistant graphite. Journal of Nuclear Materials. 1992;187(3):204-208.

[56] Shabana YM, Bruck HA, Pines ML, Kruft JG. Modeling the evolution of stress due to differential shrinkage in powder-processed functionally graded metal–ceramic composites during pressureless sintering. International Journal of Solids and Structures. 2006;43(25):7852-7868.

[57] Fukui Y, Takashima K, Ponton C. Measurement of Young's modulus and internal friction of an in situ Al-Al3Ni functionally gradient material. Journal of Materials Science. 1994;29(9):2281-2288.

[58] Ben-Oumrane S, Abedlouahed T, Ismail M, Mohamed BB, Mustapha M, El Abbas AB. A theoretical analysis of flexional bending of Al/Al2O3 S-FGM thick beams. Computational Materials Science. 2009;44(4):1344-1350.

[59] Jamaati R, Toroghinejad MR. Manufacturing of high-strength aluminum/alumina composite by accumulative roll bonding. Materials Science and Engineering: A. 2010;527(16-17):4146-4151.

[60] Daehn GS, Starck B, Xu L, Elfishawy KF, Ringnalda J, Fraser HL. Elastic and plastic behavior of a co-continuous alumina/aluminum composite. Acta Materialia. 1996;44(1):249-261.

[61] Zhang W, Gu M, Chen J, Wu Z, Zhang F, Deve HE. Tensile and fatigue response of alumina-fiber-reinforced aluminum matrix composite. Materials Science and Engineering A. 2003;341(1-2):9-17.

[62] Ulrich TJ, McCall KR, Guyer RA. Determination of elastic moduli of rock samples using resonant ultrasound spectroscopy. J Acoust Soc Am. 2002;111(4):1667-1674.

[63] Suryanarayana C. Mechanical alloying and milling. Progress in Materials Science. 2001;46(1-2):1-184.

[64] Standard test methods for apparent porosity, water absorption, apparent specific gravity, and bulk density of burned refractory brick and shapes by boiling water. ASTM C 20: American Society Testing & Materials. 2010;15.01.

[65] Barsoum MW, Radovic M, Ganguly A, Zhen T, Finkel P, Kalidindi SR, et al. On the elastic properties and mechanical damping of Ti(3)SiC(2), Ti(3)GeC(2), Ti(3)Si(0.5)Al(0.5)C(2) and Ti(2)AlC in the 300-1573 K temperature range. Acta Materialia. 2006;54(10):2757-2767.

[66] Migliori A, Sarrao JL. Resonant ultrasound spectroscopy: applications to physics, materials measurements, and nondestructive evaluation: John Wiley; 1997.

[67] Test method for linear thermal expansion of solid materials by thermomechanical analysis. ASTM E 831: American Society Testing & Materials. 2009;14.02.

[68] Popescu IN, Zamfir S, Anghelina VF, Rusanescu CO. Processing by P/M route and characterization of new ecological aluminum matrix composites (AMC). International Journal of Mechanics. 2010;4(3):43-52.

[69] Pham HH, Williams ME, Mahaffey P, Radovic M, Arroyave R, Cagin T. Finite temperature elasticity of fcc Al: atomistic simulations and ultrasonic measurements. Phys Rev B. 2010.

[70] Lim T, Kim YH, Lee CS, Han KS. Fabrication and mechanical-properties of aluminum matrix composite-materials. J Compos Mater. 1992;26(7):1062-1086.

[71] Weast RC. CRC handbook of chem. & phys. 70th ed. Boca Raton: CRC Press; 1990.

[72] Matweb. The online materials information reference. Automation Creations Inc.; 2001.

[73] Muliana AH. A micromechanical model for predicting thermal properties and thermo-viscoelastic responses of functionally graded materials. International Journal of Solids and Structures. 2009;46(9):1911-1924.

[74] Gudlur P, Forness A, Lentz J, Radovic M, Muliana A. Thermal and mechanical properties of Al/Al203 composites at elevated temperatures. Materials Science and Engineering A. 2011.

[75] Aluminum Oxide, Al2O3 material characteristics. Phillipsburg: Accuratus Ceramic Corporation.

[76] Moosbrugger C. Atlas of stress-strain curves. 2nd ed: ASM International; 2002.

[77] Hong S, Gray III G, Lewandowski J. Dynamic deformation behavior of Al-Zn-Mg-Cu alloy matrix composites reinforced with 20 Vol.% SiC. Acta Metallurgica et Materialia. 1993;41(8):2337-2351.

[78] Kalambur A, Hall I. Dynamic compressive behavior of a SiC {sub w}/Al composite. Scripta Materialia. 1997;37(2).

[79] Perng C-C, Hwang J-R, Doong J-L. High strain rate tensile properties of an (Al2O3 particles)-(Al alloy 6061-T6) metal matrix composite. Materials Science and Engineering: A. 1993;171(1):213-221.

[80] San Marchi C, Cao F, Kouzeli M, Mortensen A. Quasistatic and dynamic compression of aluminum-oxide particle reinforced pure aluminum. Materials Science and Engineering: A. 2002;337(1):202-211.

[81] LLC. Influence factors for flow stress. Metal Pass; 2002.

[82] Callister WD, Rethwisch DG. Fundamentals of materials science and engineering: an integrated approach: John Wiley & Sons; 2012.

[83] Groover MP. Fundamentals of modern manufacturing: materials processes, and systems: John Wiley & Sons; 2007.

[84] Askeland DR, Fulay PP, Wright WJ. The science and engineering of materials: Thomson Engineering; 2011.

[85] Totten GE, Mackenzie DS. Handbook of aluminum: vol. 1: physical metallurgy and processes: CRC; 2003.

[86] Wefers K, Misra C. Oxides and hydroxides of aluminum. Aluminum Company of America, 92. 1987:1987.

[87] Bauccio M. ASM engineered materials reference book. 2nd ed. Materials Park, OH: ASM International; 1994.

[88] Gauthier MM, ASM International Handbook Committee. Engineered materials handbook. Desk ed. Materials Park, OH: ASM International; 1995.

APPENDIX

A.1) VF of alumina given in Table 2.1 of A-20 sample along with calculation of %Porosity are demonstrated below:

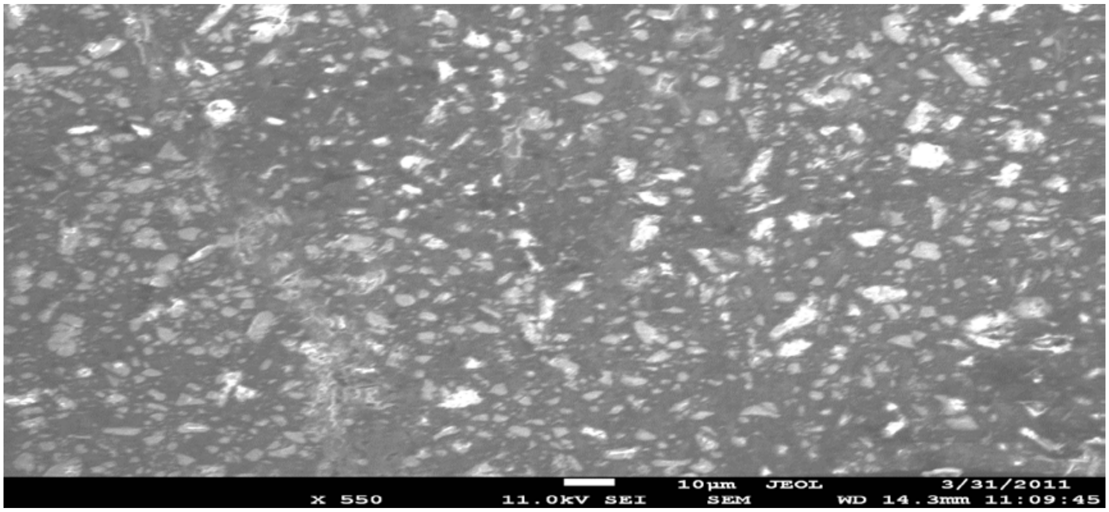

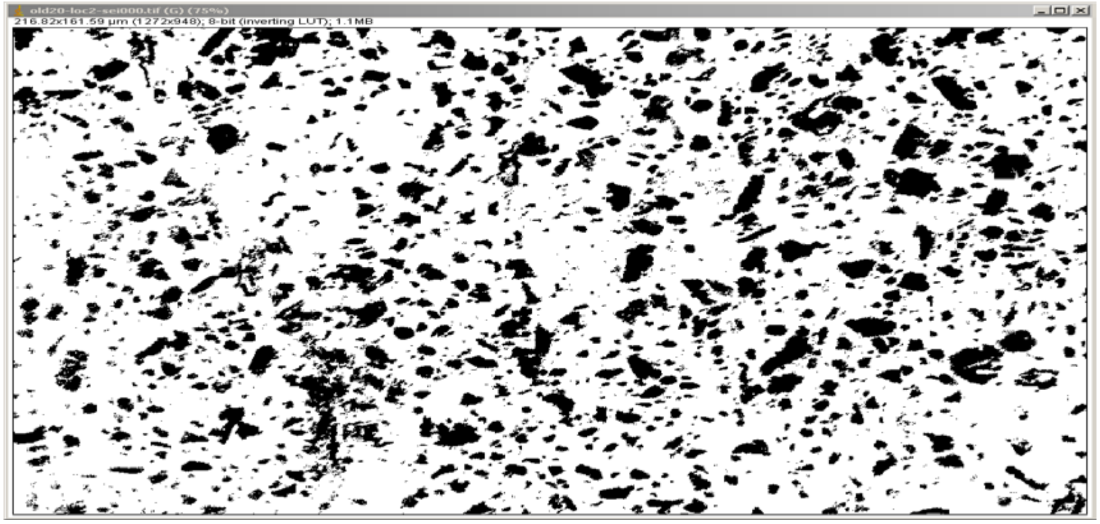

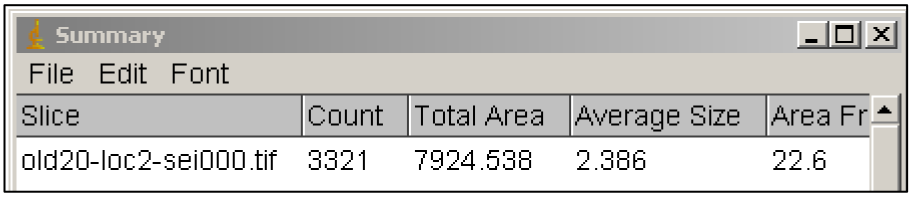

Slice	Count	Total Area	Average Size	Area Fr
old20-loc2-sei000.tif	3321	7924.538	2.386	22.6

To find porosity, brigthness & contrast were varied. Pores are identified as dark black regions as shown below.

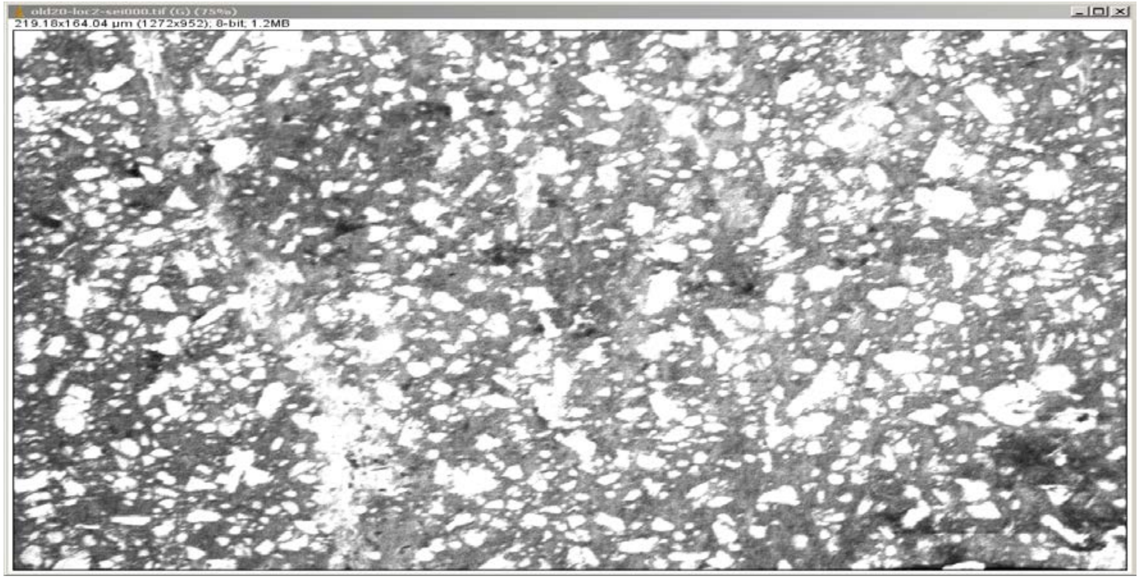

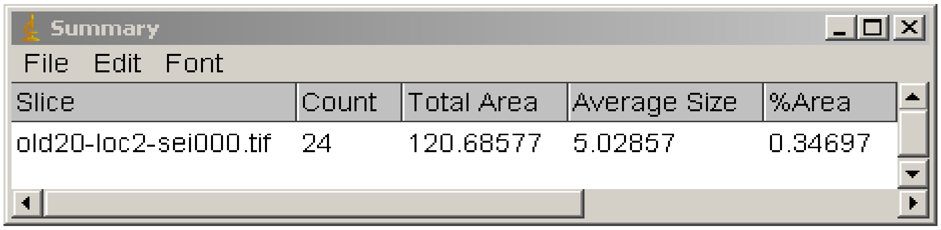

Slice	Count	Total Area	Average Size	%Area
old20-loc2-sei000.tif	24	120.68577	5.02857	0.34697

A.2) FE meshes of 10 and 20 vol% composite systems A and B:

a) FE meshes of A-10 composite samples

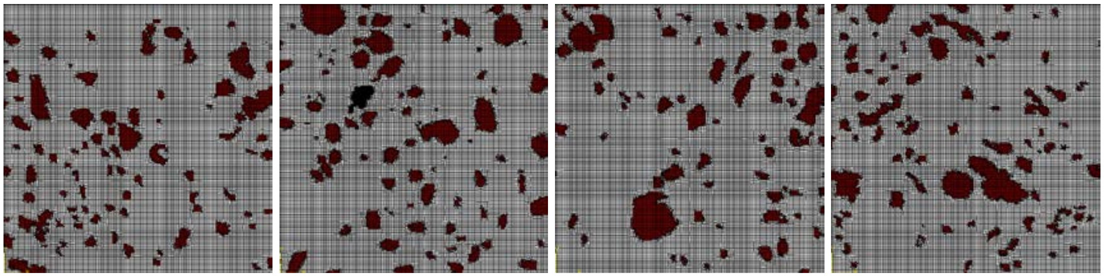

b) FE meshes of B-10 composite samples

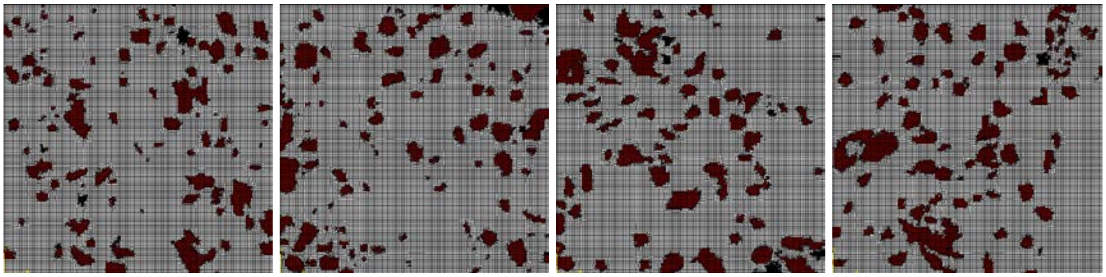

c) FE meshes of A-20 composite samples

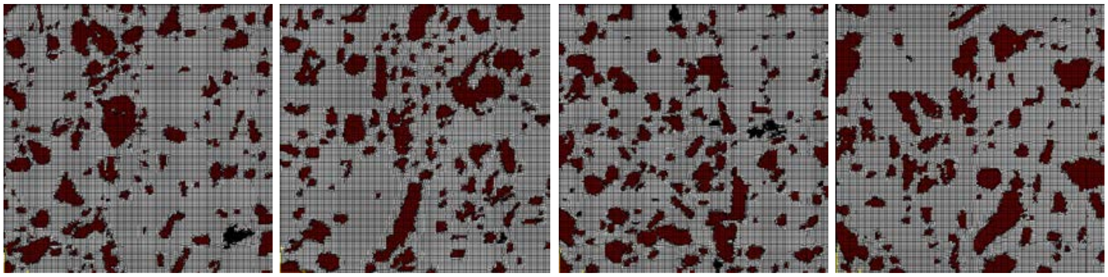

d) FE meshes of B-20 composite samples

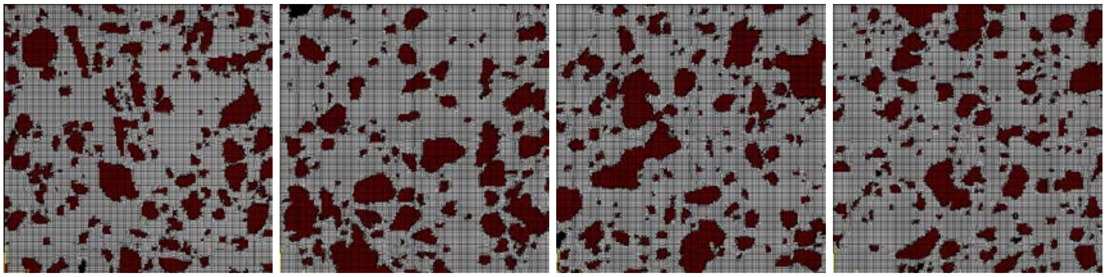

A.3) VF & porosity for FEmodel#5 in Figure 4.14b are calculated as shown below:

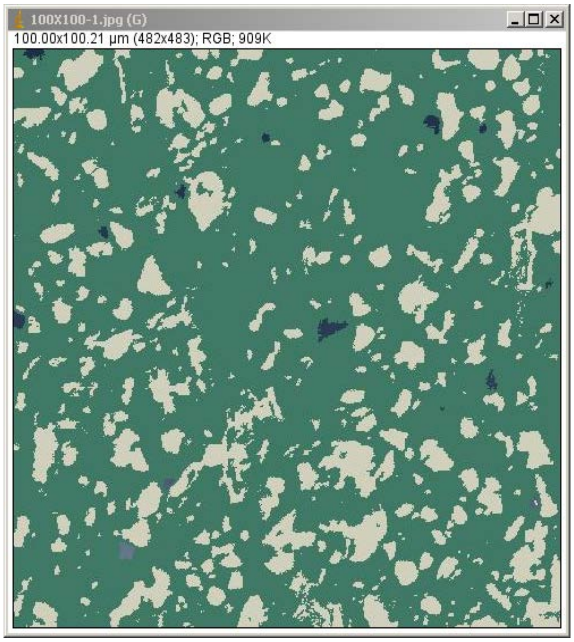

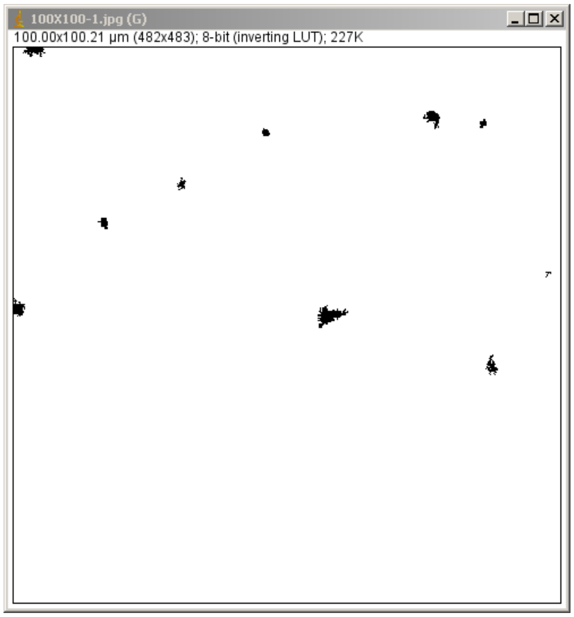

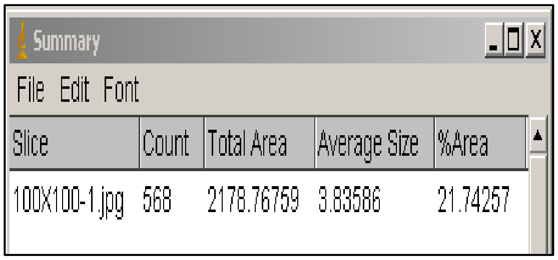

Slice	Count	Total Area	Average Size	%Area
100X100-1.jpg	568	2178.76759	3.83586	21.74257

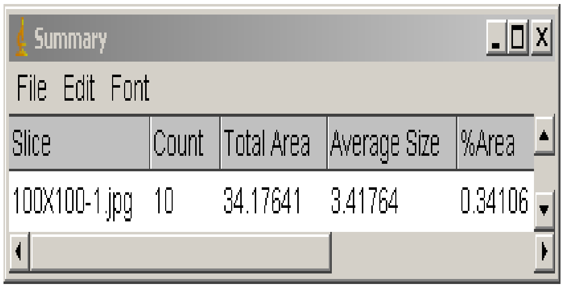

Slice	Count	Total Area	Average Size	%Area
100X100-1.jpg	10	34.17641	3.41764	0.34106

A.4) VF & porosity for FEmodel#6 in Figure 4.14b are calculated as shown below

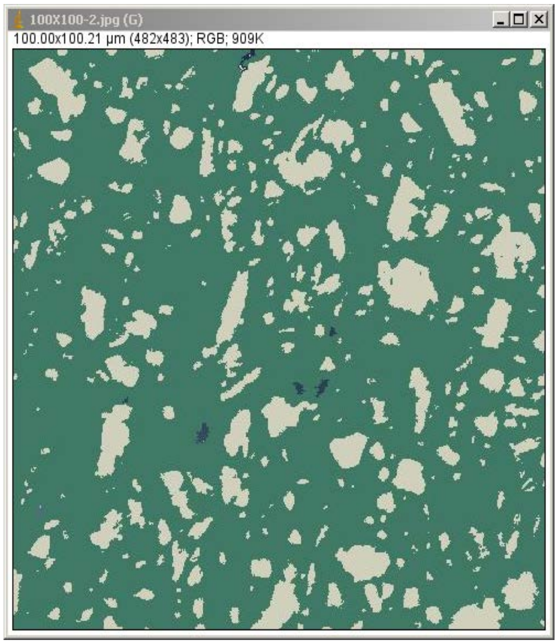

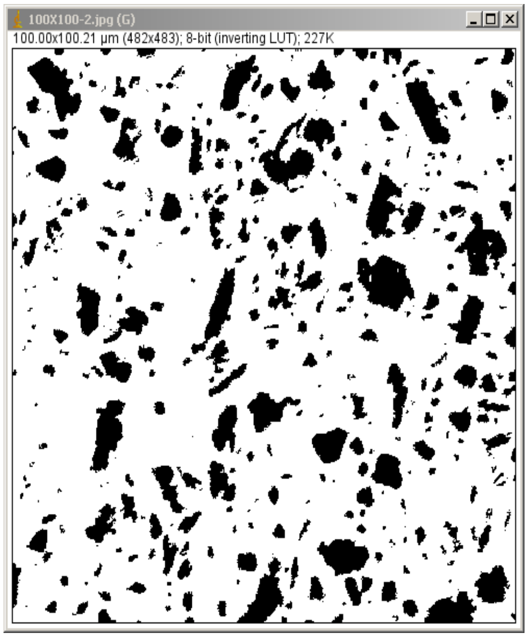

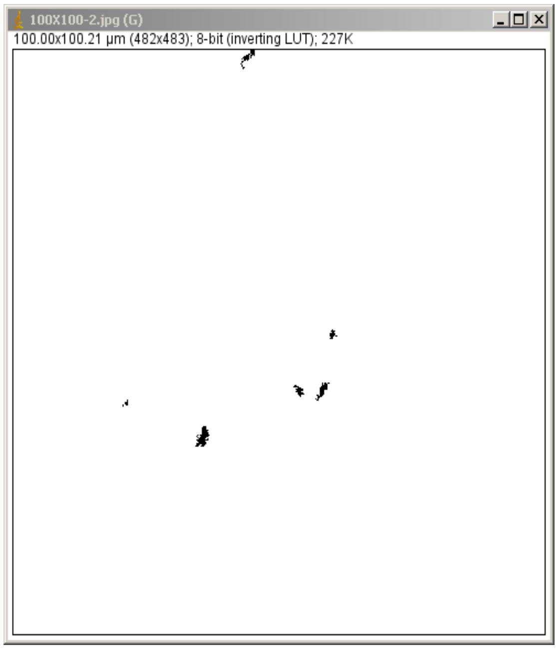

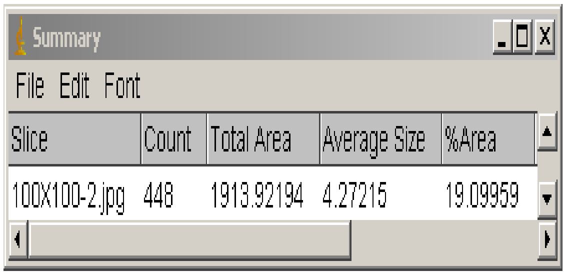

Slice	Count	Total Area	Average Size	%Area
100X100-2.jpg	448	1913.92194	4.27215	19.09959

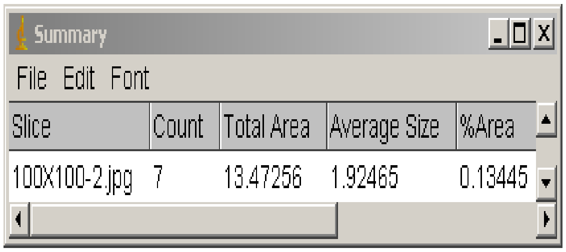

Slice	Count	Total Area	Average Size	%Area
100X100-2.jpg	7	13.47256	1.92465	0.13445

A.5) The following section shows VF& porosity determination for Figures 4.16-4.19 along with determination of centroids & area of each reinforcement and pores

a) For FE model #1:

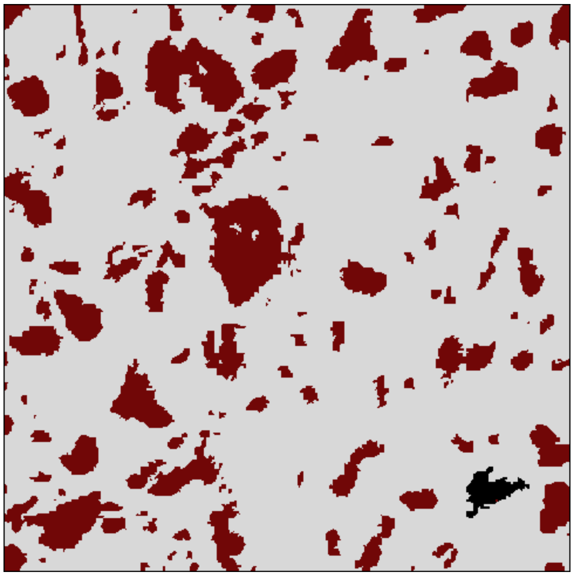

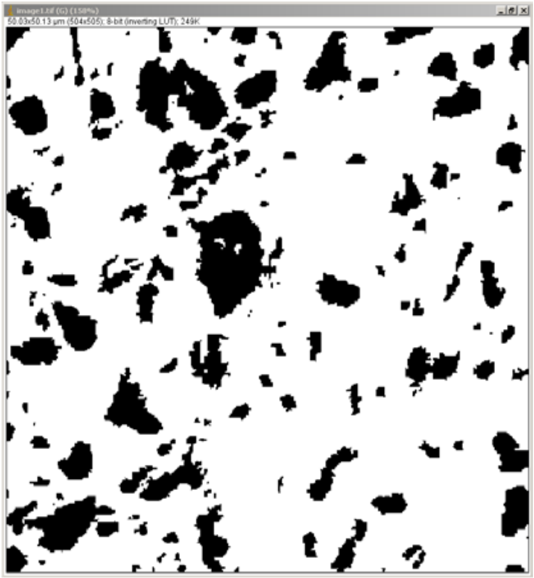

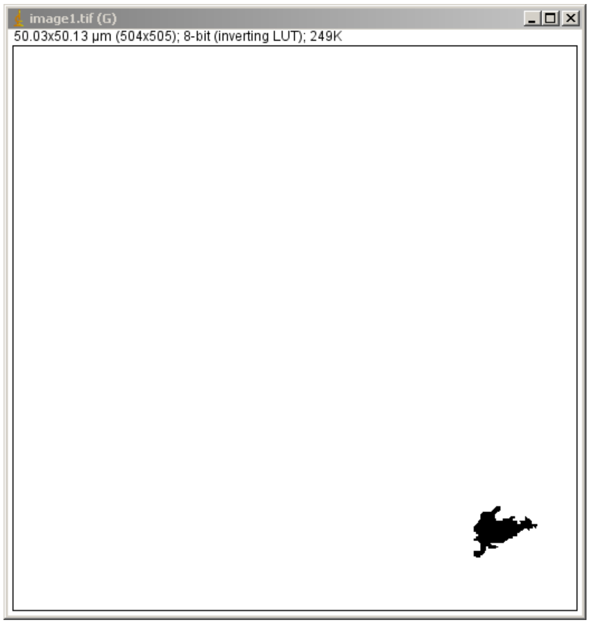

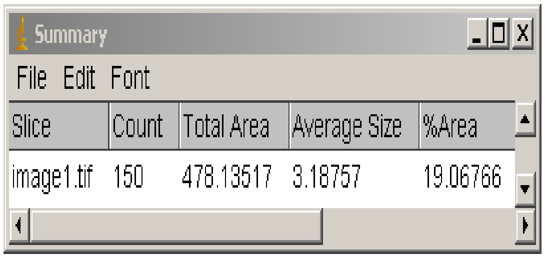

Slice	Count	Total Area	Average Size	%Area
image1.tif	150	478.13517	3.18757	19.06766

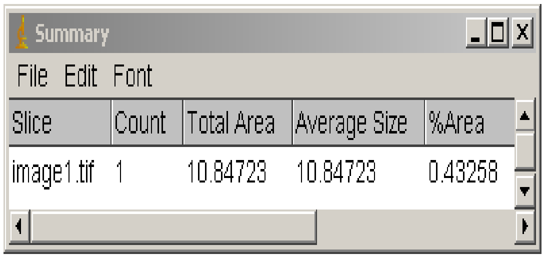

Slice	Count	Total Area	Average Size	%Area
image1.tif	1	10.84723	10.84723	0.43258

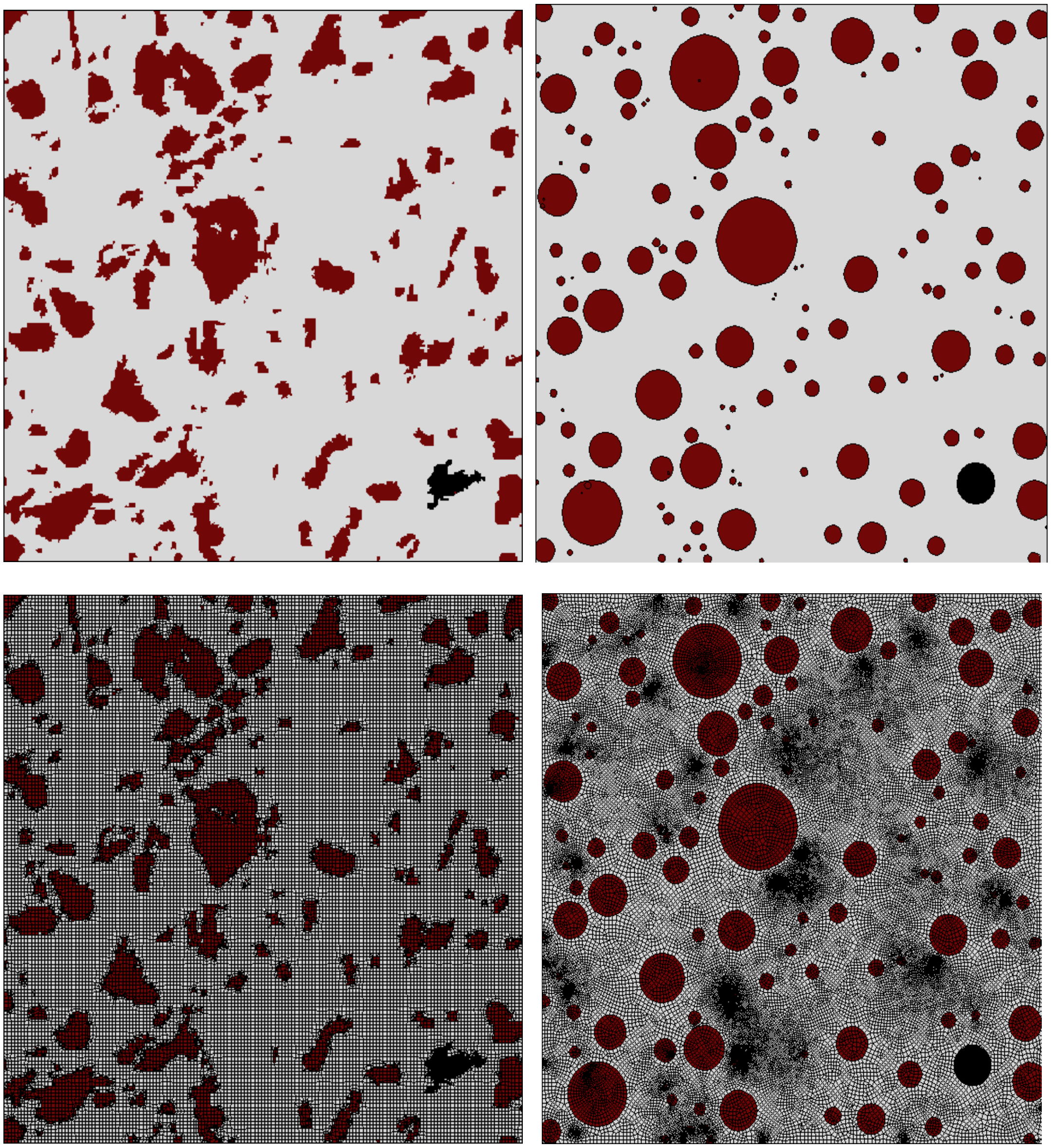

b) For FE model #2:

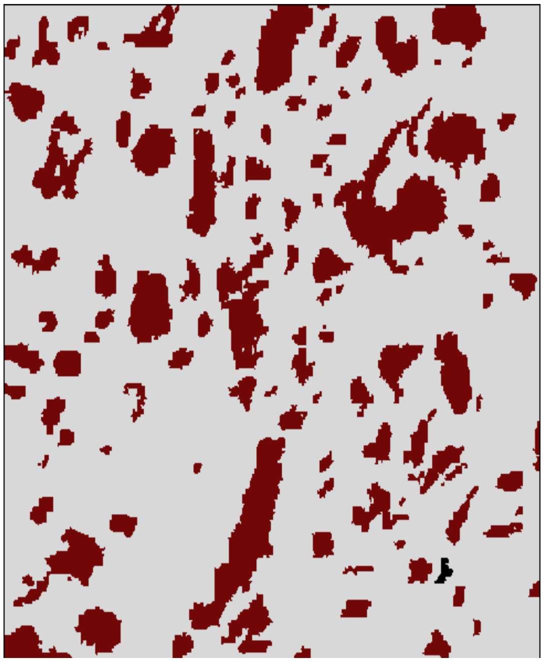

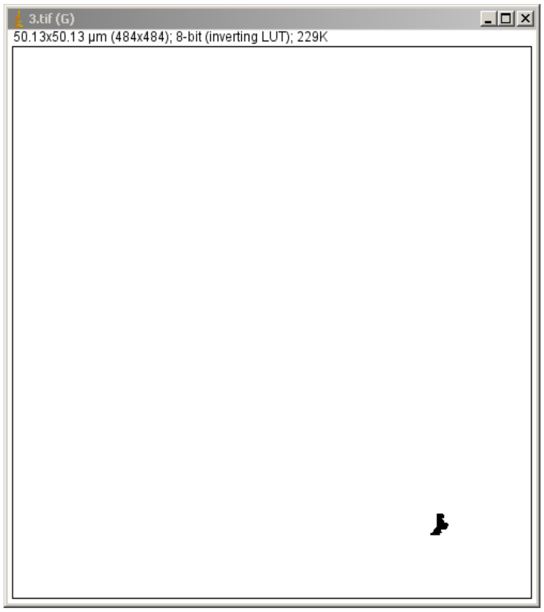

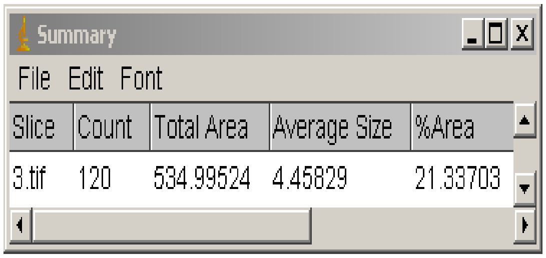

Slice	Count	Total Area	Average Size	%Area
3.tif	120	534.99524	4.45829	21.33703

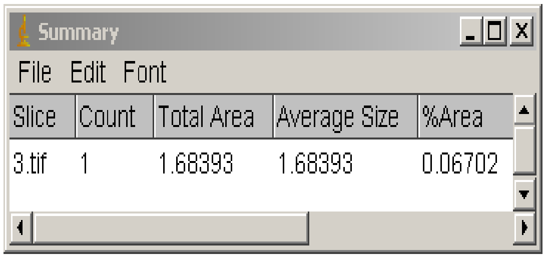

Slice	Count	Total Area	Average Size	%Area
3.tif	1	1.68393	1.68393	0.06702

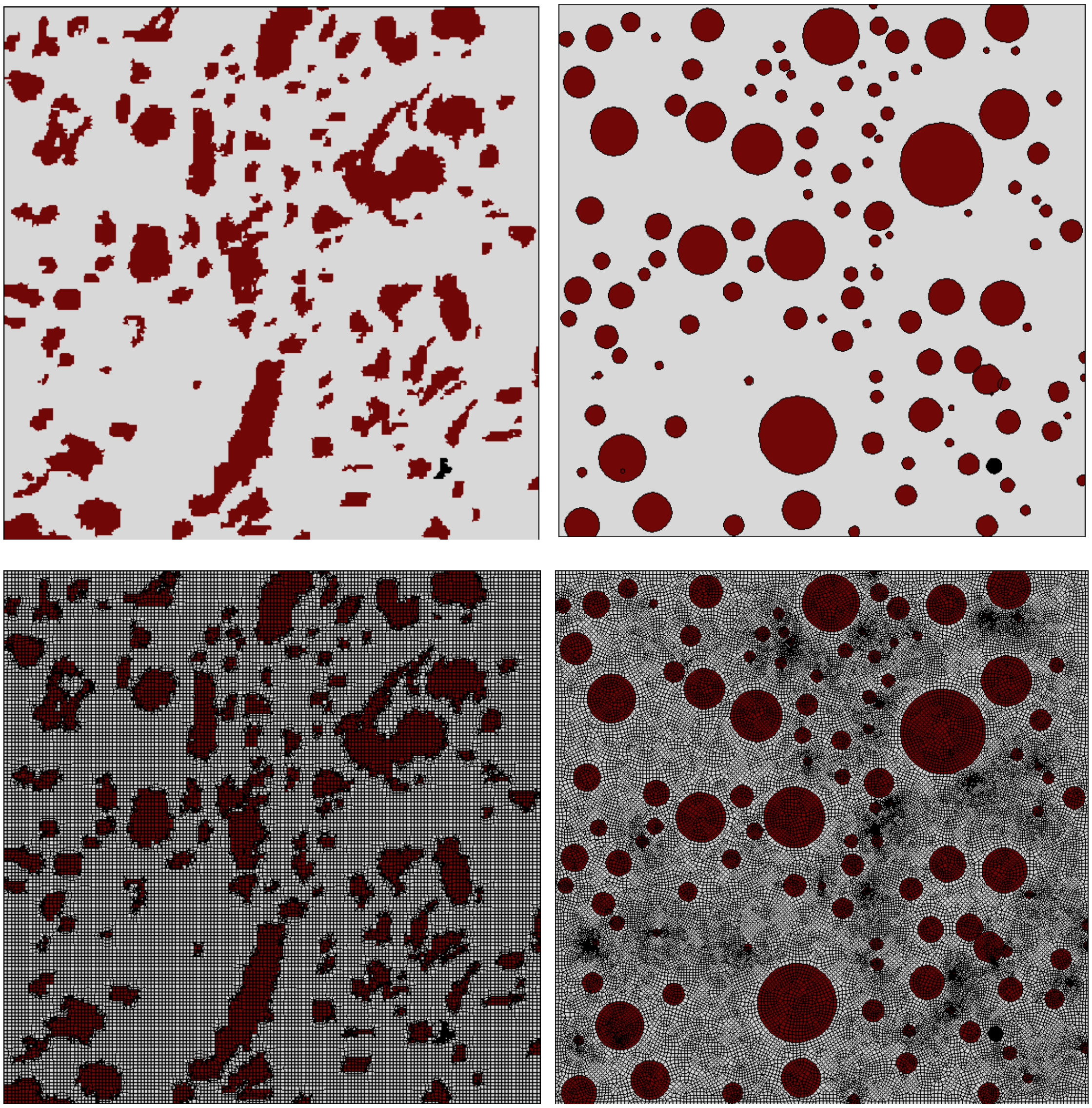

c) For FE model #3:

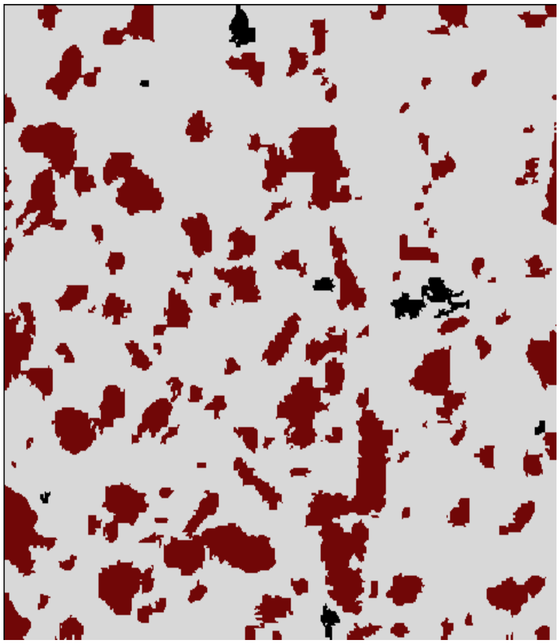

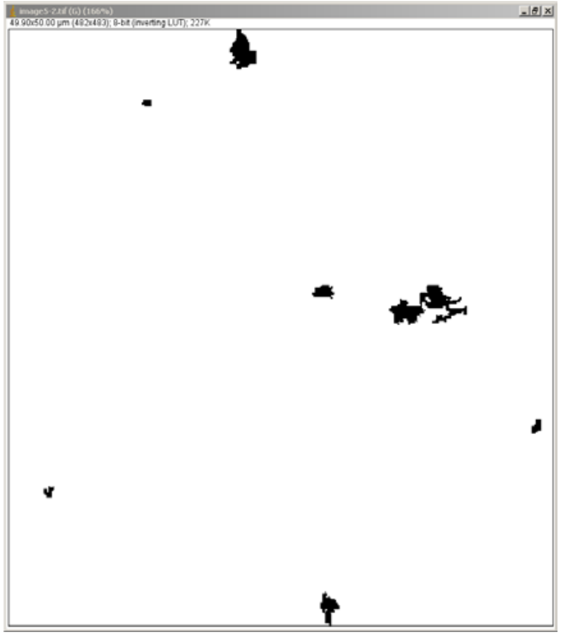

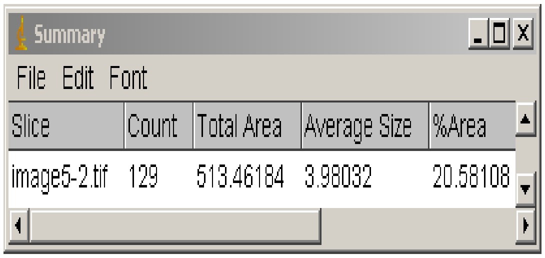

Slice	Count	Total Area	Average Size	%Area
image5-2.tif	129	513.46184	3.98032	20.58108

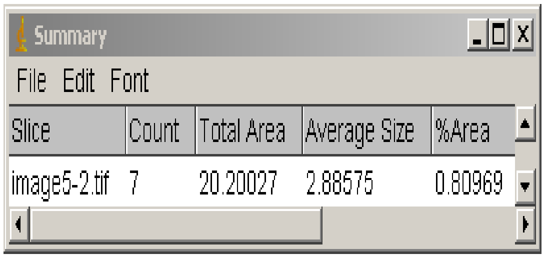

Slice	Count	Total Area	Average Size	%Area
image5-2.tif	7	20.20027	2.88575	0.80969

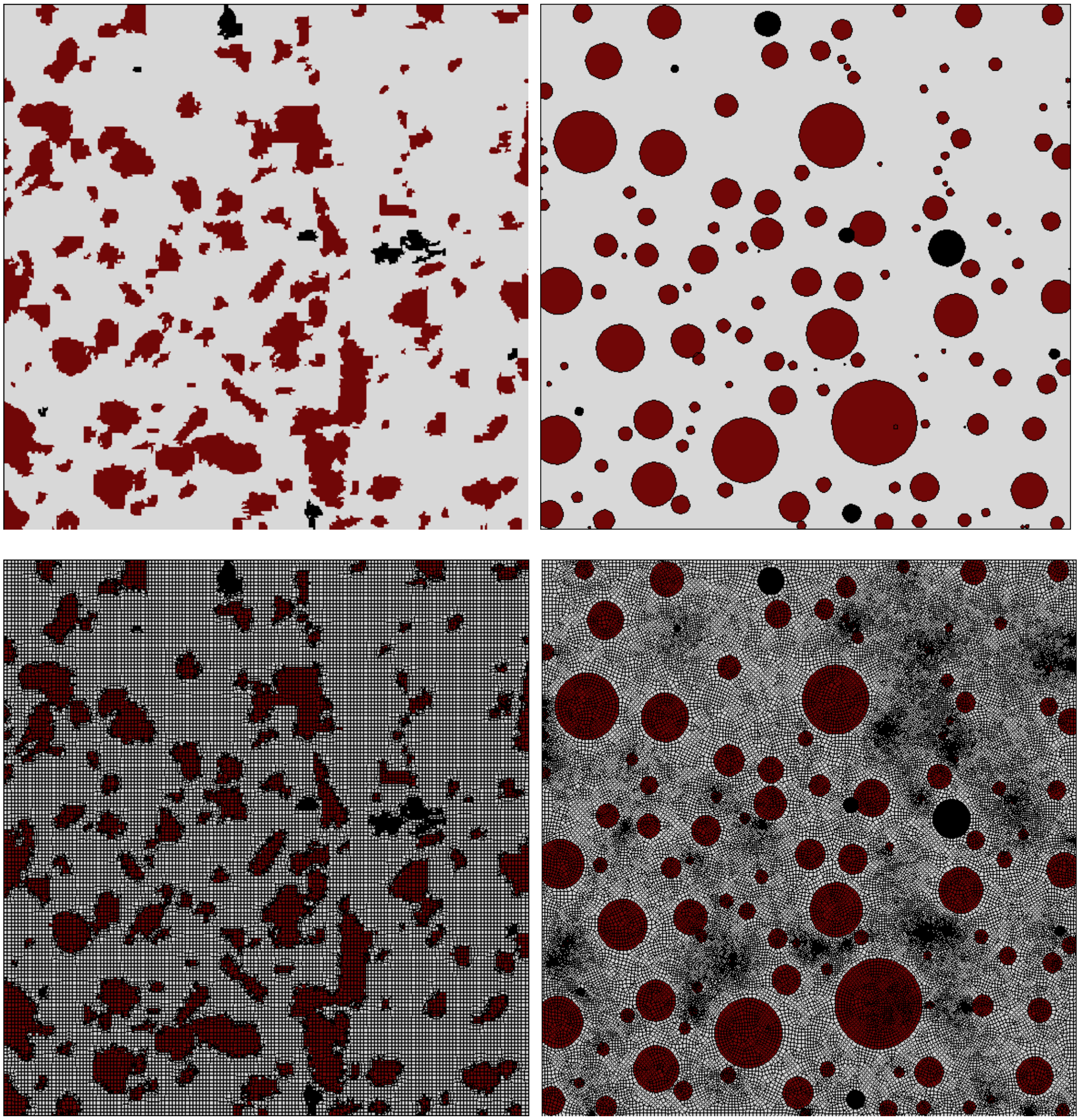

d) For FE model #4:

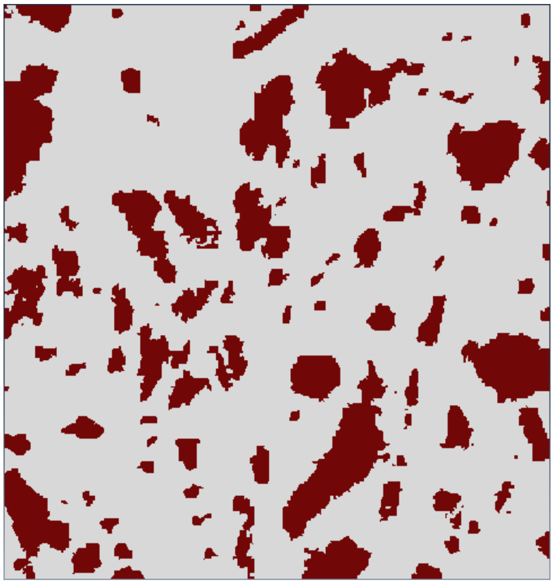

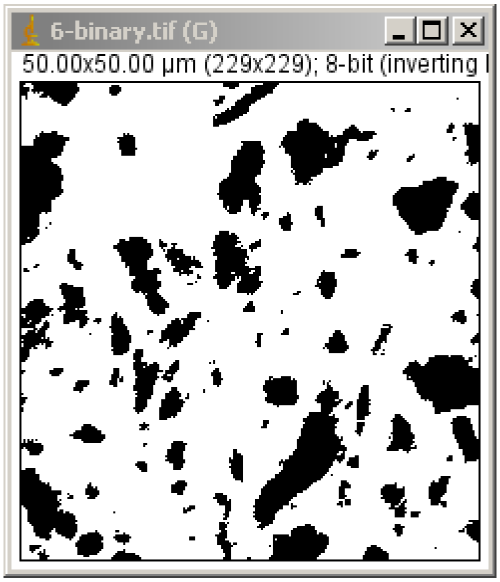

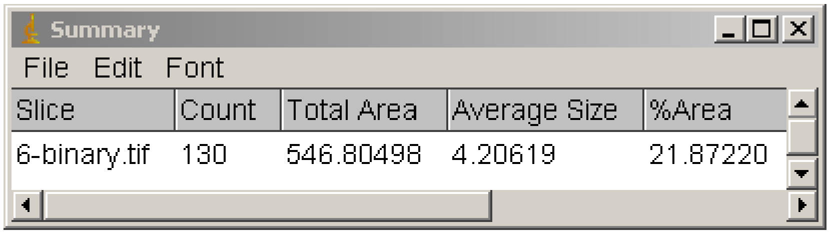

Slice	Count	Total Area	Average Size	%Area
6-binary.tif	130	546.80498	4.20619	21.87220

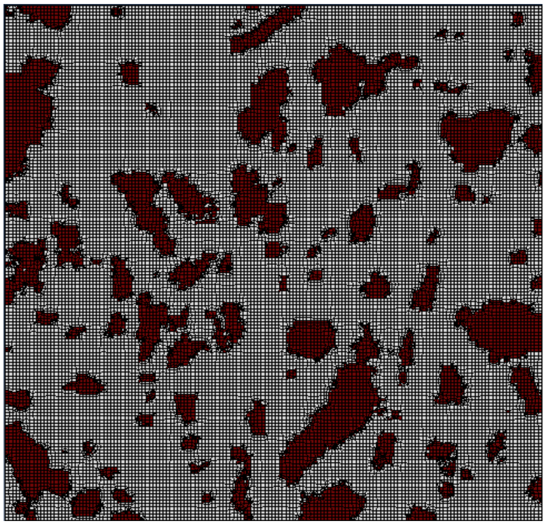

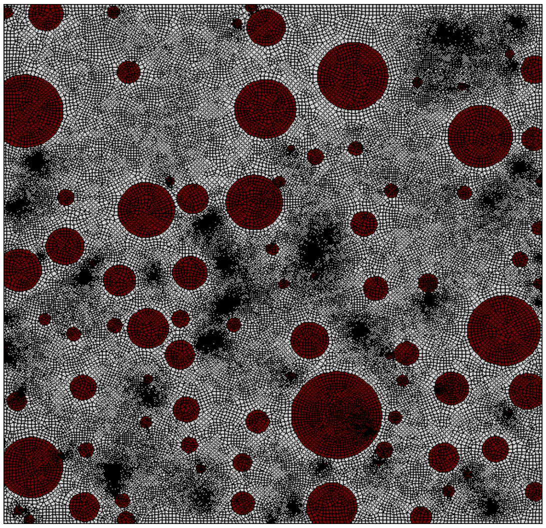

A.6) Actual shaped reinforcements replaced with circular shaped reinforcements

Using FEmodel#3(Fig 4.18), in the following section we show how centroid & area information of actual shaped reinforcement and pores are used in turn to determine center and a point on perimeter for circular shaped reinforcement and pores.

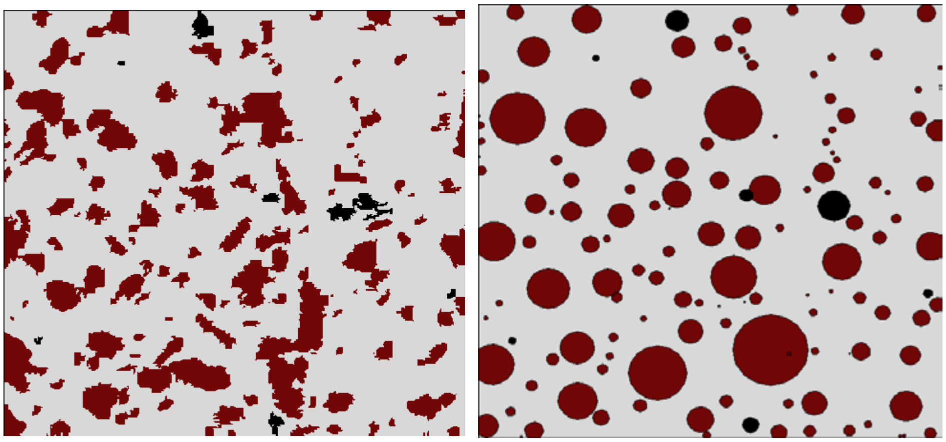

Reinforcement number	Area of actual shaped reinforcement (μm^2)	Centroid of actual shaped reinforcement		Perimeter of actual shaped reinforcement (μm)	Circularity of actual shaped reinforcement	Radius (r) for circular shaped reinforcement (μm)	Point on perimeter of circular shaped reinforcement	
		X	Y				$X^1=X+r$	$Y^1=Y$
1	2.58263	3.9808	49.157	7.44732	0.58516	0.906684433	4.88746	49.157
2	7.97294	11.681	48.292	16.29368	0.37739	1.593067991	13.2738	48.292
3	1.13593	33.837	49.388	4.5947	0.67616	0.601313353	34.4386	49.388
..	....	....	....	....	....	....	....	....
..	....	....	....	....	....	....	....	....
128	0.08573	45.445	0.207	0.99967	1	0.165192937	45.6103	0.207
129	0.04287	4.6325	0.1294	0.79264	0.85737	0.116815859	4.74933	0.1294

Pore number	Area of actual shaped pore (μm^2)	Centroid of actual shaped pore		Perimeter of actual shaped pore (μm)	Circularity of actual shaped pore	Radius (r) for circular shaped pore (μm)	Point on perimeter of circular shaped pore	
		X	Y				$X^1=X+r$	$Y^1=Y$
1	4.7902	21.425	48.135	10.15355	0.58389	1.234814973	22.6593	48.135
2	0.38579	12.667	43.843	2.32767	0.89478	0.350429409	13.0172	43.843
..	....	....	....	....	....	....	....	....
6	0.54653	3.6668	11.216	3.76654	0.48411	0.417092199	4.08392	11.216
7	2.45404	29.349	1.5096	8.38636	0.43847	0.883824187	30.2326	1.5096

ABAQUS Python code used to model the circular shaped reinforcements in a square matrix of size 0.05 mm X 0.05 mm

```
from abaqus import *
from abaqusConstants import *
import __main__

def vinayaka():
    import section
    import regionToolset
    import displayGroupMdbToolset as dgm
    import part
    import material
    import assembly
    import step
    import interaction
    import load
    import mesh
    import optimization
    import job
    import sketch
    import visualization
    import xyPlot
    import displayGroupOdbToolset as dgo
    import connectorBehavior
    s = mdb.models['Model-1'].ConstrainedSketch(name='__profile__', sheetSize=0.15)
    g, v, d, c = s.geometry, s.vertices, s.dimensions, s.constraints
    s.sketchOptions.setValues(decimalPlaces=6)
    s.setPrimaryObject(option=STANDALONE)
    s.rectangle(point1=(0.00, 0.00), point2=(0.05, 0.05))
    s.CircleByCenterPerimeter(center=(0.02142452,0.04813468), point1=(0.022659335,0.04813468))
    s.CircleByCenterPerimeter(center=(0.01266678,0.04384346), point1=(0.013017209,0.04384346))
    s.CircleByCenterPerimeter(center=(0.02887068,0.0279911), point1=(0.029588368,0.0279911))
    s.CircleByCenterPerimeter(center=(0.03831212,0.02676283), point1=(0.040063288,0.02676283))
    s.CircleByCenterPerimeter(center=(0.04843858,0.0166868), point1=(0.048934162,0.0166868))
    s.CircleByCenterPerimeter(center=(0.00366683,0.01121565), point1=(0.004083922,0.01121565))
    s.CircleByCenterPerimeter(center=(0.02934873,0.00150962), point1=(0.030232554,0.00150962))
    session.viewports['Viewport: 1'].view.fitView()
    p = mdb.models['Model-1'].Part(name='Part-1', dimensionality=TWO_D_PLANAR,
        type=DEFORMABLE_BODY)
    p = mdb.models['Model-1'].parts['Part-1']
    p.BaseShell(sketch=s)
    s.unsetPrimaryObject()
    p = mdb.models['Model-1'].parts['Part-1']
    session.viewports['Viewport: 1'].setValues(displayedObject=p)
    del mdb.models['Model-1'].sketches['__profile__']
    p = mdb.models['Model-1'].parts['Part-1']
    f, e, d1 = p.faces, p.edges, p.datums
    t = p.MakeSketchTransform(sketchPlane=f[0], sketchPlaneSide=SIDE1, origin=(
        0.0, 0.0, 0.0))
    s1 = mdb.models['Model-1'].ConstrainedSketch(name='__profile__',
        sheetSize=0.141, gridSpacing=0.003, transform=t)
    g, v, d, c = s1.geometry, s1.vertices, s1.dimensions, s1.constraints
    s1.sketchOptions.setValues(decimalPlaces=6)
    s1.setPrimaryObject(option=SUPERIMPOSE)
    p = mdb.models['Model-1'].parts['Part-1']
    p.projectReferencesOntoSketch(sketch=s1, filter=COPLANAR_EDGES)
    s1.CircleByCenterPerimeter(center=(0.00398078,0.04915702), point1=(0.004887464,0.04915702))
    s1.CircleByCenterPerimeter(center=(0.01168075,0.04829179), point1=(0.013273818,0.04829179))
    s1.CircleByCenterPerimeter(center=(0.03383726,0.04938767), point1=(0.034438573,0.04938767))
```

```
.............................................................................
.............................................................................
s1.CircleByCenterPerimeter(center=(0.01339116,0.00794017), point1=(0.013972281,0.00794017))
s1.CircleByCenterPerimeter(center=(0.00575985,0.00602881), point1=(0.006363994,0.00602881))
s1.CircleByCenterPerimeter(center=(0.0107184,0.00426607), point1=(0.012830682,0.00426607))
s1.CircleByCenterPerimeter(center=(0.03619912,0.00398114), point1=(0.037562592,0.00398114))
s1.CircleByCenterPerimeter(center=(0.04607762,0.00364068), point1=(0.0478092,0.00364068))
s1.CircleByCenterPerimeter(center=(0.02670807,0.00423013), point1=(0.027413776,0.00423013))
s1.CircleByCenterPerimeter(center=(0.0174424,0.00370547), point1=(0.018171876,0.00370547))
s1.CircleByCenterPerimeter(center=(0.03340554,0.00396634), point1=(0.033931182,0.00396634))
s1.CircleByCenterPerimeter(center=(0.00089975,0.00140185), point1=(0.002207025,0.00140185))
s1.CircleByCenterPerimeter(center=(0.00348698,0.00302795), point1=(0.00399614,0.00302795))
s1.CircleByCenterPerimeter(center=(0.02393626,0.00212148), point1=(0.025382293,0.00212148))
s1.CircleByCenterPerimeter(center=(0.01322771,0.00231647), point1=(0.01412494,0.00231647))
s1.CircleByCenterPerimeter(center=(0.04196644,0.00155495), point1=(0.042371078,0.00155495))
s1.CircleByCenterPerimeter(center=(0.00601963,0.00083133), point1=(0.007021063,0.00083133))
s1.CircleByCenterPerimeter(center=(0.03998065,0.00085111), point1=(0.040606972,0.00085111))
s1.CircleByCenterPerimeter(center=(0.03238118,0.00062135), point1=(0.03325725,0.00062135))
s1.CircleByCenterPerimeter(center=(0.03570654,0.00078536), point1=(0.036364727,0.00078536))
s1.CircleByCenterPerimeter(center=(0.04868339,0.00053543), point1=(0.04932051,0.00053543))
s1.CircleByCenterPerimeter(center=(0.02460622,0.00033999), point1=(0.025023312,0.00033999))
s1.CircleByCenterPerimeter(center=(0.04586957,0.00026915), point1=(0.046054259,0.00026915))
s1.CircleByCenterPerimeter(center=(0.04544513,0.00020704), point1=(0.045610323,0.00020704))
s1.CircleByCenterPerimeter(center=(0.00463251,0.0001294), point1=(0.004749326,0.0001294))
p = mdb.models['Model-1'].parts['Part-1']
f = p.faces
pickedFaces = f.getSequenceFromMask(mask=('[#1 ]', ), )
e1, d2 = p.edges, p.datums
p.PartitionFaceBySketch(faces=pickedFaces, sketch=s1)
s1.unsetPrimaryObject()
del mdb.models['Model-1'].sketches['__profile__']
```